The Study of Transition Metal Oxides using Dynamical Mean Field Theory

Hung The Dang

Submitted in partial fulfillment of the
Requirements for the degree
of Doctor of Philosophy
in the Graduate School of Arts and Sciences

COLUMBIA UNIVERSITY

2013

Abstract

The Study of Transition Metal Oxides using Dynamical Mean Field Theory

Hung The Dang

In this thesis, we study strong electron correlation in transition metal oxides. In the systems with large Coulomb interaction, especially the on-site interaction, electrons are much more correlated and cannot be described using traditional one-electron picture, thus the name "strongly correlated systems". With strong correlation, there exists a variety of interesting phenomena in these systems that attract long-standing interests from both theorists and experimentalists. Transition metal oxides (TMOs) play a central role in strongly correlated systems, exhibiting many exotic phenomena. The fabrication of heterostructures of transition metal oxides opens many possible directions to control bulk properties of TMOs as well as revealing physical phases not observed in bulk systems.

Dynamical mean-field theory (DMFT) emerges as a successful numerical method to treat the strong correlation. The combination of density functional and dynamical mean-field theory (DFT+DMFT) is a prospective *ab initio* approach for studying realistic strongly correlated materials. We use DMFT as well as DFT+DMFT methods as main approaches to study the strong correlation in these materials.

We focus on some aspects and properties of TMOs in this work. We study the magnetic properties in bulk TMOs and the possibility of enhancing the magnetic order in TMO heterostructures. We work on the metallic/insulating behaviors of these

systems to understand how the metal-insulator transition depends on the intrinsic parameters of materials. We also investigate the effect of a charged impurity to the neighborhood of a correlated material, which can be applied, for example, to the study of muon spin relaxation measurements in high-T_c superconductors.

Contents

List of Tables

List of Figures

Acknowledgments

First, I would like to thank my advisor, Prof. Andrew J. Millis, for his instructions and encouragement during my time in Columbia University. I also appreciate his patience in leading me into this field of physics. Many lessons and ideas that I have learned from him will be useful for my life and career.

I thank Philipp Werner and Emanuel Gull for their computer program, which is a fundamental part for most of my calculations. I also need to thank Prof. Chris Marianetti for useful collaboration. To the students and postdocs, Emanuel Gull, 'Sunny' Xin Wang, Chungwei Lin, Nan Lin, Junichi Okamoto, Seyoung Park, Chris Ching-Kit Chan, Jemma Wolcott-Green, Hyowon Park, Hanghui Chen, Ara Go, Dominika Zgid, Bayo Lau and many other people in the department that I have a chance to work with but forget to name here, I thank them all for many fruitful discussions and all their help during my time in Columbia. I must also thank Armin Comanac, the formal student whom I have never met, but his wonderful thesis and codes are useful for me until even the last day in the research group.

I would like to express my appreciation to the professors in the defense committee - Boris Altshuler, Robert Mawhinney, Yasutomo Uemura and David Reichman - for their careful examination on my dissertation. I

also offer my thanks to Vietnam Education Foundation for their support during my Ph.D program.

Finally, I would like to thank my parents and my wife for their great support and patience. They have given me the motivation and determination to go to the end of this “long and winding road”.

To my family

Chapter 1

Introduction

1.1 Transition metal oxides

Transition metal oxides (TMOs) are materials composed by at least a transition metal atom M and oxygen. They can be mono-oxide, an important class containing only transition metal and oxygen atoms such as MnO, NiO, or dioxides such as VO_2, or more complicated structures. This thesis will mainly focus on the most widely studied case, the perovskite structure RMO_3 with R an alkaline or rare earth atom, M a transition metal and O the oxygen. Examples include $LaMnO_3$, $SrVO_3$, etc.

In free space, the outermost shells of a transition metal element contain a partially filled d shell together with filled s shell. Electron configurations of other transition metal elements can be found in the upper panel of Figure 1.1. In oxide compounds, transition metal can easily combine with oxygen to form covalent bond, it gives all s electrons and some d electrons to oxygen, there are only d electrons remaining in its outer shell. The alkaline or rare earth, if included, is a source to provide additional electrons to oxygen and, depending on its atomic radius, can distort the lattice structure. For example, Ti has the electron configuration $[Ar]3d^24s^2$; in $LaTiO_3$, each La or Ti gives 3 electrons to oxygen to become La^{+3} or Ti^{+3} so that each oxygen atom receive 2 electrons and becomes O^{-2}, Ti^{+3} has configuration $[Ar]3d^1$, thus there is only 1 d electron near the Fermi level (see the lower panel of Figure 1.1). Therefore, the basic electronic structure of TMOs has transition metal d bands as frontier bands,

21	22	23	24	25	26	27	28	29	30
44.955910	47.867	50.9415	51.9961	54.938049	55.845	58.933200	58.6934	63.546	65.409
Sc	Ti	V	Cr	Mn	Fe	Co	Ni	Cu	Zn
$^2D_{3/2}$ 1.36	$^3F_2$ 1.54	$^4F_{3/2}$ 1.63	$^7S_3$ 1.66	$^6S_{5/2}$ 1.55	$^5D_4$ 1.83	$^4F_{9/2}$ 1.88	$^3F_4$ 1.91	$^2S_{1/2}$ 1.90	$^1S_0$ 1.65
Scandium	Titanium	Vanadium	Chromium	Manganese	Iron	Cobalt	Nickel	Copper	Zinc
2.985 6.5615	4.507 6.8281	6.11 6.7462	7.14 6.7665	7.47 7.4340	7.874 7.9024	8.9 7.8810	8.908 7.6398	8.92 7.7264	7.14 9.3942
1541 2830	1668 3287	1910 3407	1907 2671	1246 2061	1538 2861	1495 2927	1455 2913	1084.62 2927	419.53 907
(m) 162 HCP	(m) 147 HCP	(m) 134 BCC	(m) 128 BCC	(m) 127 §cubic	(m) 126 BCC	(m) 125 HCP	(m) 124 FCC	(m) 128 FCC	(m) 134 §hex
[Ar] $3d^1\,4s^2$ +3	[Ar] $3d^2\,4s^2$ +2,3,4	[Ar] $3d^3\,4s^2$ +2,3,4,5	[Ar] $3d^5\,4s^1$ +2,3,6	[Ar] $3d^5\,4s^2$ +2,3,4,6,7	[Ar] $3d^6\,4s^2$ +2,3	[Ar] $3d^7\,4s^2$ +2,3	[Ar] $3d^8\,4s^2$ +2,3	[Ar] $3d^{10}\,4s^1$ +1,2	[Ar] $3d^{10}\,4s^2$ +2
39	40	41	42	43	44	45	46	47	48
88.90585	91.224	92.90638	95.94	(98)	101.07	102.90550	106.42	107.8682	112.411
Y	Zr	Nb	Mo	Tc	Ru	Rh	Pd	Ag	Cd
$^2D_{3/2}$ 1.22	$^3F_2$ 1.33	$^6D_{1/2}$ 1.60	$^7S_3$ 2.16	$^6S_{5/2}$ 1.9	$^5F_5$ 2.20	$^4F_{9/2}$ 2.28	$^1S_0$ 2.20	$^2S_{1/2}$ 1.93	$^1S_0$ 1.69
Yttrium	Zirconium	Niobium	Molybdenum	Technetium	Ruthenium	Rhodium	Palladium	Silver	Cadmium
4.472 6.2173	6.511 6.6339	8.57 6.7589	10.28 7.0924	11.5 7.28	12.37 7.3605	12.45 7.4589	12.023 8.3369	10.49 7.5762	8.65 8.9938
1526 3345	1855 4409	2477 4744	2623 4639	2157 4265	2334 4150	1964 3695	1554.9 2963	961.78 2162	321.07 767
(m) 180 HCP	(m) 160 HCP	(m) 146 BCC	(m) 139 BCC	(m) 136 HCP	(m) 134 HCP	(m) 134 FCC	(m) 137 FCC	(m) 144 FCC	(m) 151 §hex
[Kr] $4d^1\,5s^2$ +3	[Kr] $4d^2\,5s^2$ +4	[Kr] $4d^4\,5s^1$ +3,5	[Kr] $4d^5\,5s^1$ +2,3,4,5,6	[Kr] $4d^5\,5s^2$ +4,7	[Kr] $4d^7\,5s^1$ +2,3,4,6,8	[Kr] $4d^8\,5s^1$ +2,3,4	[Kr] $4d^{10}$ +2,4	[Kr] $4d^{10}\,5s^1$ +1	[Kr] $4d^{10}\,5s^2$ +2
Lanthanide Series	72	73	74	75	76	77	78	79	80
	178.49	180.9479	183.84	186.207	190.23	192.217	195.078	196.96655	200.59
	Hf	Ta	W	Re	Os	Ir	Pt	Au	Hg
	$^3F_2$ 1.3	$^4F_{3/2}$ 1.5	$^5D_0$ 2.36	$^6S_{5/2}$ 1.9	$^5D_4$ 2.2	$^4F_{9/2}$ 2.2	$^3D_3$ 2.28	$^2S_{1/2}$ 2.54	$^1S_0$ 2
	Hafnium	Tantalum	Tungsten	Rhenium	Osmium	Iridium	Platinum	Gold	Mercury
	13.31 6.8251	16.65 7.5496	19.25 7.8640	21.02 7.8335	22.61 8.4382	22.65 8.9670	21.09 8.9588	19.3 9.2255	13.534 10.4375
	2233 4603	3017 5458	3422 5555	3186 5596	3033 5012	2466 4428	1768.3 3825	1064.18 2856	-38.83 356.73
	(m) 159 HCP	(m) 146 BCC	(m) 139 BCC	(m) 137 HCP	(m) 135 HCP	(m) 136 FCC	(m) 139 FCC	(m) 144 FCC	(m) 151 §rhom.
	[Xe] $4f^{14}\,5d^2\,6s^2$ +4	[Xe] $4f^{14}\,5d^3\,6s^2$ +5	[Xe] $4f^{14}\,5d^4\,6s^2$ +2,3,4,5,6	[Xe] $4f^{14}\,5d^5\,6s^2$ +2,4,6,7,-1	[Xe] $4f^{14}\,5d^6\,6s^2$ +2,3,4,6,8	[Xe] $4f^{14}\,5d^7\,6s^2$ +2,3,4,6	[Xe] $4f^{14}\,5d^9\,6s^1$ +2,4	[Xe] $4f^{14}\,5d^{10}\,6s^1$ +1,3	[Xe] $4f^{14}\,5d^{10}\,6s^2$ +1,2

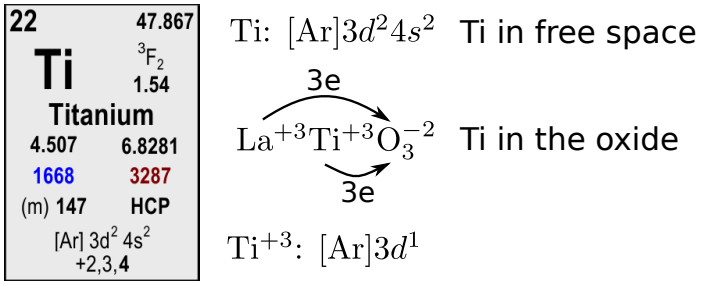

Figure 1.1: Upper panel: The part of transition metal elements in the periodic table. The electron configuration is at the bottom of each element block. From www.vertex42.com. Lower panel: Electron configuration of Ti element in the free space and in the perovskite $LaTiO_3$.

staying at the Fermi level, the second most energetic bands are oxygen p bands, other bands have less significant impact to the electronic properties of these materials.

Keeping the partially filled d bands as the frontier bands and varying the filling of the d bands, many physics may occur. By changing the transition metal from light to heavy elements or manipulating $R_kM_mO_n$ compound by adjusting k, m, n or choosing the appropriate rare earth R, the number of d electrons can be nominally varied from 0 to 10. For example, TMOs in perovskite forms RMO_3 can have d electron varying by replacing M by transition metals in the 4^{th} row of the periodic table, e.g. in the series $LaTiO_3$, $LaVO_3$, ..., $LaNiO_3$, the nominal number of electrons in the d shell changes from d^1 to d^7. Depending on n, the corresponding d^n systems may exhibit

different physics. To list a few, one can find Mott insulator in d^1, d^2 or d^3 systems such as $LaTiO_3$, $YTiO_3$, $LaVO_3$ or $LaCrO_3$ accompany with ferromagnetic or antiferromagnetic order [Imada et al. (1998)], the colossal magnetoresistance in manganites $R_{1-x}A_xMnO_3$ (R is a trivalent and A is a divalent atom) [Jonker and Van Santen (1950); Jin et al. (1994)], or the d^9 systems, cuprates, the parent compound for high temperature superconductors [Bednorz and Müller (1986)].

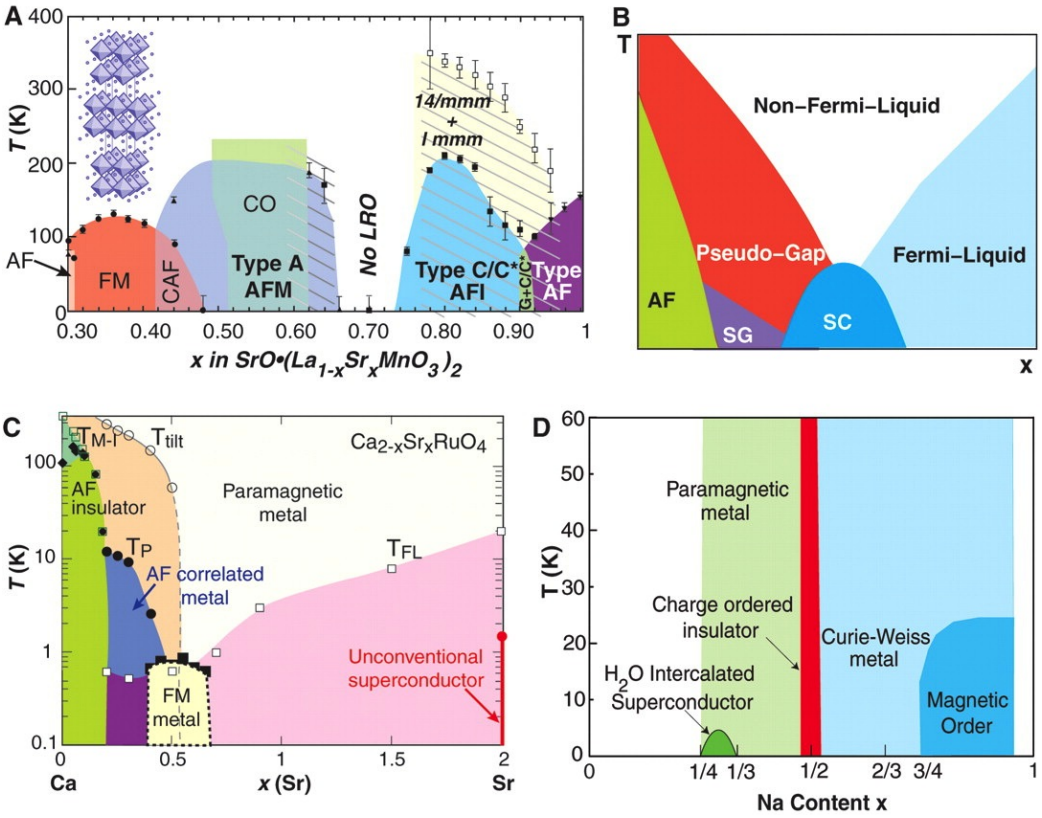

Figure 1.2: Phase diagrams of several strongly correlated materials: (A) Bilayer manganites $La_{2-2x}Sr_{1+2x}Mn_2O_7$, (B) Schematic phase diagram for high T_c superconductors, (C) Single-layer ruthenates $Ca_{2-x}Sr_xRuO_4$, (D) Layered cobaltate Na_xCoO_2. From Dagotto (2005).

The interesting physics mentioned above is because of the frontier d electrons. The d electrons are localized, their wavefunctions are restricted in a small space around the atom. The d electrons are distributed inside a sphere with radius of

about 0.5Å around the atom, while the typical lattice constant for e.g. perovskite is 4Å, there is almost no overlap between d orbitals. As a result, the chance that d electrons at the transition metal site meet each other are higher than other bands, the onsite Coulomb interaction is thus larger. These electrons become highly correlated and cannot be described using one-electron picture, it requires more modern methods to treat this correlation. However, the strong correlation is the reason for very rich physics in TMOs, represented by complicated phase diagrams. Figure 1.2 are the phase diagrams of some representative TMOs. As illustrated in Fig. 1.2, with a vast number of materials and various behaviors on its phase diagram, TMO is considered as the central topic of strongly correlated systems.

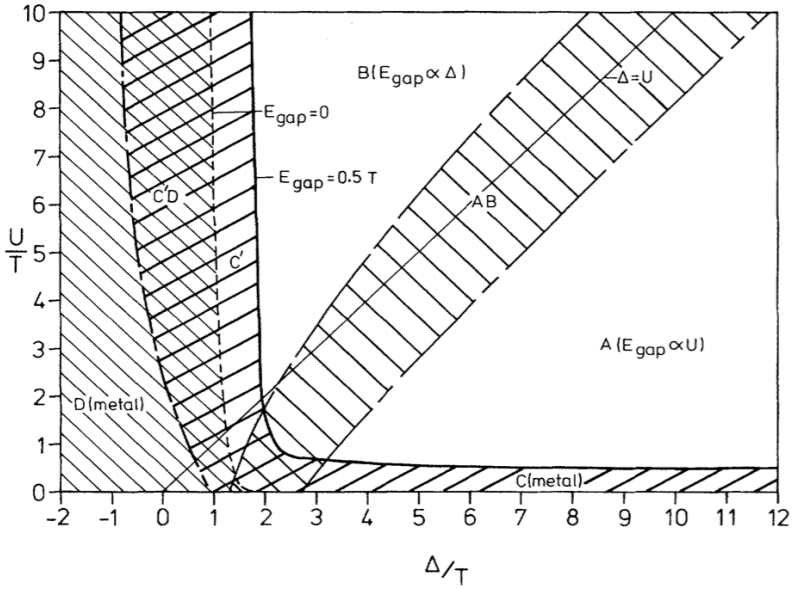

Figure 1.3: Zaanen-Sawatzky-Allen diagram: (A) charge-transfer insulator, (B) Mott-Hubbard insulator, (C) intermediate regime. From Zaanen et al. (1985).

The most famous classification for TMOs is given by Zaanen, Sawatzky and Allen [Zaanen et al. (1985)]. In this picture, the magnitude of the onsite interaction and the relative position between oxygen p bands and transition metal d bands can give different behaviors for a TMO. Figure 1.3 shows their diagram for the classification.

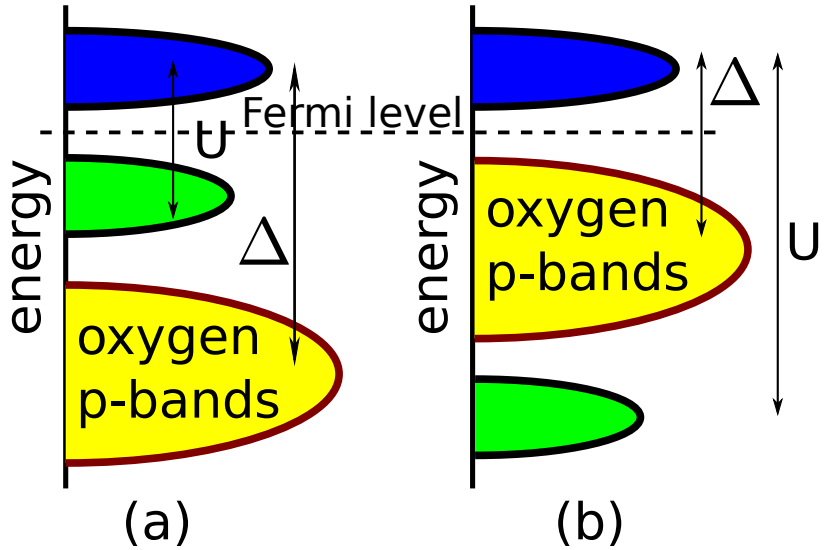

Figure 1.4: Schematic energy levels for (a) Mott-Hubbard insulator and (b) charge-transfer insulator.

The onsite interaction is dominated by the Hubbard value U, the energy cost for increasing occupancy in a d site, it thus contributes a charging energy $UN_d(N_d - 1)$. The distance between d and p bands is characterized by the charge transfer energy Δ, the energy needed to excite an electron from a p band to a d band and create a hole in that p band. When the charge transfer energy is larger than the onsite interaction ($\Delta > U$), the low energy physics is dominated by the onsite interaction, the Hubbard value U, if U is large enough, the material becomes a Mott insulator, thus the name Mott-Hubbard regime (Fig. 1.4a). In contrast, when the onsite interaction is larger $U > \Delta$, the physics is controlled by the charge transfer energy, depending on how close the oxygen bands to the Fermi level, the system can be a metal or a charge-transfer insulator (Fig. 1.4b). It is so-called charge transfer regime. There is also an intermediate region where two types of excitations are of similar magnitude. Therefore in their work, Zaanen, Sawatzky and Allen point out that oxygen bands can play an important role in controlling the physics of these materials.

According Zaanen et al. (1985), going along the series of transition metals, TMOs in which the filling of d bands is low ("early transition metal oxides" with transition

metal elements on the left of Figure 1.1 such as Ti, V, Cr) have oxygen p bands far from the Fermi level, the low energy excitations between frontier d bands are more important, they are assumed as belonging to the Mott-Hubbard regime. On the other hand, materials with large filling of the d bands ("late transition metal oxides" with transition metal elements on the right of Figure 1.1 such as Ni, Cu) have large positive ion charge at transition metal ion, it attracts electrons at oxygen bands more strongly. As a result, the oxygen p bands rise to higher energies, closer to the Fermi level. These materials are identified as belonging to the charge transfer regime. TMOs with nearly half-filled d bands (nominally around d^5 with elements in the middle of Figure 1.1) are in the crossover between the Mott-Hubbard and the charge-transfer regimes.

In this thesis, we will consider the oxygen bands and the charge transfer physics together with the correlated d bands and study the assumption given by the work of Zaanen, Sawatzky and Allen. We will show that the oxygen bands, via the p-d covalency, are also important even for the early TMOs.

1.2 Heterostructures of transition metal oxides

Pioneering by the experimental work of Ohtomo and Hwang (2004) and theoretical study of Okamoto and Millis (2004), the topic of heterostructures of transition metal oxides has gained more attention recently. By fabricating a heterostructure (superlattices, quantum well structures, etc.) composed of two TMOs or a TMO with a band insulator, one can obtain a new artificial material with significant charge density of high mobility confined at the interface. Heterostructure is promising to have a wide range of applications, it is thus a potential structure for new electronic devices [Mannhart et al. (2008)].

For example, the pioneering work from Ohtomo and Hwang (2004) considered the interface of SrTiO3 and $LaAlO_3$. In bulk form, both materials are insulators with large band gaps: $3.2eV$ for $SrTiO_3$ and $5.6eV$ for $LaAlO_3$ [Ohtomo and Hwang (2004)]. By stacking two band insulators, $SrTiO_3$ on $LaAlO_3$, depending on the termination, they obtained the interface which is metallic with half an electron per site and high mobility (LaO/TiO_2 interface) or insulating with half a hole per site (AlO_2/SrO interface).

More interestingly, with the very rich physics already in the bulk TMOs, the fabrication for heterostructures and heterointerfaces allows to enter new phases not observed in the corresponding bulk systems [Millis (2011)]. Heterostructure therefore can give possibilities to obtain and control properties of TMOs, it becomes a research interest for many scientists. Starting from the study of $SrTiO_3/LaAlO_3$ interface by Ohtomo and Hwang, many exotic phenomena have been found. They are ferromagnetism [Ariando et al. (2011)], superconductivity [Reyren et al. (2007)], the coexistence of ferromagnetism and superconductivity is observed experimentally [Bert et al. (2011); Li et al. (2011)] at this interface. The fabrication of thin films of TMOs can also drive material through metal-insulator transition, e.g. $SrVO_3$, a well-known moderately correlated metal, becomes insulating when the thickness of its thin film is within a few layers [Yoshimatsu et al. (2010, 2011)].

An important example for phases found in heterostructure but not in bulk system is the ferromagnetism observed in vanadium-based oxide superlattices [Lüders et al. (2009)]. When there are m layers of $LaVO_3$ sandwiched by one layer of $SrVO_3$ in a unit cell to form the superlattice $(LaVO_3)_m(SrVO_3)_1$, the ferromagnetism is found in the structure (see Figure 1.5) while there is no ferromagnetic order for the corresponding bulk solid solution $La_{1-x}Sr_xVO_3$ for any value of x. The ferromagnetism is stable in a wide range of temperature, up to room temperature (the inset of Fig. 1.5). It is also found to be strongly dependent on the number of $LaVO_3$ layers m.

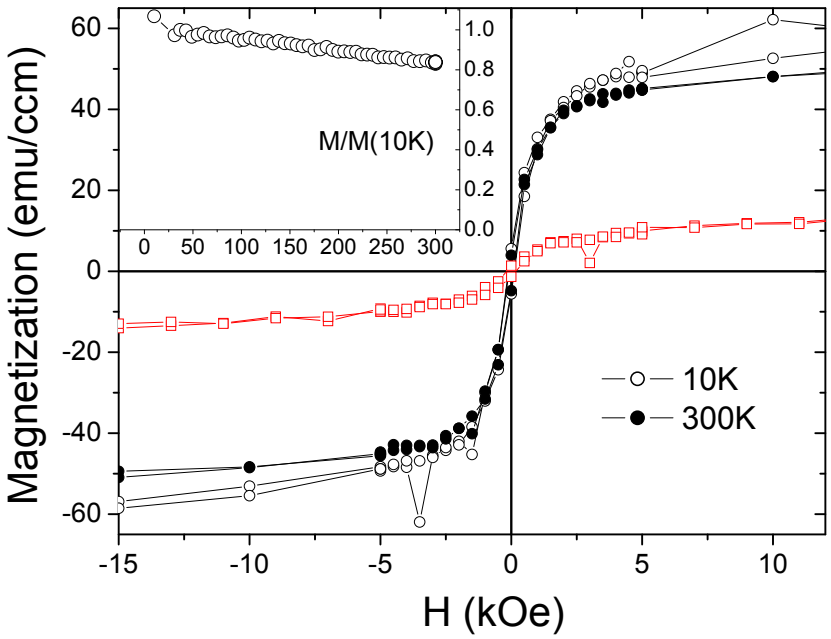

Figure 1.5: The measurement of magnetization under small external magnetic field for bulk $La_{1-x}Sr_xVO_3$ and superlattice structure $(LaVO_3)_m(SrVO_3)_1$ with $m = 6$ at $T = 10$ and $300K$. Inset: temperature-dependence of the saturated magnetization of the superlattice. From Lüders et al. (2009).

These vast number of interesting but also challenging phenomena in bulk and heterostructures make TMOs the main topic in condensed matter physics. Moreover, with the wide range of potential applications in bulk and heterostructures of TMOs, understanding the physics behind these materials becomes essential in order to control their properties. In this thesis, we choose to study the ferromagnetism in the superlattices of vanadates to understand the possibilities that allow the heterostructure to enter the regime of ferromagnetic order. We also suggest design that can optimize this ferromagnetism.

1.3 Metal-insulator transition

Metallic/insulating state is one of the first properties to consider when studying a material. Based on the electric conductivity, one can simply defines an insulator as a material that forbids electric charge to move inside the medium freely, an insulator thus does not allow charge current to flow if there is a voltage bias applied to the material. A metal, in contrast, has high electric conductivity that charge current can flow through it easily. The conductivity or resistivity, measurements to determine metallic or insulating state, can vary in a wide range, e.g. the resistivity can be from $10^{-8}\Omega m$ for metals to $10^{13}\Omega m$ for insulator, and also depend on temperature. By changing parameters such as pressure, temperature or the doping level, some materials can exhibit the metal-insulator transition (MIT), the transition from a metallic phase to an insulating phase and vice versa. Studying the metallic or insulating states of a material and how the MIT occurs is essential in understanding electronic properties of that material.

Band structure theory[Martin (2004)] is the traditional theory to study the electronic properties of materials. The idea of band theory is that when all atoms forming a material are separate apart, each of them has a distinguished discrete set of energy levels. Putting atoms together, this set of energy levels becomes denser, and eventually a continuum in solids is formed, which is called an energy band. The range of energy which is not covered by any band forms the energy gap. Electrons are filled in energy bands from the bottom of the bands to the level when all electrons are settled (the Fermi level). From this band theory picture, insulators are defined as systems having the Fermi level lying on an energy gap, while metals are materials with the Fermi level overlapping with an energy band.

Band theory has been developed for a long time, since the beginning of quantum physics era, achieving successes in describing electronic structure of materials. The methods to construct the band structure are well-described in the textbooks

[Martin04, Marder00]. Among these methods, density functional theory (DFT) [Hohenberg and Kohn (1964); Kohn and Sham (1965)] has achieved many successes in investigating materials. It can predict the band gap and band structure comparable with experiments, hence the metallic/insulating state of many materials are well-determined using DFT calculations. Nowadays, DFT is the workhorse for studying materials, the standard choice for material science and engineering.

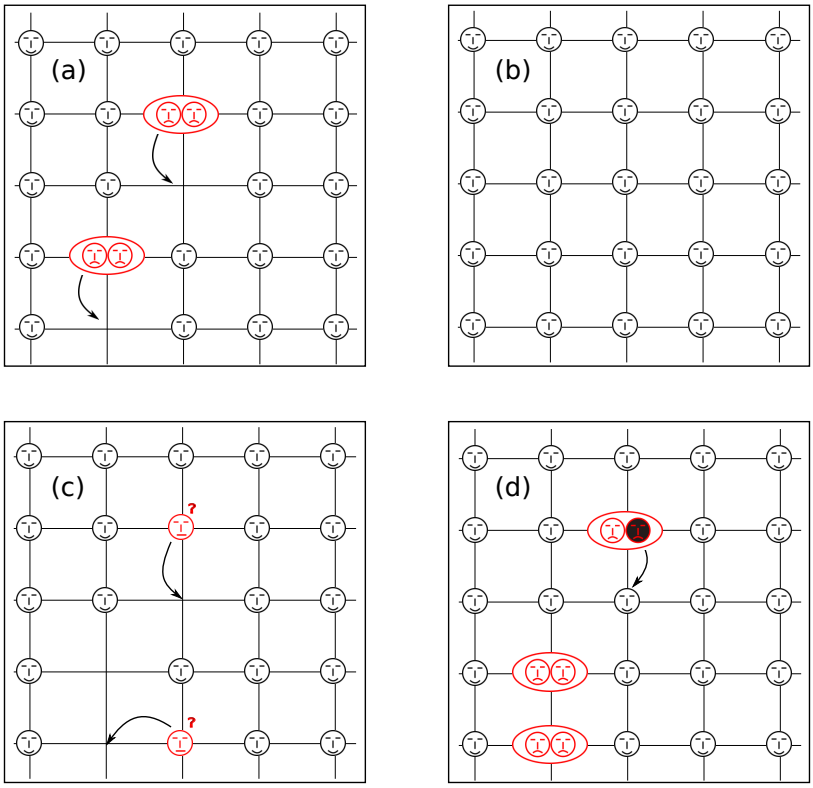

Figure 1.6: "Mott behavior": the energy cost for double occupation is equivalent to the unhappiness for students living in a shared bedroom. (a, b) If the number of rooms is equal to the number of students (half-filling case), students will move in/out until every student occupied a single room, the happiness is maximized (Mott insulating state). (c,d) If the number of rooms is larger or smaller than the number of students (doped case), moving from one room to another does not change the total happiness, the moving in/out process will never stop (metallic state).

From band theory point of view, each energy band can accommodate at most 2 electrons per band per unit cell, because electrons with spin up and down can

stay together in the same energy state. If, for example, there is an odd number of electrons, an electron in a singly occupied state can itinerate from site to site without much cost of energy, the system is obviously metallic. However, some materials with partially filled band are found to be insulating. The first observation is from de Boer and Verwey (1937) who found that mono-oxides such as NiO, MnO or CoO are all insulators although they have partially filled $3d$ bands. Mott and Peierls (1937) argued that these are insulators because of the strong electron-electron repulsion that prohibits double occupancy in each energy state, the result is that each site is singly occupied, any electron hopping, if occurring, would cost a large amount of energy of the order of the onsite Coulomb interaction. Figure 1.6ab shows an analogy to this type of insulators (Mott insulators). Mott (1949) generalized his argument for transition metal oxides, showing that electrons of the d bands experience strong electron-electron interaction, thus explaining phenomenologically why many transition metal oxides are indeed insulators despite having partially filled d bands.

The band theory, the one-electron picture, fails to describe materials with strong electron-electron interaction. It requires an appropriate model and approach to treat the correlation beyond the one-electron picture, so as at first to understand the Mott insulator. In 1963, Hubbard, Gutzwiller, Kanamori proposed a single-band model including only the nearest neighbor hopping t with onsite interaction U, the "simplest nontrivial model" for strongly correlated systems, which may contain the Mott insulating phase [Hubbard (1963); Gutzwiller (1963); Kanamori (1963)]. In second quantization, the Hamiltonian for this model (the Hubbard model) is

$$H = -t \sum_{\langle i,j \rangle} c^{\dagger}_{i\sigma} c_{j\sigma} + U \sum_{i} n_{i\uparrow} n_{j\downarrow}, \tag{1.1}$$

where i, j are site indices and σ is the spin index, $\langle i, j \rangle$ denotes nearest neighbor sites. This model is solved exactly in one-dimensional system using Bethe ansatz [Lieb

and Wu (1968)], showing that at half-filling case (1 electron per site) the system is insulating for $\forall U > 0$, being metallic only at $U = 0$. For larger dimension, the model cannot be solved exactly. Even though in the special case in (1.1) where there is only nearest neighbor hopping t at half-filling, the occurrence of magnetic order can drive the system to insulator for $U > 0$. In a general case with a different type of dispersion, there can be non-magnetic insulating state and there is metal-insulator transition as $U > U_c$. Starting in 1990s, dynamical mean-field theory [Georges et al. (1996)] (described in the next chapter) emerges as a prominent method to study this model, giving more information of the solution. Figure 1.7 demonstrates the MIT driven by the strong onsite interaction U. As U increases, the bands are split into two bands below and above the Fermi level (lower and upper Hubbard bands), other aspects such as the divergence of the mass enhancement at the transition point [Brinkman and Rice (1970)] are also obtained.

Nevertheless, the Hubbard model is a simple model which neglects important features of a realistic correlated system. First, the correlated bands are not quite separate from other bands, it may be mixed with other less correlated bands, especially when the interaction is stronger, the correlated bands are split more (to lower and upper Hubbard bands), this mixing becomes more significant. It is therefore necessary to consider the effect of other bands in addition to the correlated ones. Second, there are usually more than one correlated bands (e.g. d or f bands) staying nearly at the same energy level, i.e nearly degenerate, the Hubbard model has to be generalized to take into account more than one correlated band.

Figure 1.8 summarizes the metals/insulators for various TMOs in perovskite structures. Under the crystal field splitting due to the octahedron MO_6, the d bands are split into 3 t_{2g} bands and 2 e_g bands staying at higher energy level. Early TMOs, which consist of light transition metal elements, have partially filled t_{2g} bands at the Fermi level, the low positive charge of the transition metal ion allows the d bands

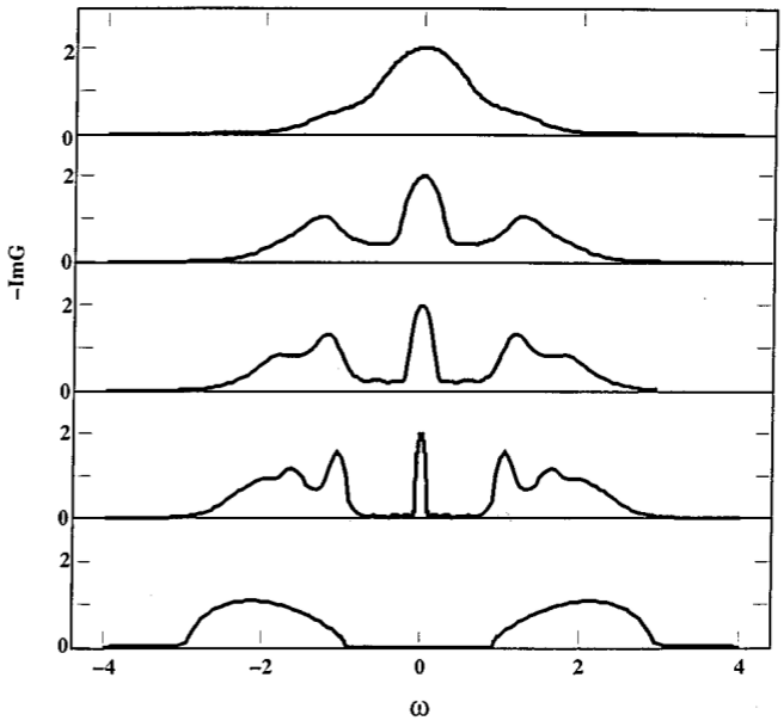

Figure 1.7: The evolution of spectral functions for the metal-insulator transition as onsite interaction U increases (from top to bottom panel). From Georges et al. (1996).

to rise to higher energy levels than the p bands, they are in Mott-Hubbard regime. Whereas late TMOs, which has heavier transition metal elements, have filled t_{2g} shell but partially filled e_g shell, the large positive charge of the late transition metal ion pushes the d bands to lower energy comparable with the p bands, the systems are usually in the charge transfer regime. The magnitude of p-d admixture increases as going from light to heavy transition metal. Understanding how the p-d covalency (the admixture between p and d bands) affects the electron correlation is an important aspect.

The splitting of the d bands into the 3 t_{2g} and 2 e_g nearly degenerate bands also implies that a multiorbital interaction is required to replace the Hubbard terms $Un_{i\uparrow}n_{i\downarrow}$ in the Hamiltonian. In a multiorbital system, beside the Hubbard U value,

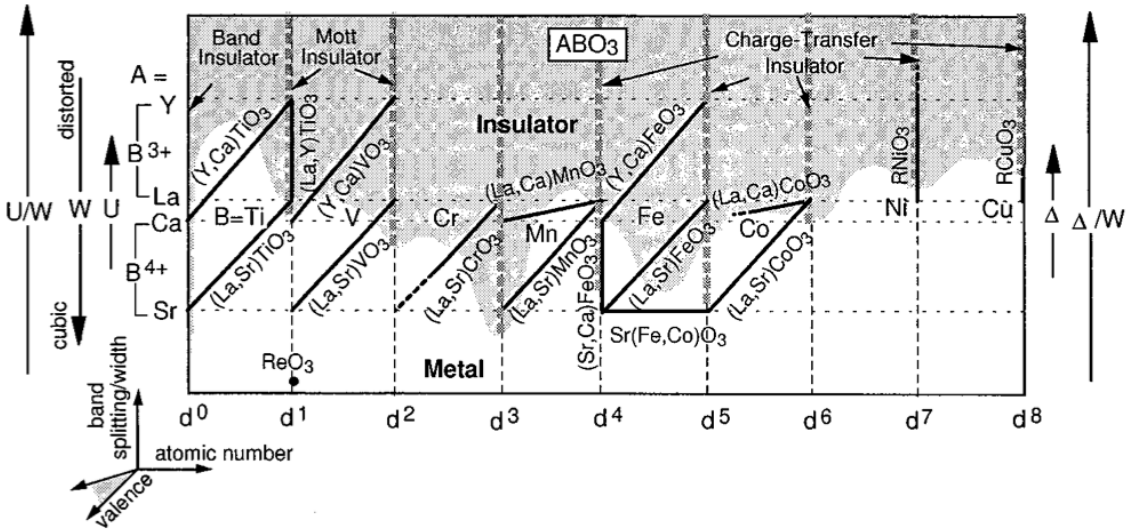

Figure 1.8: The schematic diagram for the metal-insulator transition in TMO perovskite structure $ReMO_3$. The number of d electrons increases from 0 to 8, while the U/W or Δ/W ratio increases by replacing the rare earth Re by elements of smaller atomic radii. From Imada et al. (1998).

the charging energy or the energy cost to add more d electrons, the Hund's rules are applied such that the electron spin of different orbitals are aligned first followed by the condition of maximal angular momentum. For example, the onsite interaction can have the form

$$H_{onsite} = \frac{U - 3J}{2}\hat{N}(\hat{N} - 1) - 2J\hat{S}^2 - \frac{J}{2}\hat{L}^2. \tag{1.2}$$

where J is the Hund's coupling representing the Hund's rules. In multiorbital system, the correlation is not only represented by U but also by J value [Georges et al. (2013)]. The MIT becomes more complicated with the appearance of the Hund's coupling, and can occur not only at half-filling but also, for example, at quarter filling (e_g systems) or one-third or two-third filling (t_{2g} systems).

Until recently, there are many advances in understanding the MIT in the Hubbard model. However, there are still many unsolved problems such as how the MIT occurs

in the multiorbital systems or the effect of oxygen bands to this transition. In this thesis, we study the metal-insulator transition in TMOs using dynamical mean-field theory in combination with density functional theory, which have a more complicated multiorbital interaction such as in (1.2), and consider the effect of p-d covalency. The study has contribution to the understanding of the MIT and may suggests direction towards more realistic calculations of TMOs.

1.4 Magnetism

Magnetism was discovered a long time ago. The first written evidence comes from the ancient Greece, where Aristotle "reported that Thales of Miletus (625 BC - 547 BC) knew lodestone" [du Trémolet de Lacheisserie et al. (2005)]. However, until now, it is still a problem of interest in condensed matter physics. Magnetism behaves differently in materials, especially when there is electron correlations, a material may have several types of magnetic phases in its phase diagram. Geometrical frustration can also give complicated magnetic structure, the so-called "frustrated magnetism" may give quantum spin liquid phase or other exotic excitations [Balents (2010)].

There are several basic types of magnetism: ferromagnetism, antiferromagnetism or ferrimagnetism (see Figure 1.9). In many TMOs, there are magnetic order patterns different from the usual diamagnetism or paramagnetism. These types of magnetism are very often related to the electron correlation. The rich physics of correlated materials is expressed in their complex phase diagrams such that when a parameter such as the doping level or pressure is changed, the material can change from one type of magnetic order to a different type or to a disordered phase (see Fig. 1.2 for some representative phase diagrams).

Antiferromagnetic order is usually observed in TMOs at low temperature in different patterns accompany by a specific orbital order. The pattern of staggered spin

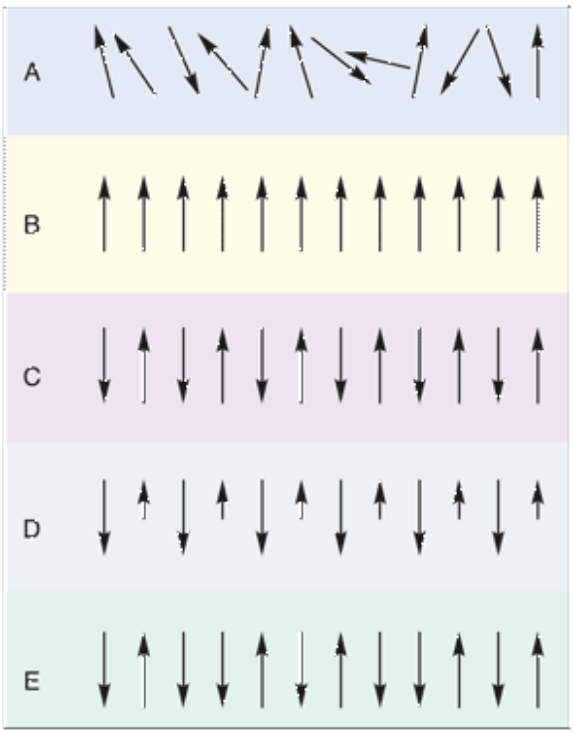

Figure 1.9: Types of magnetic order phases: (A) disordered phase, (B) ferromagnetism, (C) antiferromagnetism, (D) ferrimagnetism, (E) long periodic magnetic pattern. From Sigma-Aldrich.

and orbital orders is described phenomenologically using Goodenough-Kanamori rules [Goodenough (1958); Kanamori (1959)]. More fruitful discussions about antiferromagnetism in TMOs can be found in Imada et al. (1998) and the references therein.

In our study, we focus more on the ferromagnetic order. Ferromagnetism is a straightforward magnetic phase, there is no translation or gauge invariant symmetry breaking, only the spin symmetry is broken. It allows to use the smallest possible unit cell for investigating ferromagnetic order, which simplifies the calculation and separates ferromagnetism from other phases. Ferromagnetism is important in technology such as in spintronics or building memory devices. Ferromagnetism in strongly correlated systems has been studied since the 1930s, however, the correlation effect makes it difficult to solve the problem completely. Therefore, many aspects of ferromagnetism are not well understood until now.

Ferromagnetism in correlated materials can be divided into two classes. The first class includes materials with localized magnetic moments, usually the rare earth compound with partially filled f shell, which are aligned to form the ferromagnetic order. Because of their localized characteristic, these materials can be mapped to spin systems, in which the most famous one is the Heisenberg model

$$H = -\sum_{\langle ij \rangle} J_{ij} \mathbf{S}_i \mathbf{S}_j. \tag{1.3}$$

In the other class of materials, which includes transition metal compounds and TMOs, the charge motion is also important, the electrons of conduction bands can carry magnetic moment, it is called "itinerant ferromagnetism".

The first attempt to study itinerant ferromagnetism in the theoretical side is from Stoner (1938). By considering the exchange interaction J between two nearest neighbor sites and the electrons near the Fermi level, he found that when there is $\delta\epsilon$ difference in energy between spin up and down bands (see Figure 1.10), there is a competition in energy between the cost in kinetic energy and the energy saved from the spin aligned. The increase in kinetic energy is $\delta K \sim \nu_F \delta\epsilon^2$ where ν_F is the density of states at the Fermi level while the decrease because of spin aligned is $\sim J\mathbf{M}^2 \sim J\nu_F^2 \delta\epsilon^2$ ($\mathbf{M}$ is the magnetization). The ferromagnetism is stable if the change in energy between ferromagnetic and paramagnetic order is negative

$$\delta K - J\mathbf{M}^2 = \nu_F \delta\epsilon^2 - J\nu_F^2 \delta\epsilon^2 < 0, \tag{1.4}$$

or

$$J\nu_F > 1 \tag{1.5}$$

Eq. (1.5) is the Stoner's criteria needed to stabilize ferromagnetism.

Because magnetism in TMOs is closely related to the electron correlation, it is

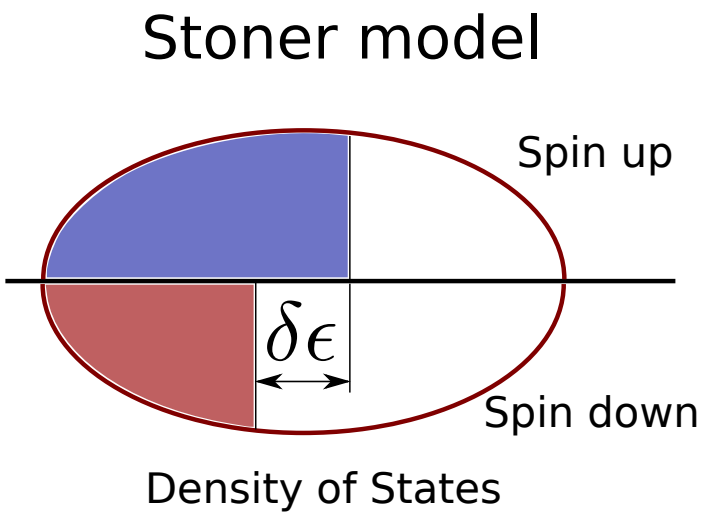

Figure 1.10: Stoner model for itinerant ferromagnetism: spin up and down electrons have different occupancy.

reasonable to use a model with correlation to study the magnetic order. Hubbard model (Eq. (1.1)) has been also used for the study of magnetism to understand how correlation drives the magnetic order. A few years after Hubbard proposed his model, Nagaoka proved that if the onsite interaction U is infinitely large, the system with a single hole away from half filling is ferromagnetic with fully spin polarized [Nagaoka (1966)]. However, the conditions for Nagaoka ferromagnetism are extreme, in thermodynamic limit where the hole density and the U value are finite, it is still unclear about the ferromagnetism [Park et al. (2008)]. At least there exists ferromagnetic order in the Hubbard model if certain conditions are satisfied. Mean field study for the Hubbard model supports Nagaoka's statement about the ferromagnetism, for example, Figure 1.11 shows the phase diagram for a two-dimensional Hubbard model in which the ferromagnetic order favors large U values and being doped away from half-filling [Hirsch (1985)].

However, the Hubbard model is a non-trivial model, mean field theory cannot capture the fluctuation around its solution, while perturbation approach may face divergence in the solution with respect to the non-interacting result, especially when

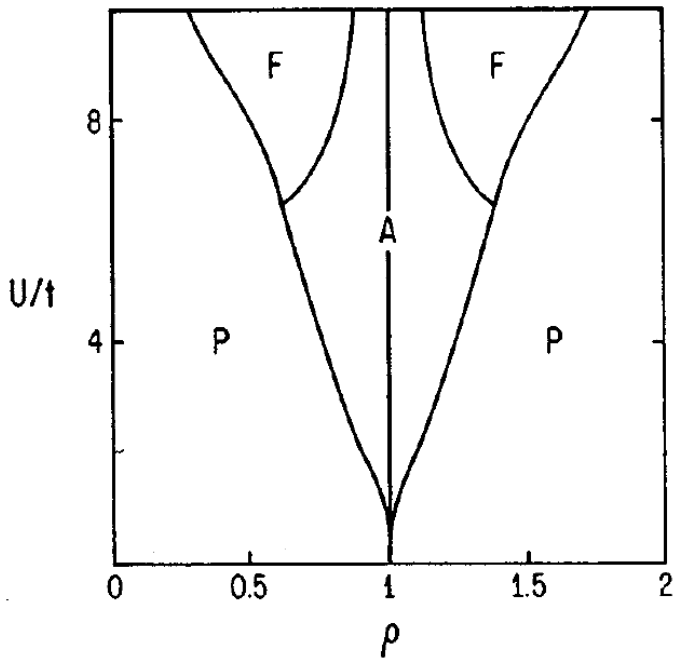

Figure 1.11: The magnetic phase diagram for the Hubbard model from mean field calculation with only nearest neighbor hopping t for the two-dimensional square lattice. The notations are: ρ is the filling, P is paramagnetic order, A is antiferromagnetic order, and F is ferromagnetic order. From Hirsch (1985).

U gets larger. It requires non-perturbative methods to treat the Hubbard model. Until recently, non-perturbative approaches with advances in computational power allow more accurate calculations for the Hubbard model. For one-dimensional Hubbard model, ferromagnetic order is excluded if there is only nearest neighbor hopping [Lieb and Mattis (1962)], only when extending to longer range electron hopping, ferromagnetism is allowed under certain circumstances [Müller-Hartmann (1995); Daul and Noack (1997)]. In two-dimensional case, it is more difficult with complicated phase diagram. Dynamical mean-field theory (DMFT), the state-of-the-art method for strongly correlated systems, becomes important and gain more insights into the 2D model. DMFT has shown to be able to treat the Hubbard model, capturing the Mott insulating physics [Georges et al. (1996)]. In the topic of magnetism, DMFT shows clearly the antiferromagnetic order exists at half-filling for two-dimensional Hubbard

model [Jarrell et al. (2001); Wang et al. (2009)]. For ferromagnetism, by applying single-site DMFT, Ulmke, Vollhardt et al. showed that the itinerant ferromagnetism in the Hubbard model, beside the U value, depends strongly on the kinetic energy and the lattice structure [Ulmke (1998); Vollhardt et al. (1999)]. It goes far beyond Stoner's criteria and mean field calculations for the Hubbard model and supports the idea that a density of states peak near the band edge may allow ferromagnetism [Kanamori (1963)].

The Hubbard model, despite being non-trivial, is simple model, far from the realistic correlated systems. As mentioned in Section 1.3, extensions for the Hubbard model are the multiorbital models, in which there are more than one degenerate correlated bands and the interaction is more general with the Hund's coupling J. The wide range of carrier density (or the filling) and the involvement of the Hund's coupling lead to various behaviors of magnetism. The works on these models, however, are limited, mostly at the extent of model calculations, for example, the theoretical Bethe lattice [Chan et al. (2009); Peters and Pruschke (2010); Peters et al. (2011)]. Similar to the Hubbard model, the magnetism may depend strongly on the lattice structure and the electron hopping in a more general multiorbital model. Therefore, in TMOs, rigorous calculations considering realistic structures are important and can reveal the physics of different lattice structures affect magnetism.

In this thesis, we study the ferromagnetism in early TMOs including the general multiorbital onsite interaction and the realistic lattice structure of materials by using density function theory plus dynamical mean-field theory. We find several conditions under which ferromagnetism may occur and explain why ferromagnetic order occurs in some materials of TMOs but no in others. Our study also considers the ferromagnetism in heterostructures of TMOs and suggests potential designs which can enhance the ferromagnetic order.

1.5 Charged impurity

There is no perfect single crystal for realistic materials. Defects in materials such as dislocation, vacancies or impurities can be found frequently when fabricating a material. There are also impurities staying temporarily inside materials which come from flux of particles used to measure physical properties of materials. These defects and impurities perturb the lattice, modify the lattice constant and change the electronic properties of materials significantly.

Impurity in strongly correlated systems is also an interesting problem [Millis (2003); Alloul et al. (2009)]. A prominent example is the Kondo problem [Hewson (1997)], where diluted magnetic impurities put into a metallic system and causes a minimum in resistivity as a small value of temperature. It is a "classic" problem of strongly correlated systems and has attracted researchers' interest for many years. Other impurity problems such as nonmagnetic or charged impurity, lattice defects in correlated systems are also interesting for investigation.

The motivation of our study of charged impurity is to understand how it perturbs the correlated system. When a charge impurity stays on the lattice, it will be screened by electrons (or holes). In a correlated material, the density fluctuation is suppressed, it is interesting to investigate how the screening works. Moreover, charge impurity induces more carrier density in the vicinity, as the density is crucial in strongly correlated systems which can increase the charge energy significantly (see (1.2)), it is also important to study how the impurity changes the physics of the neighborhood.

Our work has application in cuprates. Cuprates are TMO compounds which can be high-T_c superconductors. Fig. 1.2B is a schematic phase diagram for cuprates where superconducting phase can be obtained at low enough temperature and intermediate doping. The pseudogap phase exists in the phase diagram of cuprates as a phase where the excitation gap is not well-formed [Damascelli et al. (2003)]. Its physics is believed to give insights to the formation of the Cooper's pairs is, however,

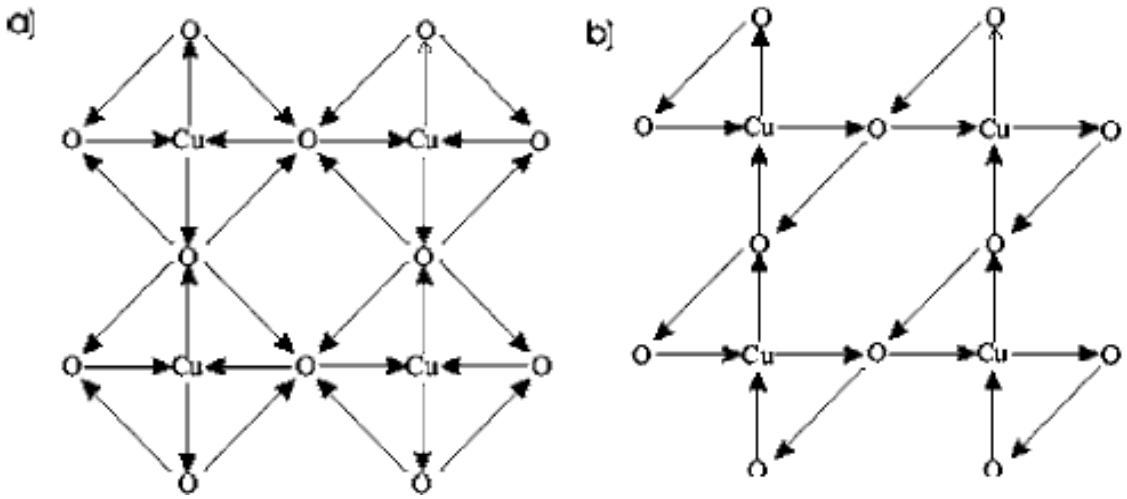

Figure 1.12: Some patterns of orbital current in the pseudogap phase of cuprates. From Varma (2006).

not fully understood. Varma stated that the pseudogap phase is a time reversal symmetry breaking phase, in which there is orbital current forming a closed loop that induces local magnetic moment [Varma (1997, 2006)] (see Figure 1.12 for possible patterns of the orbital currents).

There are many attempts from experimentalists to search for this local moment. People mainly use neutron scattering or muon spin relaxation (μSR) to detect this tiny local magnetic field. The results from neutron scattering indeed show that there exists nonzero local moment in the pseudogap phase which vanishes if the material is out of that phase, and thus support Varma's argument about the orbital current in the pseudogap phase [Fauqué et al. (2006); Li et al. (2008); Mook et al. (2008)]. In contrast, it is hardly seen clear evidence for that magnetic moment from μSR measurements [Sonier et al. (2001); MacDougall et al. (2008)], contradicts the results obtained from neutron scattering. Consider the difference between the two methods, μSR implants a usually positive muon μ^+, a charged particle into the lattice, while neutron scattering only uses neutral particles (neutrons) to measure local moment, it is essential to understand how charged particles perturb the lattice in order to explain

the measurements.

Inspired by these experimental work, we study the problem of a charged impurity in strongly correlated systems. Our work using dynamical mean-field theory method gives some insights to this interesting controversy and also to the understanding of the feedback from the lattice to the μSR measurements. Our study shows that dynamical mean-field theory can be a useful method to study impurities and defects in correlated materials.

Chapter 2

Formalism

2.1 General description

In most of the cases that we study, materials are in perovskite form RMO_3, where each transition metal M is surrounded by 6 oxygens. The octahedron MO_6 decides the electronic structure of the system. The physics is controlled by the charge transfer between the oxygen and transition metal ions and by the strong electronic correlation on the transition metal sites. On the other hand, lattice structure is different for different materials. The octahedra MO_6 are not usually aligned, they can be tilted or rotated depending on specific material. The rotations and tilts can act to lift the degeneracy of the transition metal d levels and to change the bandwidth. It is important to understand the connection between lattice structure and the correlation and how they affect the physics.

In this section, we will give an overview of the electronic structure of TMOs, which range of energy to be considered and how it might be changed when there is strong electron correlation. We also introduce possible realistic structure of TMOs in the perovskite form and a general way to describe the structure in the calculations.

2.1.1 Lattice structure

TMOs are crystallized into various forms. The most common one is the perovskite structure RMO_3 (Fig. 2.1a). However, they can be found in the form of layered structure such as the Ruddlesden-Popper series $A_{m+2}B_{m+1}O_{3m+4}$ (notice that the perovskite structure is the special case of the series with $m \to \infty$) where the lanthanum cuprate La_2CuO_4 or the spin-triplet superconductor Sr_2RuO_4 are members (Fig. 2.1b). There are mono-oxide NiO, MnO or CoO which are rock salt structure (Fig. 2.1c). In all of these forms, the octahedral structure MO_6 is often observed, it is thus the basic structure to consider when studying TMOs.

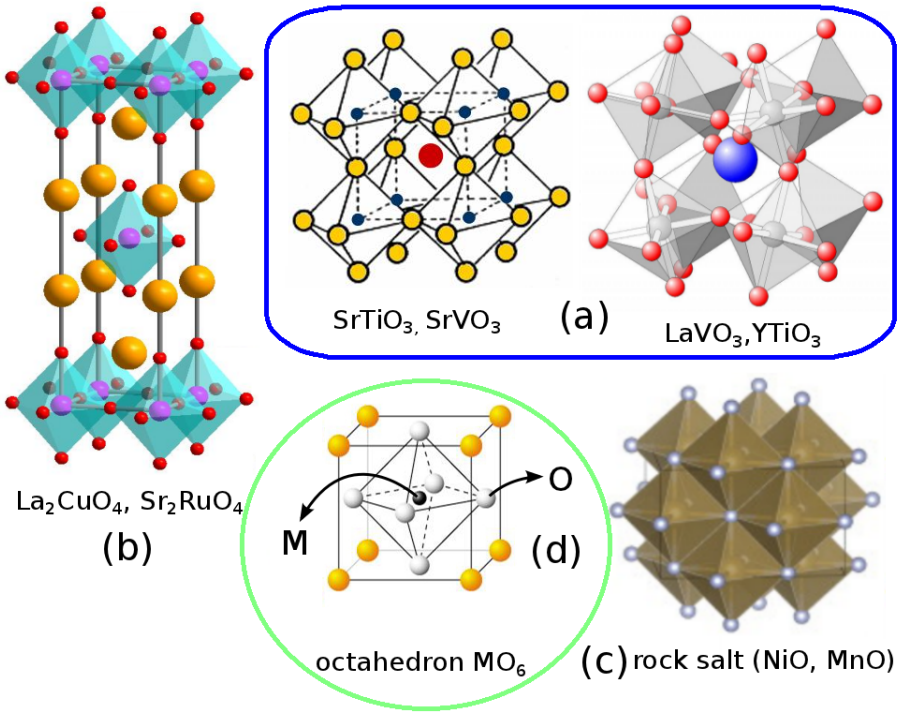

Figure 2.1: (a,b,c) Some example of lattice structures of transition metal oxides. (d) Octahedron MO_6, the common structure found in these TMOs. From various sources on Internet.

We focus on the perovskite structure because it is a typical structure of TMOs and is the structure for almost all materials we consider in this thesis. The simplest real-

ization of perovskite, the so-called cubic structure, is in the left panel of Fig. 2.1a. In this cubic form, all octahedra are aligned, the bond angle M-O-$M = 180°$. However, the realistic structures of perovskites are various, distorted away from the cubic one. There are a few TMO perovskites in cubic structure (e.g. $SrVO_3$, $SrTiO_3$) where the rare earth Re has a large atomic radius that prevents octahedra from tilting. When replacing the rare earth Re by a smaller element, octahedral rotation appears to reduce the total energy (right panel of Fig. 2.1a).

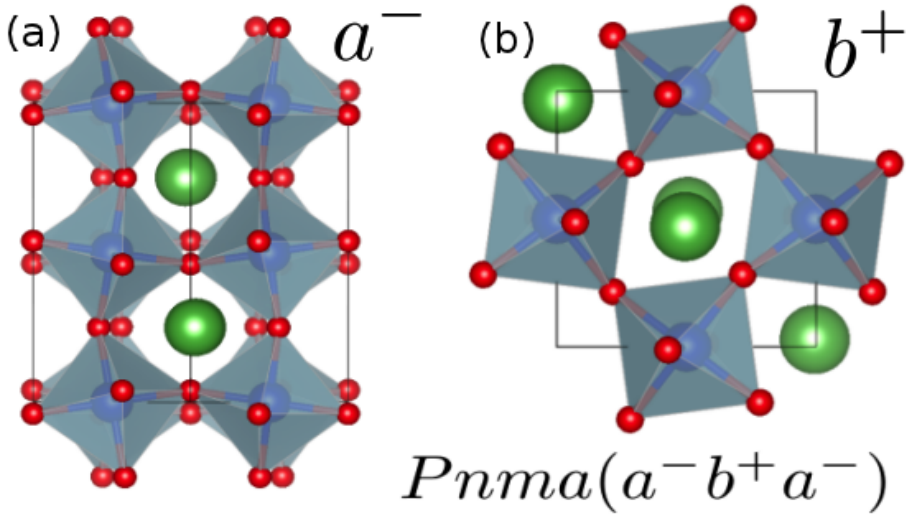

Figure 2.2: Perovskite $Pnma$ structure ($a^-b^+c^-$) projected along $\hat{x}$ (panel (a)) and $\hat{y}$ (panel (b)) directions. $LaVO_3$, $CaRuO_3$ or $SrRuO_3$, for example, belong to this class.

Based on the space group and the octahedral rotation, Glazer classified perovskites into 23 groups [Glazer (1972)]. In his notations, an octahedral rotation α along the $\hat{n}$ direction is accompanied by one of $+,-$ or 0 where

- $(+)$ means "in-phase rotation": octahedra along $\hat{n}$ direction rotate in the same way, either clockwise or counter-clockwise.
- $(-)$ means "anti-phase rotation": octahedra along $\hat{n}$ direction rotate alternatively.

- (0) means there is no rotation along that direction.

A perovskite structure can be described as $a^i b^j c^k$ where a, b, c are rotation angles along octahedral axes and i, j, k are one of $+, -$ or 0. For example, the structure with $Pnma$ space group, in Glazer's notations, is $a^- b^+ a^-$, i.e. there are anti-phase rotations along $\hat{x}$ and $\hat{z}$ directions with angle a (Fig. 2.2a) and an in-phase rotation along $\hat{y}$ direction with angle b (Fig. 2.2b). The classification is useful in understanding and constructing the lattice structure for perovskites in a systematic way. Moreover, Glazer's notations are more intuitive, easier to remember than the more general space group notations.

We focus on the $a^- b^+ c^-$ ($Pnma$) structure because it is the most common perovskite, occurring very often in our study (although we also consider the cubic $a^0 a^0 a^0$ ($Pm\bar{3}m$) and $a^- a^+ b^-$ ($P2_1/m$) structures). The $Pnma$ structure, as in Fig. 2.2, requires two angles a and b for the octahedral rotation. Its unit cell contains 4 $ReMO_3$ cells, thus there are 4 octahedra rotating in alternative directions. Equivalently, Pavarini et al. (2005) uses rotation angles along different directions, θ along [010] and ϕ along [101] directions (these direction indices are in the axes of the cubic lattice). In our study, we use both Glazer's notations (for general perovskites) and Pavarini's notations (specifically for $Pnma$ structure) in constructing the lattice and varying the degree of distortion in the structures.

2.1.2 General band structure for TMOs

TMO is the topic of ongoing research, there is no precise band structure for this class of materials, the difficulties mostly come from the strong electron correlation. We present here a qualitative picture for the electronic structure of TMOs. It is however not complete, more study in future may reveal more interesting features of the band structure.

For simplicity, we first ignore the electron-electron interaction. The energy levels of each band in TMO (RMO_3) can be determined, to an approximation, by diagonalizing the one-electron Hamiltonian

$$H = -\frac{1}{2m}\nabla^2 + V(\mathbf{r}). \tag{2.1}$$

$V(\mathbf{r})$ is the Coulomb interaction between the electron and ions on the lattice, if assuming ions are point charges and the electron is not close to any ion, $V(\mathbf{r})$ is

$$V(\mathbf{r}) = -\sum_R \frac{e^2|q_R|}{|\mathbf{r}-\mathbf{R}_R|} - \sum_M \frac{e^2|q_M|}{|\mathbf{r}-\mathbf{R}_M|} + \sum_O \frac{e^2|q_O|}{|\mathbf{r}-\mathbf{R}_O|}, \tag{2.2}$$

where each pair $(q_R, \mathbf{R}_R)$, $(q_M, \mathbf{R}_M)$, $(q_O = -2, \mathbf{R}_O)$ are ion charge and lattice position for each R, M or O sites.

If a is the lattice constant, the atomic positions of ions with respect to a are $R = (1/2, 1/2, 1/2)$, $M = (0,0,0)$ and $O_1 = (1/2, 0, 0), O_2 = (0, 1/2, 0), O_3 = (0, 0, 1/2)$. If the electron orbits around M atom at $\mathbf{R}^0_M = (0,0,0)$ with ion charge $q_M > 0$, there is an attractive ionization potential $-V_0 < 0$ in addition to the potential from other ions acting on that electron

$$V(\mathbf{r}) = -\sum_R \frac{e^2|q_R|}{|\mathbf{r}-\mathbf{R}_R|} - \sum_{R_M \neq R^0_M} \frac{e^2|q_M|}{|\mathbf{r}-\mathbf{R}_M|} + \sum_O \frac{e^2|q_O|}{|\mathbf{r}-\mathbf{R}_O|} - V_0. \tag{2.3}$$

Using the multipole expansion with $R \gg r$

$$\begin{aligned} \frac{1}{|\mathbf{R}-\mathbf{r}|} &= 4\pi \sum_{l=0}^{\infty} \sum_{m=-l}^{l} \frac{Y_{lm}(\theta,\phi) Y^*_{lm}(\theta_R,\phi_R)}{2l+1} \frac{r^l}{R^{l+1}} \\ &= \frac{1}{R} + 4\pi \sum_{l=1}^{\infty} \sum_{m=-l}^{l} \frac{Y_{lm}(\theta,\phi) Y^*_{lm}(\theta_R,\phi_R)}{2l+1} \frac{r^l}{R^{l+1}}, \end{aligned} \tag{2.4}$$

$V(\mathbf{r})$ becomes

$$V(\mathbf{r}) = V_M - V_0 + V_{mp}, \tag{2.5}$$

where V_M is the Madelung potential coming from the zeroth order term of (2.4)

$$V_M = -\sum_R \frac{e^2|q_R|}{R_R} - \sum_{R_M \neq 0} \frac{e^2|q_M|}{R_M} + \sum_O \frac{e^2|q_O|}{R_O}, \tag{2.6}$$

and V_{mp} is the higher order terms of (2.4), in which contributions from nearby oxygen ions are significant because oxygen ions are the nearest sites, while contributions from other sites can be neglected

$$V_{mp}(r) = 4\pi e^2|q_O| \sum_O \sum_{l=1}^{\infty} \sum_{m=-l}^{l} \frac{Y_{lm}(\theta,\phi)Y^*_{lm}(\theta_O,\phi_O)}{2l+1} \frac{r^l}{(a/2)^{l+1}}. \tag{2.7}$$

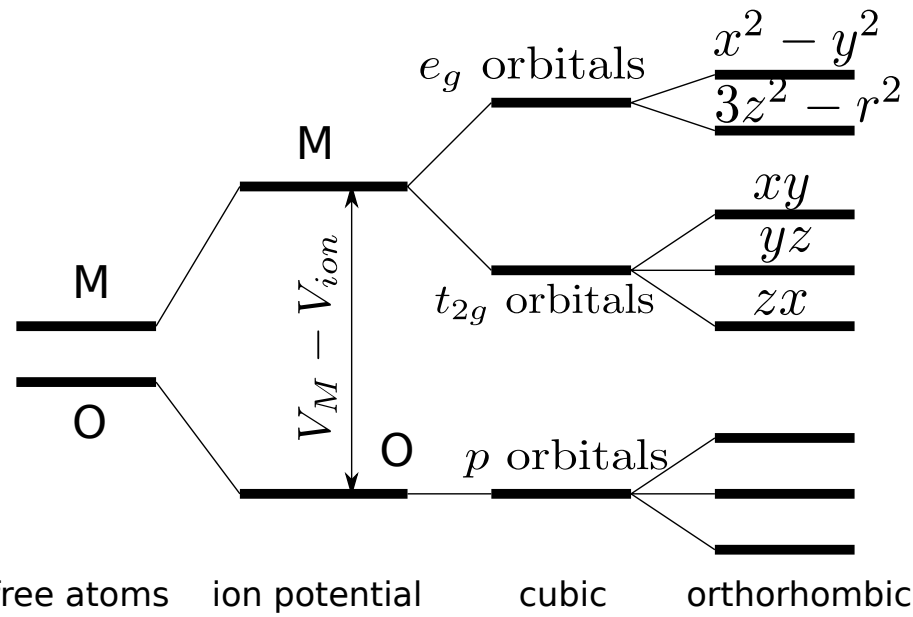

Figure 2.3: The energy levels of oxygen p orbitals and transition metal M d orbitals when going from free atoms to lower symmetries in atomic limit. Notice that in orthorhombic systems, the energy levels of, for example, xy, yz, zx are split depending on the actual system.

Similar analysis is done for oxygen atoms. There is one main difference: the

oxygen ion O^{-2} repels electrons. The ionization potential for transition metal M should be replaced by the electron affinity for oxygen.

$$V_O(\mathbf{r}) = V_M + V_{affin} + V_{mp}, \tag{2.8}$$

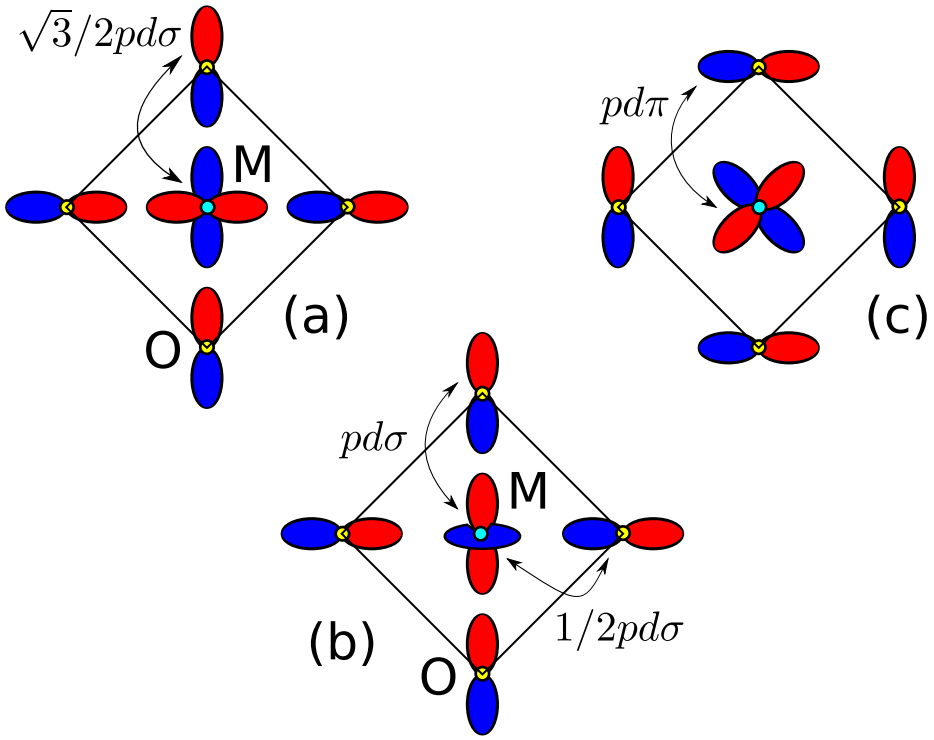

Figure 2.4: Illustration of crystal field splitting for each different transition metal d oribtals and oxygen p orbitals. (a) The $x^2 - y^2$ orbital on xy plane spreads towards oxygen ions, the Coulomb repulsion from ion O^{-2} acting on the x^2-y^2 orbital is large, it is at high energy, the hopping $pd\sigma$ from the x^2-y^2 orbital to the p orbitals is also large due to large overlap of wavefunctions. (b) Similar situation for the $3z^2 - r^2$ orbital, it spreads towards oxygen ions in the z direction, thus it is at high energy level. (c) The xy orbital spread differently, the repulsion from oxygen ions is less than the case of e_g orbitals, it is at lower energy level, the hopping $pd\pi$ from xy to p orbitals is smaller than that of e_g orbitals due to small wavefunction overlap.

Figure 2.3 shows the energy levels of the most relevant orbitals (oxygen p and transition metal d orbitals) when going from free atoms to low symmetry structure.

The relative positions of p and d orbitals can be understood from the potentials above. First, consider only the Madelung potential and the ionization potential (or electron affinity), d electrons around M experience strong repulsion from 6 oxygen ion O^{-2} nearby, the Madelung potential V_M is large, their ionization potential cannot completely compensate, $V_M - V_0 > 0$ is large, therefore d electrons of M is at higher energy level. The p electrons around O^{-2}, on the other hand, experience attraction from only 2 M ions nearby, p electrons are at lower energy (even though this attraction is reduced by the electron affinity). The first part of Fig. 2.3 demonstrates the energy levels of p and d orbitals due to the ion potential (Madelung potential, ionization potential and electron affinity).

The term $V_{mp}(r)$ is in charge of energy splitting for each p and d orbitals. This splitting represents the breaking of the rotation symmetry into finite symmetry when going from free atoms to cubic structure (because of the octahedra). While there are 3 degenerate p bands orbiting around oxygen, the d orbitals of transition metal is split into two subgroups, e_g and t_{2g} (see the middle part of Fig. 2.3). By diagonalizing the matrix $H_{mm'} = \langle 2m|V_{mp}|2m'\rangle$, one can find that the e_g orbitals are at higher energy. Intuitive explanation is that the t_{2g} orbitals (xy, yz, zx) overlap with O^{-2} ion less than the e_g orbitals $(x^2-y^2, 3z^2-r^2)$ (see Fig. 2.4), the Coulomb repulsion from O^{-2} acting on these t_{2g} orbitals is less than that of e_g orbitals. The e_g orbitals should be at higher energy.

One can further split the e_g, t_{2g} or p orbitals by going to lower symmetry, for example, as in the right part of Fig. 2.3, if the lattice constants along $\hat{x}, \hat{y}$ and $\hat{z}$ directions are different (orthorhombic structure), the orbital degeneracy are lifted. More details for this so-called crystal field splitting can be found, for example, in Wolfram and Ellialtioglu (2006); Pavarini et al. (2012).

In solids, these orbitals form electronic bands and do not stay separately. There is admixture between p and d bands (p-d covalency) such that certain d character is

in the p bands and vice versa. The p-d covalency generates 3 bands: the antibonding band (mostly d character) near the Fermi level, the bonding band (mostly p character) at lower energy, and the nonbonding band (p character). Fig. 2.5 shows the density of states for $SrVO_3$ using *ab initio* calculation, this is the typical density of states for cubic perovskites where all these bands can be observed.

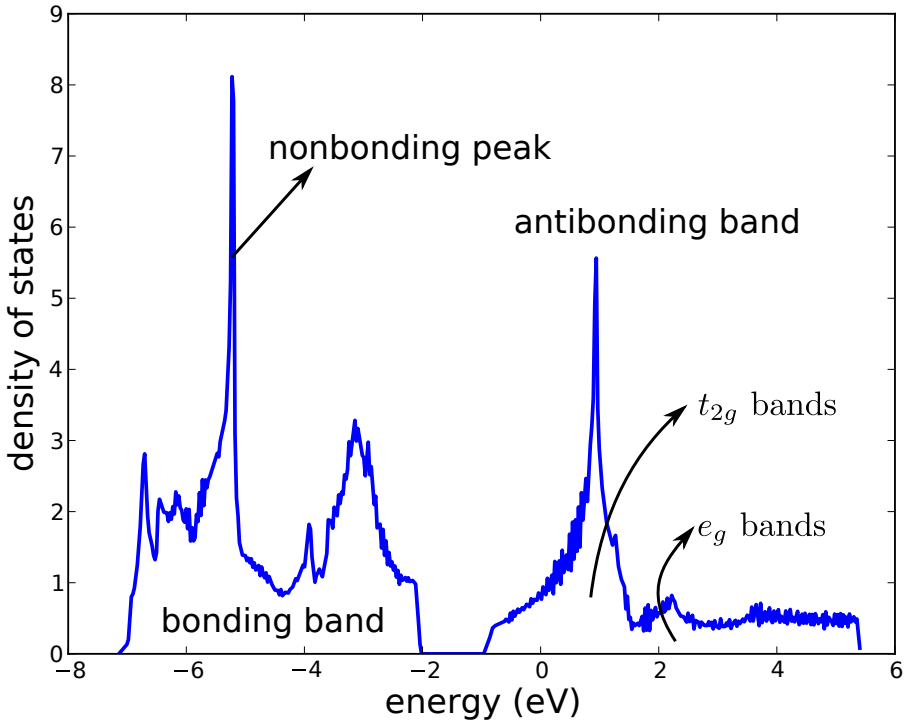

Figure 2.5: Density of states for $SrVO_3$ obtained from density functional theory calculation. The p-d admixture leads to the antibonding part at the Fermi level (composed mainly of t_{2g} and e_g bands with small p admixture), the bonding part at lower energy (mostly p character with some d admixture) and the nonbonding part (purely p character), which is the δ peak because of the weakly dispersion of the nonbonding band. The amount of p-d admixture depends on specific transition metal oxides.

When the electron-electron interaction is taken into account, the scenario becomes more complicated. In the correlated d bands, and assume single band Hubbard model (1.1) at half-filling, a hopping of electron from one transition metal site to another may cost an energy U, the Hubbard value, because of the forming of the double

occupancy. The d band splits into lower and upper Hubbard bands with the gap $\sim U$ (see Fig. 1.7). As we already mentioned in Section 1.3, depending on the magnitude of U, the system can be in Mott-Hubbard or charge transfer regime. The schematic density of states for materials in Mott-Hubbard regime can be seen in Fig. 1.4a. In the latter case, the density of states may be slightly different from Fig. 1.4b, oxygen bands are close to the upper Hubbard bands, they can donate electron to the d bands to form a hole, the electron on the d bands and hole on the p bands may form a singlet, the Zhang-Rice singlet [Zhang and Rice (1988)], the corresponding Zhang-Rice band stays in front of the p bands but below the antibonding d bands, as depicted in Fig. 2.6.

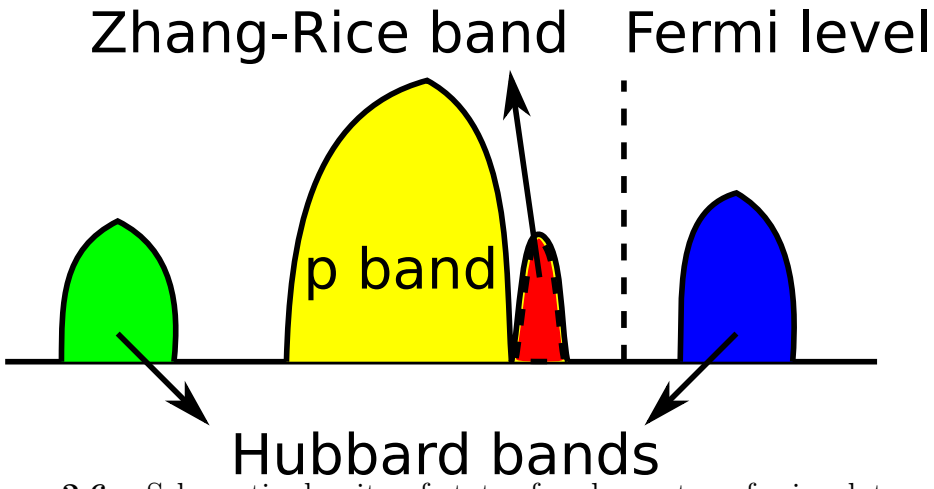

Figure 2.6: Schematic density of states for charge-transfer insulator with Zhang-Rice band included because of the formation of the Zhang-Rice singlet formed by a hole in the oxygen p band and an electron in the transition metal d band.

2.2 Models

The general Hamiltonian for our problem is

$$H = H_{kin} + H_{onsite} + H_{coulomb} - H_{DC}. \tag{2.9}$$

Below is the brief description of each term in (2.9) while the details are given later in this section.

- H_{kin} is the kinetic Hamiltonian containing all possible electron hoppings between sites and between different orbitals.
- H_{onsite} is the onsite Coulomb interaction, acting on the correlated d bands only.
- $H_{coulomb}$ is the intersite Coulomb interaction, which is important in the case of heterostructures where the ion charges of different sites are not the same. It is neglected in bulk systems.
- H_{DC} is the double counting corrections, which is nonzero when the oxygen p bands are considered.

In our works, we consider two main models

1. The downfolded d-only model: we project the Kohn-Sham wavefunctions obtained from *ab initio* calculation into the subspace of antibonding d bands near the Fermi level and treat these bands as correlated bands.
2. The model with both p and d bands: we project the Kohn-Sham wavefunctions into the subspace of oxygen p and transition metal d orbitals, the p bands are uncorrelated while the d bands are correlated.

The details of the Hamiltonian (2.9) depend on specific model.

2.2.1 The kinetic Hamiltonian H_{kin}

H_{kin} contains all possible electron hoppings between sites and orbitals, but hopping between different spins (spin-orbit coupling) is excluded. In second quantization, it has a quadratic formalism

$$H_{kin} = \sum_{\mathbf{k}\alpha\beta\sigma} h^{\alpha\beta}_{band}(\mathbf{k}) c^{\dagger}_{\mathbf{k}\alpha\sigma} c_{\mathbf{k}\beta\sigma}, \tag{2.10}$$

where α, β are orbital indices, σ is the spin index and $\mathbf{k}$ is the vector in reciprocal space (the sum of $\mathbf{k}$ is over the Brillouin zone BZ1), $\hat{h}_{band}(\mathbf{k})$ is the tight binding matrix restricted to the subspace under consideration.

For the sake of simplicity and demonstration, we assume that the lattice structure is a simple cubic perovskite $RM\mathrm{O}_3$. The unit cell contains only one cell of $RM\mathrm{O}_3$ with three primitive vectors $\mathbf{a} = (a_0, 0, 0)$, $\mathbf{b} = (0, a_0, 0)$ and $\mathbf{c} = (0, 0, a_0)$, where a_0 is the lattice constant, typically around 4Å. The atomic positions are $R = (1/2, 1/2, 1/2)$, $M = (0, 0, 0)$,$\mathrm{O}_1 = (1/2, 0, 0)$, $\mathrm{O}_2 = (0, 1/2, 0$ and $\mathrm{O}_3 = (0, 0, 1/2)$. In this unit cell, there are 5 d bands of transition metal (xy, yz, zx for t_{2g} bands and $3z^2 - r^2$, $x^2 - y^2$ for e_g bands) and 9 p bands of oxygen (there are 3 oxygen atoms, each has 3 bands p_x, p_y and p_z). The tight binding matrix $\hat{h}_{band}(\mathbf{k})$ is a 14×14 matrix and is well-approximated by using Slater-Koster method [Slater and Koster (1954)], where all kinds of orbital overlap are represented by a few number of Slater-Koster parameters. The $\hat{h}_{band}(\mathbf{k})$ for 5 d bands and 9 p bands is divided into two blocks, the t_{2g} block including t_{2g} orbitals and related oxygen p orbitals ($\hat{h}_{t_{2g}}(\mathbf{k})$) and the e_g block including e_g orbitals and related oxygen p orbitals ($\hat{h}_{e_g}(\mathbf{k})$), the off-diagonal matrix $\hat{h}_{t_{2g}-e_g}(\mathbf{k})$ is a sparse matrix

$$\hat{h}_{t_{2g}-e_g}(\mathbf{k}) = \left(\begin{array}{c|ccccc} & 3z^2-r^2 & p_x\mathrm{O}(1/2,0,0) & p_y\mathrm{O}(0,1/2,0) & p_z\mathrm{O}(0,0,1/2) & x^2-y^2 \\ \hline xy & 0 & 0 & 0 & 0 & 0 \\ p_x\mathrm{O}(0,1/2,0) & 0 & 2C_xC_yb^+ & 0 & 0 & 0 \\ p_y\mathrm{O}(1/2,0,0) & 0 & 0 & 2C_xC_yb^+ & 0 & 0 \\ yz & 0 & 0 & 0 & 0 & 0 \\ p_y\mathrm{O}(0,0,1/2) & 0 & 0 & 2C_yC_zb^+ & 0 & 0 \\ p_z\mathrm{O}(0,1/2,0) & 0 & 0 & 0 & 2C_yC_zb^+ & 0 \\ zx & 0 & 0 & 0 & 0 & 0 \\ p_x\mathrm{O}(0,0,1/2) & 0 & 2C_xC_zb^+ & 0 & 0 & 0 \\ p_z\mathrm{O}(1/2,0,0) & 0 & 0 & 0 & 2C_xC_zb^+ & 0 \end{array}\right), \tag{2.11}$$

$$\hat{h}_{t_{2g}}(\mathbf{k}) = \left(\begin{array}{c|ccccccccc} xy & \epsilon_{t_{2g}} & 2ipd\pi S_y & 2ipd\pi S_x & 0 & 0 & 0 & 0 & 0 & 0 \\ p_x\mathrm{O}(0,1/2,0) & -2ipd\pi S_y & \epsilon_{p1} & 2S_xS_yb^- & 0 & 0 & 0 & 0 & 4pp\pi C_yC_z & 0 \\ p_y\mathrm{O}(1/2,0,0) & -2ipd\pi S_x & 2S_xS_yb^- & \epsilon_{p1} & 0 & 4pp\pi C_xC_z & 0 & 0 & 0 & 0 \\ yz & 0 & 0 & 0 & \epsilon_{t_{2g}} & 2ipd\pi S_z & 2ipd\pi S_y & 0 & 0 & 0 \\ p_y\mathrm{O}(0,0,1/2) & 0 & 0 & 4pp\pi C_xC_z & -2ipd\pi S_z & \epsilon_{p1} & 2S_yS_zb^- & 0 & 0 & 0 \\ p_z\mathrm{O}(0,1/2,0) & 0 & 0 & 0 & -2ipd\pi S_y & 2S_yS_zb^- & \epsilon_{p1} & 0 & 0 & 4pp\pi C_xC_y \\ zx & 0 & 0 & 0 & 0 & 0 & 0 & \epsilon_{t_{2g}} & 2ipd\pi S_z & 2ipd\pi S_x \\ p_x\mathrm{O}(0,0,1/2) & 0 & 4pp\pi C_yC_z & 0 & 0 & 0 & 0 & -2ipd\pi S_z & \epsilon_{p1} & 2S_xS_zb^- \\ p_z\mathrm{O}(1/2,0,0) & 0 & 0 & 0 & 0 & 0 & 4pp\pi C_xC_y & -2ipd\pi S_x & 2S_xS_zb^- & \epsilon_{p1} \end{array}\right), \tag{2.12}$$

$$\hat{h}_{e_g}(\mathbf{k}) = \left(\begin{array}{ccccc} 3z^2-r^2 & p_x\mathrm{O}(1/2,0,0) & p_y\mathrm{O}(0,1/2,0) & p_z\mathrm{O}(0,0,1/2) & x^2-y^2 \\ \hline \epsilon_{e_g} & -ipd\sigma S_x & -ipd\sigma S_y & 2ipd\sigma S_z & 0 \\ ipd\sigma S_x & \epsilon_{p2} & 2S_xS_yb^- & 2S_xS_zb^- & -i\sqrt{3}pd\sigma S_x \\ ipd\sigma S_y & 2S_xS_yb^- & \epsilon_{p2} & 2S_yS_zb^- & i\sqrt{3}pd\sigma S_y \\ -2ipd\sigma S_z & 2S_xS_zb^- & 2S_yS_zb^- & \epsilon_{p2} & 0 \\ 0 & i\sqrt{3}pd\sigma S_x & -i\sqrt{3}pd\sigma S_y & 0 & \epsilon_{e_g} \end{array}\right), \tag{2.13}$$

$$\hat{h}_{band}(\mathbf{k}) = \left(\begin{array}{c|c} \hat{h}_{t_{2g}}(\mathbf{k}) & \hat{h}_{t_{2g}-e_g}(\mathbf{k}) \\ \hline \hat{h}_{t_{2g}-e_g}(\mathbf{k}) & \hat{h}_{e_g}(\mathbf{k}) \end{array}\right), \tag{2.14}$$

where $S_i = \sin\frac{k_i}{2}$, $C_i = \cos\frac{k_i}{2}$, $b^{\pm} = pp\pi \pm pp\sigma$. The Slater-Koster parameters $pd\pi$ and $pd\sigma$ are hoppings between oxygen p to t_{2g} or e_g orbitals, respectively (see Fig. 2.4); while $pp\sigma$ and $pp\pi$ are hoppings between oxygen p orbitals.

The Slater-Koster parameters can be obtained by fitting the band structure from *ab initio* calculation, for example, Table 2.1 shows the parameters extracted from the band structure calculation for various early TMOs in cubic perovskite form. The hopping $pd\pi$ between the t_{2g} orbitals and oxygen p orbitals is a factor of two smaller than that of the e_g orbitals ($pd\sigma$) because the wavefunction overlap between the t_{2g} orbitals and oxygen p orbitals is smaller than for the e_g orbitals, as depicted in Fig. 2.4. Therefore the t_{2g} bands have smaller bandwidth than the e_g bands, i.e. t_{2g} orbitals are more localized.

The division into two blocks in the tight binding matrix (2.14) is the direct result

from the octahedral crystal field splitting which splits the t_{2g} and e_g energy levels, as in Table 2.1, the e_g level is $1 \rightarrow 2eV$ in higher energy than the t_{2g} level. The oxygen p orbitals are divided into two groups, either strongly overlap with t_{2g} or e_g orbitals. From Fig. 2.4, one easily finds that three orbitals p_x of $O_1 = (1/2, 0, 0)$, p_y of $O_2 = (0, 1/2, 0$ and p_z of $O_3 = (0, 0, 1/2)$ overlap more strongly with the e_g orbitals, while p_y, p_z of $O_1 = (1/2, 0, 0)$, p_x, p_z of $O_2 = (0, 1/2, 0$ and p_x, p_y of $O_3 = (0, 0, 1/2)$ overlap more with the t_{2g} orbitals, thus the two blocks (2.13) and (2.12). In an approximation, the off-diagonal part (2.11) can be ignored, the tight binding matrix is block diagonalized as

$$\hat{h}_{band}(\mathbf{k}) = \left(\begin{array}{c|c} \hat{h}_{t_{2g}}(\mathbf{k}) & 0 \\ \hline 0 & \hat{h}_{e_g}(\mathbf{k}) \end{array}\right), \tag{2.15}$$

Depending on the filling of the d bands, the Fermi level lies on the t_{2g} bands (for early TMOs) or the e_g bands (for late TMOs), the high energy bands above the Fermi level or the inert bands below it can be safely neglected. However, for many materials in the crossover between early and late TMOs, the full 5 d bands have to be taken into account. We will discuss in details the case of early TMOs when the model without the e_g bands is applicable in Chapter 4.

When the energy splitting between oxygen p bands and transition metal d bands is large compared with the p-d hybridization, it is common in literature to focus on the frontier d bands near the Fermi level. Thus the model with only d orbitals (so-called "d-only" model) is used. It is a more simplified model where all effects from the p-d admixture are removed and consider only the electron-electron correlation.

	ϵ_{eg}	ϵ_{t2g}	ϵ_{p1}	ϵ_{p2}	$pd\sigma$	$pd\pi$	$pp\pi_1$	$pp\sigma_1$	b_2^-
$SrVO_3$	12.14	10.68	7.47	7.22	2.31	-1.13	-0.060	0.64	-0.45
$SrCrO_3$	12.88	11.40	8.94	8.31	2.12	-1.05	-0.060	0.67	-0.44
$LaTiO_3$	17.15	15.29	10.11	9.84	2.28	-1.17	-0.011	0.57	-0.39
$LaVO_3$	14.80	13.32	8.83	8.77	2.18	-1.08	-0.012	0.59	-0.43
$LaCrO_3$	15.73	14.21	10.39	10.14	2.03	-1.02	-0.006	0.64	-0.43

Table 2.1: The Slater-Koster parameters extracted from band structure calculation for several TMOs in (hypothetical) cubic perovskite structure. The index 1 is for parameters belonging to the t_{2g} block (2.12) while the index 2 is for parameters belonging to the e_g block (2.13) and $b_2^- = pp\pi_2 - pp\sigma_2$.

The projection from a large wavefunction space into a smaller subspace, e.g the d manifold, is carried out using the Löwdin downfolding technique [Löwdin (1951); Andersen et al. (1995)]

$$H_{ij}(\epsilon) = H_{ij} - H_{ik}\left[(\hat{H}_P - \epsilon\mathbf{1})^{-1}\right]_{kl} H_{kj}. \tag{2.16}$$

In this formula, the full Hamiltonian is downfolded into the Hamiltonian $H_{ij}(\epsilon)$ of smaller subspace for orbitals near the Fermi level with ϵ is approximately set equal to the Fermi energy. The matrix $\hat{H}_P$ contains the part far away from the Fermi level. The indices i and j are for the downfolded part, the indices k, l are for the $\hat{H}_P$ part. In the scenario of oxygen p and transition metal d orbitals, $\hat{H}_P$ is for the p orbitals, and H_{ij} has indices i, j running on the d orbitals. This downfolding procedure is actually a second-order perturbation, the effective hoppings between sites and orbitals in the d-only model mostly come from the virtual hoppings between transition metal d and oxygen p orbitals, it depends strongly on the overlap of the p and d orbitals and the difference of the two energy levels, $t \sim \dfrac{2t_{pd}^2}{|\epsilon_d - \epsilon_p|}$ (t_{pd} is the hopping integral between p and d bands, either $pd\sigma$ or $pd\pi$). In a realistic situation, there exist nonzero direct hopping between d orbitals, the effective hopping is thus $t \sim \dfrac{2t_{pd}^2}{|\epsilon_d - \epsilon_p|} + t_{dd}^{direct}$. The next-nearest neighbor hopping t' may also appear in the calculation and can play

certain important role. The tight binding Hamiltonian of the d-only model for cubic structure is thus usually condensed into a two-dimensional energy dispersion

$$\epsilon(\mathbf{k}) = -2t(\cos k_x + \cos k_y) - 4t' \cos k_x \cos k_y. \tag{2.17}$$

However, realistic structures are usually not ideally cubic but have certain lattice distortion, as introduced in Section 2.1. Constructing an analytic form for the tight binding matrix becomes a difficult task. Instead, maximally-localized Wannier functions (MLWF) together with *ab initio* method is used to obtain this tight binding matrix numerically. The advantage of this method is that all types of lattice distortion such as octahedral rotations or any octahedral tensile or compressive strains are embedded into the numerical tight binding matrix. By adjusting the energy window in the band structure calculation, one can easily focus on the downfolded d-only model or a model of wider energy including both p and d orbitals. The kinetic energy is written as in (2.10) where $\hat{h}_{band}$ is determined numerically. The method (Maximally-localized Wannier functions) is presented below in this Subsection.

Another difficulty coming from the lattice distortion is that all the familiar orbitals defined based on atomic orbitals (spherical harmonics) are distorted. In principle, the final results are independent of the chosen basis. However, choosing the basis to have orbitals similar to spherical harmonics is important for approximation to focus on the bands near the Fermi level and neglect those of high energy. For example, in early TMOs, if the chosen basis has orbitals similar to the atomic ones, the e_g and t_{2g} bands are separate, thus allowing to neglect the e_g bands in the calculation. For technical reason, distorted structure causes nonzero off-diagonal hoppings between different d orbitals which in turns causes exponential barrier in the simulations, the infamous "sign problem" in the Quantum Monte Carlo simulation [Gull et al. (2011)]. Choosing the appropriate basis to reduce the off-diagonal terms is thus essential. More details of finding a good basis in distorted structure are discussed in Appendix C.

Maximally-localized Wannier functions

Our approach to obtain the numerical $\hat{h}_{band}(\mathbf{k})$ is using maximally-localized Wannier functions (MLWF) in combination with density function calculation. MLWF is described in details in Marzari and Vanderbilt (1997); Souza et al. (2001); Marzari et al. (2012) with its popular implementation `wannier90` fully documented [Mostofi et al. (2008)]. The transformation from the Bloch $\psi_{n\mathbf{k}}$ to the Wannier wavefunctions $\omega_{n\mathbf{R}}$ is

$$\omega_{n\mathbf{R}} = \frac{1}{N}\sum_{\mathbf{k}} U^{\mathbf{k}}_{nm} e^{-i\mathbf{k}\mathbf{R}} \psi_{m\mathbf{k}}. \tag{2.18}$$

Because there are many choices of the unitary matrix $U^{\mathbf{k}}_{nm}$, this transformation is not unique. Marzari and Vanderbilt (1997) suggested a condition to obtain appropriate values of $U^{\mathbf{k}}_{nm}$ and the Wannier functions by minimizing the spreading Ω of the wavefunction

$$\Omega = \sum_{n} \left[\langle \omega_{n\mathbf{R}} | r^2 | \omega_{n\mathbf{R}} \rangle - \langle \omega_{n\mathbf{R}} | r | \omega_{n\mathbf{R}} \rangle^2 \right]. \tag{2.19}$$

(In Ω, the translation invariant is assumed, $\mathbf{R}$ can be fixed to $\mathbf{R} = 0$.)

The Wannier functions obtained by minimizing Ω are the maximally localized ones, thus the name MLWF. There are many applications of MLWF in physics and chemistry [Marzari et al. (2012)]. Especially in the topic of strongly correlated systems, MLWF method allows to construct basis set with very localized correlated orbitals, it is thus easy to put the interaction terms (with the Hubbard U and the Hund's coupling J) on the correlated orbitals while leaving other bands uncorrelated. MLWF method also has an advantage that the produced Wannier functions make a complete basis set in the projected subspace, there is no issue about unrenormalized bands, i.e. $\int A(\omega) d\omega = 1$ where $A(\omega)$ is a spectral function of a band in this subspace.

Our procedure to obtain MLWF and the corresponding tight binding matrix $\hat{h}_{band}(\mathbf{k})$ is as follows. Given the lattice structure of a material, we use density functional theory (Quantum Espresso code [Giannozzi et al. (2009)]) to obtain the elec-

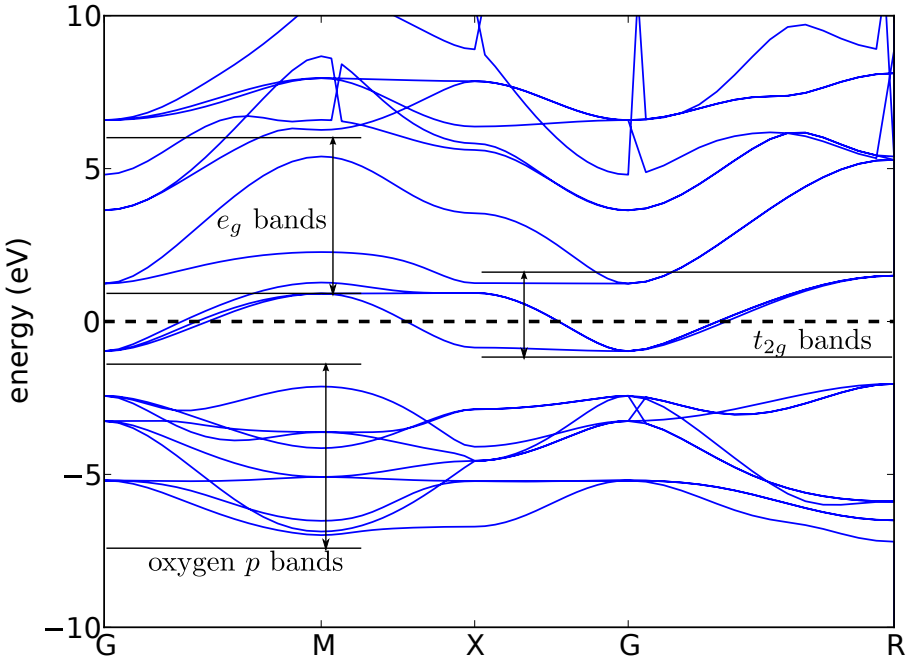

Figure 2.7: Band structure of $SrVO_3$ obtained from DFT calculation corresponding to the density of states in Figure 2.5. Oxygen p bands are between $-7 \rightarrow -1.5eV$, t_{2g} bands are between $-1.5 \rightarrow 1.8eV$ and e_g bands are between $0.8 \rightarrow 6eV$.

tronic band structure and the corresponding Bloch wavefunctions in a large space with many bands. `wannier90` is then used to minimize the spreading Ω and obtain the MLWF. The important point in carrying out MLWF method is to choose an appropriate energy window containing bands to be projected. For example, Figure 2.7 shows the band structure of $SrVO_3$, if only considering the t_{2g} bands, the energy window should be $-1.5 \rightarrow 1.8eV$, if considering both t_{2g} bands and oxygen bands, the energy window must be enlarged $-7 \rightarrow 1.8eV$.

In more complicated cases, the optimization for Ω becomes difficult, it is necessary to put in more constrains to reduce the number of variables for the minimization, the popular choice is to fix the positions of the centers of the wavefunctions, which usually are the atomic positions related to those wavefunctions. When there are band entanglements, i.e. band crossings, the MLWF fitting is not perfect as it is difficult to

disentangle those bands, one may accept the result when it reasonably approximates the DFT band structure.

The resulted MLWF should be checked by comparing the band structure and the density of states with the DFT results. For some delicate cases, other quantities such as the shape of MLWF orbitals or the center of wavefunctions should also be considered.

2.2.2 Onsite Coulomb interaction H_{onsite}

As mentioned previously, the d bands are narrow and thus exhibit strong onsite Coulomb interaction, the p bands, if included, are more extended and usually considered as uncorrelated. As a result, in this thesis, we only consider the onsite interaction term acting on the transition metal d bands.

Let $\hat{V}(\mathbf{r}_1, \mathbf{r}_2)$ be the Coulomb operator, a two-body operator. In the basis of Wannier orbitals $\{\psi^{\mathbf{R}}_{\alpha\sigma}\}(\mathbf{r})$, where α and σ are orbital and spin indices, $\mathbf{R}$ is the wavefunction center, the field operator is

$$\Psi_\sigma(\mathbf{r}) = \sum_{\mathbf{R}\alpha} \psi^{\mathbf{R}}_{\alpha\sigma}(\mathbf{r}) c_{\mathbf{R}\alpha\sigma}. \tag{2.20}$$

In second quantization representation, the Coulomb interaction is

$$\begin{aligned} H &= \frac{1}{2} \sum_{\sigma\sigma'} \int d^3r \int d^3r' \Psi^\dagger_\sigma(\mathbf{r}) \Psi^\dagger_{\sigma'}(\mathbf{r}') V(\mathbf{r}, \mathbf{r}') \Psi_{\sigma'}(\mathbf{r}') \Psi_\sigma(\mathbf{r}) \\ &= \frac{1}{2} \sum_{\alpha\beta,\gamma\delta} V^{\mathbf{R}_1\mathbf{R}_2,\mathbf{R}_3\mathbf{R}_4}_{\alpha\beta,\gamma\delta} c^\dagger_{\mathbf{R}_1\alpha\sigma} c^\dagger_{\mathbf{R}_2\beta\sigma'} c_{\mathbf{R}_3\gamma\sigma'} c_{\mathbf{R}_4\delta\sigma}, \end{aligned} \tag{2.21}$$

where the Coulomb matrix is

$$V^{\mathbf{R}_1\mathbf{R}_2,\mathbf{R}_3\mathbf{R}_4}_{\alpha\beta,\gamma\delta} = \int d^3r \int d^3r' \psi^{*\mathbf{R}_1}_{\alpha\sigma}(r) \psi^{*\mathbf{R}_2}_{\beta\sigma'}(r') V(\mathbf{r}, \mathbf{r}') \psi^{\mathbf{R}_3}_{\gamma\sigma'}(r') \Psi^{\mathbf{R}_4}_{\delta\sigma}(r). \tag{2.22}$$

In solids, electron cloud act to suppress the long-range Coulomb interaction. The screening is so strong that the off-site Coulomb interaction becomes small. In practice, only the onsite Coulomb interaction is considered. The Coulomb matrix becomes $U_{\alpha\beta,\gamma\delta} = V^{\mathbf{RR},\mathbf{RR}}_{\alpha\beta,\gamma\delta}$, independent of the lattice vector.

There are many attempts to obtain the Coulomb matrix elements so that it is reasonable and tractable for numerical simulation. In numerical approach, the Coulomb matrix elements are obtained directly from the band structure calculation. The two major methods are the constrained density function method [Cococcioni and de Gironcoli (2005)] and the constrained random phase approximation [Aryasetiawan et al. (2004)]. The interaction can be determined and have an analytic form, which can not only well approximate the numerical form but also useful for analyzing and understanding the correlation effect phenomenologically. By assuming that the interaction operator is spherical symmetric $V(\mathbf{r}, \mathbf{r}') = V(|\mathbf{r} - \mathbf{r}'|)$ and using the basis of atomic orbitals, Slater (1960) derived a general Coulomb matrix that only depends on a few parameters called Slater's integrals F_n. From Slater's work, the onsite interaction is simplified, containing only density-density interaction (diagonal terms) and exchange and pair hopping terms (off-diagonal terms). Appendix A presents the summary of this derivation.

Another effort for constructing a simple onsite interaction is from Kanamori (1963). In his work, Kanamori considered directly the overlap between d orbitals and found that only a few terms are important and proposed an onsite interaction with U, U' and J, Kanamori's notations

$$\begin{aligned} H_{onsite} = U \sum_{\alpha} n_{\alpha\uparrow} n_{\alpha\downarrow} + U' \sum_{\alpha \neq \beta} n_{\alpha\uparrow} n_{\beta\downarrow} + (U' - J) \sum_{\alpha > \beta, \sigma} n_{\alpha\sigma} n_{\beta\sigma} + \\ + J \sum_{\alpha \neq \beta} (c^{\dagger}_{\alpha\uparrow} c^{\dagger}_{\beta\downarrow} c_{\alpha\downarrow} c_{\beta\uparrow} + c^{\dagger}_{\alpha\uparrow} c^{\dagger}_{\alpha\downarrow} c_{\beta\downarrow} c_{\beta\uparrow}). \end{aligned} \tag{2.23}$$

As discussed in details in Appendix A, Kanamori's form of onsite interaction

(2.23) is an approximation for the Slater's form. Especially, when projecting onto the subspace of e_g or t_{2g} orbitals, Slater's form of interaction becomes Kanamori's form if $U' = U - 2J$. The two forms are compatible. Therefore, for simplicity, in our calculation, we mostly use Kanamori's notations for the onsite interaction H_{onsite} (2.23), the other form, if in use, is stated otherwise. Using Kanamori's interaction has several advantages. First, the form is simpler and easier to remember than the other form, thus it is useful for qualitatively analyzing the correlation effect while being a close approximation to the more accurate Slater's form. Second, with $U' = U-2J$ and focusing on the e_g or t_{2g} manifold, the form is rotationally invariant (see Appendix A). Any orbital or spin rotation does not change H_{onsite}, i.e. it is independent of the choice of basis.

However, in practice, the exchange and pair hopping terms in (2.23) causes extra cost of computation in Quantum Monte Carlo simulation. The eliminations of the terms leave H_{onsite} with only density-density interaction (Ising interaction), the density operators all commute with the Hamiltonian, which means there are more conserved numbers allowing block-diagonalizing the Hamiltonian. The simulation is thus can be run much faster. The Ising interaction and the more accurate rotationally invariant interaction affect differently on different model and also depend on phenomenon under consideration. More discusses about Ising vs. rotationally invariant interaction will be presented in the next chapters.

2.2.3 Double counting correction H_{DC}

As discussed previously in this section, the parameters for the tight binding matrix of the kinetic Hamiltonian (2.10) are usually obtained from the band structure calculations, either by fitting the band structure or projecting directly to localized Wannier orbital basis. The solution from *ab initio* calculation already contains cor-

relation effect, which is nearly the mean field contribution of the interaction. This contribution is important in determining the energy difference between correlated and uncorrelated bands, e.g. the p-d energy splitting. The origin of this contribution is from constructing the correlation functional, for example, the local density approximation has coefficients determined numerically by the Quantum Monte Carlo simulation for the interacting homogeneous electron gas [Ceperley and Alder (1980)], and in the DFT self consistent calculation, the Coulomb interaction is added into the result. The correlation effect exists in the result of band structure calculations but the exact amount is unknown.

Because the correlation effect in the band structure calculation is more or less mean field calculation, to treat the correlation effect more appropriately, one has to use a more state-of-the-art method to solve the problem by taking into account the H_{onsite} part, given the background electron calculated by *ab initio* calculation embedded in H_{kin}. With the correlation already in the Hamiltonian, treating H_{onsite} again means adding another correlation effect into the calculation, it is doubly counted. There is no such a problem in the model with only correlated bands, because double counting effect only shifts all the bands by a constant, adjusting the Fermi energy will fix the problem. However, for the model including both correlated (transition metal d) and uncorrelated (oxygen p) bands, the relative band positions will be misplaced. Hence it is necessary to subtract the amount of correlation contributed by the *ab initio* calculations by adjusting the bare energy level of the correlated bands by Δ, the "double counting correction". Therefore the double counting term H_{DC} of the Hamiltonian (2.9) (notice the minus sign of H_{DC} in (2.9)) has the form

$$H_{DC} = \sum_{\alpha\sigma} \Delta_{\alpha\sigma} \hat{n}_{\alpha\sigma}, \tag{2.24}$$

where α and σ are orbital and spin indices, $\hat{n}_{\alpha\sigma}$ is the α-orbital occupancy. The summation is only on α correlated orbitals. For simplicity, the double counting correction

is set to be the same for all correlated orbitals and spins $\Delta_{\alpha\sigma} = \Delta$.

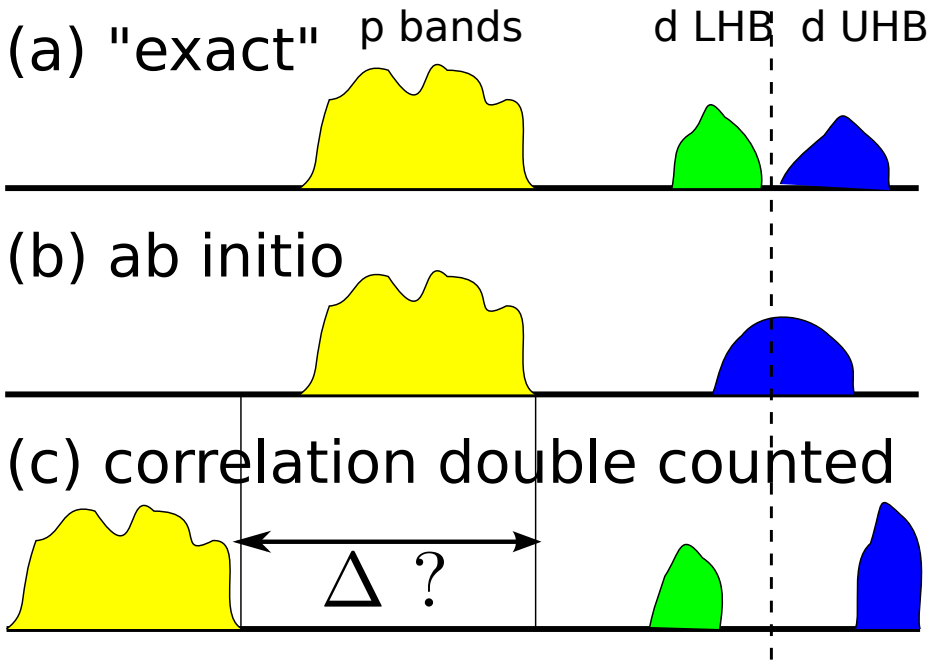

Figure 2.8: A cartoon for the double counting correction: consider oxygen p bands (yellow) and transition metal d bands (green and blue) for insulator. The Fermi level is marked by the vertical dashed line. (a) The exact solution give the correct p and d positions as well as the splitting of d bands into lower (LHB) and upper Hubbard bands (UHB). (b) Band structure calculation estimates the p and d positions near the exact results. (c) Going beyond band structure calculation, the correlation is counted twice, leading to the large shift in the d level with respect to the p level. The d level needs to be shifted to lower energy by an amount Δ (or the p level needs to be lifted up by the same amount) to obtain the correct solution.

The common treatment of the double counting issue in literature is to use one of several analytic forms of Δ. The two most common form of double counting correction are the around-the-mean-field (AMF) [Anisimov et al. (1991)] and the fully-localized limit (FLL) [Czyżyk and Sawatzky (1994)] forms. Assume the interaction has a general density-density form without exchange or pair hopping terms (these two terms do not affect either the AMF or FLL form)

$$H_{onsite} = U_{\alpha\beta} n_{\alpha\sigma} n_{\beta\bar{\sigma}} + (U_{\alpha\beta} - J_{\alpha\beta}) n_{\alpha\sigma} n_{\beta\sigma}, \tag{2.25}$$

where the sums for α and β are implied. If double counting energy $E_{DC} = \langle H_{DC} \rangle$ can be calculated, the double counting correction is obtained easily $\Delta_{\alpha\sigma} = \dfrac{\partial E_{DC}}{\partial n_{\alpha\sigma}}$

In AMF form, the correlation effect from band structure calculation is claimed to be the mean field contribution of the interaction, thus $E_{DC} = \langle H_{onsite} \rangle$, detailed calculation [Czyżyk and Sawatzky (1994)] gives

$$E_{dc} = \bar{U} N_\uparrow N_\downarrow + \frac{1}{2}(N_\uparrow^2 + N_\downarrow^2)\frac{2l}{2l+1}(\bar{U} - \bar{J}), \tag{2.26}$$

where $N_\sigma = \sum_\alpha n_{\alpha\sigma}$, the total number of correlated orbitals is $2l+1$ and

$$\bar{U} = \frac{1}{(2l+1)^2}\sum_{\alpha\beta} U_{\alpha\beta}, \tag{2.27}$$

$$\bar{J} = \bar{U} - \frac{1}{2l(2l+1)}\sum_{\alpha\beta}(U_{\alpha\beta} - J_{\alpha\beta}). \tag{2.28}$$

The AMF double counting correction is thus

$$\Delta_{AMF} = \frac{\partial E_{DC}}{\partial n_{\alpha\sigma}} = \bar{U}N - \bar{J}N_\sigma - \frac{N_\sigma}{2l+1}(\bar{U} - \bar{J}). \tag{2.29}$$

The FLL form is, on the other hand, from a different perspective. If the sites of the solid are so separate that there is no hybridization between sites, the system can be solved completely by exactly diagonalizing the Hamiltonian (2.25) of a site (in atomic limit). Given N_{at} and N_σ^{at} the total number of particle and the number of particle per spin per site, respectively, the ground state energy is

$$E_{at} = \frac{1}{2}\bar{U}N_{at}(N_{at} - 1) - \frac{1}{2}J\sum_\sigma N_\sigma^{at}(N_\sigma^{at} - 1). \tag{2.30}$$

The FLL double counting correction is claimed to have a form similar to the ground state energy in atomic limit with N_{at} and N_σ^{at} replaced by the actual average value of the number of electron per spin N_σ and the total number of particle $N = N_\uparrow + N_\downarrow$.

From that, the FLL double counting correction is

$$\Delta_{FLL} = \bar{U}(N - \frac{1}{2}) - \bar{J}(N_\sigma - \frac{1}{2}). \tag{2.31}$$

Beside the AMF and FLL double counting corrections, there are other forms of double counting correction such as from Lichtenstein et al. (2001); Held (2007); Kunes et al. (2007). The various forms of double counting correction implies that analytic formula for Δ is not well established and unstable. In our work, we approach the problem in a different way, we adjust the double counting correction (by adjusting the energy levels of the d bands) numerically and use other physical criteria to fix the double counting correction and locate the material, i.e. $H_{DC} = \Delta \sum_{\alpha\sigma} n_{\alpha\sigma}$ with Δ adjusted manually. This Δ is then mapped into a more physical quantity, the d occupancy N_d. It will be discussed in details in Subsection 4.2.3.

2.2.4 Intersite Coulomb interaction $H_{coulomb}$

In bulk systems, the ion charge is the same in every unit cell of the lattice, it is a common approximation to ignore the intersite Coulomb interaction. However, in heterostructures, e.g. superlattice or quantum well structures, the ion charge can be different when going from one layer to another, the electron density distribution is therefore varied from layers to layers. The intersite Coulomb interaction is necessary to define a heterostructure in numerical simulation.

The intersite Coulomb interaction always has two parts

$$H_{coulomb} = H_{e-e} + H_{e-ion}. \tag{2.32}$$

The intersite electron-electron interaction H_{e-e} is

$$H_{e-e} = \frac{1}{2}\sum_{i\neq j}\frac{e^2\hat{n}_i n_j}{\epsilon|\mathbf{R}_i - \mathbf{R}_j|}. \tag{2.33}$$

where ϵ is the dielectric constant and $\mathbf{R}_i$ is the lattice unit cell position. In this formula, the interaction is treated within mean field approximation such that $\hat{n}_i$ is the occupancy operator and $n_j = \langle\hat{n}_j\rangle$.

The part H_{e-ion} has a general form

$$H_{e-ion} = -\sum\frac{e^2 q_j\hat{n}_i}{\epsilon|\mathbf{R}_i - \mathbf{R}_j|}. \tag{2.34}$$

The unit cell at position $\mathbf{R}_j$ has total positive charge $+q_j$ so that $\sum_j q_j = \sum_i\langle\hat{n}_i\rangle$ the charge neutrality is preserved.

It is obvious that in bulk system where there is only uniform electron charge distribution, $\langle\hat{n}_i\rangle$ is the same in every unit cell, hence $q_i = \langle\hat{n}_i\rangle$. The two parts H_{e-e} and H_{e-ion} are canceled, (2.32) vanishes. Only in heterostructure, where the charge distribution is not uniform, (2.32) is required.

2.3 Dynamical mean-field theory (DMFT)

2.3.1 Introduction

When the onsite interaction H_{onsite} (2.21) is taken into account, the problem becomes highly nontrivial. The tradition approach is to use mean field theory where the quartic terms of the Hamiltonian are approximated as quadratic terms together with the mean field. For example, consider d occupancy as the mean field $\langle n_{\alpha\sigma}\rangle$, the

Hubbard term $Un_\uparrow n_\downarrow$ is treated as having no charge fluctuation

$$(n_\uparrow - \langle n_\uparrow \rangle)(n_\downarrow - \langle n_\downarrow \rangle) = 0 \tag{2.35}$$

or

$$n_\uparrow n_\downarrow = n_\uparrow \langle n_\downarrow \rangle + \langle n_\uparrow \rangle n_\downarrow - \langle n_\uparrow \rangle \langle n_\downarrow \rangle \tag{2.36}$$

The right hand side of (2.36) is quadratic and can be solved easily with the mean field $\langle n_\sigma \rangle$ determined self consistently.

However, for intermediate and large U, the quantum fluctuate of the occupancy n_σ around the mean field $\langle n_\sigma \rangle$ becomes large, mean field theory is unable to describe correctly the electron correlation. For example, it overestimates the ordered phases or unable to capture the Mott insulating phase, which exists in the Hubbard model. It is therefore necessary for a beyond-the-mean-field approach for strongly correlated systems.

Since 1990s, dynamical mean-field theory (DMFT) emerges as the state-of-the-art method to go beyond the mean field calculation. The method is also a mean-field based approach but the mean field is dynamical, i.e. depending on time or frequency and therefore can include certain quantum fluctuation in the solution. The details of the approach is described in details in Georges et al. (1996) for the original single-site DMFT, the extended versions of the method can be found in Maier et al. (2005) or Kotliar et al. (2001).

The basic idea of DMFT is to map the lattice model into a simpler model with an impurity embedded in a fermion bath (Figure 2.9). The hybridization between the impurity and the bath is represented by the hybridization $\hat{V}_{\mathbf{k}}$. The dynamical mean field is generated using this hybridization and is determined self consistently.

A general description[1] for DMFT starts from the thermodynamic potential (in

[1] This description is based on the Summer Lecture of DMFT by Prof. A. J. Millis, Columbia University, 2012

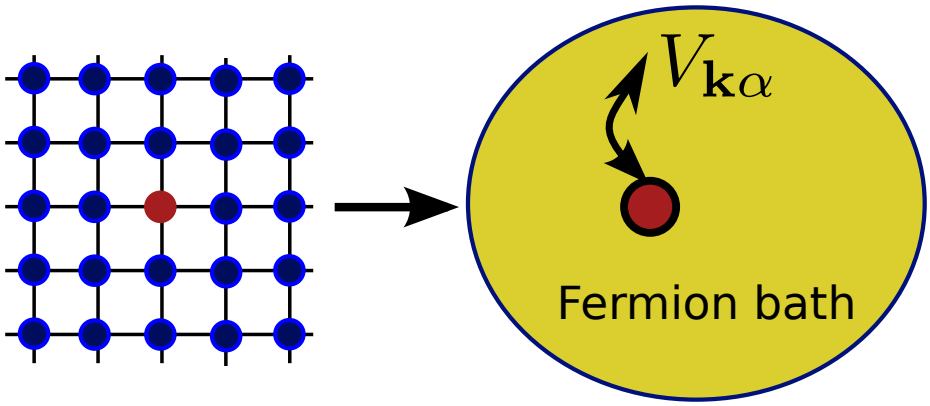

Figure 2.9: DMFT method: the lattice is mapped into an impurity model where there is an impurity site embedded in a fermion bath. Electrons can hop between impurity and the bath with an amplitude $V_{\mathbf{k}\alpha}$.

this case, the Helmholtz free energy Ω) expressed in terms of the single particle Green's function G and the self energy Σ. For simplicity, we assume there is no spin polarization and only a single-band model, but it is easily written generally with spin dependence and for multiorbital case. Consider a general Hamiltonian H, the Helmholtz free energy is defined as

$$\Omega = -T \log Z, \tag{2.37}$$

where Z is the partition function in grand canonical ensemble

$$Z = Tr \exp\left[-\beta(\hat{H} - \mu\hat{N})\right]. \tag{2.38}$$

From Abrikosov et al. (1975), the free energy Ω can be written in terms of the Green's functions and the self energy

$$\Omega = \Omega_0 - \frac{2}{\beta}\sum_{i\omega_n}\int \frac{d^3k}{(2\pi)^3}\left[\log(1 - G_0\Sigma) + \Sigma G\right] + \Omega', \tag{2.39}$$

where $\beta = \dfrac{1}{T}$, the self energy and the Green's function are in Matsubara form $G =$

$G(\mathbf{k}, i\omega_n)$ and $\Sigma = \Sigma(\mathbf{k}, i\omega_n)$, Ω_0 and G_0 is the free energy and Green's function of the noninteracting system, Ω' is the Luttinger-Ward functional containing all irreducible Feynmann's diagrams of exact Green's function. This potential has the following properties [Abrikosov et al. (1975)]

$$\delta\Omega' = \frac{2}{\beta}\sum_{i\omega_n}\int \frac{d^3k}{(2\pi)^3}\Sigma(\mathbf{k}, i\omega_n)\delta G(\mathbf{k}, i\omega_n) \tag{2.40}$$

or

$$\Sigma = \frac{\delta\Omega'}{\delta G}. \tag{2.41}$$

The system is stable in equilibrium if $\dfrac{\delta\Omega}{\delta\Sigma} = 0$. From (2.39), the following Dyson's equation is obtained to satisfy that stationary condition

$$\Sigma = G_0^{-1} - G^{-1}. \tag{2.42}$$

With these equations, we start to derive the DMFT method by consider the basis transformation from the lattice Green's function G_{ab} to a particular Green's function $G^I_{\alpha\beta}$ (which will then be approximated as impurity Green's function).

$$G^I_{\alpha\beta} = f^{ab}_{\alpha\beta}G_{ab}. \tag{2.43}$$

(the sum over repeated indices is implied)

If this basis transformation is exact, $G^I_{\alpha\beta}$ can be used in place of the lattice Green's function G_{ab} in the free energy Ω and the Luttinger-Ward functional Ω'. Therefore, the transformation for the self energy is

$$\Sigma_{ab} = \frac{\delta\Omega'}{\delta G_{ab}} = \frac{\delta\Omega'}{\delta G^I_{\alpha\beta}}\frac{\delta G^I_{\alpha\beta}}{\delta G_{ab}} = f^{\alpha\beta}_{ab}\Sigma_{\alpha\beta}. \tag{2.44}$$

where $\sum_{\alpha\beta} f^{\alpha\beta}_{a'b'} f^{ab}_{\alpha\beta} = \delta_{aa'}\delta_{bb'}$.

The DMFT is derived by truncating the $\{\alpha\}$ basis such that the space spanned by the truncated $\{\alpha\}$ basis is much smaller than the original $\{a\}$ basis. The self energy transformation (2.44) becomes an approximation where the approximated self energy has a much smaller number of indices $\Sigma_{\alpha\beta}$.

Because of the small number of indices, one can think of constructing an impurity model that can produce $\Sigma_{\alpha\beta}$. Suppose the Hamiltonian of the original lattice has a general form

$$H = \sum_{ab} h_{ab} c_a^\dagger c_b + \sum_{abcd} I_{abcd} c_a^\dagger c_b c_c^\dagger c_d. \tag{2.45}$$

If the basis transformation (2.43) is exact, the Hamiltonian becomes

$$H = \sum_{\alpha\beta} \bar{h}_{\alpha\beta} c_\alpha^\dagger c_\beta + \sum_{\alpha\beta\gamma\delta} \bar{I}_{\alpha\beta\gamma\delta} c_\alpha^\dagger c_\beta c_\gamma^\dagger c_\delta, \tag{2.46}$$

where $\bar{h}_{\alpha\beta} = f_{\alpha\beta}^{ab} h_{ab}$ and $\bar{I}_{\alpha\beta\gamma\delta} = f_{\alpha\beta}^{ab} f_{\gamma\delta}^{cd} I_{abcd}$.

As the transformation is not exact, a fermion bath is introduced that accounts for all the difference as the basis is truncated. The transformed Hamiltonian thus has the form of an impurity model where $\alpha, \beta, \gamma, \delta$ are impurity indices

$$H_{imp} = \sum_{\mathbf{k}} \epsilon_{\mathbf{k}} a_{\mathbf{k}}^\dagger a_{\mathbf{k}} + \sum_{\mathbf{k}\alpha} \left(V_{\mathbf{k}}^\alpha a_{\mathbf{k}}^\dagger c_\alpha + h.c. \right) + \sum_{\alpha\beta} \bar{h}_{\alpha\beta} c_\alpha^\dagger c_\beta + \sum_{\alpha\beta\gamma\delta} \bar{I}_{\alpha\beta\gamma\delta} c_\alpha^\dagger c_\beta c_\gamma^\dagger c_\delta, \tag{2.47}$$

where $a_{\mathbf{k}}^\dagger$ and $a_{\mathbf{k}}$ are creation and annihilation operators for bath fermions and $c_\alpha^\dagger, c_\alpha$ are that for impurity fermions, $V_{\mathbf{k}}^\alpha$ is the hybridization between the bath and the impurity, as introduced in Fig. 2.9.

The impurity Green's function derived from solving (2.47) is

$$\hat{G}^I(i\omega_n) = \left[(i\omega_n + \mu)\not\mathbb{1} - \hat{\bar{h}} - \hat{\Delta} - \hat{\Sigma} \right]^{-1}, \tag{2.48}$$

where the hybridization is obtained by integrating the bath fermions directly

$$\Delta^{\sigma}_{\alpha\beta}(i\omega_n) = \sum_{\mathbf{k}} \frac{V^{\alpha\sigma}_{\mathbf{k}} V^{*\beta\sigma}_{\mathbf{k}}}{i\omega_n - \epsilon_{\mathbf{k}}}. \tag{2.49}$$

The noninteracting Green's function (when $I_{\alpha\beta\gamma\delta} = 0$) is

$$\hat{G}^{I}_{0}(i\omega_n) = \left[(i\omega_n + \mu)\mathbb{1} - \hat{\bar{h}} - \hat{\Delta}\right]^{-1}. \tag{2.50}$$

This is the dynamical mean field (the Weiss field) which can be used as an input for the impurity solver and will be determined self consistently from the self consistent equation $G^{I}_{\alpha\beta} = f^{ab}_{\alpha\beta} G_{ab}$.

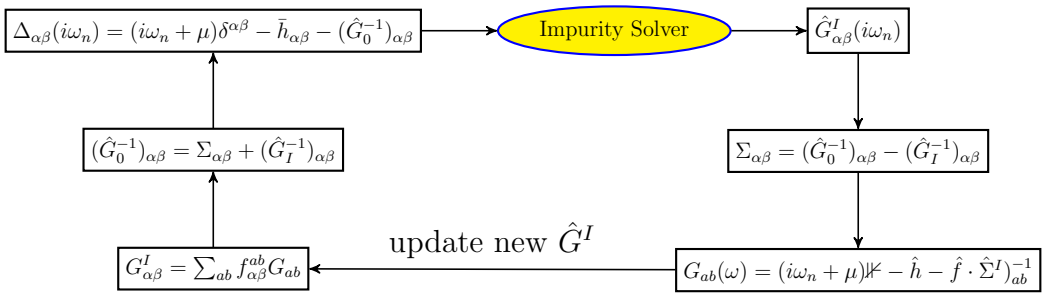

Figure 2.10: General diagram for the DMFT self consistent loop.

With this knowledge, the DMFT procedure is constructed in following steps (with Figure 2.10 for the diagram of the self consistent loop)

1. Construct the impurity Hamiltonian H_{imp} given the hybridization $V^{\alpha}_{\mathbf{k}}$ and the energy dispersion of the bath $\epsilon_{\mathbf{k}}$, the impurity energy level $\bar{h}_{\alpha\beta}$ and the interaction $\bar{I}_{\alpha\beta\gamma\delta}$ are determined from the equations above.

2. Solve the impurity model (2.47) to obtain the impurity Green's function $G^{I}_{\alpha\beta}$, the impurity self energy is thus obtained using the Dyson's equation (2.42)

3. With $\Sigma_{ab} = f_{ab}^{\alpha\beta}\Sigma_{\alpha\beta}$, the lattice Green's function is

$$\hat{G}(i\omega_n) = \left[(i\omega_n + \mu)\not{1} - \hat{h} - \hat{\Sigma}\right]^{-1}, \tag{2.51}$$

with $\hat{h}$ is the hopping matrix which, in the simple form, is the tight binding matrix in (2.10).

4. The impurity Green's function is updated using the relation between impurity and lattice Green's functions $G_{\alpha\beta}^{I} = f_{\alpha\beta}^{ab}G_{ab}$.

5. Dyson's equation (2.42) is used again to obtain the updated noninteracting Green's function $\hat{G}_0$ (the dynamical mean field).

6. $\hat{G}_0$ provides the bath fermion dispersion $\epsilon_{\mathbf{k}}$ and $V_{\mathbf{k}}^{\alpha\sigma}$ for the next iteration. The self consistent calculation runs until $\hat{G}^I$ converges.

Depending on how $f_{ab}^{\alpha\beta}$ is constructed, there are several types of DMFT calculation

- Single-site DMFT: the self energy is approximated to be independent of $\mathbf{k}$-vector $f_{ab}^{\alpha\beta} = f_{\mathbf{k}}^{0} = \delta_{\mathbf{k},0}$.

- Cellular DMFT [Kotliar et al. (2001)] is a cluster version of DMFT focusing on the real space Green's function, the cluster impurity is denoted by I

$$f_{ab}^{\alpha\beta} = f_{ij}^{I} = \begin{cases} 0 & \text{if } |i-j| \notin I \\ 1 & \text{if } |i-j| \in I \end{cases} \tag{2.52}$$

- Dynamical cluster approximation (DCA) [Maier et al. (2005)] is another cluster extension of DMFT focusing on the reciprocal space, in which the Brillouin zone BZ1 is divided into several sectors $\mathbf{K}$, $\Sigma(\mathbf{k}) \approx \Sigma_{\mathbf{K}}$ if $\mathbf{k} \in \mathbf{K}$, therefore

$$f_{ab}^{\alpha\beta} = f_{\mathbf{k}}^{\mathbf{K}} = \begin{cases} 0 & \text{if } \mathbf{k} \notin \mathbf{K} \\ 1 & \text{if } \mathbf{k} \in \mathbf{K} \end{cases} \tag{2.53}$$

2.3.2 Impurity solver

By mapping the lattice to the impurity model, the problem becomes much more simpler, however, the impurity model is still nontrivial to solve. Solving the impurity is thus the bottleneck of the DMFT self consistent loop (see Fig. 2.10).

There is a wide variety of impurity solvers having been developed. They can be impurity solvers based on infinite sum of certain classes of the Feynmann's diagrams such as the non-crossing and one-crossing approximations [Bickers (1987); Pruschke and Grewe (1989)]. The model can also be approximated as belonging to a Hilbert space with finite dimensions which can be solved exactly for the eigenstates and eigenvectors, this is the class of exact diagonalization (ED) solver [Caffarel and Krauth (1994)] and its extension [Zgid et al. (2012)]. Another popular class of solvers based on stochastic approach (Quantum Monte Carlo method) can also provide numerically exact solution of the impurity problem, they can range from the traditional solver based on the Hirsch-Fye algorithm [Hirsch and Fye (1986)] or the modern continuous time QMC (CTQMC) method [Gull et al. (2011)].

In this thesis, we use only the hybridization expansion version of the CTQMC (CT-HYB)[2] as the main solver for the DMFT. The details of this solver can be found in Gull et al. (2011). It starts from the partition function $Z = Tr \exp\left[-\beta(H - \mu N)\right]$ with H the impurity Hamiltonian as in (2.47). Rewrite $H = H_{bath} + H_{hyb} + H_{local}$, so that H_{bath} contains only the fermion bath kinetic energy, H_{hyb} has the $V_{\mathbf{k}}^{\alpha\sigma}$ part, while H_{local} has the onsite interaction and the bare energy of the impurity electron. In this CTQMC solver, the partition function Z is expanded in H_{hyb} and is transformed into the sum over all possible configuration with corresponding probability, the form which is ready for the Monte Carlo simulation. More technical details for this solver is presented in Appendix F.

[2] We used the code for CT-HYB solver from the TRIQS project [Ferrero and Parcollet (2011)] and the one written by P. Werner and E. Gull based on the ALPS library [Albuquerque et al. (2007)].

As the interaction is untouched, the solver is suitable for strong and arbitrary interaction and can also go to rather low temperature. Therefore, it is an appropriate solver to study multiorbital systems, as in the TMOs. Moreover, when off-diagonal interaction such as the exchange and pair hopping terms in (2.23) are removed, the density-density interaction allows the use of "segment" algorithm which can speed up the calculation by 4-5 times. Using conserved quantum numbers for block diagonalizing H_{local} also decrease the running time significantly [Haule (2007); Parragh et al. (2012)].

The disadvantage of the CT-HYB solver is that the cost of computation increases exponentially as the size of the impurity cluster increases. Therefore, for multiorbital systems, only single-site DMFT is available at the current stage. Moreover, with this solver, the Green's function has to be in imaginary time (or Matsubara frequency) representation. Analytic continuation (see Appendix B) is required to obtain the real time/frequency form so as the spectra can be derived $A(\omega) = -\frac{1}{\pi} ImG(\omega)$. This continuation procedure however is unstable and contains uncertainties.

2.3.3 Applications of DMFT in TMOs

Density functional theory plus dynamical mean-field theory (DFT+DMFT) is the common numerical approach towards realistic structure calculation [Kotliar et al. (2006)]. DFT is responsible for the background electronic properties of the systems, for example, together with the projector method [Amadon et al. (2008); Haule et al. (2010)] or with the maximally localized Wannier function (MLWF) method [Marzari and Vanderbilt (1997); Souza et al. (2001)] DFT can generate the tight binding matrix as in (2.10), DFT data is also required for the cRPA [Aryasetiawan et al. (2004)] or cLDA [Cococcioni and de Gironcoli (2005)] calculations to obtain the Coulomb matrix elements. DMFT uses DFT results as the input parameters to treat the electron

correlation. The result from the DMFT calculation may be put into the DFT again to maintain the charge self consistency between the two methods, however, as will be seen in the next chapters, this step is not important and is ignored in most of our calculations.

DMFT is also applied to the study of heterostructures made of TMOs, as found in Chapter 3. The procedure is similar to the standard DMFT as described in Subsection 2.3.1, however the impurity must be large enough to contain all inequivalent layers of the heterostructure. Nonvanishing intersite Coulomb interaction (2.32) is also required for a proper density distribution in the structure. Solving such a large impurity is impossible, instead one has to divide the impurity into smaller parts that are weakly correlated (e.g. into many layers) and run the impurity solver once for each part. The output Green's function or self energy has the block-diagonal matrix with each block corresponding to each part of the heterostructure. The update for the next iteration is the same as in the standard DMFT calculation.

Another application of DMFT that is employed in this thesis is for solving the problem of an impurity perturbing the local physics of a correlated system. When a charge impurity stays in a correlated material, its Coulomb potential can perturb the neighbor sites, however the electron nearby will strongly screen the potential so that it only affects the area with radius of a few lattice constants. DMFT can be used in combination with solving the Poisson's equation to obtain the correlation effect as well as the charge profile induced by the impurity. DMFT is used to treat the correlation and yield the local charge distribution given the local potential induced by the impurity, the charge profile is the input for the Poisson's equation to calculate the local potential, which is then used for the DMFT calculation in the next iteration. This self consistent calculation continues until a well-converged charge profile is obtained. The details of the method are discussed in Chapter 5.

Chapter 3

Ferromagnetism in early TMOs

In this chapter, we present our study of ferromagnetism in early transition metal oxides, focusing on the vanadate systems $SrVO_3$ and $LaVO_3$ (the formal valences are d^1 and d^2, respectively) and the ruthenates systems $CaRuO_3$ and $SrRuO_3$ (the formal valences are d^4). We pointed out the conditions for ferromagnetism to occur and thus explained why ferromagnetic order appears in some materials under consideration but not in others and suggested design of heterostructures to enhance ferromagnetism. The chapter is organized as follows. Section 3.1 introduces the materials under consideration. Section 3.2 gives more details about the lattice structure, model and methods. Section 3.3 presents results for bulk and superlattice structure of vanadium-based oxides. Section 3.4 are results for Ca/Sr ruthenates systems. We conclude the chapter by Section 3.5. Parts of the chapter are published in Dang and Millis (2013b,a).

3.1 Introduction

Transition metal oxides [Imada et al. (1998)] are of great interest in condensed matter physics because they exhibit a rich variety of exotic phenomena which remain incompletely understood. While "late" transition metal oxides (involving Cu or Ni) have been very extensively studied due to their connection to high-T_c superconductivity and Mn-based compounds have attracted attention for their colossal magnetoresis-

tance, the "early" transition metal oxides such as vanadium oxides, have, despite some important studies [Pavarini et al. (2004); De Raychaudhury et al. (2007)], received less attention in recent years. However, following the pioneering work of Ohtomo and Hwang [Ohtomo and Hwang (2004)], early transition metal oxides are increasingly used as components of atomic-scale oxide-based heterostructures [Kourkoutis et al. (2010); Lüders et al. (2009)]. One goal of heterostructure research is to design materials exhibiting phases not observed in bulk [Millis (2011); Hwang et al. (2012)]. An essential step towards realizing this goal is obtaining a clear understanding of the relationship between physical structure and observed electronic phenomena.

In this work, we investigate the relationship between lattice structure, correlation strength and electronic properties in the context of ferromagnetism in early transition metal oxides. Ferromagnetism is a correlated electronic property which is both technologically important and (because only a spin symmetry and not translation or gauge symmetry is broken) more straightforward from the theoretical and computational points of view than other phases such as antiferromagnetism or superconductivity. We choose the early transition metal oxides in part because of the intriguing recent report [Lüders et al. (2009)] of ferromagnetism in superlattice systems involving $LaVO_3$ and $SrVO_3$. The report is of interest because ferromagnetism is reported for the superlattice even though no ferromagnetism is observed in bulk solid solutions of the form $La_{1-x}Sr_xVO_3$. Another motivation is from the ruthenate systems $CaRuO_3$ and $SrRuO_3$ in which there exists ferromagnetism in $SrRuO_3$ while $CaRuO_3$ is paramagnetic down to the lowest temperature [Longo et al. (1968)] even though both materials are similar in structure except the stronger $GdFeO_3$ distortion in $CaRuO_3$. The explanation is that the superlattice enables a different structure (for vanadate superlattice) and the smaller lattice distortion (for $SrRuO_3$) prefer ferromagnetism. Understanding whether this explanation is viable, and more generally being able to design superlattices with desired magnetic properties, requires deeper

insight into the conditions

The conditions under which ferromagnetism may occur is a question of long-standing theoretical interest [Stoner (1938); Nagaoka (1966); Shastry et al. (1990); Müller-Hartmann (1995)]. The development of dynamical mean field theory [Georges et al. (1996)] has opened a new avenue of research, but apart from some pioneering investigations of the Curie temperatures of Fe and Ni [Lichtenstein et al. (2001)] the studies have mainly been based on model systems. Vollhardt, Ulmke and collaborators have studied the single-band Hubbard model, finding that in this model ferromagnetism occurs at generic carrier concentrations only when there is a large density of states peak at or near the lower band edge [Vollhardt et al. (1997); Ulmke (1998)]. For a fixed value of the Hubbard U, the Curie temperature T_c was found to depend sensitively on the peak position, becoming unmeasurably small as the density of states peak was moved a small distance away from the lower band edge [Wahle et al. (1998)]. However, many materials of physical and technological interest involve transition metals with partially filled degenerate (or nearly degenerate) d-levels, where the Hund's interaction may play an important role. While the importance of the Hund's interaction in partially filled d-levels has been appreciated for decades, the issue has been systematically studied only in the case of the Bethe lattice [Held and Vollhardt (1998); Peters et al. (2011); Chan et al. (2009)] in which the density of states has a simple semi-circular structure. In this situation large values of the Hund's coupling and correlation strength (the Hubbard U) are required for ferromagnetism.

In this chapter, we study the conditions for ferromagnetism to occur in these materials (vanadate bulk and superlattice structures and ruthenate systems). In structures composed of $LaVO_3$ and $SrVO_3$, the d level is partly filled, ranging from 1 to 2 electrons per vanadium atom, the d electron is subject to strong correlation and large Hund's coupling. $LaVO_3$ is classified as a Mott insulator with rather large $GdFeO_3$ distortion [Imada et al. (1998)]. It has structural and antiferromagnetic transitions at

around 140K but is insulating to high temperatures [Bordet et al. (1993); Miyasaka et al. (2000)]. $SrVO_3$ in contrast is an intermediate correlated metal and only has paramagnetic order. The ruthenate family exhibits ferromagnetism in opposite way. $SrRuO_3$ is ferromagnetic with a Curie temperature of $\sim 160K$ despite having small $GdFeO_3$ distortion, $CaRuO_3$ with a larger distortion amplitude is simply a paramagnetic Fermi liquid metal at the lowest temperatures studied [Longo et al. (1968)]. Our investigations are based on density functional theory (DFT) calculations and include in particular the effects of $GdFeO_3$-type rotations of the MO_6 structural motif of the ideal perovskite structure. We treat the many body physics using the single-site dynamical mean field approximation [Georges et al. (1996)], which is widely used in real-material many-body physics calculations [Kotliar et al. (2006); Held (2007)] and in particular in studies of ferromagnetism [Vollhardt et al. (2001, 1997)].

Our main result is an understanding of the dependence of ferromagnetism on carrier concentration, octahedral rotation and correlation strength. We find that for d^1 and d^2 systems (vanadate systems), for small and intermediate correlation, increasing the octahedral rotation amplitude increases the tendency to ferromagnetism. The physics underlying this result is a density of states effect related to that previously noted in the one-band Hubbard model [Vollhardt et al. (2001, 1997)]. For strong correlation, the Mott insulator for integer filling (such as $LaVO_3$) suppresses ferromagnetic order, thus doping away from integer filling enhances ferromagnetism. For d^4 systems (Ca and Sr ruthenates), they have two holes in the t_{2g} shell, thus they are particle-hole transform of the La vanadate. It leads to an opposite effect of $GdFeO_3$ rotation on the ferromagnetism in the ruthenate materials. However, Mott insulating state is still an important factor to suppress the ferromagnetic order.

We remark that in the literature, the many-body physics properties of transition metal oxides have been modeled in two ways. One, which we refer to as the "d-only model", treats the frontier orbitals (in the case of the vanadium-based ma-

terials, antibonding bands derived mainly from V t_{2g}-symmetry d-orbitals admixed with oxygen p_π states) as a multi-orbital Hubbard model. This approach is generally accepted [Imada et al. (1998)] as the relevant description of the early transition metal perovskites such as the systems we study here. A second approach is based on atomic-like d-orbitals which are subject to on-site correlations and are hybridized with the full p-manifold. This approach is used in the DFT+U and DFT+DMFT [Kotliar et al. (2006); Held (2007)] approaches. It is generally believed to be essential to a correct description of the late (e.g. Cu-based or Ni-based) transition metal oxides [Zaanen et al. (1985)] but has been less widely used in the study of early transition metal oxides. We consider both approaches, finding similar qualitative conclusions but significant quantitative differences which arise from the richer physics of the "*pd* model" situation. Thorough study of this model will be presented in Chapter 4.

3.2 Model and Methods

3.2.1 Geometrical structure

In bulk systems, only bulk $SrVO_3$ crystallizes in the ideal cubic RMO_3 perovskite structure [Rey et al. (1990)], other materials ($LaVO_3$, $CaRuO_3$ and $SrRuO_3$) may be thought of as a cubic perovskite with an additional $GdFeO_3$-type rotational distortion leading to a tilted structure with symmetry group $Pnma$ [Bordet et al. (1993); Jones et al. (1989); Bensch et al. (1990)]. Fig. 3.1 shows the lattice structure of a $GdFeO_3$-distorted perovskite. The basic structural motif of the perovskite structure is the oxygen octahedron. In the $GdFeO_3$ rotated structure there are four inquivalent octahedra characterized by different directions of the principal axes and by slight ($\sim 5\%$) distortions of the M-O bond length. We have found (not shown) that varying the relative magnitudes of the M-O bond lengths over the physical range causes only

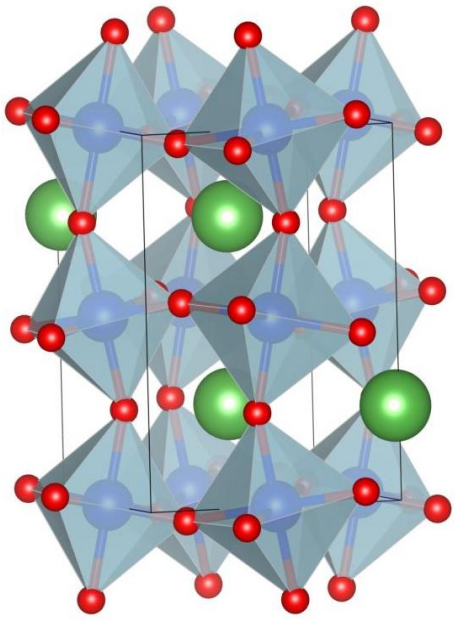

Figure 3.1: (Color online) Representation of ABO_3 perovskite structure with $GdFeO_3$-type (octahedral rotation) distortion generated using the VESTA program [Momma and Izumi (2011)]. Large spheres (green online): A atoms (here La or Sr), small spheres (red online): O atoms, intermediate size spheres at the centers of the octahedra (blue online) : B-site atoms (here, V).

small changes to the non-interacting DOS or to the DMFT solution. Therefore, for the vanadates, we set all V-O distances to $d = 1.95$Å and focus on the effect of rotation by studying a range of θ and ϕ, while for ruthenates we only use the structure from experimental measurements.

The octahedral rotations in the $GdFeO_3$-distorted *Pnma* systems can be characterized by two angles, θ and ϕ [Pavarini et al. (2005)] with corresponding rotation axes $\hat{n}_\theta$, $\hat{n}_\phi$ and wavevectors $\vec{Q}_\theta$, $\vec{Q}_\phi$ characterizing the changes in rotation axis from cell to cell. We choose coordinates such that the rotation axis $\hat{n}_\theta$ is [110] while $\hat{n}_\phi$ is [001]. The corresponding wavevectors are $\vec{Q}_\theta = (\pi, \pi, \pi)$ and $\vec{Q}_\phi = (\pi, \pi, 0)$. For vanadates, bulk $LaVO_3$ has $\theta = 11.5°$ and $\phi = 8.8°$ [Bordet et al. (1993)]. As La is progressively replaced by Sr in bulk solid solution $La_{1-x}Sr_xVO_3$, θ and ϕ go to 0. For ruthenates $SrRuO_3$ with a Ru-O-Ru bond angle of about 163° ($\theta = 8.5°$) is less

distorted than $CaRuO_3$ with a Ru-O-Ru bond angle of 150° ($\theta = 15°$ [Jones et al. (1989); Bensch et al. (1990)].

In the superlattices composed of layers of $SrVO_3$ alternating with layers of $LaVO_3$, if we idealize the structures as cubic perovskites, then the layers alternate along the [001] direction. The presence of a substrate and the breaking of translation symmetry can lead to different rotational distortions of the basic perovskite structure as compared with the corresponding bulk solid solution and also to a difference between lattice constants parallel and perpendicular to the growth direction.

For superlattices, substrate-induced strain may change the situation in a way which depends on the growth direction. Boullay et al. (2011); Rotella et al. (2012) confirm that the growth direction for the experimentally relevant superlattices is [001] (in the ideal cubic perovskite notation) and we focus on this case here. Recent experimental studies of superlattices [Rotella et al. (2012)] and of $LaVO_3$ thin films, which apparently have the same growth direction [Boullay et al. (2011)] suggest that the rotations are of the type $a^-a^+c^-$ [Glazer (1972)] and indicate that the dominant rotation is around the axis defined by the growth direction: $\alpha = \beta \approx 3°$ and $\gamma \approx 11.5°$. This distortion pattern is different from that occurring in bulk. To explore its effects we set $\alpha = \beta = 3°$ and consider the consequences of varying γ.

In bulk $La_{1-x}Sr_xVO_3$, while the 4-sublattice *Pnma* structure implies a difference in lattice constants, all V-O bond lengths are the same [Bordet et al. (1993)]. The difference in lattice constants arises from a difference in tilting pattern. Superlattices are typically grown on a substrate, and in epitaxial growth conditions the lattice constants perpendicular to the growth direction (which we denote here by a) are fixed by the substrate, while the lattice parameter along the growth direction (c) is free to relax. The result is a c/a ratio typically $\neq 1$ contributed by both tilting and anisotropy in V-O bond lengths and possibly varying from layer to layer of the superlattice. For the experimentally studied superlattices, $c/a \sim 1.02$ [Boullay et al.

(2011); Rotella et al. (2012)]. The V-O bond lengths have not been determined but our studies indicate that all V-O bonds have essentially the same length, moreover a few percent differences have no significant effect on our study of ferromagnetism [Dang and Millis (2013a)]. Similar to the bulk case, we set all V-O bond lengths to be equal.

3.2.2 Electronic structure

The large energy splitting between the transition metal d-bands and oxygen p-bands characteristic of early transition metal oxides is generally believed [Imada et al. (1998)] to justify a downfolding to a model containing only the frontier bands, which in the present case are composed mainly of t_{2g} symmetry d-states from transition metal atom with only a small admixture of oxygen p-states. We refer to this as the d-only model. In Subsection 3.3.2 we present an examination of a more general "charge transfer" model in which the full p-d complex is considered.

The Hamiltonian of the d-only model, as a short form of (2.9), is

$$H = H_{kin} + H_{onsite} + H_{coulomb}. \tag{3.1}$$

where $H_{coulomb}$ is only nonzero for the case of superlattice structures.

The kinetic Hamiltonian has the form (2.10). While for the cubic structure, the $\hat{H}_{band}(\mathbf{k})$ describing the t_{2g}-derived antibonding bands is easily constructed using phenomenological tight binding methods described in Section 2.2, in tilted structure, the form of $\hat{h}_{band}(\mathbf{k})$ is more difficult to express in the simple tight binding language. Therefore, we construct $\hat{h}_{band}(\mathbf{k})$ numerically from density functional theory (DFT) band structure calculations using maximally-localized Wannier function (MLWF) techniques [Marzari and Vanderbilt (1997)].

The on-site interaction term in the Hamiltonian, H_{onsite}, is assumed to take the

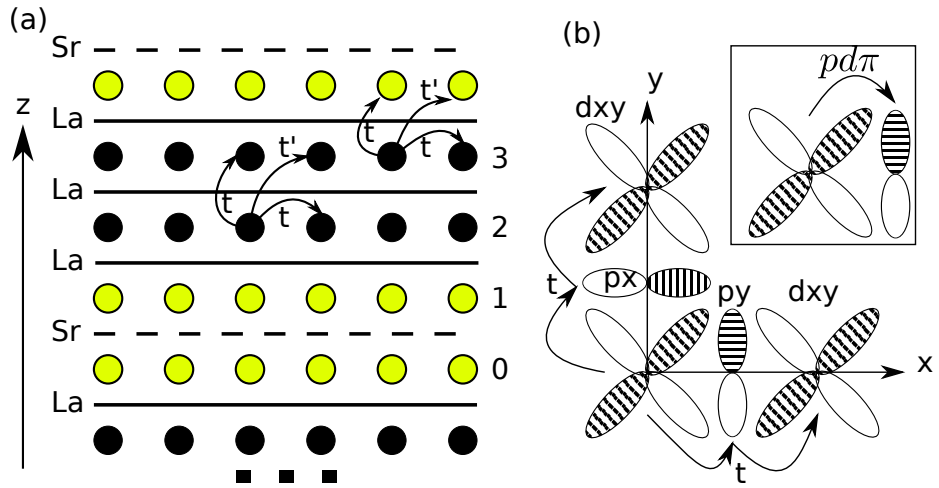

Figure 3.2: (Color online) (a) Schematic of superlattice lattice structure $(LaVO_3)_m(SrVO_3)_1$ with $m = 3$. Vanadium sites indicated as circles with charge density indicated by shading: heavy shading (black online) indicating higher charge density and light shading (yellow online) indicating lower charge density. LaO and SrO planes are shown as solid and dashed lines respectively. Nearest neighbor (t) and next-nearest neighbor (t') hoppings between vanadium sites indicated by arrows. The numbers on the right are VO_2 layer indices. (b) Inset: $pd\pi$ hopping between t_{2g} orbital and p-orbital. Main panel: two-dimensional nearest neighbor hopping t made of two $pd\pi$ hoppings from xy orbital of one vanadium site to oxygen p_x or p_y orbital, then to xy orbital of another vanadium site.

Kanamori's form [Kanamori (1963)] as in (2.23) with $U' = U - 2J$ for rotationally invariant interaction. For vanadate systems, we consider several values of U and J but focus most attention on the values $U = 6\text{eV} \sim 22t$ and $J = 1\text{eV}$. These values of U and J are similar to but slightly larger than those used in recent papers [Sekiyama et al. (2004); Nekrasov et al. (2006); De Raychaudhury et al. (2007)] and are chosen to reproduce the crucial feature of the phase diagram, which is that $LaVO_3$ is a Mott insulator while $SrVO_3$ is a metal. However, for $CaRuO_3$ and $SrRuO_3$, we study in a wide range of U and J.

In superlattice structure, we study superlattices designed to be similar to the system studied in [Lüders et al. (2009)]. In these superlattices, units of m layers of $LaVO_3$ are separated by one layer of $SrVO_3$. To define the superlattice, we begin from

LVO in the appropriate bulk structure, then break translation invariance along the [001] (z-direction) by replacing every (m+1)$^{\text{st}}$ LaO plane with an SrO plane. Fig. 3.2a shows such a superlattice with $m = 3$.

We assume that the superlattice is grown epitaxially so that in-plane bond lengths and other aspects of the local structure including rotations are the same for all layers. We therefore take the electron transfer integrals which define the band structure to the be same for all layers. In this case the electronic structure of a superlattice is defined by adding the electrostatic potentials of the Sr and La ions to the basic translationally invariant hopping Hamiltonian describing the bulk materials.

In the approximation employed here, the superlattice is defined by the Coulomb interaction between the La/Sr ions and electrons. This, and the off-site part of the electron-electron interaction [Okamoto and Millis (2004)] is contained in

$$H_{coulomb} = H_{el-ion} + H_{el-el}. \tag{3.2}$$

To construct H_{el-ion}, we assume that the whole ion charge of SVO or LVO unit cell comes into the Sr or La site. Consider $SrVO_3$, the valence of V is +4 (d^1). If this one d-electron is removed, the SVO unit cell will have charge +1, hence, in our model, Sr site has charge +1. Similarly, $LaVO_3$ has V^{+3} (d^2), thus La site has charge +2. As a result, H_{el-ion} has the form

$$H_{el-ion} = \sum_{i,R_{Sr}} \frac{-e^2\hat{n}_i}{4\pi\epsilon\epsilon_0|R_i - R_{Sr}|} + \sum_{i,R_{La}} \frac{-2e^2\hat{n}_i}{4\pi\epsilon\epsilon_0|R_i - R_{La}|}. \tag{3.3}$$

where n_i is electron-occupation operator at V-site i, ϵ is the relative dielectric constant. The part H_{el-el} is the inter-site Coulomb interaction of vanadium d-electrons

$$H_{el-el} = \frac{1}{2}\sum_{\substack{i,j \\ i\neq j}} \frac{e^2\hat{n}_i n_j}{4\pi\epsilon\epsilon_0|R_i - R_j|}. \tag{3.4}$$

H_{el-el} is treated in the Hartree approximation. Note that in Eq. (3.4), $\hat{n}_i$ is the operator giving the total d-electron occupation of site i, while $n_j = \langle \hat{n}_j \rangle$ is the expectation value of d-electron occupancy at site j, which is determined self consistently. From $H_{coulomb}$, the Coulomb potential V_i for site i is calculated using Ewald summation [Ewald (1921)].

The dielectric constant ϵ is an important parameter in Eqs. (3.3, 3.4). It accounts for screening on the scale of a lattice constant so bulk measurements are not directly relevant and an appropriate value has not been determined. Values ranging from 4 to 15 have been reported in the literature for similar systems [Okamoto et al. (2006); Shekhter et al. (2008)]. Because the appropriate value of ϵ has not been determined, we have studied several cases and present results mainly for $\epsilon = 8, 15$.

We treat the onsite Coulomb interaction using DMFT method (the details of the method is in Section 2.3). There is a slight difference in the DMFT implementation for vanadate and ruthenate systems with $GdFeO_3$ distortion. In vanadate systems, the full 5 d bands are considered. As mentioned in Chapter 2, it is necessary to rotate to local basis of each octahedron when formulating the impurity problem (see Appendix C). However, in ruthenate systems, we improve the method by focusing only on the t_{2g} manifold as the e_g bands are higher energy, seperated by energy gap of $0.5 \rightarrow 1eV$. The MLWF basis of t_{2g} subspace is almost rotated, the DMFT calculation is thus straightforward without further basis rotation.

3.2.3 The magnetic phase boundary

In order to detect magnetic order, one can allow for broken symmetry states in the DMFT procedure and lower the temperature until an ordered state is reached. However, ordering temperatures are typically so low relative to the basic energy scales in the problem that our simulations become prohibitively expensive. We therefore

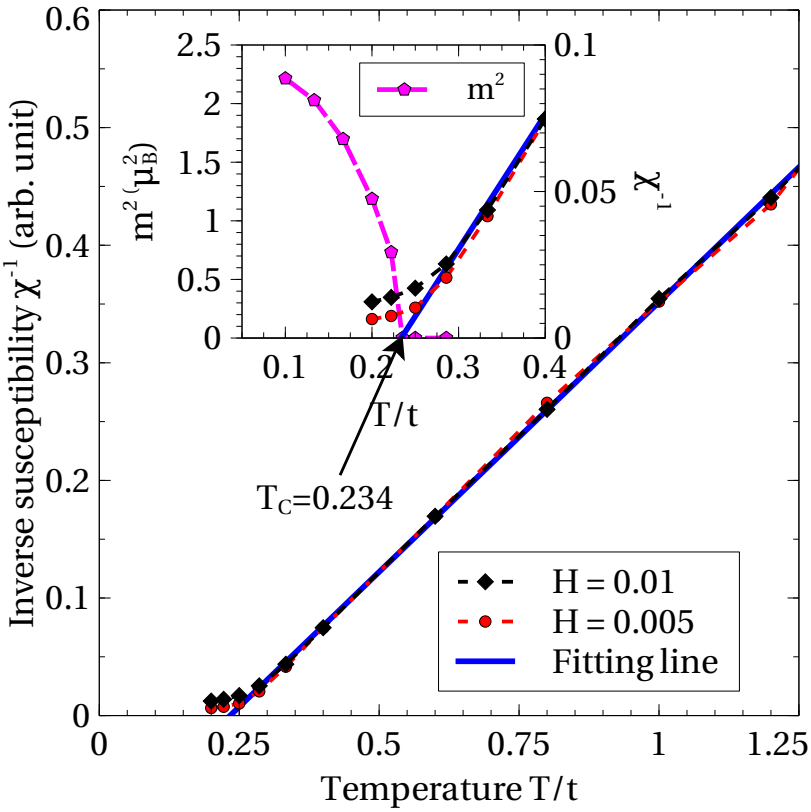

Figure 3.3: (Color online) Inverse magnetic susceptibility $\chi^{-1} = \dfrac{H}{m(H)}$ plotted vs. temperature T obtained from single-site DMFT solution to (3.1),(2.17) with H_{kin} taken to have the form appropriate to a simple cubic lattice with nearest neighbor hopping t and second neighbor hopping $t' = -0.3t$. Carrier density is fixed to $n = 1.5$ and applied magnetic field $H = 0.005$ (circles) and $H = 0.01$ (diamonds). The Curie temperature $T_c = 0.234t$ is estimated by linear extrapolation of χ^{-1} in the region where m is linear in H. Inset: expanded view of the near T_c region, together with the magnetization squared (m^2) (left y-axis) calculated by allowing for broken symmetry DMFT solution at $H = 0$ which also shows that $T_c \approx 0.234t$. The parameters are $t = 0.5, t' = -0.3t, U = 16 = 32t$ and $J = \dfrac{U}{6}$.

compute the susceptibility which is found to have a Curie-Weiss form $\chi^{-1} \sim T - T_c$. Extrapolation of χ^{-1} to 0 yields an estimate of the Curie temperature T_c. We interpret positive T_c as evidence of magnetism. To compute χ^{-1}, we add a uniform field $\vec{H} \cdot \vec{\sigma}$ to our Hamiltonian, compute the magnetization $m(H)$, verify that m is linear in H

and then define $\chi^{-1} = \frac{H}{m}$.

Fig. 3.3 demonstrates the method on a model with a high Curie temperature, where the magnetic state can easily be constructed. This model is defined by (3.1),(2.17) with H_{kin} taking the same form as in the simple cubic lattice but with t' chosen as $\frac{t'}{t} = -0.3$, so that the sign of t'/t is opposite to the sign implied by band structure calculations on the actual materials. For this unphysical sign of t'/t the model has a ferromagnetic ground state with a high Curie temperature. We set carrier density $n = 1.5$ and calculate T_c in two ways: by lowering the temperature until ferromagnetic order is observed, which is at $T_c = \frac{2t}{9} \approx 0.222t$; or by measuring $\chi^{-1}(T)$ for several values of T above T_c and linearly extrapolating to $\chi^{-1} = 0$. The extrapolation shows $T_c = 0.234t$. The two values are very close. We conclude that extrapolating T_c from $\chi^{-1}(T)$ is a reliable way to determine whether the model exhibits ferromagnetic order.

3.3 Vanadate bulk and superlattices

3.3.1 Magnetic phase diagram

In this subsection, we study the magnetic phase diagram of model systems derived from the calculated band structure of $LaVO_3$ but with variable amplitude for the $GdFeO_3$ distortion and different values for the carrier concentration.

Fig. 3.4 shows the evolution of the non-interacting density of states with increasing amplitude of the $GdFeO_3$ distortion. If the structure is cubic, the energy dispersion in the t_{2g} manifold is almost two dimensional. The sign and magnitude of t' place the van Hove peaks of the non-interacting DOS are at high energy (see top panel ($\theta = \phi = 0$) of Fig. 3.4). As the distortion amplitude is increased the lowest DOS peak shifts to lower energy and the bandwidth decreases. Previous literature suggests

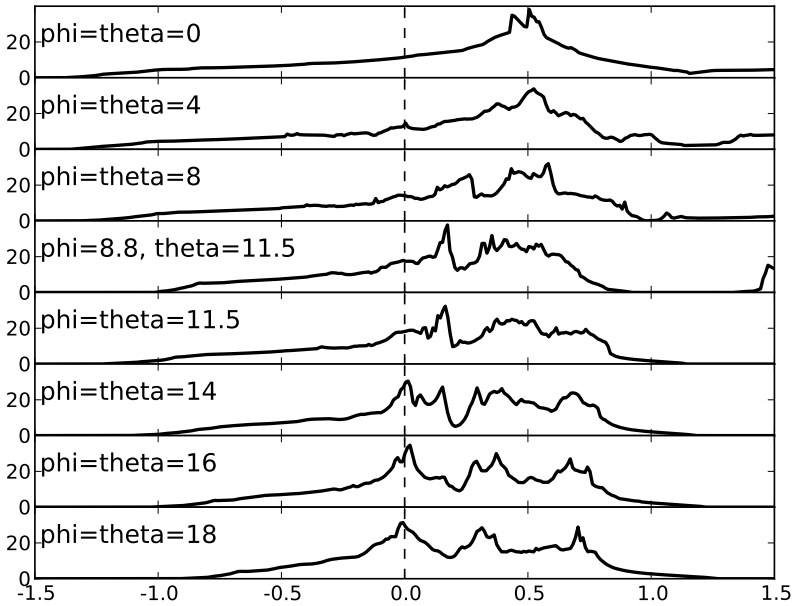

Figure 3.4: Density of states for bulk $LaVO_3$ (d-carrier density $n = 2$) calculated from DFT with different values of tilt angle θ and rotation angle ϕ in which $\theta = \phi$ together with the DOS of realistic LVO structure ($\theta = 11.5°, \phi = 8.8°$). A van Hove peak at the Fermi level develops as θ and ϕ increase, and is well-formed at $\theta = \phi = 14°$ and above. The bandwidth W decreases as the θ and ϕ increases. The Fermi energy is at 0.

a connection between peak position and ferromagnetism [Vollhardt et al. (1997, 2001)] while standard Stoner theory [Stoner (1938)] suggests that bandwidth may also be important.

We begin our study of the connection by examining the cubic structure. The solid curve with filled circles (black online) in Fig. 3.5 is the inverse susceptibility calculated for temperatures down to $T = 0.03$eV for the case $U = 6$eV, $J = 1$eV and carrier density $n = 1.5$ using the DOS shown in top panel of Fig. 3.4, which has the bandwidth $W \approx 2.4$eV. The inverse susceptibility curve is seen to deviate from the Curie form at low temperature. The extrapolation to zero of the high temperature linear regime implies a $T_c < 0$.

We attribute the flattening out of the susceptibility curve to the onset of Fermi-liquid coherence. To verify this, and to gain additional insight into the nature of

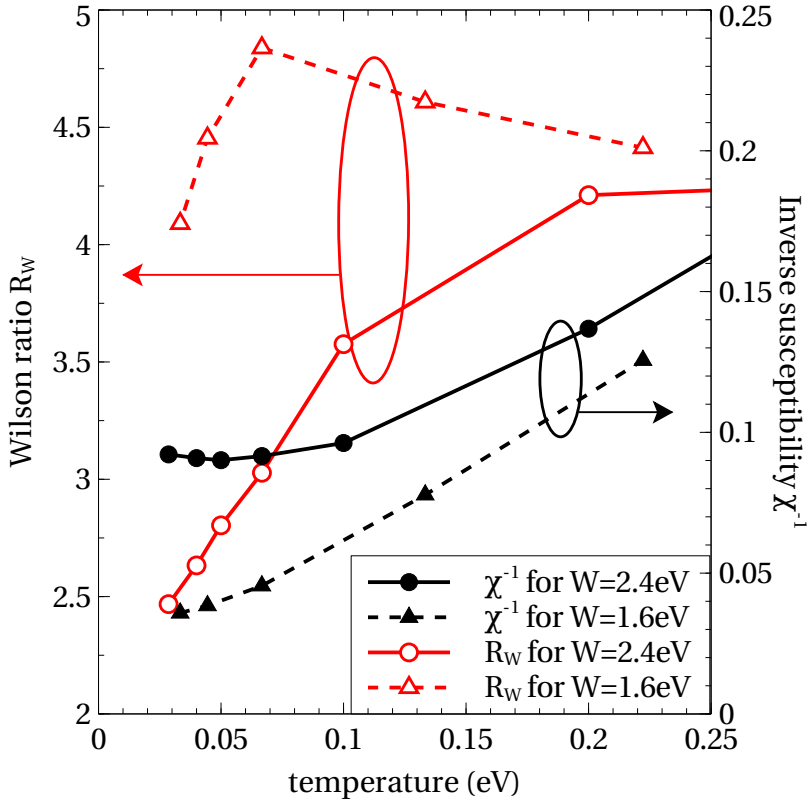

Figure 3.5: (Color online) Inverse magnetic susceptibility χ^{-1} (closed symbols, black on-line; right axis) and Wilson ratio R_W (open symbols, red on-line, left axis) calculated for $La_{1-x}Sr_xVO_3$ cubic structure as functions of temperature at carrier density $n = 1.5$ and on-site interactions $U = 6$eV, $J = 1$eV using two bandwidths, $W = 2.4eV$ (circles and solid lines) and $W = 1.6eV$ (triangles and dashed lines).

spin correlations in this model, we computed the Wilson ratio $R_W = \frac{\pi^2}{3}\frac{\chi}{\gamma}$ [Wilson (1975)] (in our conventions the dimensional factors $\frac{k_B}{\mu_B} = 1$). Here γ is the coefficient of the linear specific heat $\gamma = \left.\frac{dC_V}{dT}\right|_{T=0} = \frac{\pi^2}{3}\mathrm{Tr}[\nu_F Z^{-1}]$ [Pourovskii et al. (2007)]. We estimated the linear coefficient of the specific heat from the density of states ν_F at the Fermi level and calculated renormalization factor Z, which are obtained from the measured imaginary time Green function via $\nu_F \approx -\frac{\beta}{\pi}G(\tau = \beta/2)$ and from the Matsubara frequency self energy via $Z^{-1} \approx 1 - \frac{\mathrm{Im}\Sigma(\omega_1 = 3\pi/\beta) - \mathrm{Im}\Sigma(\omega_0 = \pi/\beta)}{\omega_1 - \omega_0}$

(not shown).

The solid curve with open circles (red online) in Fig. 3.5 shows that, for the DOS in the top panel of Fig. 3.4 with $U = 6$eV and $J = 1$eV, the Wilson ratio extrapolates to the value $R_W = 2$ as temperature $T \to 0$. The value $R_W = 2$ is expected for a Kondo lattice with a low quasiparticle coherence scale but no intersite correlations, while a system with strong ferromagnetic correlation would be characterized by an $R_W \gg 2$. We therefore conclude that there is no evidence for ferromagnetism in the cubic structure at $U = 6, J = 1$eV and $W = 2.4$eV and that the flattening of the $\chi^{-1}(T)$ curve indicates the onset of the Fermi liquid coherence.

We now turn to the effects of the $GdFeO_3$ distortion. For simplicity of presentation, we focus mainly on the case $\theta = \phi$. Fig. 3.4 shows the evolution of DOS with tilting angle. We see that, as the tilt angle is increased, the position in energy of the lowest density of states peak shifts down in energy.

Fig. 3.6 shows the evolution of the inverse susceptibility with increasing amplitude of $GdFeO_3$ distortion at $U = 6$eV and $J = 1$eV for two carrier density values $n = 1.55$ and $n = 1.95$. For $n = 1.55$, ferromagnetic order can be observed starting at $\theta = \phi = 14°$. In contrast, for $n = 1.95$, the Curie temperature is nonzero within errors only for $\theta = \phi > 16°$.

The shaded areas (color online) in Fig. 3.7 show the phase diagram resulting from a detailed study of the dependence of Curie temperature on carrier density and tilt (rotation) angle at $U = 6$eV and $J = 1$eV obtained from curves such as those shown in Fig. 3.6. The expense of the computation and the uncertainties inherent in our extrapolation means that the phase boundary is not precisely determined. We regard $T_c < 0.004$eV as consistent with $T_c = 0$ within uncertainties. The width of the strip separating $T_c = 0.004$ and 0.008 gives a measure of the error bars on the locations of the phase boundary. The divergence in tilt angle required to obtain a nonzero transition temperature as $n \to 2$ may be understood from the fact that for the interaction

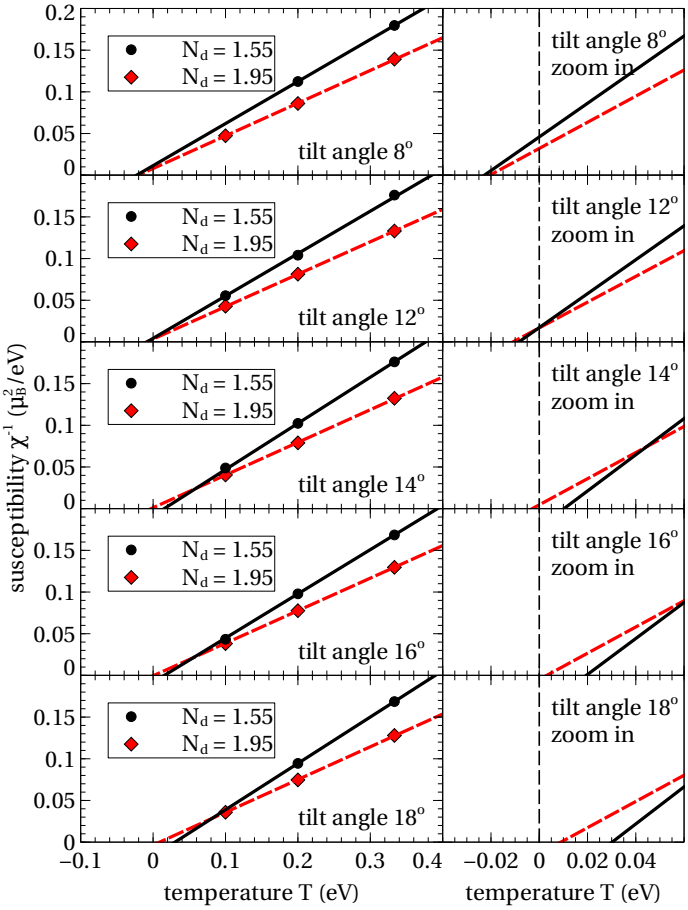

Figure 3.6: (Color online) Temperature dependence of inverse susceptibility computed for model $La_{1-x}Sr_xVO_3$ computed for tilt angles $\theta = \phi$ from 8° to 18° computed at densities $n = 1.55$ (black circle lines) and $n = 1.95$ (diamond dashed lines) and interaction parameters $U = 6$eV, $J = 1$eV from Eq. (3.1) with H_{kin} derived from MLWF fits to band structure. The diamonds and circles are data points measured by DMFT. The lines are fitted from data points. Left column: plot over wide temperature range; right column: expanded view of small χ^{-1} region. The vertical dashed line marks zero temperature.

strength considered here the $n = 2$ compound is a Mott insulator. Ferromagnetism is favored by metallic motion of the carriers and is suppressed in proximity to the Mott insulating phase which for the parameters we consider is antiferromagnetically ordered. To summarize, we see that for these values of U and J obtaining a ferro-

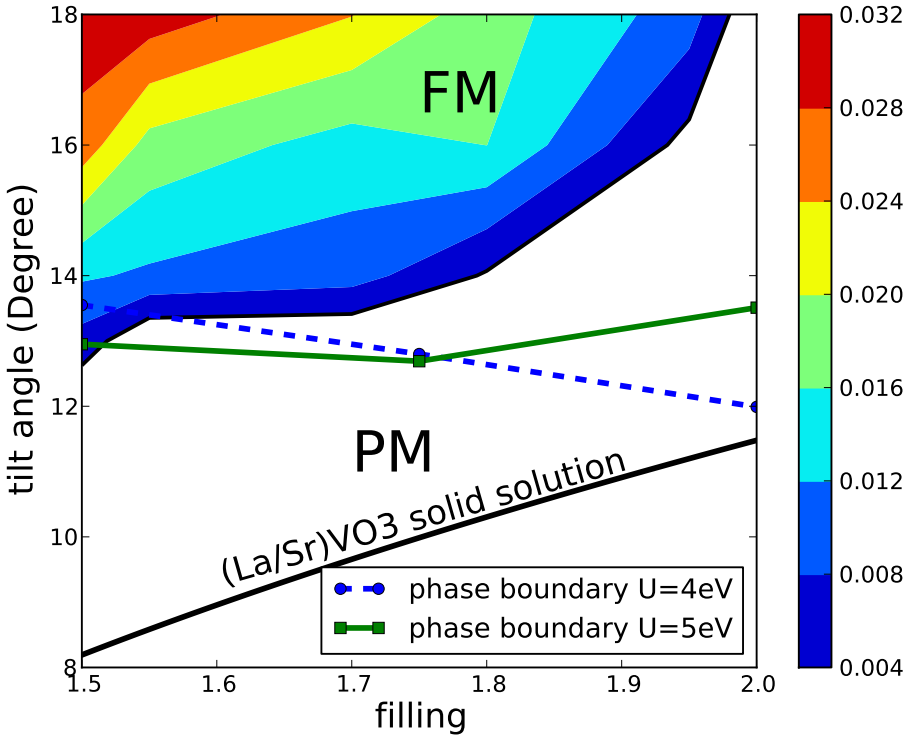

Figure 3.7: (Color online) The magnetic phase diagram in the space of carrier density n (x-axis) and tilt and rotation angles $\theta = \phi$ (y-axis) for the solid solution $La_{1-x}Sr_xVO_3$ with on-site interactions $U = 6$eV, $J = 1$eV. The white region indicates paramagnetic order ($T_c < 0.004$eV), the colored regions denote ferromagnetic order with the transition temperature T_c given by the scale bar (color on-line). The solid curve is the $\theta = \theta(n)$ curve estimated for $La_{1-x}Sr_xVO_3$. The estimated phase boundaries for $U = 4$ (circle and dashed line, blue on-line) and 5eV (squares and solid line, green on-line) with $J = 1$eV are also plotted.

magnetic state requires two conditions: (1) large hole doping away from $LaVO_3$ and (2) large $GeFeO_3$-type distortion.

We now consider the physics behind the dependence of transition temperature on tilt angle. Inspection of Fig. 3.4 shows that increasing the magnitude of the $GdFeO_3$ both reduces the bandwidth (from 2.4eV at $\theta = \phi = 0$ to 1.8eV at the critical angle) and moves the position of the lowest density of states peak to lower energy. To investigate the relative importance of the two effects we have performed

computations for the cubic structure using $U = 6$eV, $J = 1$eV but with reduced bandwidth $W = 1.6$ eV. The dashed curves in Fig. 3.5 show the Wilson ratio R_W (open triangles, red on-line) and the inverse susceptibility χ^{-1} (filled triangles, black on-line) for the smaller bandwidth $W = 1.6$eV. The susceptibility curve indicates that the intercept is increased relative to the larger bandwidth case, but remains negative. The sharp downturn in the Wilson ratio at the lowest temperatures suggests that the decrease in intercept is a consequence of a lowered Fermi liquid coherence scale and does not indicate stronger ferromagnetic correlations. We therefore conclude that for reasonable values of the bandwidth and interaction strength the crucial factor for ferromagnetism is the position of the density of states peak. For very large values of the Hund's coupling $J(\gtrsim 3\text{eV})$, ferromagnetism may occur over a much wider parameter range, as seen in previous Bethe lattice studies [Held and Vollhardt (1998); Peters et al. (2011); Chan et al. (2009)].

The importance of the position of the density of states peak was previously noticed in the context of the one-band Hubbard model [Vollhardt et al. (1997); Ulmke (1998); Wahle et al. (1998)]. However, in that case ferromagnetism was only found if the density of states peak is far below the Fermi level of the paramagnetic state. In the present case inspection of Fig. 3.4 shows that it is only necessary for the density of states peak to be not too far above the Fermi level. We believe that the difference arises from the "double exchange" physics of Hund's coupling in partially filled d-shells. The Hund's coupling favors high spin states, which means that hopping between two sites is optimal if the spins are parallel and is suppressed if they are not parallel. This strongly favors ferromagnetism. A natural question is how far above the Fermi level can the density of states peak be and still support ferromagnetism. For a reasonable range of J (~ 1eV, see Fig. 3.8) we find that a good rule of thumb is that ferromagnetism occurs if the density of states peak lies at or below the Fermi level of the *fully polarized ferromagnetic state*. This answer is clearly not universal

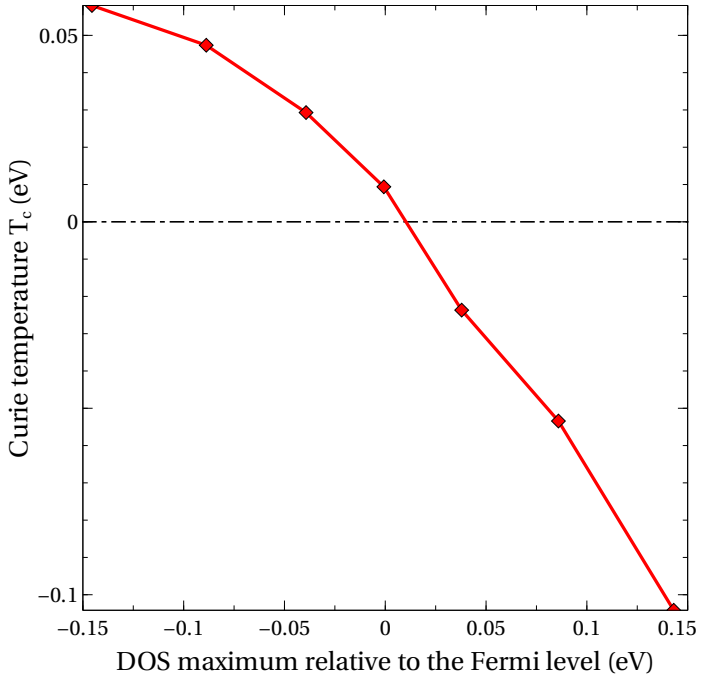

Figure 3.8: (Color online) The dependence of Curie temperature T_c on van Hove peak position with respect to the Fermi level of fully spin-polarized state calculated from Eqn. (2.17) with $t = 0.264$eV, t'/t changes from $-0.3 \rightarrow 0.3$. On-site interactions $U = 6$eV and $J = 1$eV. The dashed line marks the zero temperature.

since model system studies [Held and Vollhardt (1998); Peters et al. (2011); Chan et al. (2009)] indicate that increasing J to very large values favor ferromagnetism even if the density of states peak lies very high in energy.

We have also studied selected densities at the smaller interaction strengths $U = 4$eV and $U = 5$eV. Estimates of the resulting phase boundaries are shown as dashed and solid lines in Fig. 3.7. We see that for intermediate n the phase boundary is only weakly dependent on U and n. For carrier concentrations near $n = 2$ weakening the correlations to move the system out of the Mott phase greatly increases the range in which ferromagnetism is observed.

3.3.2 The effect of oxygen bands

In early transition metal oxides, the bands that cross the Fermi level are well separated from other bands and are of mainly transition metal d-character, arising from t_{2g} symmetry orbitals. In many body calculations, it is common to focus only on these bands, which are treated as a multiband Hubbard model, while all other bands are neglected [Imada et al. (1998); Pavarini et al. (2004)]. However, it is generally believed that the fundamentally correct model of the transition metal oxides should be based on atomic-like d-orbitals coupled to weakly correlated oxygen p-states [Zaanen et al. (1985)]. In this section we examine the magnetic phase diagram of the vanadate system by applying the methods described in previous sections to the model including transition metal d bands and oxygen p bands ("pd" model) and comparing the results to those from the "d-only" model.

The pd model has two important energy scales: the on-site interaction U which as before is the energy cost for changing d-occupancy and the charge transfer energy, in other words, the energy cost for an electron to hop from a ligand to a transition metal atom. The charge transfer energy may be defined in different ways but the correct value is not well established, either from ab initio considerations or from experiment. The important points for our subsequent discussion are the physics depends sensitively on the charge transfer energy as well as on U and that for reasonable U a metal-insulator transition may be driven at integer band filling by varying the charge-transfer energy [Zaanen et al. (1985)]. We will see that, as was found in the d-only model, the doping and tilt angle dependence of the ferromagnetic phase boundary depends on whether the parameters are such as to place $LaVO_3$ on the metallic or insulating sides of the metal-insulator phase diagram.

As mentioned in Chapter 2, the kinetic Hamiltonian H_{kin} has to be enlarged to contain both both vanadium d and oxygen p-orbitals. The corresponding $h^{\alpha\beta}_{band}(\mathbf{k})$ is a larger tight-binding matrix with α and β are indices for both p and d oribtals and

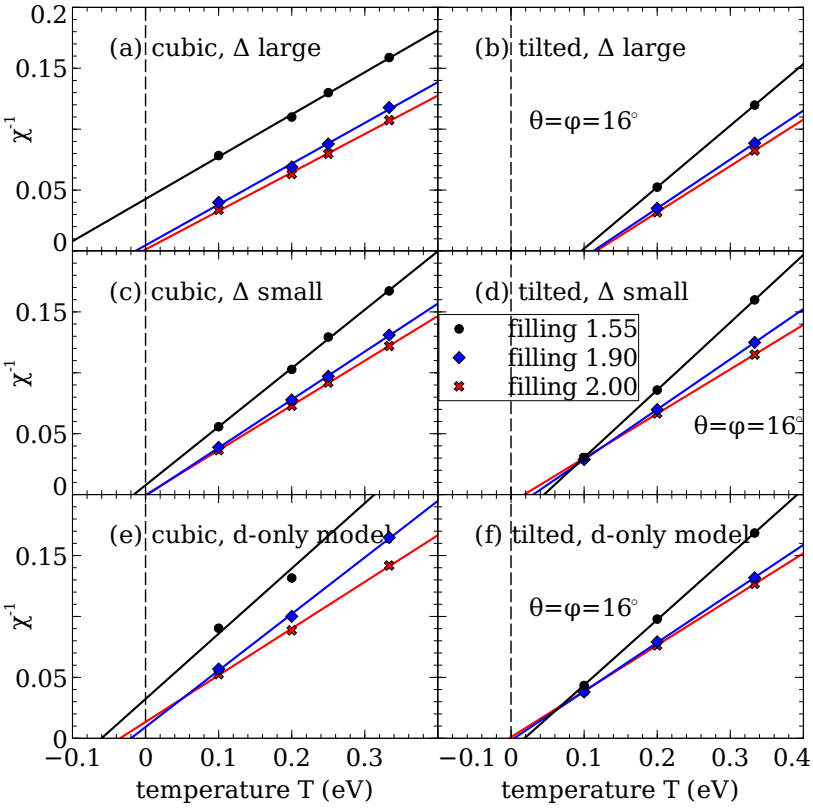

Figure 3.9: (Color online) Inverse susceptibility vs. temperature for three different filling values 1.55, 1.90 and 2.00 for cubic (left column) and $GdFeO_3$-distorted $LaVO_3$ with tilt angle $\theta = \phi = 16°$ (right column). (a,b) *pd* model with large Δ (approximately that predicted by standard double counting correction [Lichtenstein and Katsnelson (1998)]); (c,d) *pd* model with small Δ; (e,f) *d*-only model. On-site interactions $U = 6$eV, $J = 1$eV. For cubic case, $\Delta_{large} = 10.97$eV, $\Delta_{small} = 2$eV. For tilted case, $\Delta_{large} = 10$eV, $\Delta_{small} = 0$eV. The vertical dashed lines mark zero temperature.

is generated using MLWF methods with a wide energy window including both bands.

However, as only *d* orbitals are correlated, there must be double counting correction Δ, i.e., the *d* level is renormalized as $\epsilon_d = \epsilon_d^0 - \Delta$. We consider two values for Δ: one, which we refer to as $\Delta_{large} \sim 10$eV, is essentially the value obtained by applying the standard double counting correction [Lichtenstein and Katsnelson (1998)] to basic band theory and is such that $LaVO_3$ is predicted to be metallic, in contradiction to experiment. The other value, which we refer to as $\Delta_{small} \sim 0 - 2$eV, is such that the

material is insulating at $n = 2$ in agreement with experiment.

The resulting model is solved using single-site DMFT as described in Chapter 2, but with one important addition. The full p-d manifold includes V e_g orbitals. While the e_g energy lies above the Fermi level, so that the e_g-derived antibonding bands are empty, some of the filled bands are e_g-oxygen bonding states which have a small but non-zero e_g content. One must therefore solve a 5-orbital impurity model. Performing this calculation in full generality would be prohibitively expensive. We therefore follow standard procedure and treat the e_g orbital contribution to the impurity model in a Hartree approximation.

Fig. 3.9 shows representative computations of the inverse susceptibility for cubic and tilted systems at several carrier concentrations. The top row (panels a and b) displays pd model results obtained for the standard double counting correction (so that $LaVO_3$ is wrongly predicted to be a metal) while the middle rows (panels c and d) show results obtained if the double counting correction is tuned so that the calculation places $LaVO_3$ in the Mott/charge-transfer insulating regime of the phase diagram. The bottom two panels (e and f) present d-only model results for comparison. In the d-only model the U value is such as to place the $n = 2$ ($LaVO_3$) material in the Mott insulating region of the phase diagram). The transition temperature estimates obtained by linearly extrapolating the χ^{-1} curves to 0 are given in Table 3.1.

Examination of the results in Table. 3.1 shows that the qualitative trends are the same in the pd and d-only model calculations. In particular, in both models increasing the tilt angle increases the tendency towards ferromagnetism. However, significant differences are visible; in particular the pd model has a significantly greater tendency to ferromagnetism than does the d-only model and (especially in the small-Δ case) the differences are more pronounced for the cubic than for the tilted structure.

We believe that there are two main origins for the differences. First, in the small Δ cubic system case, the change in the charge transfer energy relative to band theory

	$n = 1.55$	$n = 1.90$	$n = 2.00$
cubic, $\Delta_{large} = 10.97$eV	-0.1230	-0.0139	-0.0040
tilted, $\Delta_{large} = 10$eV	0.0963	0.1127	0.1167
cubic, $\Delta_{small} = 2$eV	-0.0161	0.0025	0.0007
tilted, $\Delta_{small} = 0$eV	0.0452	0.0303	0.0178
cubic, d-only model	-0.0602	-0.0200	-0.0349
tilted, d-only model	0.0185	0.0042	-0.0025
cubic, d-only model, $U = 4$eV	-0.2347	-0.1368	-0.1250
tilted, d-only model, $U = 4$eV	0.0267	0.0345	0.0366

Table 3.1: Values for Curie temperature T_c (in eV) for each case considered in Fig. 3.9 together with results for $U = 4$eV for three different fillings $n = 1.55, 1.90$ and 2.00. All computations are for $J = 1$eV; except where indicated, $U = 6$eV is used.

affects the density of states, moving the peaks closer to the Fermi level while for the tilted structure the shift in charge transfer energy does not change the peak positions as much (see Dang and Millis (2013b)). Second, and perhaps more important, the e_g state occupancy arising from the $p - d$ bonding bands (omitted in the d-only model) increases the effective moment on the d-site, thereby enhancing the tendency towards magnetism. This effect is more pronounced in the larger Δ (smaller charge transfer energy) case, because the p-d mixing is larger.

To demonstrate this point we present in Fig. 3.10a,b calculations of the inverse susceptibility under different conditions. The curves in the left panel compare calculations in which the e_g occupancy is frozen at the spin unpolarized values (dashed lines) and calculations in which the e_g orbitals are treated within the Hartree-Fock approximation as described above. We see that the feedback from the polarization of the e_g orbitals makes a significant contribution to the transition temperature. The right panels show that calculations performed in the "frozen e_g" model agree reasonably well with the corresponding calculations in the d-only model for $U = 4eV < U_c$ [Dang and Millis (2013b)].

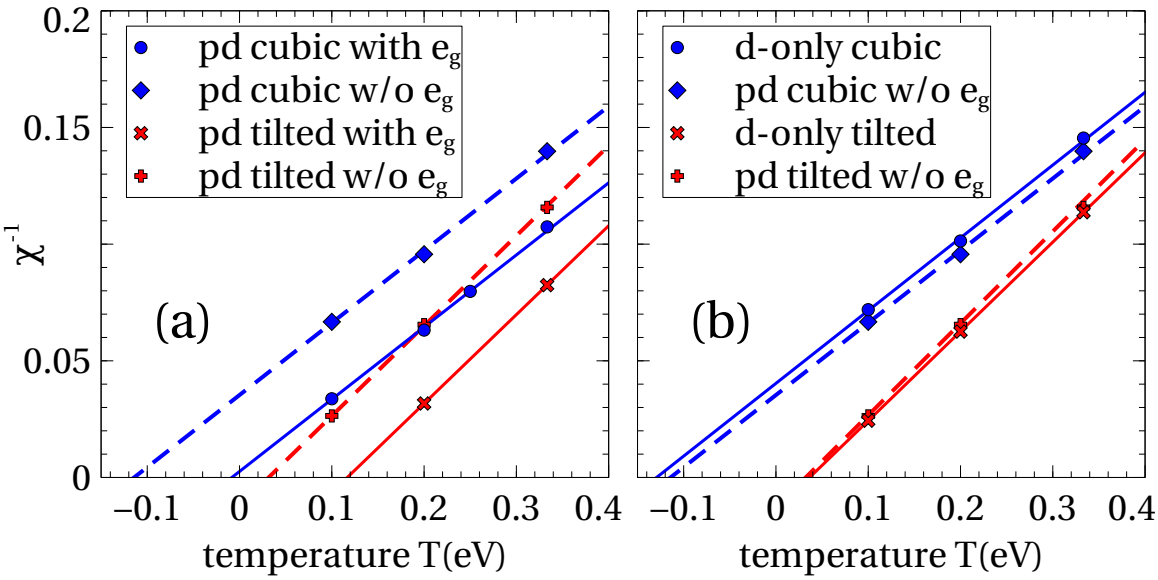

Figure 3.10: (Color online) Inverse susceptibility vs. temperature for cubic (blue color) and 16°-tilted (red color) structures at filling $n = 2.0$. (a) Comparison for pd model with (solid lines) and without (dashed lines) e_g band spin polarization. (b) Comparison between d-only model (solid lines) and pd model without e_g band spin polarization (dashed lines). Parameters for calculations with pd model are the same as in Fig. 3.9a,b. Calculations with d-only model use $U = 4\text{eV} < U_c$, $J = 1\text{eV}$ for both structures.

3.3.3 Relation between superlattice and bulk system calculations

In this section, we demonstrate that the magnetic phase diagrams of superlattice systems may be inferred, to reasonable accuracy, from the study of appropriately chosen bulk systems. This enables a considerable reduction in the computation resources required.

We begin with a study of "untilted" or "cubic" superlattices: those in which all V-O-V bond angles are 180°. We focus specifically on [001] superlattices in which the unit cell contains m layers LVO and one layer SVO, where $m = 3, 4, 5$. For orientation, we present the density of states (DOS) of the non-interacting system in Fig. 3.11. In obtaining these densities of states we used the simple tight binding

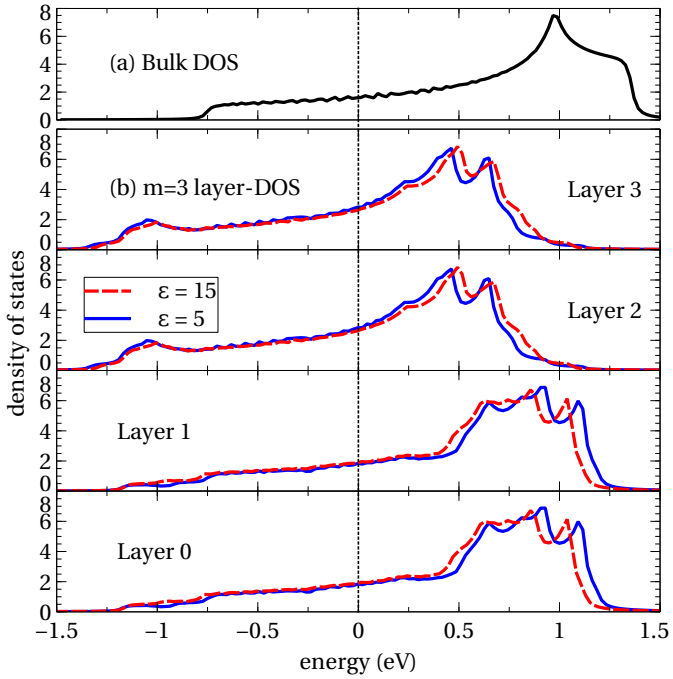

Figure 3.11: (Color online) Panel (a): Non-interacting density of states for bulk system at carrier density $n = 1$. Panels (b): Non-interacting density of states for different layers of $(LVO)_3(SVO)_1$ superlattice for two different values of dielectric constant $\epsilon = 5$ (solid) and $\epsilon = 15$ (dashed) with hopping parameters $t = 0.264$eV and $t' = 0.084$eV. SrO plane is between layers 0 and 1 (the index is defined in Fig. 3.2). The Fermi energy is at 0.

parametrization. The DOS for the bulk system is shown in panel (a). One sees the typical three-fold degenerate DOS for t_{2g} band, the Van Hove singularity is visible as a peak near the upper band edge. It is at high energy because the next-nearest neighbor hopping $t' > 0$. The remaining panels show the layer-resolved densities of states for the $m = 3$ superlattice. The upper two panels show layers sandwiched by La on both sides; the lower two panels show the layers adjacent to the SrO plane. The superlattice-induced changes in the density of states are seen to be relatively minor: the main effects are a weak splitting of the van Hove peaks reflecting the breaking of translational invariance in the z-direction, and a relative shift in the positions of the van Hove peaks arising from band bending associated with the different charges

of the Sr and La ions.

Fig. 3.12 shows the layer-resolved charge density and inverse susceptibility $\frac{H}{m(H)}$ plotted against temperature for three different superlattice structures corresponding to $m = 3, 4, 5$. As expected from electrostatic considerations, the charge is lower for the VO_2 planes nearer the SrO layer and the charge variation between layers is controlled by the dielectric constant.

The magnetization m the V sites on each layer was computed at field $H = 0.01\text{eV}/\mu_B$ and the inverse susceptibility was obtained as H/m. Linearity was verified by repeating the computation using $H = 0.02\text{eV}/\mu_B$ (not shown). For the $m = 3, \epsilon = 15$ case (Fig. 3.12a), we extended the computation to the lower temperature $T = 0.03\text{eV}$; for the other two cases $T = 0.06\text{eV}$ was the lowest temperature studied. The inverse susceptibilities are approximately linear in temperature at higher temperatures and in all cases, extrapolation to $\chi^{-1} = 0$ reveals $T_c < 0$, implying absence of ferromagnetism.

Especially for the layer nearest the SrO plane the χ^{-1} curves exhibit weak upward curvature at the lowest temperatures studied. As discussed in Subsection 3.3.1, the curvature is a signature that the system is entering a Fermi-liquid coherence regime. The Fermi liquid coherence temperature is highest for the layers nearest the SrO because the charge in these planes is farther from the $n = 2$ Mott insulating state. To verify this we repeated the calculation in Subsection 3.3.1 and computed the Wilson ratio R_W for each layer of the superlattice for the case $m = 3, \epsilon = 15$, finding (not shown) that for each layer the R_W extrapolates to 2 at low temperature. The approach to the low temperature value is faster for layers with low density (near SrO planes) than for layers with high density (far from SrO planes). $R_W = 2$ is the value for a Kondo lattice, while ferromagnetism is characterized by an $R_W > 2$. We therefore believe that for "untilted" superlattices, the differences in χ^{-1} among layers arise from differences in quasiparticle coherence scale, there is no evidence for ferromagnetism

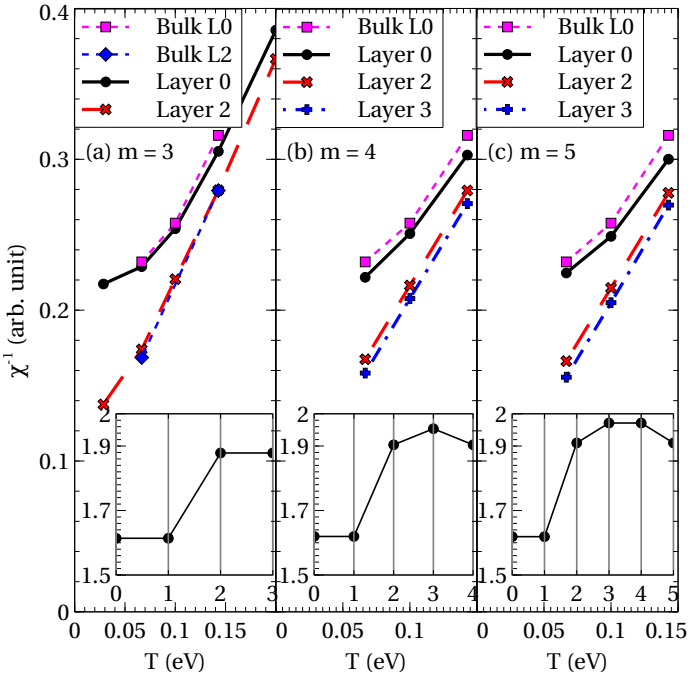

Figure 3.12: (Color online) Temperature-dependent layer-resolved inverse magnetic susceptibilities for symmetry-inequivalent layers of untilted $(\mathrm{LVO})_m(\mathrm{SVO})_1$ superlattice structures with different numbers of LVO layers $m = 3, 4$ and 5. Layer 0 is adjacent to SrO and layers 2 and 3 are between two LaO layers. The relative dielectric constant is $\epsilon = 15$, magnetic field $H = 0.01\mathrm{eV}/\mu_B$. The $\chi^{-1}(T)$ obtained from solution of bulk cubic systems with charge density set to the density on the given layer are also shown. "Bulk L0" ("BulkL2") denotes a calculation performed for a bulk system with density the same as for $L = 0$ ($L = 2$) layer density. Inset: the electron layer density distribution corresponding to the susceptibility plot, x-axis is the layer index, y-axis is the layer density. On-site interactions $U = 6\mathrm{eV}$, $J = 1\mathrm{eV}$.

in this system, consistent with the solution of the corresponding bulk problem.

To gain insight into the physics underlying the layer dependence of χ^{-1} we have computed $\chi^{-1}(T)$ for the cubic bulk system ($H_{coulomb} = 0$, H_{kin} is constructed from the two-dimensional dispersion $\epsilon(\mathbf{k}) = -2t(\cos k_x + \cos k_y) - 4t' \cos k_x \cos k_y$) for carrier densities equal to those on the different VO_2 layers. In Fig. 3.12, we present bulk calculations for $n = 1.62$ and $n = 1.88$ corresponding to the densities calculated

for layer 0 and 2 of the superlattice for all cases $m = 3, 4, 5$. For $n = 1.88$, bulk χ^{-1} at $T = 0.06, 0.10$ and 0.14eV are very close to those of $L = 2$ layer of $m = 3$ superlattice, which has the same density. For $m = 4, 5$ superlattices, bulk $n = 1.88$, $\chi^{-1}(T)$ (not shown) almost coincides with those of $L = 2$ layer. For bulk $n = 1.62$, the difference between bulk and superlattice $L = 0$ layer is small. These calculations demonstrate a general rule: within the single-site DMFT approximation, the layer-resolved properties of a superlattice correspond closely to those of the corresponding bulk system at a density equal to that of the superlattice.

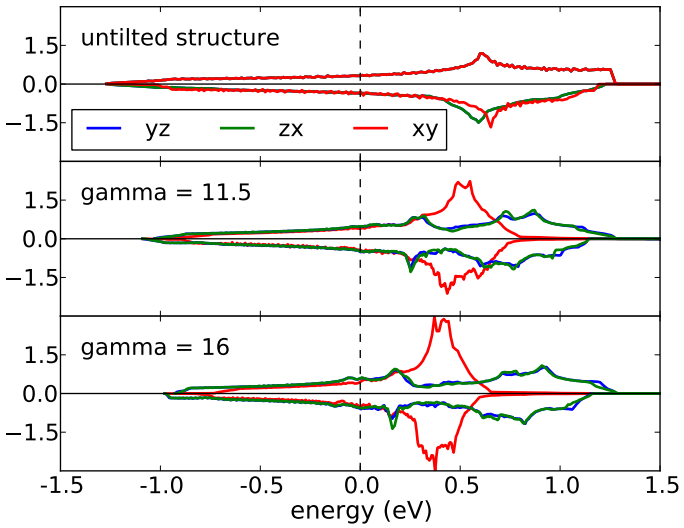

Figure 3.13: (Color online) Comparison between bulk LVO partial DOS (positive curves) and $(LaVO_3)_3(SrVO_3)_1$ superlattice layer DOS of layers near SrO (negative curves) derived from band structure calculations (DFT+MLWF). Both systems have the same lattice structure for each case: untilted structure for the top panel and $P2_1/m$ structure (Glazer's notation $a^-a^+c^-$) with $\alpha = \beta = a = 3°$ and $\gamma = c = 11.5°$ and 16° for other panels. The DOS of bulk system is shifted towards higher energy so that bulk carrier density is the same as layer density of superlattices for the layers near SrO ($n \approx 1.55$). The vertical dashed line marks the Fermi level.

The superlattices of experimental relevance have crystal structures which are distortions of the "untilted" one, involving in particular a $P2_1/m$ structure characterized by a rotational distortion of the $a^-a^+c^-$ type [Glazer (1972)] involving a large rota-

tion about an axis approximately parallel to the growth direction and much smaller rotations about the two perpendicular axes. Fig. 3.13 compares the non-interacting DOS of bulk and $(LVO)_3(SVO)_1$ superlattice systems (both with the same $P2_1/m$ structure) calculated using DFT and a MLWF parametrization of the frontier bands. The DOS of bulk system is shifted so that it has the same carrier density as layers of the superlattices near SrO plane. For three different structures (untilted structure and $P2_1/m$ structure with $\gamma = 11.5°$ and $16°$), the basic features of the partial DOS are similar between bulk and superlattice. The translation symmetry breaking in z-direction leads to small extra peaks in the superlattice DOS. These differences are smoothed out by the large imaginary part of the DMFT self energy. Because the DMFT equations depend only on the density of states it is reasonable to expect that, as in the untilted case, they will therefore give the same results in the superlattice as in the bulk material with corresponding density of states.

To verify that this is the case we have also compared bulk and superlattice susceptibilities for tilted structures. The four VO_6 octahedra in a unit cell are related by rotation, so an appropriate choice of local basis means that only one calculation needs to be carried out for a given layer. Fig. 3.14 compares the inverse susceptibilities for an $m = 3$ superlattice to calculations performed on a bulk system with the same $P2_1/m$ structure. In these calculations, we choose $\gamma = 11.5°, 16°, 18°$ and dielectric constant $\epsilon = 8$. We see that in this case, as in the "untilted" case, the superlattice inverse susceptibilities $\chi^{-1}(T)$ are almost the same as those for bulk system calculated at the same density, with differences only resolvable in the expanded view for the largest tilt angles.

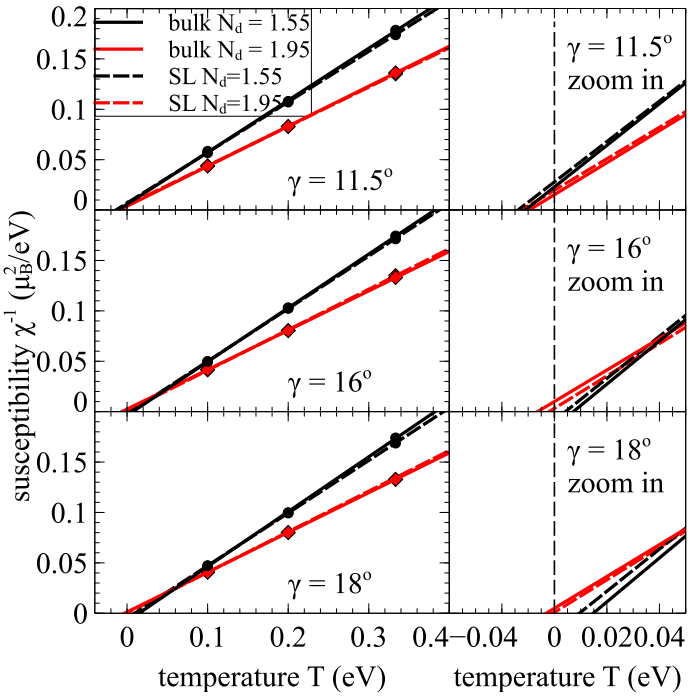

Figure 3.14: (Color online) Comparison in temperature dependent inverse susceptibility between bulk LVO (solid lines) and $(LaVO_3)_3(SrVO_3)_1$ superlattice (dashed lines). Both have the same lattice structure $P2_1/m$ with tilt angle $\gamma = 11.5, 16$ and $18°$. Bulk system has the same densities as those of layers of superlattice near and far from SrO planes ($n = 1.55, 1.95$). Left column: the plots in wide temperature range. Right column: the expanded views near zero temperature.

3.3.4 Superlattices with GdFeO3-type rotation

In this section we present and explain our results for the magnetic phase diagram of $(LVO)_m(SVO)_1$ superlattices with the $P2_1/m$ structure (Glazer's notation $a^-a^+c^-$) reported for the experimental systems [Boullay et al. (2011); Rotella et al. (2012)]. In these structures in-plane rotation along the growth direction $\hat{z} = [001]$ is large $\gamma = c = 11.5°$ (presumably because of the strain imposed by the substrate), while the out-of-plane rotation is small ($\alpha = \beta = a = 3°$) perhaps because the system is free to relax along the growth direction. We concentrate on the effect of the large rotation by fixing the in-plane angles to 3° while varying the out-of-plane angles over a wide

range from $10° \rightarrow 18°$.

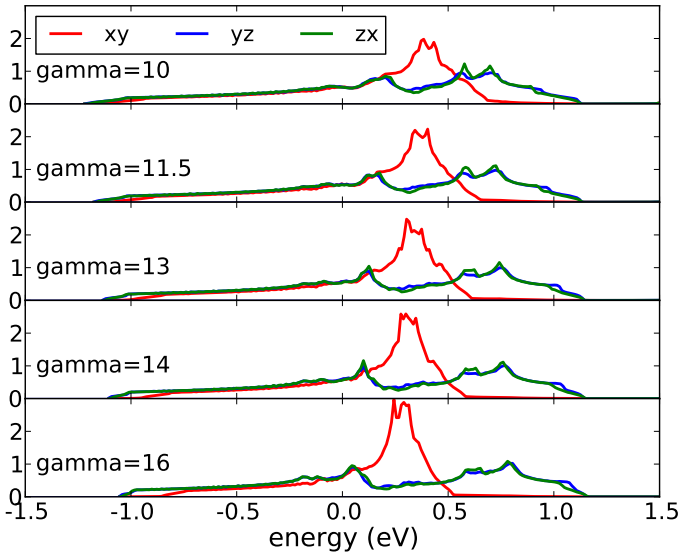

Figure 3.15: (Color online) Partial DOS derived from DFT+MLWF for "bulk" $P2_1/m$ structure (Glazer's notation $a^-a^+c^-$) with $\alpha = \beta = a = 3°$ and $\gamma = c$ changing from 10° to 16°. Only t_{2g} bands are plotted because e_g bands are negligible in this range of energy.

Based on the results of Section 3.3.3 we generate a phase diagram for the superlattice from calculations for a bulk system which is a $P2_1/m$ distortion of the ideal cubic perovskite structure of chemical composition $LaVO_3$. The bulk system results are presented as a phase diagram in the plane of carrier concentration and γ-rotation. Specific layers of the superlattice will correspond to particular points on the phase diagram, with the layer dependent density fixed by number of LVO layers m and the dielectric constant ϵ and the rotation fixed by the substrate lattice parameter.

We use DFT+MLWF methods to obtain the frontier orbital band structure for the t_{2g}-derived antibonding bands. Fig. 3.15 presents representative results for the orbitally resolved local density of states. In this figure the orbitals are defined with respect to the local basis defined by the 3 V-O bonds of a given VO_6 octahedron. We define $\hat{z} = [001]$ as the axis (approximately parallel to the growth direction) about which the large rotation occurs. Fig. 3.15 shows that yz and zx orbitals are almost

degenerate, while xy orbital is strikingly different. The DOS of xy orbital maintains the shape of a two-dimensional energy dispersion with a van Hove peak well above the chemical potential, similar to the bulk cubic structure (see e.g. Fig. 3.11a). There are noticeable differences only at very high rotation angles. On the other hand, yz and zx orbitals are spread out with two small peaks, because hoppings along x or y directions (more distorted) are different from those along z-direction (less distorted). When the distortion gets larger, the d-bandwidth becomes smaller, the xy peak gets larger and slightly closer to the Fermi level, and yz and zx peaks near the Fermi level also develop.

In the same approach as for the bulk calculation in Subsection 3.3.1, based on $\hat{h}_{band}(\mathbf{k})$ generated by DFT+MLWF, we carry out DMFT calculations for in-plane rotation angle γ to get χ^{-1} curves whose extrapolations define the Curie temperatures T_c. By varying the doping and tilt angle, we have constructed the superlattice magnetic phase diagram shown in Fig. 3.16. We consider 0.004eV as the error bar for positions on the phase diagram, the same as in calculations of bulk vanadates. We see that ferromagnetism is favored only for very large rotations, much larger than the 11° determined experimentally, and only for carrier concentrations far removed from $n = 2$. We may locate the experimentally studied superlattices on this phase diagram. For an $m = 3$ superlattice, band structure calculations indicate layer densities 1.55 for layers near SrO plane and 1.95 for the other layers. The experimentally determined rotation angle is $\sim 11.5°$. These two points are indicated by squares in Fig. 3.16.

It is interesting to compare our results to those previously obtained in Subsection 3.3.1 for the bulk solid solution $La_{1-x}Sr_xVO_3$ ($Pnma$ structure). The dashed line in Fig. 3.16 shows the theoretically estimated phase diagram for the bulk solid solution. We see that the bulk structure is more favorable for ferromagnetism than the superlattice structure. An important difference between the $Pnma$ structure and

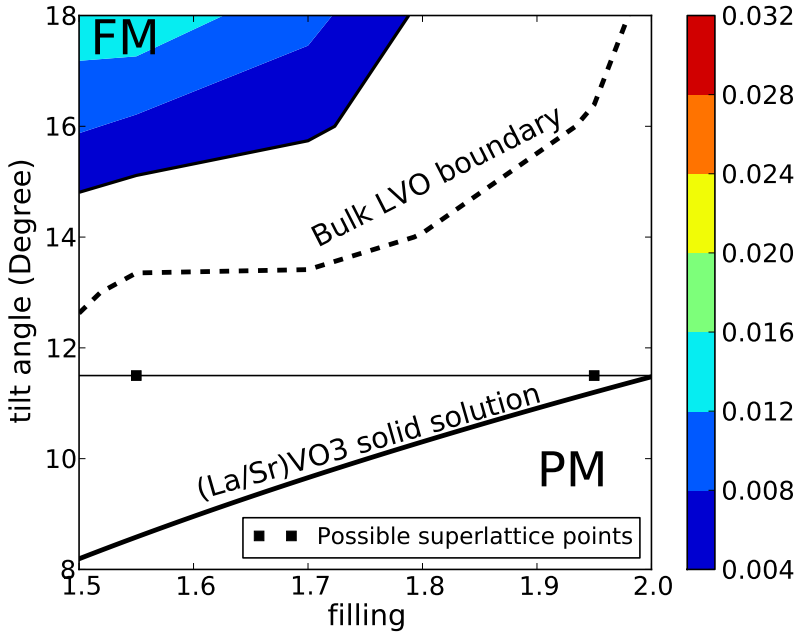

Figure 3.16: (Color online) The magnetic phase diagram with x-axis carrier density n and y-axis tilt and rotation angle along $\hat{z} = [001]$ direction γ for bulk system LVO with the same type of distortion as for $(\mathrm{LVO})_m(\mathrm{SVO})_1$ superlattices ($P2_1/m$ structure), in-plane tilt angles $\alpha, \beta \approx 3°$. On-site interactions $U = 6\mathrm{eV}$, $J = 1\mathrm{eV}$. The white regime indicates absence of ferromagnetism ($T_c < 0.004eV$), the colored regime indicates ferromagnetism with T_c indicated by the color bar. Also indicated are results for bulk $\mathrm{La}_{1-x}\mathrm{Sr}_x\mathrm{VO}_3$ in the $Pnma$ structure, from Fig. 3.7. Note that in the calculations for the $Pnma$ structure all three tilt angles are almost the same.

the $P2_1/m$ of the superlattice is that in the former case all three tilt angles are of comparable magnitude whereas in the $P2_1/m$ structure only one rotation is large. We believe that this difference is responsible for the difference in phase boundary.

3.4 Ruthenate systems $\mathrm{CaRuO_3}$ and $\mathrm{SrRuO_3}$

In this section, we focus on the family of ruthenium-based oxides, $\mathrm{CaRuO_3}$ and $\mathrm{SrRuO_3}$. As mentioned in Section 3.1, these two materials are in similar structures, both have Ru^{+4}, i.e. 4 nominal d valence electrons. However, while $\mathrm{CaRuO_3}$ is

a paramagnetic metal, $SrRuO_3$ becomes ferromagnetic at $T < 160K$ [Longo et al. (1968)]. Because $CaRuO_3$ is slightly more $GdFeO_3$ distorted, we consider the realistic structure of the two materials, studying how ferromagnetism depends on the lattice structure and the electron correlation in these materials. From these results, we show possible reasons that can explain why ferromagnetism only occurs in $SrRuO_3$.

For the ruthenate materials, as there is no doping, the filling is fixed as 4 d electron per Ru atom. We also fix the lattice structures with data from experiments [Jones et al. (1989); Bensch et al. (1990)], in which the $GdFeO_3$ distortion in $CaRuO_3$ is stronger than in $SrRuO_3$. We study the ferromagnetism in different aspects, the dependence on the onsite interaction U and the Hund's coupling J.

The noninteracting density of states for these two materials are easily obtained band structure calculations, in which we use MLWF to project onto the subspace of t_{2g} orbitals. Figure 3.17 shows the comparison of density of states between the two materials. As known from vanadate systems, $CaRuO_3$, which is more distorted, has DOS peaks below the Fermi level. In $SrRuO_3$, the peaks are concentrated near the Fermi level. The distortion also reduces the bandwidth $CaRuO_3$ more than $SrRuO_3$.

By extrapolating the Curie temperature using inverse susceptibility, we present the paramagnetic/ferromagnetic phase diagram in Figure 3.18. The upper two panels of Figure 3.18 show the phase diagrams computed for $SrRuO_3$ (upper left panel) and $CaRuO_3$ (upper right panel). The symbols indicate (U, J) pairs at which the properties were computed. Black circles denote paramagnetic regions of the phase diagram and red squares denote ferromagnetic regions. The line $U = 3J$ separating the physical regime from the regime of unphysically large J is also indicated. We observe that, for $U \gtrsim 4eV$ in both materials, the metal-insulator and ferromagnetic-paramagnetic phase boundaries nearly coincide and are, to a good approximation, parallel to the $U = 3J$ line. Thus at larger U, magnetism is controlled by proximity to the metal-insulator phase boundary. However at smaller U, below the critical value

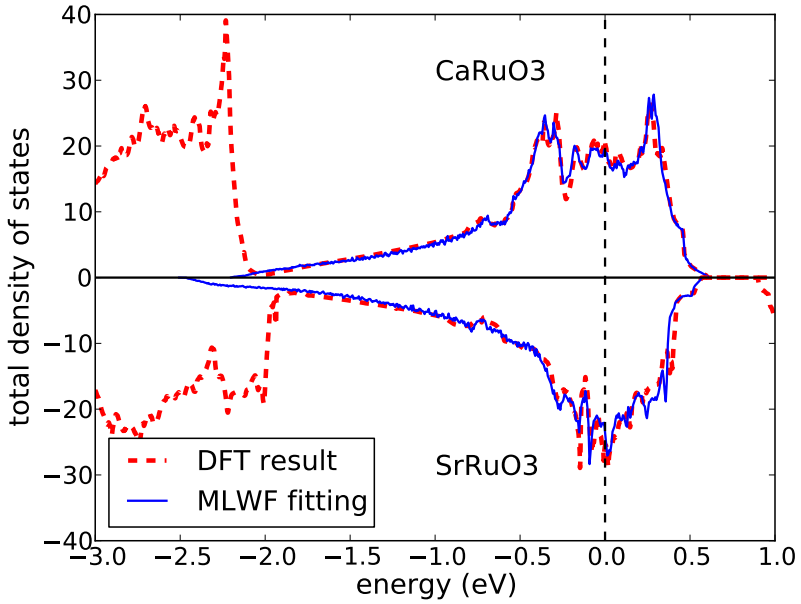

Figure 3.17: (Color online) Comparison between density of states generated from DFT calculation (dashed curves, red online) and from MLWF fitting (solid curves, blue online) DOS for $CaRuO_3$ ($SrRuO_3$) is on the positive (negative) half plane. The vertical dashed line mark the Fermi level.

needed to drive a Mott transition, the ferromagnetic-paramagnetic phase boundary curves sharply, indicating that different physics becomes important.

To understand this behavior more clearly, we present in the lower two panels of Fig. 3.18 a comparison of the phase diagrams for the two materials. The lower left panel presents the two phase diagrams in the same plot. At larger U the phase boundaries are parallel; at smaller U a clear deviation occurs, with the $CaRuO_3$ calculation exhibiting a significantly smaller region of ferromagnetism than the $SrRuO_3$ calculation. Further insight is obtained from the lower right hand panel, in which the U and J values of $SrRuO_3$ have been rescaled by the ratio of the $CaRuO_3$ bandwidth to the $SrRuO_3$ bandwidth. At larger U the phase diagrams coincide. This indicates that the ferromagnetic/paramagnetic as well as the metal-insulator phase boundary is controlled by the ratio of the interaction strengths to the bandwidths, independent of other details such as structures of the density of states. On the other hand, the

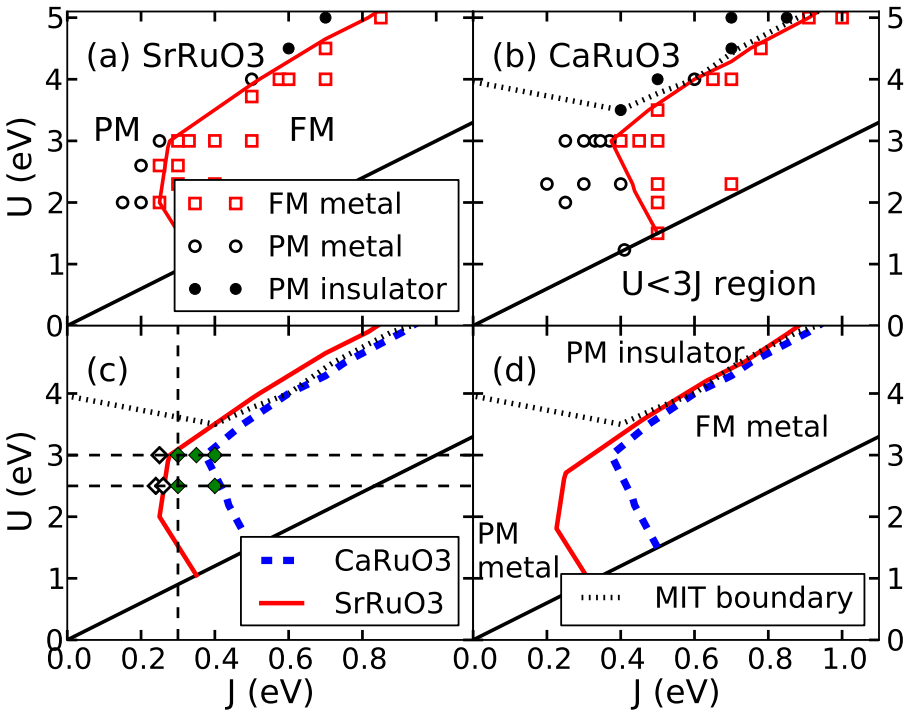

Figure 3.18: (Color online) (a) FM/PM phase diagram for $SrRuO_3$. (b) FM/PM phase diagram for $CaRuO_3$. In (a) and (b), the squares (red online) are in ferromagnetic order, the black circles are in paramagnetic order; closed symbols are insulating, and open symbols are metallic. (c) The FM/PM phase diagrams for $SrRuO_3$ and $CaRuO_3$ plotted together, the dashed vertical line at $J = 0.3eV$ marks the J value for the onset of frozen moment at $U = 2.5eV$ and $U = 3eV$, the open diamonds are out of the spin-freezing phase. The closed diamonds (red online) are in the spin-freezing phase. (d) Panel (c), but with the phase boundaries of $SrRuO_3$ is rescaled by the ratio of the $SrRuO_3$ bandwidth to the $CaRuO_3$ bandwidth. In (c) and (d), the metal-insulator phase boundary for $CaRuO_3$ (dotted thin curve) is also plotted.

difference in phase boundary observed at smaller U indicates that other physics is important in this regime.

Insight into the physics of the smaller U regime comes from previous work on systems with arbitrary incommensurate band filling. Work on the one-orbital FCC lattice Hubbard model Vollhardt et al. (1997); Ulmke (1998) identified structure in the density of states (specifically a large peak far below the Fermi level) as an important determinant of magnetism. Our work on the vanadate solid solution $La_{1-x}Sr_xVO_3$ (d valence d^{2-x}) showed that in orbitally degenerate systems with non-negligible Hund's interactions the conditions on the density of states peak could be significantly relaxed, but it remained the case that ferromagnetism is favored by density of states peaks at or near the Fermi level and disfavored by density of states peaks above the Fermi level. We further showed that the position of density of states peaks was controlled by the amplitude of the octahedral rotations and this effect was more important than the change of bandwidth in determining the magnetic phase boundary of the doped vanadates.

The d^4 ruthenate system studied here has two holes in the t_{2g} shell and thus may be thought of as a particle-hole transformation of the d^2 vanadate system. Based on the previous vanadate work we would conclude that in the ruthenate case a density of states peak *below* the Fermi level disfavored magnetism, and indeed we see from Fig. 3.17 that the larger rotations characteristic of $CaRuO_3$ produce such a below-Fermi-level density of states peak.

The results of this section may be summarized as follows. At larger U where Mott physics is important the presence of ferromagnetism is controlled by proximity to the correlation-driven ('Mott') metal-insulator transition, which in turn is controlled by the ratio of the interaction strength to the bandwidth, independent of the details of the single particle density of state. However in the smaller U regime, away from the Mott state, the location of the magnetic phase boundary is controlled by the structure

of the single particle density of states, which is in turn controlled by the octahedral rotations.

Because Ru is a $4d$ transition metal, the d electron is not as localized as the one in $3d$ materials, ruthenates are less correlated. Thus for the positions of materials, the region close to the Mott insulator, $U > 3eV$, should be excluded. As $CaRuO_3$ and $SrRuO_3$ are known as non-Fermi liquid with $\omega^{-1/2}$ behavior at high frequency [Kostic et al. (1998); Lee et al. (2002)], which is related to the spin-freezing phase in the t_{2g} model [Werner et al. (2008)], the spin-freezing phase boundary can also be used to limit the region of possible positions of these materials. From our calculation for $U = 2.5eV$ and $U = 3eV$ (not shown), $CaRuO_3$ is in the spin-freezing phase if $J > 0.3eV$ (see Fig. 3.18c). Because the spin-freezing phase depends more on the bandwidth, $SrRuO_3$ should share the same condition $J > 0.3eV$ to be in that phase. However, it is not clear of the precise positions of materials on the phase diagrams. To explain why ferromagnetism is observed in $SrRuO_3$ but not in $CaRuO_3$: if $U = 2.3eV$, $J = 0.4eV$ as suggested from Georges et al. (2013), the DOS peaks controlled by the distortion is the reason, but if $U \approx 3eV$, Mott insulating phase becomes more important which suppresses ferromagnetism in $CaRuO_3$.

3.5 Conclusions

We have investigated the conditions under which ferromagnetism might be observed in bulk solid solutions derived from $LaVO_3$, in superlattice structure composed of $SrVO_3$ and $LaVO_3$ and in ruthenium-based oxides $CaRuO_3$ and $SrRuO_3$. Our main finding is that ferromagnetism in a multiorbital correlated system depends on two factors: (1) the proximity to the Mott insulator and (2) the position of the density of states peak. For strong correlation, the formal is important as the Mott insulating phase can suppress the ferromagnetism, thus being away from that phase (e.g. by

doping or applying pressure to decrease U/W) is necessary to obtain ferromagnetic order. When it is far from Mott insulating phase, the latter factor is more dominant, which is controlled by the amplitude of the $GdFeO_3$ distortion away from the ideal cubic perovskite structure, however, the effect is different depending on the filling of the d bands.

Based on this finding, we explain the reason for no ferromagnetic order in bulk solid solutions $La_{1-x}Sr_xVO_3$. The parent compound $LaVO_3$ is a Mott insulator which suppresses ferromagnetism. When being doped away from the integer filling, $La_{1-x}Sr_xVO_3$ however is less distorted than the parent compound, thus disfavoring ferromagnetism. The material therefore stays out of the ferromagnetic region for all value of x (Fig. 3.7).

In superlattices derived from $LaVO_3$, the general idea is that the superlattice structure can decouple the lattice distortion and the doping, thus having the potential of accessing the ferromagnetic region by having large hole doping while keeping the level of distortion unchanged. However, the superlattices with $P2_1/m$ octahedral rotation is much less favorable to ferromagnetism than the $Pnma$ structure of the bulk system. Our finding is inconsistent with experiment [Lüders et al. (2009)] which reports ferromagnetic order at room temperature for $(LaVO_3)_m(SrVO_3)_1$.

In $CaRuO_3$ and $SrRuO_3$, as there are two holes in the t_{2g} bands, they are particle-hole transform of the d^2 systems (such as vanadates) and behave in opposite way for ferromagnetism. The less distorted structure ($SrRuO_3$) in contrast favors ferromagnetism. Even though it is unclear of the precise positions for the two materials, as $CaRuO_3$ is reported as more correlated [Georges et al. (2013)] and more distorted, the combination of the two factors, the proximity to Mott insulating phase and the density of states peak effect, can be used as a reasonable explanation for the ferromagnetic order observed only in $SrRuO_3$.

Our study has certain limitations. The calculations employ a frontier orbital model

which includes only the t_{2g}-derived antibonding bands. DFT+DMFT calculations based on correlated atomic-like d-states embedded in the manifold of non-correlated oxygen states provide a more fundamental description. We indicates that the two models give very similar results if both calculations are tuned so that bulk $LaVO_3$ is a Mott insulator, however the renormalization of the d-level energy ϵ_d and the contribution of the e_g bands in the pd model is still an open problem for future research. Further, our calculations are based on the single-site DMFT approximation, which includes all local effects but misses inter-site correlations. While it is generally accepted that these calculations give the correct trends and qualitative behavior, the quantitative accuracy of the methods is not known. Unfortunately, as yet cluster extensions of DMFT are prohibitively expensive for the multiband models considered here.

Our results indicate that designing ferromagnetism into a superlattice depending on materials. Vanadate superlattices will require both large amplitude rotations about the growth axis and also substantial rotations about the other two axes. Thus choosing substrates with smaller lattice parameter and replacing La by small atom such as Y to increase octahedral rotation would be desirable. The fabrication in $CaRuO_3$ should be in opposite direction so as to keep the material far from the Mott insulating phase and use the substrate to decrease the distortion to achieve ferromagnetic order.

Chapter 4

Covalency and the metal-insulator transition

In strongly correlated systems, metal-insulator transition is one of the fundamental phenomena for investigation. While the correlation-driven metal-insulator transition has been extensively studied, almost all of the existing literature has adopted a "Hubbard model" approach in which the correlated bands are taken to be the d-like near Fermi surface states. In these models the hybridization to other degrees of freedom, in particular to electrons in oxygen $2p$ orbitals, is not considered. In transition metal oxides, the oxygen bands well below the Fermi level have significant hybridization with the correlated d bands of transition metal. The charge transfer physics and p-d covalency can play important role but are not well understood. In this chapter, we take into account the oxygen p bands together with the correlated d bands and study the metal-insulator transition with the effect of p-d covalency. Part of the results in this chapter can be found in Dang et al. (2013).

The rest of this chapter is organized as follows. In Section 4.2 we present the theoretical model and the methodology. Section 4.3 is the overview of our results. In Section 4.4 we present a simplistic but revealing Hartree-Fock theory for the cubic materials. Sections 4.5 and 4.6 present our DFT+DMFT results (the metal-insulator transition phase diagrams) for the Sr and La series of materials considering both hypothetical cubic and realistic structures. In Section 4.7, we use several criteria to locate the materials in the phase diagrams. Section 4.8 is a summary and conclusion.

4.1 Introduction

The Mott insulator [Mott and Peierls (1937); Mott (1949); Imada et al. (1998)] – a correlation-driven insulating state with an odd number of electrons per unit cell so that one-electron physics would predict metallic behavior – is one of the fundamental paradigm systems of modern condensed matter physics. Many transition metal oxides are believed to be Mott insulators or to undergo "Mott" metal-insulator transitions as chemical composition, crystal structure, temperature or pressure are varied [Imada et al. (1998)]. A detailed understanding of the properties of these and related systems is an important goal of condensed matter theory.

A complete solution of the all-electron many-body problem for real materials is not available. Present-day theories [Georges (2004); Held et al. (2006); Kotliar et al. (2006)] take a multi-step approach. The electronic degrees of freedom are partitioned into two groups: a background group consisting of the majority of the electrons in the system and a correlated subspace, which is treated by more sophisticated methods which capture important aspects of beyond-mean-field correlations. A mean-field like treatment (typically density functional theory) is used to treat the background electrons and to define the basic parameters of the correlated subspace, which is then solved by a more sophisticated method (for example, dynamical mean field theory) which captures at least some of the beyond-mean-field aspects of the electronic correlations. Finally, the solution for the correlated subspace must be self-consistently embedded into the background electronic structure. Conceptual and practical uncertainties attend each of these steps, but the approach has produced significant insights into the physics of correlated materials.

In the context of transition metal oxides, it has been accepted since the time of Peierls' and Mott's original work [Mott and Peierls (1937); Mott (1949)] that the appropriate correlated subspace should be the electrons in the partly-filled transition metal d shell, and that the important interactions to include are the on-site, intra-d

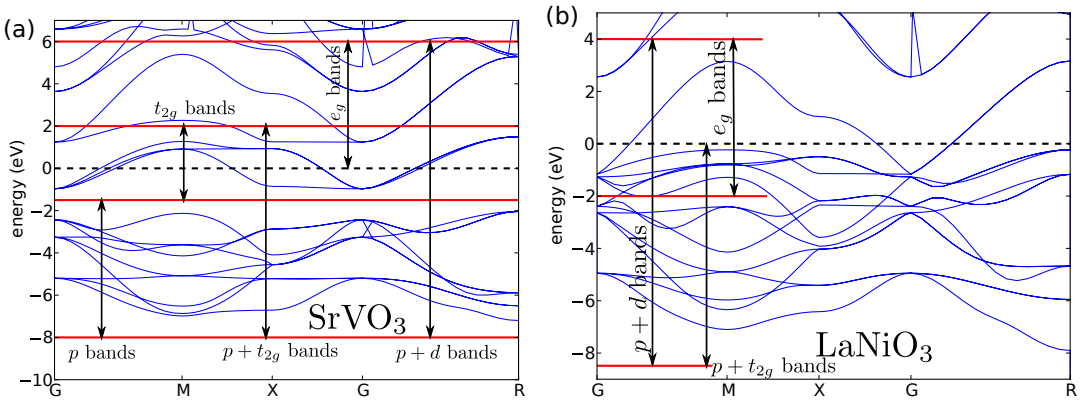

Figure 4.1: (Color online) Band structures obtained by DFT calculations for (a) $SrVO_3$ (early TMO) and (b) $LaNiO_3$ (late TMO). The energy windows for MLWF projections for selected bands are shown.

interactions. In the early stages of theoretical development the correlated subspace was defined phenomenologically [Hubbard (1963)], typically as a tight binding model of electrons hopping among sites of a lattice and coupled by an on-site repulsion U and (if each site contained more than one orbital) a Hund's coupling J. The present state of the art involves obtaining the one-electron part of the Hamiltonian from a density functional band calculation by downfolding [Andersen et al. (1995)] or Wannier function [Marzari and Vanderbilt (1997)] procedures and computing the interactions via constrained density functional [Hybertsen et al. (1989)] or constrained random phase [Miyake and Aryasetiawan (2008)] approximations.

In many transition metal oxides, the calculated density functional band structure features a broad complex of bands derived from entangled oxygen p and transition metal d states and reasonably (although not always completely) separated from other bands in the solids (see Figure 4.1 for two examples of $SrVO_3$ and $LaNiO_3$). In this circumstance it is natural to define atomic-like d orbitals via a Wannier function or a projector construction based on an energy range spanning the p-d band complex. The correlated orbitals defined by this procedure are found to correspond reasonably closely to the intuitive picture of atomic d orbitals (for example the interaction ma-

trix elements computed from constrained random phase calculations have, to a good approximation, the symmetry structure expected for the d shell in free space) [Aichhorn et al. (2009)] and the correlated electron physics of this situation may readily be treated by dynamical mean field theory methods [Georges (2004); Held et al. (2006); Kotliar et al. (2006)]. The resulting density functional plus dynamical mean field theory (DFT+DMFT) has gained considerable acceptance as a method of addressing the real-material physics of correlated electron compounds.

The atomic-like d orbital construction allows investigation of the "charge transfer insulator" physics emphasized by Zaanen, Sawatzky and Allen who noted in 1985 [Zaanen et al. (1985)] that if the energy Δ to transfer a charge from a ligand p state to a transition metal d state was less than the d level charging energy U, then the physics was controlled by Δ and not U. As one moves across the $3d$ transition metal row of the periodic table, the transition metal d shell decreases in energy relative to the p levels and it is generally accepted that in "late" transition metal oxides (those involving elements Cu, Ni and perhaps Co drawn from the right-hand side of the $3d$ transition metal row) the d levels lie low enough that the late transition metal oxides are "charge transfer" materials with low energy physics dominated by Δ (see Fig. 4.1b). On the other hand, in the "early" transition metal oxides (those involving elements Ti, V, Cr and perhaps Mn drawn from the left hand side of the $3d$ transition metal row) the d level energies are often supposed to be high enough, relative to the p levels (see Fig. 4.1a), that the early transition metal oxides are in the "Mott-Hubbard" class of materials with physics dominated by U and with charge transfer effects of less importance.

This line of argument, however, glosses over the crucial issue of the embedding of the correlated states in the background electron gas. The correlations on the d level contribute to a Hartree shift of the d level which has the potential to substantially change the charge transfer energy Δ away from the value predicted by band theory.

A large change in Δ will lead to a large change in the d occupancy (relative to the predictions of band theory); the resulting charge imbalance may be expected to change the energetics.

The purpose of this work is to challenge the conventional view. We present density functional plus U (DFT+U) and density functional plus dynamical mean field theory (DFT+DMFT) calculations which show that the metal-insulator physics of the early transition metal oxides is crucially affected by the p-d charge transfer energetics. In the DFT+U and DFT+DMFT approaches the charge transfer physics is controlled by the double-counting correction, and we show that within the standard double counting correction all of the titanate and vanadate peroskites are predicted to be metallic in contradiction to experiment which shows that the lanthanum titanate and vanadate materials are insulators. A comparison of calculation to photoemission data indicates that the difficulty arises in large part because the existing local density approximation (LDA) and generalized gradient approximation (GGA) implementations of density functional theory underestimate the p-d energy difference by about $1 \rightarrow 1.5eV$.

4.2 Model and methods

4.2.1 Overview

We focus on transition metal oxides crystallizing in RMO_3 perovskite structure. We study materials in which the R-site ion is Sr, La and (in one case) Y and the M site ion is one of Ti, V, Cr and Mn. For reference we also present results for rocksalt structure NiO. The Sr series of materials are cubic perovskites; the La-series crystallize in $GdFeO_3$-distorted variants of the cubic perovskite structure characterized by a four-sublattice pattern of tilts and rotations. We use the Quantum Espresso code

[Giannozzi et al. (2009)][1] to obtain energy bands and maximally localized Wannier function methods [Marzari and Vanderbilt (1997); Souza et al. (2001)] as implemented in Wannier90 [Mostofi et al. (2008)] to define the orbitals in the correlated subspace. (The use of Quantum Espresso is because at the starting time of the project, it was almost the only one package that had the fully fledged interface with the Wannier90 code.) As demonstrated in Wang et al. (2012), alternative "projector" methods [Haule (2007); Amadon et al. (2008)] of defining the d orbitals give essentially the same results if consistent and appropriate energy windows (comprising the full width of the d-p manifold) are adopted.

The extra interactions which define the correlation problem are taken to be site local, to act on the d orbitals on a given site and to have the standard rotationally invariant interaction in Kanamori form (2.23) acting on the d manifold. We fix J, which is only very weakly screened by solid state effects, to be $J = 0.65eV$ unless stated otherwise, but consider a range of U.

4.2.2 Solution of correlation problem

We solve the correlation problem using the single-site dynamical mean field approximation [Georges et al. (1996)] and compare the results to a Hartree-Fock solution which enables an examination of the effects of intersite correlations. Within the Hartree-Fock approximation, the quartic terms of the Hamiltonian are approximated by density mean fields $\langle n_i \rangle$ determined self consistently such that $n_i n_j \approx n_i \langle n_j \rangle + \langle n_i \rangle n_j - \langle n_i \rangle \langle n_j \rangle$.

The dynamical mean field method is described in details in Section 2.3 with the impurity solver using continuous time quantum Monte Carlo methods [Werner et al.

[1] We used the pseudopotentials Sr.pbe-nsp-van.UPF, La.pbe-nsp-van.UPF, V.pbe-n-van.UPF, Ti.pbe-sp-van_ak.UPF, Cr.pbe-sp-van.UPF and O.pbe-rrkjus.UPF from www.quantum-espresso.org.

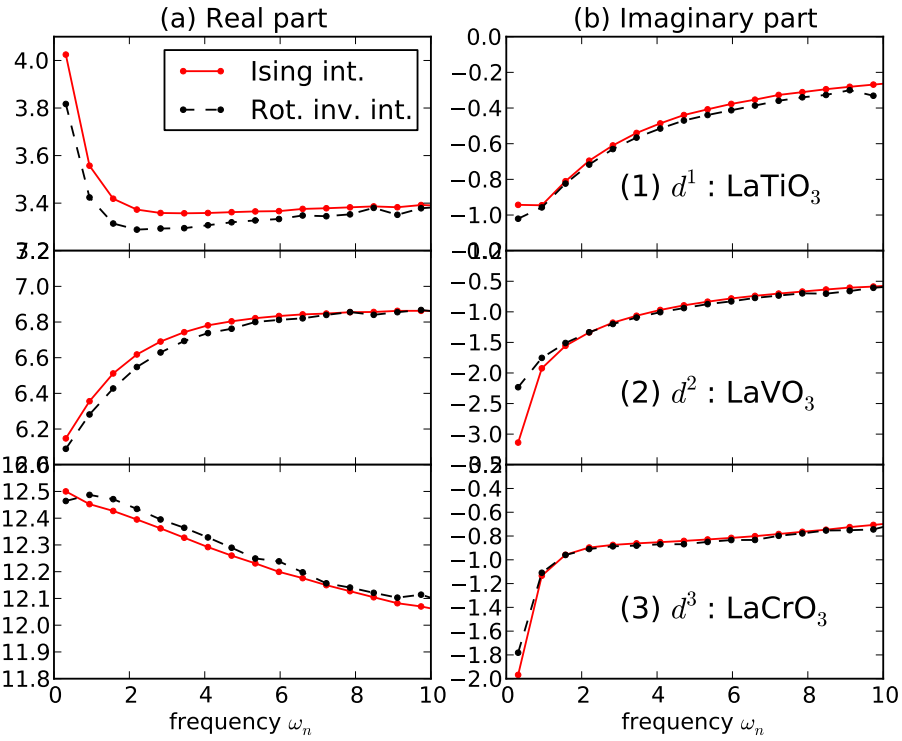

Figure 4.2: (Color online) Self energies in Matsubara frequency of Ising interaction (pair hopping and exchange terms excluded) and rotationally invariant interaction. Three systems d^1, d^2 and d^3 are tested with $U = 5eV$ and $J = 0.65eV$. The double counting corrections are chosen so that they are near the phase boundaries for the MIT (see Fig. 4.7).

(2006); Gull et al. (2011)]. We typically neglect the exchange and pair-hopping terms of the onsite interaction Hamiltonian (2.23) (Ising approximation) in order to be able to use the "segment" algorithm, which is 4 to 5 times faster, the speed needed for the phase diagram surveys. To test the quality of the interaction we present in Figure 4.2 a comparison in self energy between rotationally invariant and Ising interactions for the same $U = 5eV$ and d^1, d^2 and d^3 systems near the metal-insulator transition. The imaginary parts of the self energy, which is more related to the correlation strength, are similar for the two cases, except at the lowest frequency. The differences in self energy are found to be small so that the metal-insulator phase diagram is well approximated by the Ising interaction calculations.

As discussed in more detail below, we have found that for V and Ti based compounds, a truncation to the t_{2g} subspace provides an accurate representation of the physics; however for the $LaCrO_3$ material we find that inclusion of the e_g levels is important.

We determine the metal-insulator transition directly from the spectra obtained from analytical continuation. The details are discussed in Appendix E.

4.2.3 The double-counting correction and the d-level occupancy

We obtain the single-particle part of the Hamiltonian for the correlation problem by writing the Kohn-Sham Hamiltonian in the Wannier basis, but shifting the on-site d level energy term by a "double counting correction" [Anisimov et al. (1991); Amadon et al. (2008); Karolak et al. (2010)]. The double counting correction is an essential part of the embedding of the correlation problem in the wider band structure; it acts in effect to compensate for some or all of the Hartree shift of the d levels arising from the Slater-Kanamori interactions. We follow Wang et al. (2012) and consider a range of double counting corrections, which we parametrize by N_d, the expectation value of the operator giving the d-level occupancy. The parametrization is possible because N_d is a monotonic function of the d-level energy and is useful because (as was demonstrated for late transition metal oxides in Wang et al. (2012) and will be seen in detail below) many of the details of the materials properties affect the metal-insulator line only via their effect on the value of N_d, so the resulting phase diagrams are relatively simple when expressed in terms of N_d. Of course the precise values found for N_d depends on the precise definition of the d orbital which in turn depends on the scheme (Wannier vs projector) and the energy window chosen. However the trends are robust and different situations can be meaningfully compared if consistent

definitions of d-orbital are adopted. Further details are given in Wang et al. (2012).

Different forms of the double counting correction have been given in the literature [Anisimov et al. (1991); Amadon et al. (2008); Karolak et al. (2010)] but the correct form is not known. We believe that reasonable values of the double counting correction correspond to N_d values not too far from those predicted by the density functional calculation. For example, for the case of $SrVO_3$, both DFT+U calculations and DFT+DMFT calculations using full charge self-consistency in the implementations of Pourovskii et al. (2007) and Haule et al. (2010) lead to N_d values close to those obtained from the bare DFT calculations (see Wang et al. (2012), Fig. 4.4a and Appendix D).

However, because there is no agreement on the correct form of the double counting correction, and because the quantitative accuracy of the DFT implementations is not known, we consider a range of N_d which we vary by changing the d-level energy, while keeping the other band parameters fixed. We have not found it necessary to re-self-consist the DFT calculation, indeed (see Appendix D).

In the cases that have been studied the spectra and other physical properties obtained by varying N_d with the Wannier fits fixed are indistinguishable from the spectra obtained from the fully charged self-consistent procedure as long as the N_d value is adjusted to be the same the one from the fully-charged self consistent calculation.

4.3 Overview of results

The key result of this work is that the covalency between oxygen p bands and transition metal d bands, which is controlled by the p-d energy level difference, plays a crucial role in the physics of the transition metal oxides. Thus even for the early transition metal oxides, it is necessary to go beyond the widely accepted paradigm, which focuses on the frontier bands and treat them as a generalized Hubbard model.

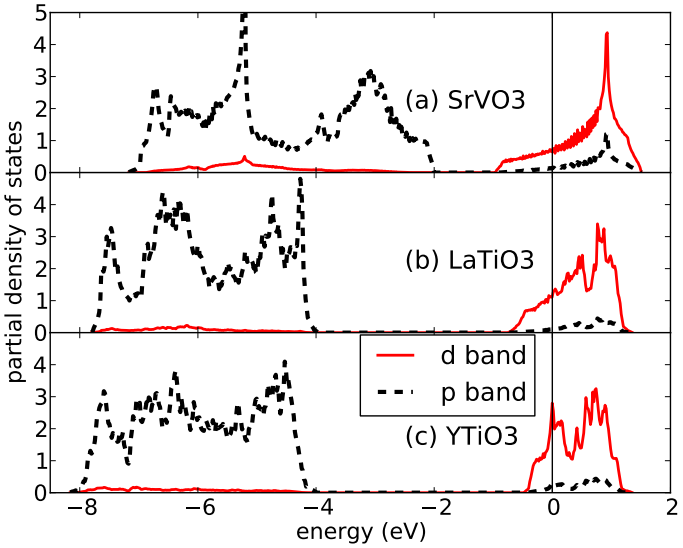

Figure 4.3: (Color online) The density of states for $SrVO_3$, $LaTiO_3$ and $YTiO_3$ derived from DFT+MLWF tight binding Hamiltonian. The lattice structure for each material is from experimental data [Rey et al. (1990); Cwik et al. (2003)]. The vertical thin solid line marks the Fermi level. The solid curve (red online) is the transition metal d band, the dashed curve (black online) is the oxygen p band.

In the Hubbard model, increasing the on-site interaction drives the metal-insulator transition. In the more realistic p-d situation, increasing the U also changes the p-d level splitting and thus need not drive the metal-insulator transition.

Figure 4.3 shows how the covalency between p and d bands is important. It presents the density of states of $SrVO_3$, $LaTiO_3$ and $YTiO_3$ derived from band structure calculations. $SrVO_3$ is a moderately correlated metal, $LaTiO_3$ is a small-gap correlated insulator and $YTiO_3$ is a wider-gap correlated insulator. From Fig. 4.3 we see that the gap between oxygen p bands and transition metal d bands of $SrVO_3$ is about $1eV$, so the oxygen bands are strongly hybridized with the d bands. On the other hand, in $LaTiO_3$ and $YTiO_3$, the gaps are larger ($\gtrsim 3.5eV$), thus the p and d bands are much less hybridized. It is this difference in hybridization that accounts for the different behavior in these materials.

We have computed the density of states using three methods: density func-

tional plus U (DFT+U, VASP implementation [Kresse and Hafner (1993); Kresse and Furthmüller (1996a,b); Kresse and Joubert (1999)], Hartree and DMFT approximations based on maximally localized Wannier fits to the band structure as described above. The DFT+U calculation treats the U-correlations in a Hartree approximation but involves a full-charge self consistency; in the DMFT and Hartree calculations, we have adjusted the d energy so that the d occupancy is close to the DFT+U value but have not performed a full-charge self consistency. The DFT+U and Hartree calculations treat the full d manifold (t_{2g} and e_g); in the DMFT calculations, only the t_{2g} states are treated. In the Hartree and DFT+U calculations, we allowed for magnetic order but not for orbital polarization. The DMFT calculation are in paramagnetic and para-orbital order.

Figure 4.4 shows the three calculations for $SrVO_3$. The fully charge self consistent DFT+U calculations in the left panel (within the widely used fully-localized limit (FLL) double counting correction) show that, as the interaction strength is increased, the electronic structure rearranges itself to keep the d occupancy and the p-d energy level differences approximately constant. The increase in energy of the "upper Hubbard band" (minority spin unoccupied states) is compensated by a decrease in the energy of the "lower Hubbard band" (majority spin partly occupied states) which come closer to the oxygen levels. This arrangement of electronic structure reveals an essential role of p-d covalency in compensating for the effects of the Hubbard U, pointing to an aspect of the physics of the materials not contained in the frontier orbital Hubbard model. The middle and right panels show that the DFT+Hartree and DFT+DMFT calculations exhibit the same physics if the double counting correction is adjusted to keep the N_d constant. The similarities of the density of states shows that full-charge self consistency is not necessary and indicates that the t_{2g} plus oxygen p band approximation is reasonable.

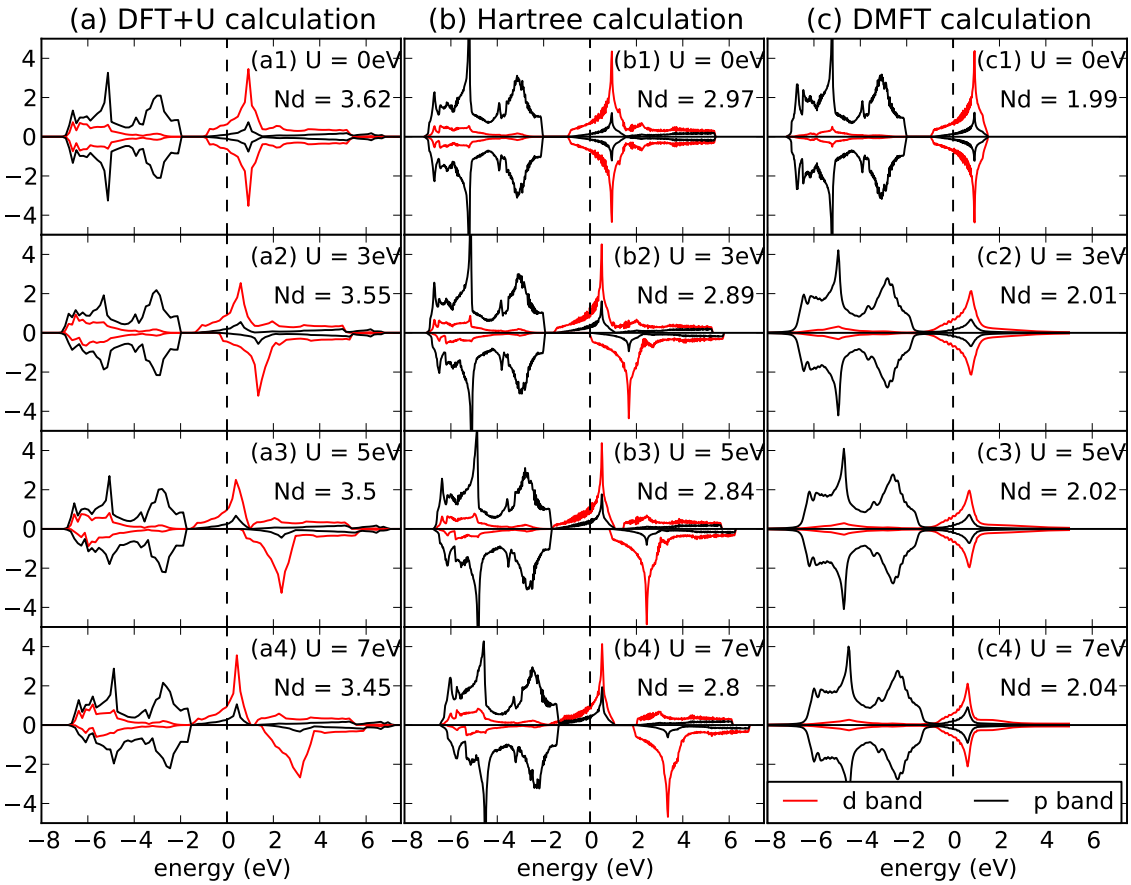

Figure 4.4: (Color online) The density of states for $SrVO_3$ obtained from DFT+U (column (a)), Hartree (column (b)) and DMFT calculations (column (c)) for $U = 0, 3, 5$ and $7eV$. The dashed lines mark the Fermi level. The red curves are the transition metal d bands, the black curves are the oxygen p bands. The Hund's coupling is $J = 0.65eV$.

4.4 Hartree calculations for cubic structures

The similarity of the DFT+Hartree and DFT+U spectra at the band theory N_d motivates us to use the flexible and computationally inexpensive Hartree approximation to investigate the metal insulator phase diagram for transition metal oxide series of interest here. In these calculations, we performed a MLWF fit to the calculated band structure, projected the Kohn-Sham Hamiltonian onto the Wannier states and then to map out the phase diagram, we adjusted the on-site d energy level. We present

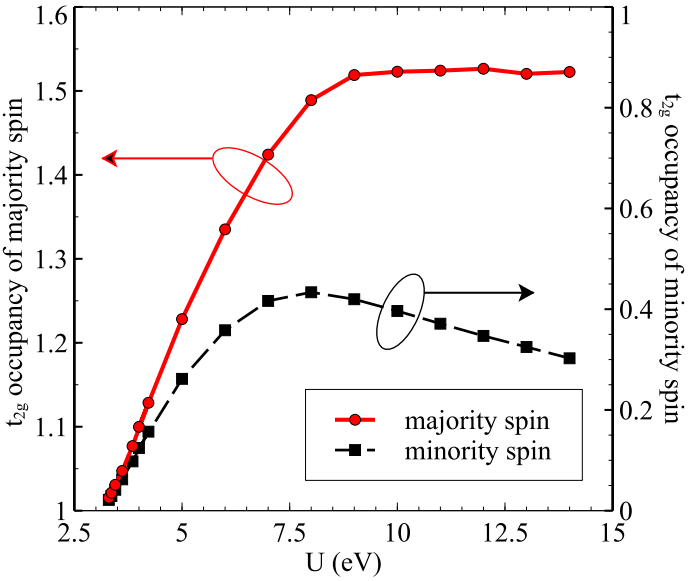

Figure 4.5: (Color online) Hartree calculation: Spin-resolved t_{2g} occupancy vs. the onsite interaction U for $SrVO_3$ with the double counting Δ adjusted to be at the MIT phase boundary.

the results in terms of the occupancy N_d of the t_{2g}-symmetry Wannier functions in Figure 4.6 for cubic structure. In the Hartree theory, insulating behavior is associated with spin and orbital order (in the d^1 and d^2 materials) and with spin order only in the d^3 systems. In the d^1 and d^2 materials, the charge excitation is to an unoccupied state in the t_{2g} manifold and the e_g manifold is irrelevant, as can be seen from the identical phase diagrams obtained in the t_{2g}-only and full d computations. However, in the d^3 situation, the relevant excitations are from the t_{2g} to the e_g manifold and a full five orbital treatment is essential.

We remark that the phase boundaries bend slightly back to smaller N_d at large U. This reflects the decrease of d occupancy of minority spin d states as they are pushed to very high energies by the large U. Calculations of the spin-resolved d occupancy show that, in the d^1 and d^2 cases (e.g. Figure 4.5 for the d^1 case $SrVO_3$), the majority spin d occupancy tends to a U-independent asymptote as U is increased while the minority spin occupancy decreases. We expect that, when U is unphysically

very large, the minority spin d occupancy goes to zero, the critical N_d approaches a constant value.

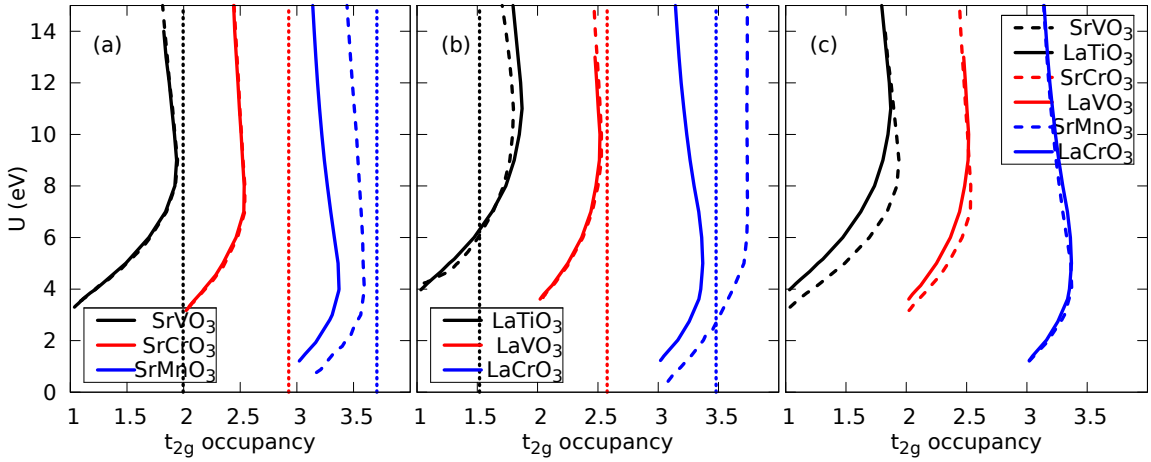

Figure 4.6: (Color online) Calculations for cubic structure: (a) Hartree phase boundaries for Sr series. (b) Hartree results for La series. (c) Comparison between Sr series and La series. For each material, the left region of the phase boundary is insulating while the right region is metallic. Vertical lines are t_{2g} N_d from DFT+MLWF calculations (N_d positions of materials). In (a) and (b), the dashed curves are for 3-t_{2g}-orbital model, the solid curves are for full 5-d-orbital model. In (c), full 5-d-orbital model is used. Hund's coupling is $J = 0.65$eV.

For d^1, d^2 or d^3, cubic lattice structure gives universal phase boundaries, increasing monotonically when U value is small (the Mott-Hubbard regime), and going vertically with N_d slightly changed at larger U (the charge transfer regime). The importance of the covalency is obvious in these phase diagrams: by increasing N_d, the p-d covalency increases to a limit that the correlation (embedded in U value) is suppressed. Thus, when N_d is large enough, there is only metallic solution despite how large the value of U is.

Fig. 4.6c compares the phase boundaries of the two La and Sr series. The difference in the two series comes from differences in tight binding parameters of the two series. The large U parts of the phase diagrams are similar for all cases. At smaller U, the difference is largest for d^1, smaller for d^2 and there is almost no difference in d^3

systems. From the tight binding Hamiltonian from MLWF fit, the hoppings between p and d bands, t_{pd}, are similar, however, there exists direct d-d hoppings which is the most different in d^1 systems (between $LaTiO_3$ and $SrVO_3$). At small U, when indirect d-d hoppings via virtual hopping with oxygen p bands ($2t_{pd}^2/(\epsilon_d - \epsilon_p)$) are small due to the adjustment of the d energy level, the direct d-d hoppings account for the difference in the phase boundary. We have checked that (not shown), if this direct d-d hoppings are adjusted to be the same in two materials ($LaTiO_3$ and $SrVO_3$), the difference in phase boundaries largely decreases.

If using N_d from band structure calculation (the vertical dashed lines in Fig. 4.6) to locate materials, there are $SrVO_3$, $SrCrO_3$, and $LaTiO_3$ having the phase diagrams compatible with the N_d positions, i.e. for metals, the N_d position stays completely in the metallic regime, for insulators, the N_d position crosses the phase boundary, the material can be insulating with a proper choice of U value. The exception are $SrMnO_3$, $LaVO_3$ and $LaCrO_3$ (if consider the 5 d band model for $LaCrO_3$), where DFT+Hartree only gives metallic solutions while from experiments, they are insulators [Miyasaka et al. (2000); Sakai et al. (2010); Arima et al. (1993)]. Within the Hartree approximation, there is inconsistency between DFT+Hartree and experimental results if the d occupancy from DFT is used to locate materials in the phase diagrams.

4.5 DFT+DMFT calculations for cubic structures

The Hartree approximation does not include quantum fluctuations due to the electron correlation. It cannot capture the Mott insulating phase, which is observed experimentally in many early transition metal oxides such as $LaTiO_3$ or $LaVO_3$.

To treat the correlation more properly, it is necessary to go beyond the mean field approximation. In this section, we use dynamical mean-field method to study the metal-insulator transition.

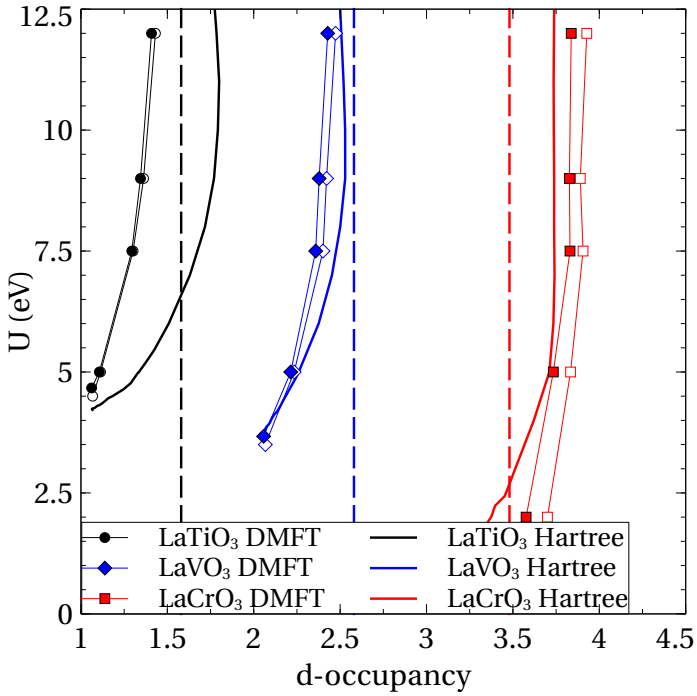

Figure 4.7: (Color online) The MIT U-N_d phase diagrams for materials in La series ($LaTiO_3$, $LaVO_3$, $LaCrO_3$) calculated within model including oxygen p bands and only 3 t_{2g} bands using DMFT and Hartree approximation. In DMFT results, the close (open) symbols are for insulating (metallic) results. The Hartree results have ferromagnetic and/or ferro-orbital orders. The vertical dashed lines are d occupancies derived from DFT+MLWF.

The procedure is similar to the calculations with Hartree approximation. We use the tight binding Hamiltonian generated by DFT+MLWF as input parameters. The Hartree approximation is replaced by the DMFT self consistency for treating the correlation. Because solving the problem with 5 correlated bands is more expensive and unstable with the solver we have, we only use the model with t_{2g} bands (and oxygen p bands) in these calculations.

Assuming cubic structure, we show the results from both DMFT and Hartree

calculations for La series in Figure 4.7. The difference between DMFT and Hartree phase diagrams decreases when going from d^1 to d^3. We explain this based on the antiferromagnetic (AFM) correlation included in the DMFT solutions (although the results are in paramagnetic order). In d^3 systems ($LaCrO_3$) and with nonzero Hund's coupling J, the AFM fluctuation is large due to the superexchange interaction, the nesting effect together with the Mott mechanism [Mott (1949)] make it easy to open the gap, which is observed in the studies for the 3-orbital model in the Bethe lattice [Werner et al. (2009)]. In this case, DMFT phase diagram is more insulating than the Hartree one because translation symmetry breaking is not allowed in the latter. We have tested that (not shown) if the AFM Hartree solution is allowed, the Hartree phase boundary is shifted much further to be more insulating. For d^2 systems ($LaVO_3$), the AFM fluctuation becomes weaker, the DMFT phase boundary is more metallic than the Hartree one. For d^1 systems ($LaTiO_3$), transition to insulating state is only due to Mott mechanism, the insulating region is confined in a small area of large U and small N_d.

We consider the one-electron spectral functions (interacting DOS) of the three systems near their phase boundaries in Figure 4.8. We choose $U = 5eV$, which is around the typical U value for La series, and N_d is adjusted so that they are close to their phase boundaries. At this value of U, three systems are Mott insulator with the d band split into lower Hubbard and upper Hubbard bands around the Fermi level even though $LaCrO_3$ (Fig. 4.8c) is close to the crossover to charge-transfer insulator with the formation of the Zhang-Rice singlet band just below the Fermi level.

The p-d covalency can suppress the correlation effect, but the strength of the suppression depends on the nominal number of electrons in the d shell. In d^1 systems (Fig. 4.8a), a small p-d admixture can drive the system into metallic state, thus for cubic $LaTiO_3$ to be insulator, there is almost no admixture, the p bands must stay at very low energy ($\sim -10eV$ far from the Fermi level). In contrast, the correlation

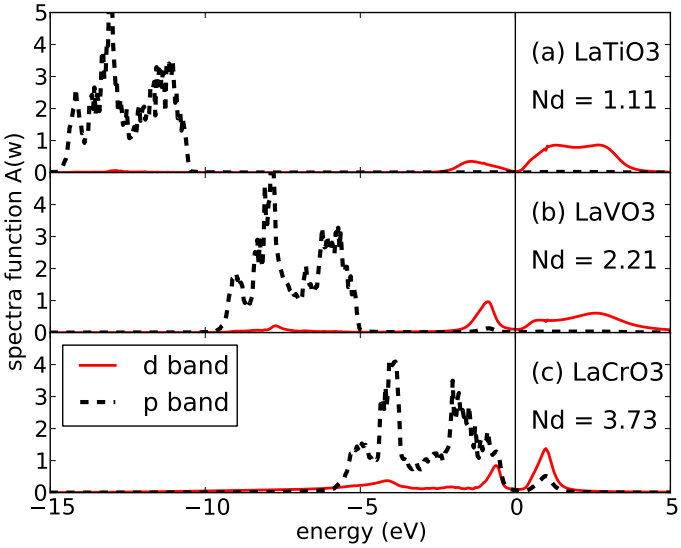

Figure 4.8: (Color online) Spectral functions $A(\omega)$ for cubic $LaTiO_3$, $LaVO_3$ and $LaCrO_3$ at $U = 5eV$, $J = 0.65eV$ and N_d chosen to be close to the MIT phase boundaries. The dashed curves (black online) are oxygen p bands, the solid curves (red online) are correlated d bands. The vertical line marks the Fermi level.

is strong in d^3 systems in the sense that it allows much more p-d admixture while still maintaining insulating state (Fig. 4.8c), the p bands stay near the Fermi level. Another way to quantify the effect of covalency is to measure $N_d - n$ where n is the nominal number of d electrons. Near the phase boundaries, the $N_d - n$ values 0.11, 0.21 and 0.73 for $LaTiO_3$, $LaVO_3$ and $LaCrO_3$ respectively show that the effect of covalency to the correlation strength reduces when the filling of the d shell increases.

4.6 $GdFeO_3$-distorted structures

In Section 4.5, we assume that all materials have cubic lattice structure. However, it only works for materials in Sr series. In most of the transition metal oxides in perovskite structure ABO_3, the small radius of the rare earth A causes significant distortion of the BO_6 octahedra, the $GdFeO_3$ distortion. This structural effect is

in turn affect the metal-insulator transition. In this section, we take into account realistic structures of materials and discuss the effect of distortion in the MIT. We consider two materials of the La series ($LaTiO_3$ and $LaVO_3$), $YTiO_3$, which has larger distortion, and $SrVO_3$, a cubic perovskite, to have a complete study of materials with distortion changing in a wide range.

As we mention in Chapter 2, classification of perovskite structure was done a long time ago by Glazer (1972), in which *Pnma* structure, or in Glazer's notation $a^-b^+c^-$ [Glazer (1972)], is the most common type of perovskites. The materials that we study in this section belong to this type, they are only different by the magnitude of the tilt angles, which is zero for $SrVO_3$ and increases from $LaTiO_3$, $LaVO_3$ to $YTiO_3$. Therefore, it guarantees that the effect of distortion only comes from the magnitude of the tilt angles, not because of different types (i.e. different space groups) of perovskites.

The procedures for calculation are the same for all of these materials. We obtain the atomic positions of materials from experiments [Rey et al. (1990); Cwik et al. (2003); Bordet et al. (1993)], pass them to DFT+MLWF calculations. The tight binding matrix of 3 t_{2g} orbitals of transition metal and 9 oxygen p bands is generated from this DFT+MLWF process. Depending on how large the off-diagonal terms (the onsite d-d hoppings) are, we rotate the t_{2g} orbitals to eliminate these terms in order to avoid the sign problem in the CTQMC solver of DMFT process. The results from the DMFT calculation are processed in the same ways as in Section 4.5 to construct the MIT phase diagrams.

Figure 4.9 presents the MIT phase diagrams for $LaTiO_3$ and $LaVO_3$ using their realistic structures ($GdFeO_3$ distortion) in comparison with those using theoretical cubic structure. With lattice distortion, there are two changes compared with cubic structure: (1) the band structure N_d slightly decreases from the cubic values, and (2) the insulating regime is enlarged, both in U and d occupancy, but wider in $LaTiO_3$

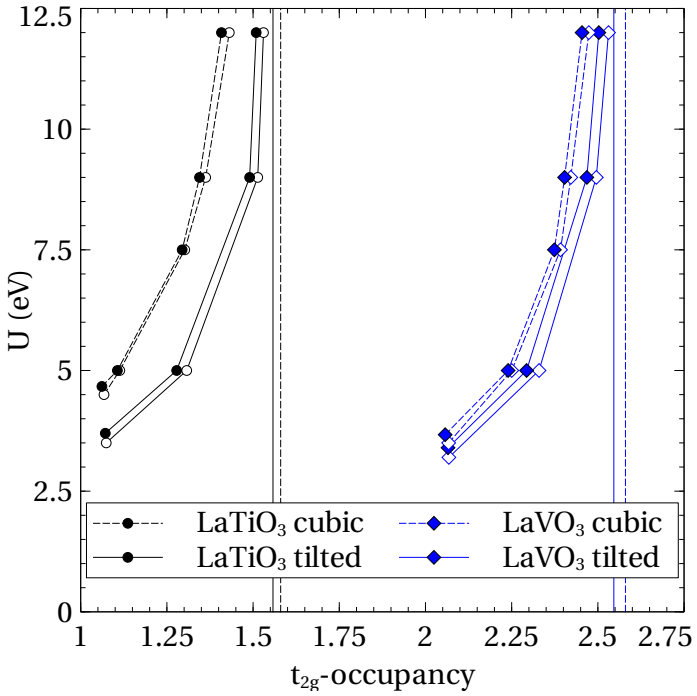

Figure 4.9: (Color online) The MIT phase diagrams for $LaTiO_3$ and $LaVO_3$. The solid (dashed) lines are phase boundary and DFT N_d for tilted (cubic) structure. Open symbols represent metallic solutions, closed symbols are insulating solutions.

than in $LaVO_3$.

The value of d occupancy N_d obtained from DFT calculation depends strongly on the relative positions of bonding bands (p bands) and antibonding bands (d bands). From the DOS of the DFT results for $LaTiO_3$ and $LaVO_3$ (not shown), the p-d distance of the distorted structure is slightly larger than that of the cubic one (mostly because the bandwidth of the antibonding d bands decreases), reflecting by a small decrease in N_d when going from cubic to tilted structure. From *ab initio* calculations, the N_d value appears to be stable under lattice distortion.

The shifting in the phase boundary towards metallic regime describes the physics that distorted structure can enhance the insulating state. The lattice distortion causes two main effect that can be the reasons for enhancement of the insulating region: (1) the reduction of the bandwidth W (especially the bandwidth for the frontier

antibonding d bands), and (2) the orbital polarization which affects differently for different materials. In distorted structure, the B-O-B bond (B is the transition metal atom) is buckled that makes the electron hopping from one B site to the nearest neighbor one more difficult than in cubic structure, the bandwidth W is therefore reduced. In our DFT results (not shown), W is reduced by 25% compared with the cubic case (note that the distance between p and d bands is almost unchanged). In Mott-insulating regime, the critical U_c for Mott transition is proportional to W, with smaller bandwidth in distorted structure, it only requires a smaller U to be insulating. At larger U, smaller bandwidth W means oxygen p bands must go to higher energy to close the gap at the Fermi level and drive the system to metallic state. The p-d admixture and the N_d value need to be larger for the MIT to occur. However, the enhancement of the insulating regime is different for $LaTiO_3$ and $LaVO_3$. Orbital ordering plays an important role here. With the lattice distortion from experiments, $LaTiO_3$ exhibits larger crystal field splitting than $LaVO_3$. Band structure calculations realize that splitting by an "1 up, 2 down" orbital order (one orbital is occupied more than the other two) which is stronger in $LaTiO_3$ than $LaVO_3$. Treating the correlation within DMFT framework, orbital ordering is enhanced significantly in $LaTiO_3$ (Fig. 4.10a), even though it depends on the value of N_d. In $LaVO_3$, with larger d occupancy, the Hund's coupling J couples the onsite electrons of the same spin more strongly, the orbital order in this system is decreased. This work confirms the results found in Pavarini et al. (2004); De Raychaudhury et al. (2007) about the enhancement of insulating state due to orbital order. However, in our study with oxygen p bands, the p-d covalency slightly decreases the orbital polarization. For example, at $U = 5, J = 0.65eV$ and $T = 0.1eV$, d-only model gives the percentage of occupancies of 3 t_{2g} orbitals $71.4\%, 13.3\%, 15.3\%$ for $LaTiO_3$ and $30.7\%, 33.9\%, 35.4\%$ for $LaVO_3$, while for the model with p and d orbitals the corresponding percentages are $61\%, 19\%, 20\%$ and $32\%, 33\%, 35\%$ for a range of Δ chosen so as the system is

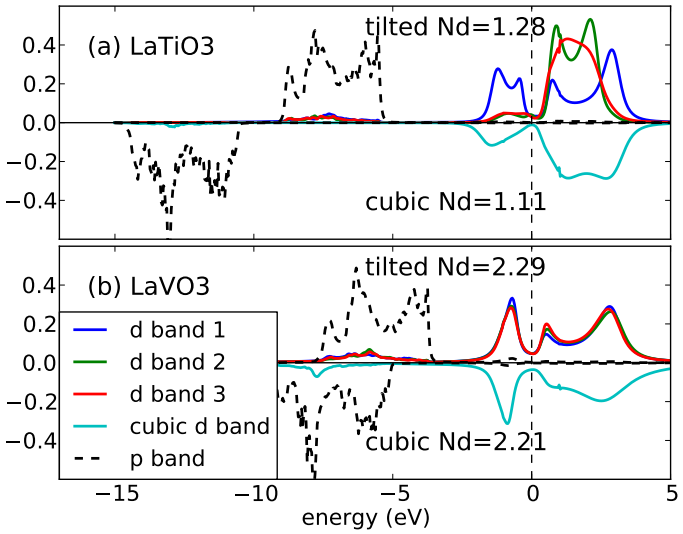

Figure 4.10: (Color online) Spectral functions $A(\omega)$ for cubic (negative value) and tilted (positive value) structure of $LaTiO_3$ and $LaVO_3$ at $U = 5eV$, $J = 0.65eV$ and N_d chosen to be close to the MIT phase boundaries. The dashed curves (black online) are the average spectra per band for oxygen p bands, the solid curves (color online) are correlated d bands. The vertical dashed line marks the Fermi level.

insulating.

Figure 4.10 shows the spectral functions of $LaTiO_3$ and $LaVO_3$ for $U = 5eV$ and $J = 0.65eV$ at the transition point in comparison with the results of theoretical cubic structures. There is clear orbital ordering in tilted $LaTiO_3$ while almost no orbital splitting in $LaVO_3$. Compared with cubic structure, the change is substantial in $LaTiO_3$, the p bands are shifted by about $6eV$ closer to the Fermi level, while they are shifted by less than $2eV$ in $LaVO_3$. This figure illustrates more the large enhancement of the insulating regime in $LaTiO_3$.

We also consider the series $SrVO_3$-$LaTiO_3$-$YTiO_3$. These are d^1 systems with tilt angle increasing: $SrVO_3$ is a cubic structure [Rey et al. (1990)], $LaTiO_3$ has bond angle Ti-O-Ti = 167.12°, while $YTiO_3$ is the most distorted with the bond angle 159.1° [Cwik et al. (2003)]. The noninteracting density of states for the three materials are shown in Fig. 4.3, in which $SrVO_3$ has the largest covalency as well as

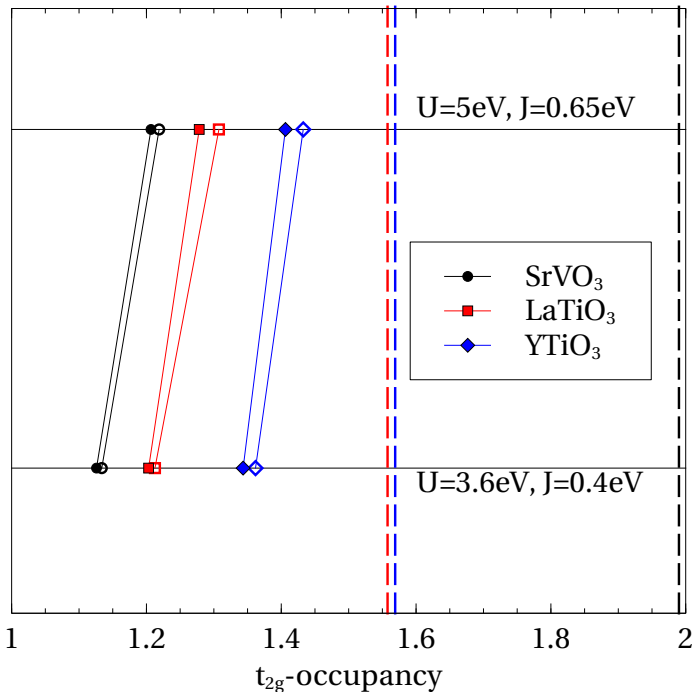

Figure 4.11: (Color online) The MIT for $SrVO_3$ (black), $LaTiO_3$ (red) and $YTiO_3$ (blue) using paramagnetic DMFT calculation. The closed symbols are for insulating state, the open symbols are for metallic state. The vertical lines are N_d positions for the materials obtained from DFT+MLWF.

the largest antibonding d bandwidth, while the most distorted structure $YTiO_3$ has the smallest d bandwidth. But the covalency of $LaTiO_3$ and $YTiO_3$ are almost the same, demonstrated by similar p and d band positions and the same $N_d = 1.57$.

We choose two sets of (U, J) for the series: $(U = 3.6eV, J = 0.4eV)$ and $(U = 5eV, J = 0.65eV)$, which are close to values chosen in Aryasetiawan et al. (2004) and Pavarini et al. (2004) respectively. The resulted phase transitions are shown in Fig. 4.11. $SrVO_3$, as expected, is the most metallic because of the large antibonding d bandwidth and no orbital splitting. The insulating regime for $LaTiO_3$ is 0.15 smaller in N_d than $YTiO_3$. However, the orbital ordering of the two materials are similar, an "1 up,2 down" pattern with the majority orbital occupying 60% in $LaTiO_3$ and 62% in $YTiO_3$. We believe that orbital ordering has the same contribution to both $LaTiO_3$ and $YTiO_3$. The enhancement of insulating regime in $YTiO_3$ can be understood

because the antibonding d bandwidth W of $YTiO_3$ is 17% smaller than $LaTiO_3$ (see Fig. 4.3 and notice both materials have nearly the same p and d band positions).

4.7 Locating materials on the phase diagrams

In previous sections, we have constructed the U-N_d phase diagrams for the MIT for various materials of interest, considering many possible cases: cubic structures with Hartree approximation (Fig. 4.6), cubic La series with DMFT (Fig. 4.7) and calculations with realistic structures using DMFT (Fig. 4.9 and Fig. 4.11). The next important question is: Where is the position of a material on the phase diagram?

First, we specify the correct values of the Hubbard value U and the Hund's coupling J (in Kanamori's notations, Eq. 2.23) for materials. The Hund's coupling is nearly unscreened [Vaugier et al. (2012)], its value is not far from the bare value, which is around $1eV$. In contrast, the U value is screened strongly [Aryasetiawan et al. (2006); Vaugier et al. (2012)], 5 or 6 times smaller than the bare one, and depends on materials. Vaugier et al. (2012) shows that J is around $0.65eV$, which is the value we use, for $SrVO_3$, $SrCrO_3$ or $SrMnO_3$ (using the energy window including p and d bands and symmetrizing over the interactions of the t_{2g} bands). The U values for $SrVO_3$ is $4.1eV$ as indicated from Vaugier et al. (2012), while La series are in Mott insulating phase and thus should have larger U. Other works [Pavarini et al. (2004); De Raychaudhury et al. (2007)] converges to the value $U \sim 5eV$ for La series. To reduce complication in using different values of U and J, we assume $U = 5eV$ and $J = 0.65eV$ for the positions of materials in the U direction.

Second, we need to fix positions of materials in the N_d direction. In Fig. 4.4, Wang et al. (2012) and Appendix D, the full-charge self consistency for $SrVO_3$ with standard double counting correction (fully-localized limit - FLL - formula) suggests N_d near the noninteracting band structure value be the position for materials. However, the

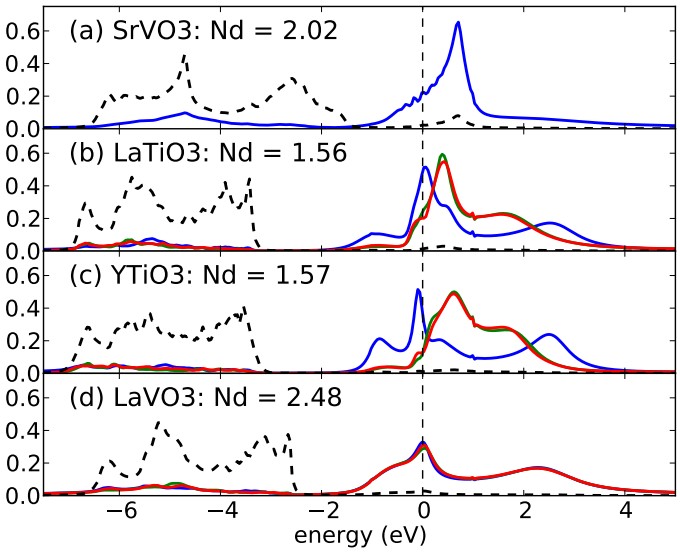

Figure 4.12: (Color online) Spectral functions $A(\omega)$ for $SrVO_3$, $LaTiO_3$, $YTiO_3$ and $LaVO_3$ using realistic lattice structure at $U = 5eV$, $J = 0.65eV$ and N_d chosen to be close to the value from *ab initio* calculations. The dashed curves (black online) are the average spectra per band for oxygen p bands, the solid curves (color online) are correlated d bands. The vertical dashed line marks the Fermi level.

phase diagrams in previous sections (Figs. 4.6,4.7,4.9,4.11) show that this N_d value predicts the wrong state (metallic state) for the insulators (e.g. $LaTiO_3$, $LaVO_3$ or $YTiO_3$). Fig. 4.12 are the spectral functions of $SrVO_3$, $LaTiO_3$, $YTiO_3$ and $LaVO_3$ at the N_d from noninteracting band structure calculation. It is clear that at this N_d position all materials are metals. The oxygen p bands are about $1eV$ closer to the Fermi level compared with the DFT density of states (Fig. 4.3), increasing the p-d covalency significantly. The covalency is even so strong in $SrVO_3$ that the upper Hubbard band is flattened. Moreover, the p positions are $1 \rightarrow 2eV$ closer to the Fermi level than the experimental values (see Table 4.2).

If considering the standard double counting correction instead of the d occupancy from DFT calculation, the N_d value can be smaller even though full-charge self consistency tends to keep this value closer to the DFT one (see Appendix D). With one-shot DMFT (without self consistency), at $U = 5eV$, the N_d values are shown in

$N_{t_{2g}}$	$SrVO_3$	$LaTiO_3$	$YTiO_3$	$LaVO_3$
FLL	1.90	1.46	1.42	2.37
AMF	2.03	1.57	1.55	2.43
exp.	1.73	1.28	1.31	2.24

Table 4.1: Estimation of t_{2g} occupancy using DFT+DMFT (without full-charge self consistency) using fully-localized limit (FLL),Czyżyk and Sawatzky (1994) around-the-mean-field (AMF)Anisimov et al. (1991) double counting corrections, and the cases that fit best with experiments (the third row). The calculations use realistic lattice structures at $U = 5eV$ and $J = 0.65eV$.

Table 4.1 using both fully-localized limit (FLL) [Czyżyk and Sawatzky (1994)] and around-the-mean-field (AMF) [Anisimov et al. (1991)] double counting corrections. AMF double counting correction gives N_d close to the noninteracting DFT values, it is thus unable to describe the materials correctly. FLL double counting correction drives the materials closer to the MIT phase boundaries. However, the N_d positions given by FLL double counting still describe $LaTiO_3$ and $LaVO_3$ as metals, and put $YTiO_3$ on the phase boundary even though $YTiO_3$ is an insulator with a large gap $\sim 1eV$. The two standard double counting corrections fail to describe materials in the DFT+DMFT framework which include both p and d bands.

We also compare directly our results with the photoemission spectra, the energy gaps and the oxygen p band positions from experiments. Table 4.2 summarizes the experimental data for energy gaps and the positions of oxygen bands for several materials that we study. For materials in Table 4.2, we adjust the double counting correction manually (by changing the d-level energy) so that the energy gap obtained from DMFT spectral function matches the experimental value (except for $SrVO_3$ where the spectrum is compared directly), the oxygen p bands are then automatically placed in the correct positions, which is the experiment value in Table 4.2. Figure 4.13 is the comparison between experimental and calculated spectral functions showing good agreement with experiments. The match of DMFT with experiments and that the N_d values for these agreements are smaller than the DFT ones (Table 4.1) confirm

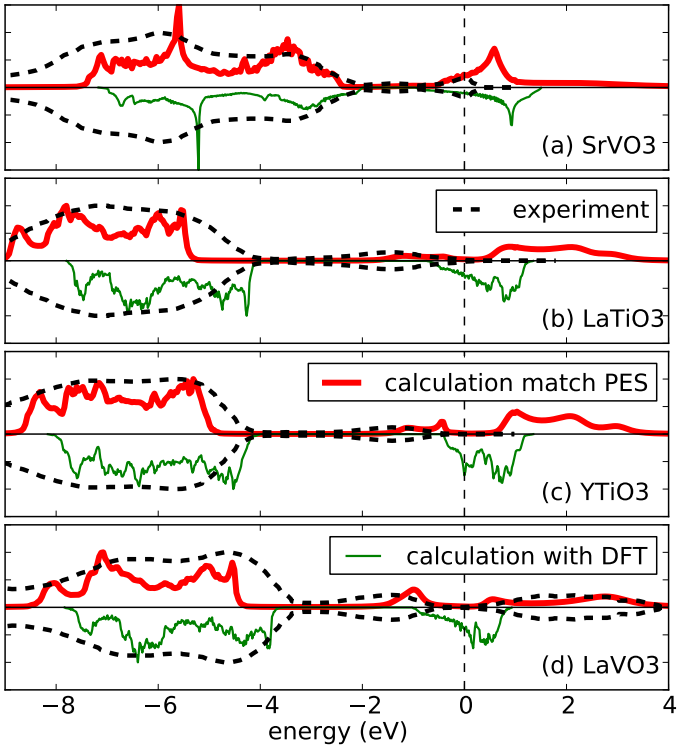

Figure 4.13: (Color online) Spectral functions $A(\omega)$ for $SrVO_3$, $LaTiO_3$, $YTiO_3$ and $LaVO_3$ using realistic lattice structure at $U = 5eV$, $J = 0.65eV$ and Δ is adjusted to match experimental photoemission spectra (PES). The PES are from Yoshimatsu et al. (2010); Maiti and Sarma (2000); Morikawa et al. (1996); Imada et al. (1998). The vertical dashed line marks the Fermi level.

	$SrVO_3$	$LaTiO_3$	$YTiO_3$	$LaVO_3$
Energy gap	NA	0.3eV	1eV	1eV
Position of oxygen bands	2.5eV	4.5eV	4.5eV	4eV

Table 4.2: Experimental data for the energy gaps and the oxygen p band positions from Fujimori et al. (1992) for $SrVO_3$ and Arima et al. (1993) for other materials.

both standard double counting corrections fail to locate the positions of materials in the phase diagrams.

We also emphasize the importance of the tilting in describing the materials properly. Figure 4.10 compares the spectral functions for cubic and tilted structures of

$LaTiO_3$, $LaVO_3$ for the same energy gap at the Fermi level at the same $U = 5eV$. While tilted structures give the oxygen bands at the correct positions, cubic structures put them $2eV$ (for $LaVO_3$) and $5eV$ (for $LaVO_3$) below the correct ones. The lattice distortion is required to obtain reasonable results.

Figure 4.13 reveals another important feature of the spectra, the position of the oxygen p bands. For all the insulators, the DFT p bands are $1 \rightarrow 1.5eV$ misplaced with respect to experimental spectra. From *ab initio* perspective, given an appropriate U value (such as $U = 5 \rightarrow 6eV$ for these materials) and if the oxygen p bands is placed in a correct position, one can adjust the double counting correction to place the calculated oxygen bands at that position, thus can solve the double counting issue. It therefore becomes the problem of calculating the correct p band positions from *ab initio* approach.

4.8 Conclusions

In this study, we have investigated materials of early transition metal oxides including the effect of p-d covalency. We used the Hartree approximation and DMFT in combination with DFT method in MLWF basis to study a wide range of early transition metal oxides. We constructed a general method to investigate materials that considers uncorrelated p and correlated d bands in the lowest energy range and can work with both cubic and $GdFeO_3$-distorted structure. By adjusting the d-level energy and the onsite interaction, we built the MIT phase diagrams for materials of interest, mapping to the space of interaction U and d occupancy. We examined possible methods for locating materials in the phase diagrams and found that standard double counting corrections, which gives d occupancy close to the noninteracting DFT values, fail to predict the correct phase of materials. However, with an appropriate

double counting correction and the U value is in a reasonable range, the spectral functions match perfectly the experimental photoemission spectra.

We have found important results in this work. First, the p-d covalency is not only important in late transition metal oxides, as predicted by Zaanen, Sawatzky and Allen [Zaanen et al. (1985)], but also crucial in the early transition metal oxides where Mott-Hubbard physics is dominant. We have shown in our study that even though in these materials the p bands are further away from the Fermi level than the d bands, there is still significant p-d admixture that contributes important physics. When the covalency is large enough, it even suppresses the electron correlation. Second, the DFT+DMFT framework, with an appropriate choice of double counting correction and within a reasonable range of U, gives results (photoemission spectra, energy gaps, oxygen p positions) largely agreed with experimental data while the standard double counting corrections fail to put materials in the correct phase. Instead of finding an appropriate form of double counting correction, one could simply adjust the d-level energy to place the oxygen p bands to the correct position. The realistic structure of materials is also essential to obtain results comparable with experimental spectra. Finally, by comparing the Hartree calculations with DMFT, we found that Hartree method can well approximate but is computationally less inexpensive than DMFT calculation. Given a Hartree phase diagram, depending on the nominal number of d electrons, one can extrapolate the DMFT phase diagram by shifting the phase boundary by an appropriate amount (see Fig. 4.7). To an approximation, the DMFT paramagnetic spectra can be obtained by averaging the spin up and down spectra generated by Hartree calculation.

However, there are several limitations in our calculations. First, with systems of 3 d electrons and above, a 5-d-band description is necessary, but our current DMFT code is unstable for such a calculation. Improving its performance is our next task to study materials in the intermediate regime between early and late transition metal

oxides. On the other hand, this DFT+DMFT employs single-site DMFT, cluster DMFT calculation that includes nonlocal effect of the correlation is available for single-orbital Hubbard model but for multiorbital system such as the t_{2g} ones, it is still beyond current computer capability.

Nevertheless, our work has proposed an appropriate approach to work on transition metal oxides by including oxygen p bands and adjusting the double counting correction in order to obtain the experimental energy gap and place the p bands at the correct positions. It suggests many prospective directions for future works. First, to solve the issue of double counting correction, at the current stage, one can use semi-empirical approach by matching the experimental position of oxygen p bands. In future, it requires improvement from band structure calculation to estimate the oxygen p band position more correctly, which will be used as a basic reference for adjusting the d-level energy, the problem then will be solved in an "*ab initio*" perspective. Second, it is important to understand the evolution of the p-d covalency and how the MIT behaves as going along the transition metal oxides series as the d shell is gradually filled, in particular the materials in the crossover between early and late transition metal oxides, in which the full 5 d bands have to be taken into account. Other aspects of the metal-insulator transition such as the temperature dependence or the metal-insulator coexistent region are also interesting topics. On the other hand, it is essential to apply this model with transition metal d and oxygen p bands to study other properties such as spin/orbital ordering or reexamine plenty of works done with d only model to understand how the p-d covalency affects the systems.

Chapter 5

Charged impurities in correlated electron materials

We use single site and CDMFT cluster dynamical mean field methods to study the response of a doped Mott insulator to a charged impurity. The theory is used to address the question of the effect of the density perturbation induced by the muon charge on the local response functions of a high temperature superconductor. The study gives some understanding of the muon spin rotation measurements in high temperature superconductor. The results in this chapter have been published in Dang et al. (2010).

5.1 Introduction

Mobile electrons act to screen a charged impurity. Screening may be understood in terms of two equations: the Poisson equation which relates the electric potential $V(r)$ to the combination of the impurity charge density $\rho_{\text{imp}}(r)$ and the change $\delta n(r)$ in free charge density, and a constitutive equation which relates δn to V. For weakly correlated metals it suffices to linearize the constitutive relation so the screening properties are determined by the density-density correlation function χ. A locality approximation is typically appropriate, so that $\delta n(r) = \chi(r = 0, \omega = 0)V(r)$ and it is also reasonable to write the Poisson equation in its continuum form. These

approximations imply that screening in weakly correlated metals is described by the familiar Thomas-Fermi equations, which lead to an exponential decay of the charge density characterized by the Thomas Fermi length $\lambda_{TF} = 1/\sqrt{4\pi e^2 \chi(r=0,\omega)/\epsilon}$.

Remarkably, while the ubiquity of impurity effects in correlated electron materials has prompted extensive theoretical studies of the consequences of local disorder for magnetic and superconducting properties [Alloul et al. (2009)], few results seem to be available for the problem of screening of a charge center in a material with strong electronic correlations. Several effects appear to be important. First, and most trivially, lattice effects are strong so a discrete version of the Poisson equation must be used. Second, most correlated materials of interest are oxides or organics with high background polarizability. Third, the constitutive relation between potential and density is likely to be strongly affected by correlation phenomena, which in particular will act to reduce the charge response. Fourth, in correlated materials, properties are typically sensitive functions of density, so that linearization in the magnitude of the density change may not be appropriate, while charge accumulation or depletion near an impurity may change the physics locally, for example nucleating or suppressing local order or fluctuations.

The possibility of local changes in the physics is of particular importance in the context of muon spin rotation spectroscopy. In this class of experiments, a positively charged muon with a known initial spin direction is injected into a solid. Coupling to magnetic order or fluctuations causes the spin of the muon to precess before it decays and the amount of precession (and hence some information about the spin fluctuations) can be inferred from the angular distribution of the muon decay products. If the charge of the muon causes a significant perturbation of the electronic properties near the muon site, then the muon does not necessarily measure the intrinsic magnetic dynamics of the material.

The question of the perturbation imposed by an injected muon has recently arisen

in the context of the possible observation of an "orbital current" phase in high temperature superconductors. Following a prediction of Varma (1997, 2006), neutron scattering experiments [Fauqué et al. (2006); Li et al. (2008); Mook et al. (2008)] reported evidence of a time reversal symmetry breaking phase characterized by local magnetic fields which are non-vanishing but average to zero over a unit cell; however, muon spin rotation experiments [Sonier et al. (2001); MacDougall et al. (2008); Sonier et al. (2009)] failed to detect the magnetic fields implied by the neutron experiments. One possible resolution of the discrepancy is that the neutron measurements detect properties of a minority phase. Another possible resolution, proposed by Shekhter, Varma and collaborators [Shekhter et al. (2008)] is that the muon, which carries unit charge, perturbs the local physics strongly enough to destroy the local order detected by neutrons. Shekhter et al. (2008) presented a Thomas-Fermi calculation which used a continuum version of the Poisson equation, a value $\varepsilon \sim 4$ of the dielectric constant rather smaller than the value $\varepsilon \sim 10 - 15$ generally accepted for oxides and a compressibility which was assumed to be linearizable and unrenormalized by many-body effects (although some consequences of the correlations were mentioned). The calculation of Shekhter *et. al.* implies that the muon would constitute a strong perturbation, dramatically changing the doping and the magnetic dynamics. However, the discussion given above implies that the assumptions on which the calculation is based may be questioned.

In this chapter we reexamine the issue. We use a tight-binding model description which captures the physics associated with the discreteness of the lattice, we examine the dependence on background dielectric constant, and most importantly we use single-site [Georges et al. (1996)] and cluster [Maier et al. (2005)] dynamical-mean-field-based methods to provide an estimate of the correlation effects on screening and on near-impurity electronic properties. We determine when linearization is appropriate and, where needed, use the full nonlinear (but local) charge response. We

compute locally defined quantities which give some insight into changes in spin correlation properties. While our specific results are obtained for a lattice, doping and interaction strength appropriate to high-T_c cuprates, we expect that our methods are more broadly applicable and our qualitative results are relevant to a wider range of systems.

We find that if dielectric constants in the physically reasonable range are used, the presence of a unit charge induces density changes which are a non-negligible fraction of the doping; however, the resulting changes in local magnetic properties are found to be modest, although observable. Further theoretical attention, perhaps using "LDA+DMFT" methods [Kotliar et al. (2006)], should be given to modeling the effects of charge centers in general and muons in particular.

5.2 Model and method

5.2.1 Model

We approximate the conduction band degrees of freedom as a one-band Hubbard model

$$H = -\sum_{ij\sigma} t_{ij} c^\dagger_{i\sigma} c_{j\sigma} + \sum_i \left(\bar{\mu} + V_i\right) c^\dagger_{i\sigma} c_{i\sigma} + U \sum_i n_{i\uparrow} n_{i\downarrow}, \tag{5.1}$$

with hopping t_{ij}, on-site repulsion U and a spatially varying electrochemical potential $\mu_i = \bar{\mu} + V_i$ determined self-consistently (see below) from the impurity charge and any induced electronic charge. For the explicit calculations presented in this work, we take a set of planes which are electronically decoupled (no interplane hopping) but coupled via the Coulomb interaction. Each plane is taken to be a two-dimensional square lattice with nearest neighbor hopping. We consider interactions of the order of the critical value U_{c2} needed to drive a metal insulator transition in a homogeneous

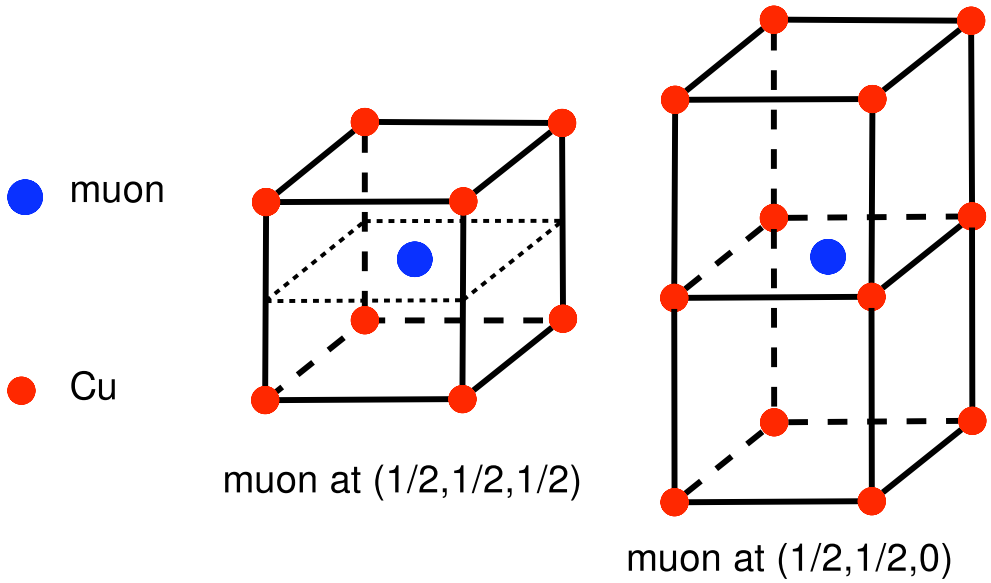

Figure 5.1: (Color online) Sketch of two cases under consideration: Left panel: charged impurity (muon) placed at center of cube of transition metal (Cu) sites. Right panel: impurity placed in plane.

bulk system with one electron per site. $\bar{\mu}$, the chemical potential far from the impurity site, is chosen to produce a carrier density $\bar{n}$ corresponding to a hole doping of $\delta = 1 - \bar{n} = 0.1$ corresponding approximately to the doping level at which pseudogap and magnetic effects occur in the high-T_c cuprates.

We suppose that the impurity is located at a position R_μ and has a charge e. We consider in detail two cases, shown in Fig. 5.1. In one we take the impurity to be located in the center of a plaquette in a CuO_2 plane (i.e. the (1/2,1/2,0) position). In the other we place the impurity symmetrically between planes at the $(1/2, 1/2, 1/2)$ position. Placing the impurity at these high symmetry points allows us to use existing codes, but as will be seen the physics we find is generic.

We treat the screening using the self-consistent Hartree approximation. The presence of the impurity potential changes the electronic density on site i (coordinate $\vec{R}_i$) from the average value $\bar{n}$ to a new value $n_i = \bar{n} + \delta n_i$ so the total electrostatic potential is

$$V_i = -\frac{e^2}{\epsilon|\vec{R}_i - \vec{R}_\mu|} + \frac{e^2}{\epsilon}\sum_{j\neq i}\frac{\delta n_j}{|\vec{R}_i - \vec{R}_j|}, \tag{5.2}$$

with ϵ the background dielectric constant. The appropriate value of ϵ is not well established. Optical conductivity measurements [Orenstein et al. (1990)] suggest that $\epsilon(\omega \to 0, q = 0) \approx 4$, a value used in Shekhter et al. (2008), however what is needed is $\epsilon(\omega = 0, q)$ for a range of q of the order of the shortest distance from a lattice site to the impurity position. Reasonable values of this quantity have not been determined. Calculations of the "screened U" for the related oxide material $SrVO_3$ yield a high frequency unscreened $U \sim 14eV$ and a low frequency screened quantity $W \approx 2eV$ suggesting an electronic contribution to ϵ of $\epsilon \approx 7$. Lattice relaxation effects may increase the short scale ϵ to a number of order 15 (see e.g. Okamoto et al. (2006)), but of course lattice relaxations may induce other changes in the model. Resolving these uncertainties is beyond the scope of this work; we have therefore performed our explicit calculations for the two values $\epsilon = 4$ and 15.

The remaining issue is the computation of δn_i for a given distribution of V_i; this is discussed in the next section. Here we note that the scale of the screening effects is set by the dimensionless parameter

$$\gamma = \frac{e^2}{\epsilon a}\frac{dn}{d\mu}, \tag{5.3}$$

with a the in-plane lattice parameter. We use the value $a \approx 3.8$Å appropriate for cuprates. The band theory estimate for the compressibility $dn/d\mu$ of weakly correlated electrons in the cuprate band structure is $dn/d\mu \approx 1.4/eV$ so that $\gamma_{\rm nonint} \approx 5/\epsilon$. As we shall see, for correlation strengths of the order of those believed to be relevant for high temperature superconductors, the actual compressibility, and therefore the actual γ are likely to be about an order of magnitude smaller.

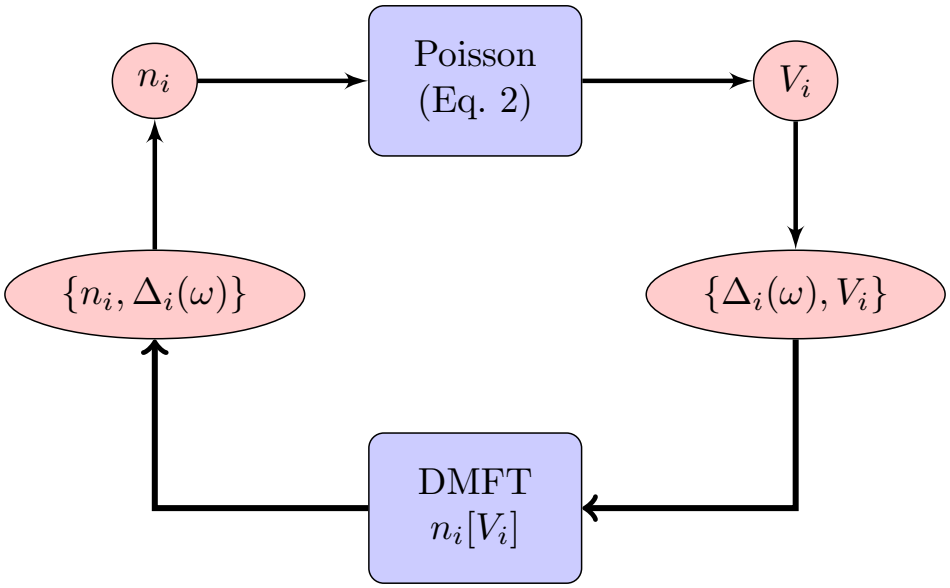

Figure 5.2: (Color online) Sketch of the self consistency procedure used to calculate the charge density and hybridization functions in the vicinity of a charged impurity. Starting from an initial guess for the potential V_i and the hybridization function $\Delta_i(\omega)$ the dynamical mean field procedure is used to obtain a new density and hybridization function; the new density is used in Eq. (5.2) to obtain new potentials, and the process is iterated to self consistency. Changes in the hybridization function are found to be sufficiently small that the DMFT loop may be solved once for the bulk material and $\partial n/\partial \mu$ obtained from this solution may then be used to update the density.

5.2.2 Method

We require the solution of a correlated electron problem in a spatially inhomogeneous, self-consistently determined potential. There is no general and exact method for obtaining this information. We adopt here the single site [Georges et al. (1996)] and CDMFT cluster [Kotliar et al. (2001)] dynamical mean field approximations. These methods capture important aspects of the strong correlation problem and in particular produce a Mott transition. The single-site method is more computationally tractable; however the cluster method includes intersite correlations and may provide a more reasonable picture of the spin dynamics.

In the single-site DMFT method, the electron self energy Σ (in general a function of two coordinates and a frequency) is taken to be site-local but may be different from site to site: $\Sigma(i,j;\omega) \to \Sigma_i(\omega)$. The self energy on each site i is determined from the solution of a quantum impurity model (also different on each site). The impurity model is specified by the interaction $Un_\uparrow n_\downarrow$ and a hybridization function $\Delta_i(\omega)$. The impurity model Green function on site i is thus

$$G_i^{\rm imp}(\omega) = \left[\omega + \bar{\mu} + V_i - \Delta_i(\omega) - \Sigma_i(\omega)\right]^{-1}. \tag{5.4}$$

The hybridization function is fixed by a self-consistency condition linking the Green function $G_i^{\rm imp}(\omega)$ of the impurity model on site i to the ii component of the lattice Green function:

$$\begin{aligned} G_i^{\rm imp}(\omega) &= G_i^{\rm lat}(\omega) \\ &\equiv \left\{\left[\left(\omega + \bar{\mu} + V_i - \Sigma_i(\omega)\right)\delta_{ij} - t_{ij}\right]^{-1}\right\}_{ii}. \end{aligned} \tag{5.5}$$

There are now two issues of self-consistency: Δ_i must be made self-consistent using Eq. (5.4,5.5) and the potentials V_i on all sites i must be made self consistent with the computed densities (which are obtained from the $G_i^{\rm imp}(\omega)$) using Eq. (5.2). To reach self-consistency one begins with an initial guess for the site densities. From this one computes the V_i via Eq. (5.2). Using these V_i and an initial guess for the hybridization function one solves the DMFT equations, obtaining converged solutions for $G_i^{\rm imp}$ and Δ_i. From these we recompute n_i and hence V and continue the cycle until convergence is reached.

Observe that the result of this procedure is that each site has a hybridization function determined by neighboring sites, which have different densities. Thus a given site "knows" that it is in a spatially inhomogeneous environment, and therefore has properties which are different from those of a hypothetical bulk system in which

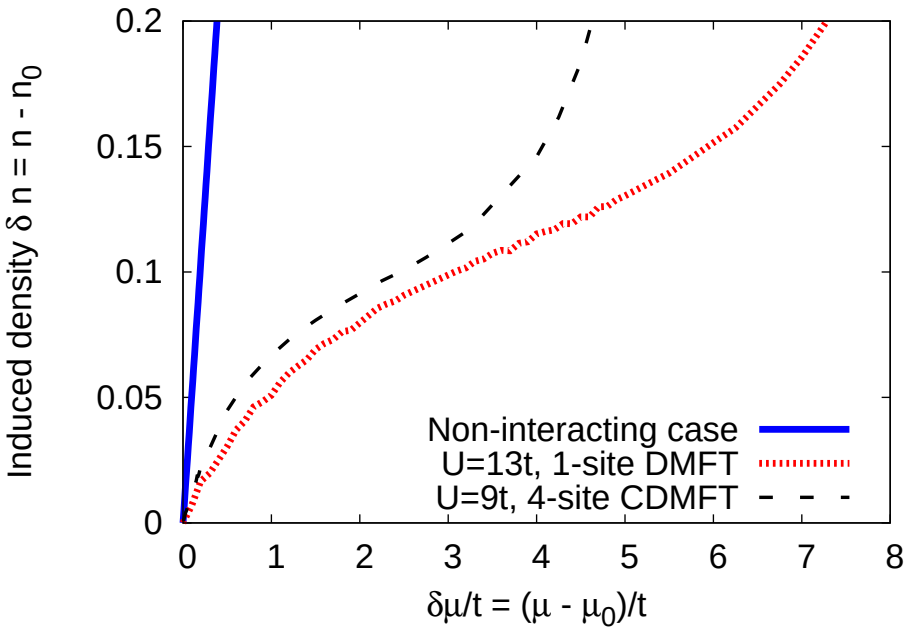

Figure 5.3: (Color online) Local density change induced by locally potential $\delta\mu_i$. In all cases bulk density is $n = 0.9$. Solid line: density change on site i, δn_i, induced by potential $\delta\mu_i$ applied on same site, computed for non-interacting electrons using tight-binding band parameters appropriate to high temperature superconductors. Dotted line: same computation, but using single-site dynamical mean field theory with $U = 13t$ and hybridization parameters taken from calculation for $U = 13t$ and $\delta = 0.1$. Dashed line: change in density on one site of a 4-site plaquette induced by potential $\delta\mu$ applied to all four sites of plaquette, computed using CDMFT dynamical mean field theory with $U = 9t$ with hybridization function corresponding to $U = 9t$ and $\delta = 0.1$.

all sites have a density equal to the density of the designated site. At various points in the ensuing discussion we will compare properties of a given lattice site i with density n_i to those that would be obtained in a bulk solid in which all sites had density n_i.

In practice the laborious procedure described above may be simplified. We have verified (for an example, see Fig 5.4) that to within an accuracy of $\sim 10\%$ the change in the hybridization function is negligible and the potential may be computed from the pure-system $n(\mu)$ curve. Thus we use the homogeneous bulk hybridization function

to compute the variation of local n with local μ and use this to define the density/potential self-consistency, with the result that it is necessary to solve the DMFT loop only once. The self consistency procedure is sketched in Fig. 5.2.

Fig. 5.3 shows the change in on-site density caused by a change in local chemical potential computed for noninteracting electrons with bulk density corresponding to 0.1 hole doping, and for two dynamical mean field cases: single-site DMFT at $U = 13t$ (slightly larger than the single-site DMFT critical U which is $12t$ for this problem) and cluster DMFT at $U = 9t$ which is rather larger than the $6t$ needed to open a gap in this approximation but is in the range believed to be reasonable for cuprates [Comanac et al. (2008)]. In the DMFT calculations the hybridization function was fixed at the form appropriate to a bulk material with density $n = 0.9$. As expected, the correlation effects substantially reduce the local charge susceptibility: the initial slope is decreased by a factor of about 5 relative to the noninteracting value and there is a substantial curvature. We also observe that even for $\delta n = 0.1$, corresponding to a local density of 1 electron per site, the charge susceptibility remains non-vanishing (as expected because the local site is embedded in a metallic bath), whereas the corresponding bulk system with density $n = 1$ per site would be in a gapped phase with vanishing compressibility.

The single-site method is reasonably computationally tractable, enabling the exploration of a wider parameter space and a relatively detailed computation of physical quantities. However, this approximation overestimates the critical interaction required to drive the Mott transition, does not describe the "pseudogap" physics associated with underdoped cuprates and more generally does not capture the physics associated with short-ranged intersite correlations. Cluster dynamical mean field methods capture more aspects of cuprate physics, including a lower critical value for the Mott transition and some aspects of intersite spin correlations. They also exhibit a pseudogap. However, the cluster methods are much more computationally expen-

sive. Further, the widely used "DCA" approximation [Maier et al. (2005)] is unsuited to impurity problems because it requires translation invariance. We therefore adopt the CDMFT method [Kotliar et al. (2001)] in which one tiles the lattice into real-space clusters; each cluster is regarded as a site of a new lattice of supercells. The hopping terms connecting sites in the same supercell are part of the cluster Hamiltonian while the hopping terms connecting sites on different clusters define the supercell band structure. The new lattice is treated via single-site dynamical mean field theory (albeit with a more complicated impurity), thus the self-consistency loop is the same as in the single-site case. We use 4-site clusters. We solve the impurity model using the continuous-time quantum Monte-Carlo method introduced in Werner et al. (2006); for the 4-site cluster we use the general ("matrix") representation of Werner and Millis (2006). The method gives access both to the physical (lattice) electron Green functions and to correlation functions defined on the cluster model. While the cluster correlation functions are not identical to the corresponding lattice quantities, they are reasonable estimators of the physical correlators.

One restriction should be noted: the impurity solver algorithm we use [Werner and Millis (2006)] makes heavy use of symmetries and therefore requires that the four sites in the cluster have the same potential. Thus for cluster calculations we are limited to the case in which the impurity potential is the same for all 4 sites in the cluster. The geometry we use guarantees that this is the case for the 4 sites closest to the impurity on each plane. However, for the farther plaquettes, a problem arises, because one side of a plaquette is necessarily closer to the impurity than the other, so the local symmetry is broken. We treat this situation by solving the Poisson equation and then on each cluster replacing the potential by the average of the calculated potential over the cluster sites. The long range of the Coulomb interaction and the relatively small changes induced on farther neighbor clusters make this a reasonable approximation.

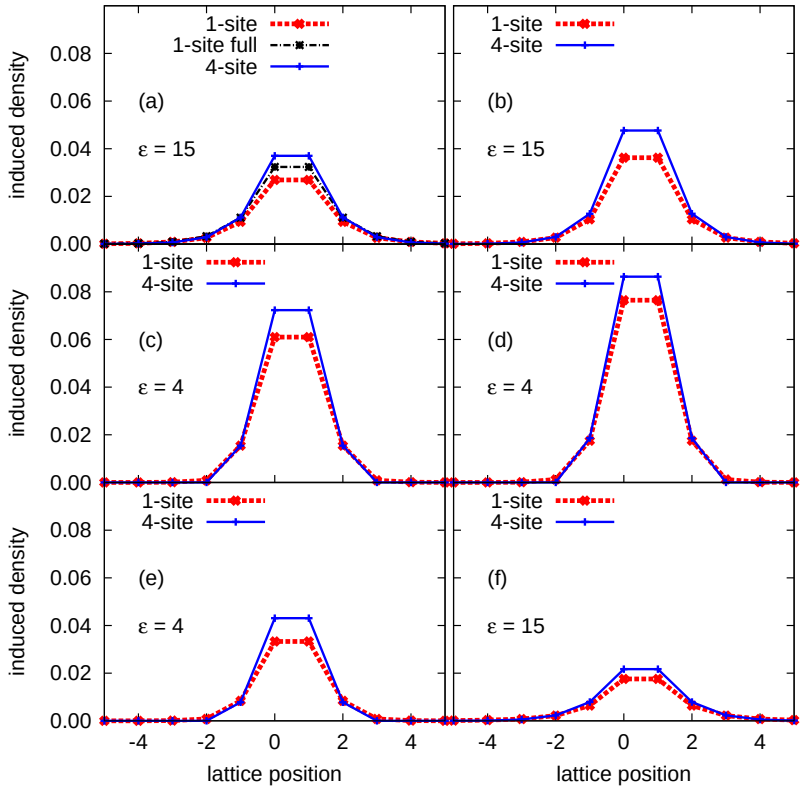

Figure 5.4: (Color online) (a,b,c,d) Variation of conduction band density per lattice site along line $(x, 0, 0)$ induced by impurities positioned at $(1/2, 1/2, 1/2)$ ((a) and (c)) and $(1/2, 1/2, 0)$ ((b) and (d)) calculated as described in the text using single site DMFT with $U = 13t$ and and 4 site DMFT with $U = 9t$. (e,f) Variation of conduction band density per lattice site along line $(x, 0, 1)$ induced by impurity positioned at $(1/2, 1/2, 0)$ for $\epsilon = 4$ (e) and $\epsilon = 15$ (f) calculated as described in the text using single site DMFT with $U = 13t$ and and 4 site DMFT with $U = 9t$.

5.3 Results: density distribution

An electrical conductor responds to a charged impurity by producing an electron density modulation ("screening cloud") which screens the impurity charge. The panels of Fig. 5.4 present the spatial distribution of the screening cloud induced by an impurity of charge +1 in a hole-doped superconductor. Shown is the charge density per lattice site along a line passing near to the impurity site for two choices of

background dielectric constant, $\epsilon = 4$ and $\epsilon = 15$, for two choices of impurity position (between planes or in the center of a plaquette in one plane) and for the two approximations we have used. We see that in all cases the density change is only appreciable on the sites adjacent to the impurity. For $\epsilon = 4$ the density change on the sites nearest the impurity is large enough to move the local density very close to the half filled value. For $\epsilon = 15$ the density change is about a factor of two smaller than for $\epsilon = 4$. The density profiles calculated for single-site and 4-site DMFT are very similar, because the density profile is controlled by the local compressibility which is similar for the two cases we have considered. The density profiles calculated for the two impurity locations and for the farther plane are also similar because the $1/r$ variation of the unscreened Coulomb interaction is relatively slow. These calculations are performed using the simplified self consistency loop described above; also shown are results obtained using the full DMFT procedure for the $\epsilon = 15$, single-site DMFT case.

The density changes induced by the impurity potential are seen to be generically of the order of 0.05 electrons per site or less, which is less than but of the order of the doping for underdoped high temperature superconductors.

5.4 Results: spin correlations

In this section we study how the screening cloud affects the local spin dynamics. This is not straightforward because the spin dynamics are expected to be strongly doping dependent in a homogeneous bulk system, while here we must treat a spatially inhomogeneous system. We study impurity-model correlation functions, which can be directly measured in our simulations. These are not identical to the spin correlations of the actual lattice problem, but are expected to have similar magnitude and similar doping and temperature dependence to those of the full lattice problem. Further,

the simulation gives results for Matsubara frequencies $\omega_n = 2\pi nT$. The $n = 0$ term is in essence the classical (thermal) part of the spin-spin correlation function while the $n \neq 0$ terms give some information on the quantum fluctuations in the system. We present results for the spin correlations on the site nearest the charge center and for the second neighbor, and compare the results to those found far from the charge center and also to those computed for a hypothetical bulk system with average density equal to that on the site nearest the charge center.

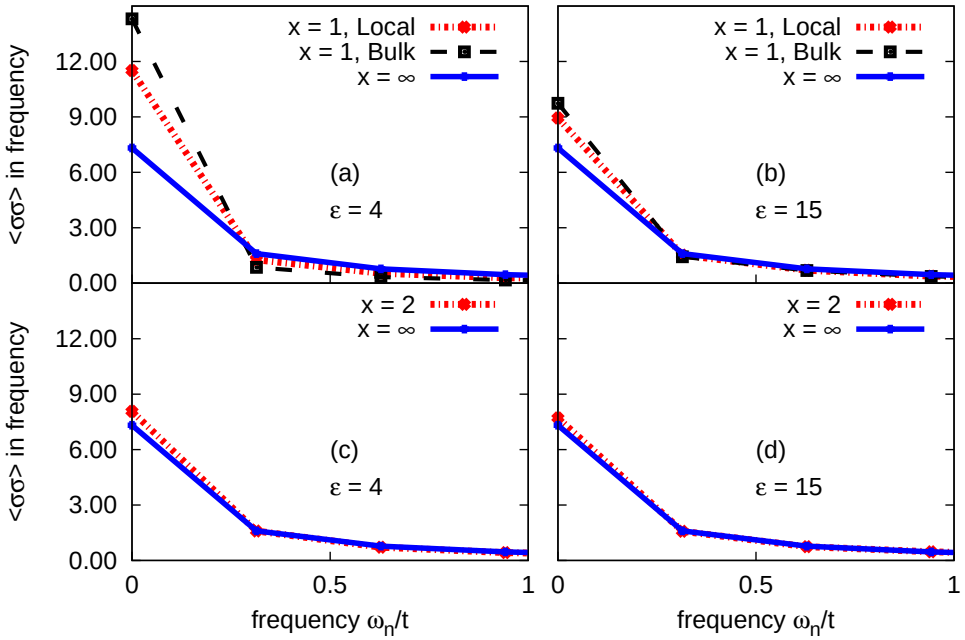

Figure 5.5: (Color online) Impurity model spin-spin correlation along line $(x, 0, 0)$ computed from single site dynamical mean field theory as function of Matsubara frequency at inverse temperature $\beta = 20$ and dielectric constants indicated for charged impurity at position $(1/2, 1/2, 0)$. Upper panels are onsite correlators for sites nearest to muon ($x = 1$), lower panels are onsite correlators for second neighbors to muon ($x = 2$), correlator for site far from muon is also included.

Fig. 5.5 shows the impurity model spin correlation functions computed using single-site dynamical mean field theory. We see that the 'classical' (zero Matsubara frequency) spin correlations of sites near the muon are enhanced relative to the

value far from the muon site, but are not as large as those of a hypothetical system with average density equal to the density on the near-muon sites. This shows that the spin correlations on a given site are controlled not only by the density on the site but also by the properties of the neighboring sites. For the case $\epsilon = 4$ we see that the changes are substantial (increasing the value at the lowest Matsubara frequency by a factor of about 1.5, which in turn is about half of the increase that would occur in a sample whose average density was set equal to the density on the impurity site). On the other hand for $\epsilon = 15$ the changes, although visible, are much smaller.

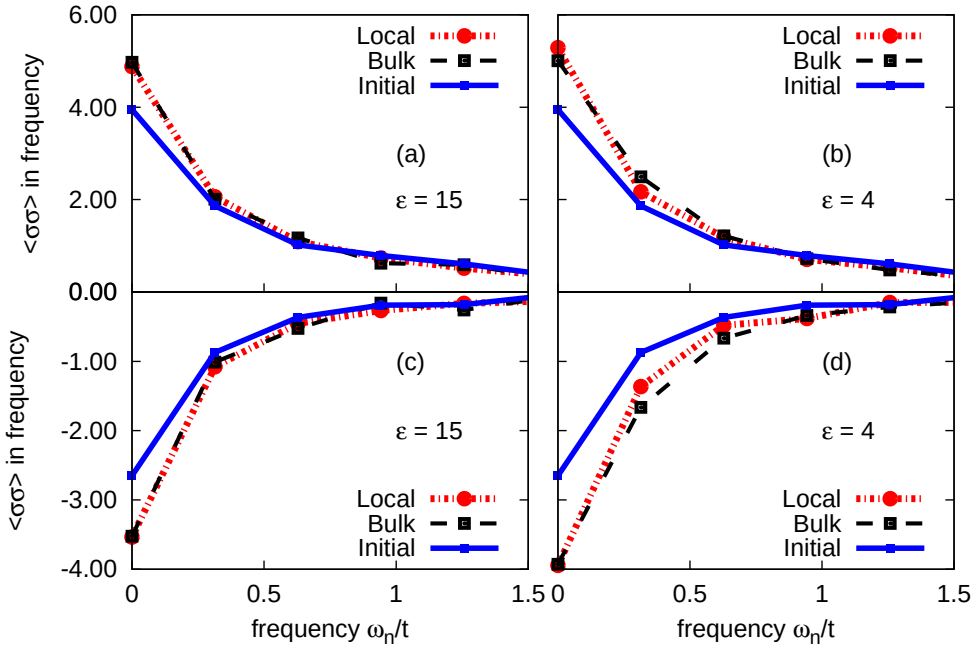

Figure 5.6: (Color online) On site (upper panels) and first neighbor (lower panels) impurity model spin-spin correlation computed from 4-site CDMFT cluster dynamical mean field theory as function of Matsubara frequency at inverse temperature $\beta = 20$ and dielectric constants indicated, for charged impurity at position $(1/2, 1/2, 0)$. Solid line with solid squares (blue on-line) shows correlator computed for sites far from impurity site. Dotted line with solid circles (red on-line) shows correlator computed on designated site. Dashed line with open squares (blue on line) shows correlated computed for bulk system with mean density equal to density on impurity site.

The single-site dynamical mean field theory is known to provide a poor approx-

imation to the spin correlations of a doped Mott insulator, at least in two spatial dimensions, because it neglects antiferromagnetic correlations. We have therefore also considered the spin correlations in the 4-site CDMFT cluster dynamical mean field theory calculations. Here the difference between on-site and first neighbor impurity model spin correlations reveals the importance of antiferromagnetic fluctuations. Fig. 5.6 shows results for the same parameters as in Fig 5.5. We see that the first neighbor correlations increase by about 40% for $\epsilon = 4$ and about 25% for $\epsilon = 15$. We have also examined other correlation functions, in particular the equal-time singlet pair correlations which are the dominant fluctuations on the four-site plaquette, finding that these are enhanced by similar amounts.

5.5 Conclusion

In this work, we have shown how "strong correlation" effects alter the response of a material to a local charge inhomogeneity. We introduced a general method, based on dynamical mean field theory, for calculating these effects and applied it to the question of the changes produced by the presence of a muon in a high temperature superconductor. We found, in qualitative agreement with previous work [Shekhter et al. (2008)], that the muon is not a "soft probe": although the main correlation effect is a suppression of the charge susceptibility by a factor of 3-4 relative to band theory, the charge field associated with the muon may produce a significant change in the charge density on nearby sites, of order 0.05 electrons per site. In a less strongly correlated material, the change in charge density on the near-muon sites would be larger. A crucial issue in determining the scale of the effects was found to be the value of the static, short wavelength, dielectric constant. The effect on the local spin correlations is smaller than the effect on the charge density, but is not negligible.

Our calculation involves several approximations. The most important is the value of the dielectric constant, which is not known *a priori*. Varying the dielectric constant over the range of values which have been proposed for cuprates or other oxides leads to factor-of-two changes in our results. A closely related issue concerns the local lattice distortions which would normally be induced near a charged impurity (see Okamoto et al. (2006) for an example in a different context). These have the potential to change local hopping amplitudes and perhaps correlation strengths, although correlation strengths, being an atomic property, will be less strongly affected. In view of the importance of muon spin rotation as a probe of correlated materials, these issues deserve further investigation, perhaps via a band theory calculations. A second approximation is the use of the dynamical mean field method. The consistency of our single-site and four-site results for the charge compressibility suggest that our basic findings for the density correlations are a reasonable estimate of the correct behavior. However, the calculated spin correlations are probably subject to larger uncertainties, which are at this point not easily quantified. We know that the charge perturbation is important only on sites immediately adjacent to the charge center. The spin correlations on these sites, which are the ones which would be probed by a muon, are affected both by the on-site property (the change in local density) and by the properties of the nearby sites, and the nearby sites in turn both affect and are affected by the near-impurity sites. If the intersite spin coupling is strong it is possible that the magnetic properties are controlled by the sites farther away from the muon. It is very likely that the dynamical mean field methods we use underestimate these spin-correlation effects. Their investigation is an important open problem.

While our specific numerical results were obtained for model parameters appropriate to high temperature superconductors, they have implications for the more general issue of the response of a correlated electron material to a charged impurity. To illustrate this point we consider a generic correlated material, which we assume to be

a more or less cubic lattice. For simplicity place the charged impurity at the center of a cube of sites. The charged impurity will induce a screening cloud containing one electron. The length scale over which this charge is distributed is set by the density-density correlation function of the charged material and the background dielectric function. If values typical of a weakly correlated material are used and the dielectric function is of the order of 10 or less, a simple extension of the estimates we have presented indicates that almost the entire screening charge sits as close to the impurity as it can get. The density change on the near-impurity sites would then (for the simple cubic situation we have considered) be approximately 1/6 electron per site, a change large enough to affect the local physics. On the other hand, if strong correlation effects are important (as in the case of high-T_c materials where they reduce the charge response by a factor of 5 or more), the total charge would be spread over a wider range and the concentration on the near impurity sites would be substantially smaller. However, the relative effect on the local physics would still not be small, as the greatest suppression of charge response occurs for a lightly doped Mott insulator, where the important scale is the doping, which would itself be small. Thus even in this case we would expect that a charged impurity would change the local physics noticeably. A quantitative test of our theory would involve measurements of the near-impurity charge density profile and a comparative measurement of spin dynamics near to and far from the impurity site.

Our results have implications for muon spin resonance experiments on transition metal oxides. Muons are an important probe of the spin dynamical of condensed matter physics, but a muon has a charge +1, and the results presented here indicate that in transition metal oxides a muon is unlikely to be a "soft" probe; rather, it significantly perturbs the medium in which it is embedded. Feyerherm et al. (1995) reached a similar conclusion in a study of $PrNi_5$, a rare earth system with more complicated physics, showing that muons significantly perturb the crystal field structure

on the near muon Pr sites. In the case studied here we showed that the perturbation due to the muon affects local properties such as the near muon spin dynamics and presumably (although we have not investigated this) the size of the ordered moment.

It is important to note that a dilute concentration of muons should have only negligible effects on "global" or long range properties such as magnetic phase boundaries or superconducting penetration depth.

Bibliography

Abrikosov, A., Gorkov, L. and Dzyaloshinski, I., *Methods of Quantum Field Theory in Statistical Physics*, Dover Books on Physics Series, Dover Publications (1975), URL.

Aichhorn, M., Pourovskii, L. and Georges, A., Importance of electronic correlations for structural and magnetic properties of the iron pnictide superconductor LaFeAsO, Phys. Rev. B **84**, 054529 (2011), URL.

Aichhorn, M., Pourovskii, L., Vildosola, V., Ferrero, M., Parcollet, O., Miyake, T., Georges, A. and Biermann, S., Dynamical mean-field theory within an augmented plane-wave framework: Assessing electronic correlations in the iron pnictide LaFeAsO, Phys. Rev. B **80**, 085101 (2009), URL.

Albuquerque, A., Alet, F., Corboz, P., Dayal, P., Feiguin, A., Fuchs, S., Gamper, L., Gull, E., Gürtler, S., Honecker, A., Igarashi, R., Körner, M., Kozhevnikov, A., Läuchli, A., Manmana, S., Matsumoto, M., McCulloch, I., Michel, F., Noack, R., Pawowski, G., Pollet, L., Pruschke, T., Schollwöck, U., Todo, S., Trebst, S., Troyer, M., Werner, P. and Wessel, S., The ALPS project release 1.3: Open-source software for strongly correlated systems, Journal of Magnetism and Magnetic Materials **310**, 1187 (2007), URL.

Alloul, H., Bobroff, J., Gabay, M. and Hirschfeld, P. J., Defects in correlated metals and superconductors, Rev. Mod. Phys. **81**, 45 (2009), URL.

Amadon, B., Lechermann, F., Georges, A., Jollet, F., Wehling, T. O. and Lichten-

stein, A. I., Plane-wave based electronic structure calculations for correlated materials using dynamical mean-field theory and projected local orbitals, Phys. Rev. B **77**, 205112 (2008), URL.

Andersen, O., Liechtenstein, A., Jepsen, O. and Paulsen, F., LDA energy bands, low-energy hamiltonians, t', t'', $t_\perp(k)$, and $J_\perp$, Journal of Physics and Chemistry of Solids **56**, 1573 (1995), URL, proceedings of the Conference on Spectroscopies in Novel Superconductors.

Anisimov, V. I., Zaanen, J. and Andersen, O. K., Band theory and Mott insulators: Hubbard U instead of Stoner I, Phys. Rev. B **44**, 943 (1991), URL.

Ariando, Wang, X., Baskaran, G., Liu, Z. Q., Huijben, J., Yi, J. B., Annadi, A., Barman, A. R., Rusydi, A., Dhar, S., Feng, Y. P., Ding, J., Hilgenkamp, H. and Venkatesan, T., Electronic phase separation at the $LaAlO_3/SrTiO_3$ interface, Nat. Commun. **2**, 188 (2011), URL.

Arima, T., Tokura, Y. and Torrance, J. B., Variation of optical gaps in perovskite-type $3d$ transition-metal oxides, Phys. Rev. B **48**, 17006 (1993), URL.

Aryasetiawan, F., Imada, M., Georges, A., Kotliar, G., Biermann, S. and Lichtenstein, A. I., Frequency-dependent local interactions and low-energy effective models from electronic structure calculations, Phys. Rev. B **70**, 195104 (2004), URL.

Aryasetiawan, F., Karlsson, K., Jepsen, O. and Schönberger, U., Calculations of Hubbard U from first-principles, Phys. Rev. B **74**, 125106 (2006), URL.

Balents, L., Spin liquids in frustrated magnets, Nature **464**, 199 (2010), URL.

Bednorz, J. G. and Müller, K. A., Possible highT c superconductivity in the Ba- La- Cu- O system, Zeitschrift für Physik B Condensed Matter **64**, 189 (1986), URL.

Bensch, W., Schmalle, H. W. and Reller, A., Structure and thermochemical reactivity of CaRuO3 and SrRuO3, Solid State Ionics **43**, 171 (1990), URL.

Bert, J. A., Kalisky, B., Bell, C., Kim, M., Hikita, Y., Hwang, H. Y. and Moler, K. A., Direct imaging of the coexistence of ferromagnetism and superconductivity at the $LaAlO_3/SrTiO_3$ interface, Nat Phys **7**, 767 (2011), URL.

Bickers, N. E., Review of techniques in the large-N expansion for dilute magnetic alloys, Rev. Mod. Phys. **59**, 845 (1987), URL.

Blaha, P., Schwarz, K., Madsen, G. K. H., Kvasnicka, D. and Luitz, J., *WIEN2K, An Augmented Plane Wave plus Local Orbitals Program for Calculating Crystal Properties*, Techn. Universität Wien, Austria (2011).

Bordet, P., Chaillout, C., Marezio, M., Huang, Q., Santoro, A., Cheong, S.-W., Takagi, H., Oglesby, C. and Batlogg, B., Structural Aspects of the Crystallographic-Magnetic Transition in LaVO3 around 140 K, Journal of Solid State Chemistry **106**, 253 (1993), URL.

Boullay, P., David, A., Sheets, W. C., Lüders, U., Prellier, W., Tan, H., Verbeeck, J., Van Tendeloo, G., Gatel, C., Vincze, G. and Radi, Z., Microstructure and interface studies of $LaVO_3/SrVO_3$ superlattices, Phys. Rev. B **83**, 125403 (2011), URL.

Brinkman, W. F. and Rice, T. M., Application of Gutzwiller's Variational Method to the Metal-Insulator Transition, Phys. Rev. B **2**, 4302 (1970), URL.

Caffarel, M. and Krauth, W., Exact diagonalization approach to correlated fermions in infinite dimensions: Mott transition and superconductivity, Phys. Rev. Lett. **72**, 1545 (1994), URL.

Ceperley, D. M. and Alder, B. J., Ground State of the Electron Gas by a Stochastic Method, Phys. Rev. Lett. **45**, 566 (1980), URL.

Chan, C.-K., Werner, P. and Millis, A. J., Magnetism and orbital ordering in an interacting three-band model: A dynamical mean-field study, Phys. Rev. B **80**, 235114 (2009), URL.

Cococcioni, M. and de Gironcoli, S., Linear response approach to the calculation of the effective interaction parameters in the LDA + U method, Phys. Rev. B **71**, 035105 (2005), URL.

Comanac, A., Dynamical mean-field theory of correlated electron systems: New algorithms and applications to local observables, Ph. D. thesis (2007), URL.

Comanac, A., deMedici, L., Capone, M. and Millis, A., Optical conductivity and the correlation strength of high-temperature copper-oxide superconductors, Nature Physics **4**, 287 (2008), URL.

Cwik, M., Lorenz, T., Baier, J., Müller, R., André, G., Bourée, F., Lichtenberg, F., Freimuth, A., Schmitz, R., Müller-Hartmann, E. and Braden, M., Crystal and magnetic structure of $LaTiO_3$: Evidence for nondegenerate t_{2g} orbitals, Phys. Rev. B **68**, 060401 (2003), URL.

Czyżyk, M. T. and Sawatzky, G. A., Local-density functional and on-site correlations: The electronic structure of La_2CuO_4 and $LaCuO_3$, Phys. Rev. B **49**, 14211 (1994), URL.

Dagotto, E., Complexity in Strongly Correlated Electronic Systems, Science **309**, 257 (2005), URL.

Damascelli, A., Hussain, Z. and Shen, Z.-X., Angle-resolved photoemission studies of the cuprate superconductors, Rev. Mod. Phys. **75**, 473 (2003), URL.

Dang, H. T., Gull, E. and Millis, A. J., Theory of charged impurities in correlated

electron materials: Application to muon spectroscopy of high-T_c superconductors, Phys. Rev. B **81**, 235124 (2010), URL.

Dang, H. T. and Millis, A. J., Designing ferromagnetism in vanadium oxide based superlattices, Phys. Rev. B **87**, 184434 (2013), URL.

Dang, H. T. and Millis, A. J., Theory of ferromagnetism in vanadium-oxide based perovskites, Phys. Rev. B **87**, 155127 (2013), URL.

Dang, H. T., Millis, A. J. and Marianetti, C. A., Covalency and the metal-insulator transition in titanate and vanadate perovskites, arXiv:1309.2995 (2013), URL.

Daul, S. and Noack, R., DMRG study of ferromagnetism in a one-dimensional Hubbard model, Zeitschrift für Physik B Condensed Matter **103**, 293 (1997), arXiv:cond-mat/9612056.

de Boer, J. H. and Verwey, E. J., Semi-conductors with partially and with completely filled 3d-lattice bands, Proceedings of the Physical Society **49**, 59 (1937), URL.

De Raychaudhury, M., Pavarini, E. and Andersen, O. K., Orbital Fluctuations in the Different Phases of $LaVO_3$ and YVO_3, Phys. Rev. Lett. **99**, 126402 (2007), URL.

du Trémolet de Lacheisserie, E., Gignoux, D. and Schlenker, M. (Eds.), *Magnetism: Fundamentals*, Springer (2005).

Ewald, P., Die Berechnung optischer und elektrostatischer Gitterpotentiale, Ann. Phys. **369**, 253 (1921).

Fauqué, B., Sidis, Y., Hinkov, V., Pailhès, S., Lin, C. T., Chaud, X. and Bourges, P., Magnetic Order in the Pseudogap Phase of High-T_C Superconductors, Phys. Rev. Lett. **96**, 197001 (2006), URL.

Ferrero, M. and Parcollet, O., TRIQS: a Toolbox for Research in Interacting Quantum Systems (2011), URL.

Feyerherm, R., Amato, A., Grayevsky, A., Gygax, F., Kaplan, N. and Schenck, A., Crystal electric field next to a hydrogen-like interstitial + in PrNi5, Zeitschrift für Physik B Condensed Matter **99**, 3 (1995), URL.

Fujimori, A., Hase, I., Namatame, H., Fujishima, Y., Tokura, Y., Eisaki, H., Uchida, S., Takegahara, K. and de Groot, F. M. F., Evolution of the spectral function in Mott-Hubbard systems with d^1 configuration, Phys. Rev. Lett. **69**, 1796 (1992), URL.

Georges, A., Strongly Correlated Electron Materials: Dynamical Mean-Field Theory and Electronic Structure, AIP Conference Proceedings **715**, 3 (2004), URL.

Georges, A., Kotliar, G., Krauth, W. and Rozenberg, M. J., Dynamical mean-field theory of strongly correlated fermion systems and the limit of infinite dimensions, Rev. Mod. Phys. **68**, 13 (1996), URL.

Georges, A., Medici, L. d. and Mravlje, J., Strong Correlations from Hunds Coupling, Annu. Rev. Condens. Matter Phys. **4**, 137 (2013), URL.

Giannozzi, P., Baroni, S., Bonini, N., Calandra, M., Car, R., Cavazzoni, C., Ceresoli, D., Chiarotti, G. L., Cococcioni, M., Dabo, I., Dal Corso, A., de Gironcoli, S., Fabris, S., Fratesi, G., Gebauer, R., Gerstmann, U., Gougoussis, C., Kokalj, A., Lazzeri, M., Martin-Samos, L., Marzari, N., Mauri, F., Mazzarello, R., Paolini, S., Pasquarello, A., Paulatto, L., Sbraccia, C., Scandolo, S., Sclauzero, G., Seitsonen, A. P., Smogunov, A., Umari, P. and Wentzcovitch, R. M., QUANTUM ESPRESSO: a modular and open-source software project for quantum simulations of materials, Journal of Physics: Condensed Matter **21**, 395502 (19pp) (2009), URL.

Glazer, A. M., The classification of tilted octahedra in perovskites, Acta Crystallographica Section B **28**, 3384 (1972), URL.

Goodenough, J. B., An interpretation of the magnetic properties of the perovskite-type mixed crystals $La_{1-x}Sr_xCoO_{3-\lambda}$, Journal of Physics and Chemistry of Solids **6**, 287 (1958), URL.

Gull, E., Millis, A. J., Lichtenstein, A. I., Rubtsov, A. N., Troyer, M. and Werner, P., Continuous-time Monte Carlo methods for quantum impurity models, Rev. Mod. Phys. **83**, 349 (2011), URL.

Gutzwiller, M. C., Effect of Correlation on the Ferromagnetism of Transition Metals, Phys. Rev. Lett. **10**, 159 (1963), URL.

Haule, K., Quantum Monte Carlo impurity solver for cluster dynamical mean-field theory and electronic structure calculations with adjustable cluster base, Phys. Rev. B **75**, 155113 (2007), URL.

Haule, K., Yee, C.-H. and Kim, K., Dynamical mean-field theory within the full-potential methods: Electronic structure of $CeIrIn_5$, $CeCoIn_5$, and $CeRhIn_5$, Phys. Rev. B **81**, 195107 (2010).

Held, K., Electronic structure calculations using dynamical mean field theory, Advances in physics **56**, 829 (2007), URL.

Held, K., Nekrasov, I. A., Keller, G., Eyert, V., Bluemer, N., McMahan, A. K., Scalettar, R. T., Pruschke, T., Anisimov, V. I. and Vollhardt, D., Realistic investigations of correlated electron systems with LDA + DMFT, Phys. Status Solidi **243**, 2599 (2006), URL.

Held, K. and Vollhardt, D., Microscopic conditions favoring itinerant ferromagnetism: Hund's rule coupling and orbital degeneracy, Eur. Phys. J. B **5**, 473 (1998), URL.

Hewson, A., *The Kondo Problem to Heavy Fermions*, Cambridge Studies in Magnetism, Cambridge University Press (1997), URL.

Hirsch, J. E., Two-dimensional Hubbard model: Numerical simulation study, Phys. Rev. B **31**, 4403 (1985), URL.

Hirsch, J. E. and Fye, R. M., Monte Carlo Method for Magnetic Impurities in Metals, Phys. Rev. Lett. **56**, 2521 (1986), URL.

Hohenberg, P. and Kohn, W., Inhomogeneous Electron Gas, Phys. Rev. **136**, B864 (1964), URL.

Hubbard, J., Electron Correlations in Narrow Energy Bands, Proc. Phys. Soc. London, Series A **276**, 238 (1963), URL.

Hwang, H. Y., Iwasa, Y., Kawasaki, M., Keimer, B., Nagaosa, N. and Tokura, Y., Emergent phenomena at oxide interfaces, Nature Materials **11**, 103 (2012), URL.

Hybertsen, M. S., Schlüter, M. and Christensen, N. E., Calculation of Coulomb-interaction parameters for La_2CuO_4 using a constrained-density-functional approach, Phys. Rev. B **39**, 9028 (1989), URL.

Imada, M., Fujimori, A. and Tokura, Y., Metal-insulator transitions, Rev. Mod. Phys. **70**, 1039 (1998), URL.

Jarrell, M. and Gubernatis, J., Bayesian inference and the analytic continuation of imaginary-time quantum Monte Carlo data, Physics Reports **269**, 133 (1996), URL.

Jarrell, M., Maier, T., Hettler, M. and Tahvildarzadeh, A., Phase diagram of the Hubbard model: Beyond the dynamical mean field, EPL (Europhysics Letters) **56**, 563 (2001), URL.

Jin, S., Tiefel, T. H., McCormack, M., Fastnacht, R., Ramesh, R. and Chen, L., Thousandfold change in resistivity in magnetoresistive La-Ca-Mn-O films, Science **264**, 413 (1994), URL.

Jones, C. W., Battle, P. D., Lightfoot, P. and Harrison, W. T. A., The structure of $SrRuO_3$ by time-of-flight neutron powder diffraction, Acta Crystallographica Section C **45**, 365 (1989), URL.

Jonker, G. and Van Santen, J., Ferromagnetic compounds of manganese with perovskite structure, Physica **16**, 337 (1950), URL.

Kanamori, J., Superexchange interaction and symmetry properties of electron orbitals, Journal of Physics and Chemistry of Solids **10**, 87 (1959), URL.

Kanamori, J., Electron correlation and ferromagnetism of transition metals, Progress of Theoretical Physics **30**, 275 (1963), URL.

Karolak, M., Ulm, G., Wehling, T., Mazurenko, V., Poteryaev, A. and Lichtenstein, A., Double counting in LDA plus DMFT-The example of NiO, Journal of Electron Spectroscopy and Related Phenomena **181**, 11 (2010).

Kohn, W. and Sham, L. J., Self-Consistent Equations Including Exchange and Correlation Effects, Phys. Rev. **140**, A1133 (1965), URL.

Kostic, P., Okada, Y., Collins, N. C., Schlesinger, Z., Reiner, J. W., Klein, L., Kapitulnik, A., Geballe, T. H. and Beasley, M. R., Non-Fermi-Liquid Behavior of $SrRuO_3$: Evidence from Infrared Conductivity, Phys. Rev. Lett. **81**, 2498 (1998), URL.

Kotliar, G., Savrasov, S. Y., Haule, K. et al., Electronic structure calculations with dynamical mean-field theory, Rev. Mod. Phys. **78**, 865 (2006).

Kotliar, G., Savrasov, S. Y., Pálsson, G. and Biroli, G., Cellular Dynamical Mean Field Approach to Strongly Correlated Systems, Phys. Rev. Lett. **87**, 186401 (2001), URL.

Kourkoutis, L. F., Xin, H., Higuchi, T., Hotta, Y., Lee, J., Hikita, Y., Schlom, D., Hwang, H. and Muller, D., Atomic-resolution spectroscopic imaging of oxide interfaces, Philosophical Magazine **90**, 4731 (2010), URL.

Kresse, G. and Furthmüller, J., Efficiency of ab-initio total energy calculations for metals and semiconductors using a plane-wave basis set, Comput. Mat. Sci. **6**, 15 (1996).

Kresse, G. and Furthmüller, J., Efficient iterative schemes for ab initio total-energy calculations using a plane-wave basis set, Phys. Rev. B **54**, 11169 (1996).

Kresse, G. and Hafner, J., Ab initio molecular dynamics for liquid metals, Phys. Rev. B **47**, 558 (1993).

Kresse, G. and Joubert, D., From ultrasoft pseudopotentials to the projector augmented-wave method, Phys. Rev. B **59**, 1758 (1999).

Kunes, J., Anisimov, V. I., Lukoyanov, A. V. and Vollhardt, D., Local correlations and hole doping in NiO: A dynamical mean-field study, Phys. Rev. B **75**, 165115 (2007), URL.

Lee, Y. S., Yu, J., Lee, J. S., Noh, T. W., Gimm, T.-H., Choi, H.-Y. and Eom, C. B., Non-Fermi liquid behavior and scaling of the low-frequency suppression in the optical conductivity spectra of $CaRuO_3$, Phys. Rev. B **66**, 041104 (2002), URL.

Li, L., Richter, C., Mannhart, J. and Ashoori, R. C., Coexistence of magnetic order and two-dimensional superconductivity at LaAlO3/SrTiO3 interfaces, Nat Phys **7**, 762 (2011), URL.

Li, Y., V Balédent, N. B., Cho, Y., Fauqué, B., Sidis, Y., Yu, G., Zhao, X. and P Bourges, M. G., Unusual magnetic order in the pseudogap region of the superconductor HgBa2CuO4+ &dgr, Nature **455**, 372 (2008), URL.

Lichtenstein, A. I. and Katsnelson, M. I., Ab initio calculations of quasiparticle band structure in correlated systems: LDA++ approach, Phys. Rev. B **57**, 6884 (1998), URL.

Lichtenstein, A. I., Katsnelson, M. I. and Kotliar, G., Finite-Temperature Magnetism of Transition Metals: An *ab initio* Dynamical Mean-Field Theory, Phys. Rev. Lett. **87**, 067205 (2001), URL.

Lieb, E. and Mattis, D., Theory of Ferromagnetism and the Ordering of Electronic Energy Levels, Phys. Rev. **125**, 164 (1962), URL.

Lieb, E. H. and Wu, F. Y., Absence of Mott Transition in an Exact Solution of the Short-Range, One-Band Model in One Dimension, Phys. Rev. Lett. **20**, 1445 (1968), URL.

Longo, J. M., Raccah, P. M. and Goodenough, J. B., Magnetic Properties of $SrRuO_3$ and $CaRuO_3$, Journal of Applied Physics **39**, 1327 (1968), URL.

Löwdin, P.-O., A Note on the Quantum-Mechanical Perturbation Theory, The Journal of Chemical Physics **19**, 1396 (1951), URL.

Lüders, U., Sheets, W. C., David, A., Prellier, W. and Fresard, R., Room-temperature magnetism in $LaVO_3/SrVO_3$ superlattices by geometrically confined doping, Phys. Rev. B **80**, 241102 (2009), URL.

MacDougall, G. J., Aczel, A. A., Carlo, J. P., Ito, T., Rodriguez, J., Russo, P. L., Uemura, Y. J., Wakimoto, S. and Luke, G. M., Absence of Broken Time-Reversal

Symmetry in the Pseudogap State of the High Temperature $La_{2-x}Sr_xCuO_4$ Superconductor from Muon-Spin-Relaxation Measurements, Phys. Rev. Lett. **101**, 017001 (2008), URL.

Maier, T., Jarrell, M., Pruschke, T. and Hettler, M. H., Quantum cluster theories, Rev. Mod. Phys. **77**, 1027 (2005), URL.

Maiti, K. and Sarma, D. D., Spectroscopic investigations of the electronic structure and metal-insulator transitions in a Mott-Hubbard system $La_{1-x}Ca_xVO_3$, Phys. Rev. B **61**, 2525 (2000), URL.

Mannhart, J., Blank, D., Hwang, H., Millis, A. and Triscone, J.-M., Two-dimensional electron gases at oxide interfaces, MRS bulletin **33**, 1027 (2008), URL.

Martin, R., *Electronic Structure: Basic Theory and Practical Methods*, Cambridge University Press (2004), URL.

Marzari, N., Mostofi, A. A., Yates, J. R., Souza, I. and Vanderbilt, D., Maximally localized Wannier functions: Theory and applications, Rev. Mod. Phys. **84**, 1419 (2012), URL.

Marzari, N. and Vanderbilt, D., Maximally localized generalized Wannier functions for composite energy bands, Phys. Rev. B **56**, 12847 (1997), URL.

Millis, A., Towards a classification of the effects of disorder on materials properties, Solid State Communications **126**, 3 (2003), URL, proceedings of the High-Tc Superconductivity Workshop.

Millis, A. J., Oxide interfaces: Moment of magnetism, Nature Physics **7**, 749 (2011), URL.

Miyake, T. and Aryasetiawan, F., Screened Coulomb interaction in the maximally localized Wannier basis, Phys. Rev. B **77**, 085122 (2008), URL.

Miyasaka, S., Okuda, T. and Tokura, Y., Critical Behavior of Metal-Insulator Transition in $La_{1-x}Sr_xVO_3$, Phys. Rev. Lett. **85**, 5388 (2000), URL.

Momma, K. and Izumi, F., *VESTA3* for three-dimensional visualization of crystal, volumetric and morphology data, Journal of Applied Crystallography **44**, 1272 (2011), URL.

Mook, H. A., Sidis, Y., Fauqué, B., Balédent, V. and Bourges, P., Observation of magnetic order in a superconducting $YBa_2Cu_3O_{6.6}$ single crystal using polarized neutron scattering, Phys. Rev. B **78**, 020506 (2008), URL.

Morikawa, K., Mizokawa, T., Fujimori, A., Taguchi, Y. and Tokura, Y., Photoemission spectral weight distribution in $Y_{1-x}Ca_xTiO_3$, Phys. Rev. B **54**, 8446 (1996), URL.

Mostofi, A. A., Yates, J. R., Lee, Y.-S., Souza, I., Vanderbilt, D. and Marzari, N., wannier90: A tool for obtaining maximally-localised Wannier functions, Computer Physics Communications **178**, 685 (2008), URL.

Mott, N. F., The Basis of the Electron Theory of Metals, with Special Reference to the Transition Metals, Proc. Phys. Soc. A **62**, 416 (1949), URL.

Mott, N. F. and Peierls, R., Discussion of the paper by de Boer and Verwey, Proceedings of the Physical Society **49**, 72 (1937), URL.

Müller-Hartmann, E., Ferromagnetism in Hubbard models: Low density route, Journal of low temperature physics **99**, 349 (1995), URL.

Nagaoka, Y., Ferromagnetism in a Narrow, Almost Half-Filled s Band, Phys. Rev. **147**, 392 (1966), URL.

Nekrasov, I. A., Held, K., Keller, G., Kondakov, D. E., Pruschke, T., Kollar, M., Andersen, O. K., Anisimov, V. I. and Vollhardt, D., Momentum-resolved spectral functions of $SrVO3$ calculated by $LDA+DMFT$, Phys. Rev. B **73**, 155112 (2006).

Ohtomo, A. and Hwang, H., A high-mobility electron gas at the $LaAlO_3/SrTiO_3$ heterointerface, Nature **427**, 423 (2004), URL.

Okamoto, S. and Millis, A. J., Electronic reconstruction at an interface between a Mott insulator and a band insulator, Nature **428**, 630 (2004), URL.

Okamoto, S., Millis, A. J. and Spaldin, N. A., Lattice Relaxation in Oxide Heterostructures: $LaTiO3/SrTiO3$ Superlattices, Phys. Rev. Lett. **97**, 056802 (2006).

Orenstein, J., Thomas, G. A., Millis, A. J., Cooper, S. L., Rapkine, D. H., Timusk, T., Schneemeyer, L. F. and Waszczak, J. V., Frequency- and temperature-dependent conductivity in $YBa_2Cu_3O_{6+x}$ crystals, Phys. Rev. B **42**, 6342 (1990), URL.

Park, H., Haule, K., Marianetti, C. A. and Kotliar, G., Dynamical mean-field theory study of Nagaoka ferromagnetism, Phys. Rev. B **77**, 035107 (2008), URL.

Parragh, N., Toschi, A., Held, K. and Sangiovanni, G., Conserved quantities of $SU(2)$-invariant interactions for correlated fermions and the advantages for quantum Monte Carlo simulations, Phys. Rev. B **86**, 155158 (2012), URL.

Pavarini, E., Biermann, S., Poteryaev, A., Lichtenstein, A. I., Georges, A. and Andersen, O. K., Mott Transition and Suppression of Orbital Fluctuations in Orthorhombic $3d^1$ Perovskites, Phys. Rev. Lett. **92**, 176403 (2004), URL.

Pavarini, E., Koch, E., Anders, F. and Jarrell, M., *Correlated Electrons: From Models to Materials*, Schriften des Forschungszentrums Jülich / Reihe Modeling and Simulation, Forschungszentrum Jülich, Zentralbibliothek, Verlag (2012), URL.

Pavarini, E., Yamasaki, A., Nuss, J. and Andersen, O. K., How chemistry controls electron localization in 3d 1 perovskites: a Wannier-function study, New Journal of Physics **7**, 188 (2005), URL.

Peters, R., Kawakami, N. and Pruschke, T., Orbital order, metal-insulator transition, and magnetoresistance effect in the two-orbital Hubbard model, Phys. Rev. B **83**, 125110 (2011), URL.

Peters, R. and Pruschke, T., Orbital and magnetic order in the two-orbital Hubbard model, Phys. Rev. B **81**, 035112 (2010), URL.

Pourovskii, L. V., Kotliar, G., Katsnelson, M. I. and Lichtenstein, A. I., Dynamical mean-field theory investigation of specific heat and electronic structure of α- and δ-plutonium, Phys. Rev. B **75**, 235107 (2007), URL.

Pruschke, T. and Grewe, N., The Anderson model with finite Coulomb repulsion, Zeitschrift für Physik B Condensed Matter **74**, 439 (1989), URL.

Rey, M., Dehaudt, P., Joubert, J., Lambert-Andron, B., Cyrot, M. and Cyrot-Lackmann, F., Preparation and structure of the compounds $SrVO_3$ and Sr_2VO_4, Journal of Solid State Chemistry **86**, 101 (1990), URL.

Reyren, N., Thiel, S., Caviglia, A. D., Kourkoutis, L. F., Hammerl, G., Richter, C., Schneider, C. W., Kopp, T., Ruetschi, A.-S., Jaccard, D., Gabay, M., Muller, D. A., Triscone, J.-M. and Mannhart, J., Superconducting Interfaces Between Insulating Oxides, Science **317**, 1196 (2007), URL.

Rotella, H., Lüders, U., Janolin, P.-E., Dao, V. H., Chateigner, D., Feyerherm, R., Dudzik, E. and Prellier, W., Octahedral tilting in strained $LaVO_3$ thin films, Phys. Rev. B **85**, 184101 (2012), URL.

Sakai, H., Ishiwata, S., Okuyama, D., Nakao, A., Nakao, H., Murakami, Y., Taguchi, Y. and Tokura, Y., Electron doping in the cubic perovskite $SrMnO_3$: Isotropic metal versus chainlike ordering of Jahn-Teller polarons, Phys. Rev. B **82**, 180409 (2010), URL.

Sekiyama, A., Fujiwara, H., Imada, S., Suga, S., Eisaki, H., Uchida, S. I., Takegahara, K., Harima, H., Saitoh, Y., Nekrasov, I. A., Keller, G., Kondakov, D. E., Kozhevnikov, A. V., Pruschke, T., Held, K., Vollhardt, D. and Anisimov, V. I., Mutual Experimental and Theoretical Validation of Bulk Photoemission Spectra of $Sr1 - xCaxVO3$, Phys. Rev. Lett. **93**, 156402 (2004).

Shastry, B. S., Krishnamurthy, H. R. and Anderson, P. W., Instability of the Nagaoka ferromagnetic state of the $U{=}\infty$ Hubbard model, Phys. Rev. B **41**, 2375 (1990), URL.

Shekhter, A., Shu, L., Aji, V., MacLaughlin, D. E. and Varma, C. M., Screening of Point Charge Impurities in Highly Anisotropic Metals: Application to μ+-Spin Relaxation in Underdoped Cuprate Superconductors, Phys. Rev. Lett. **101**, 227004 (2008).

Slater, J., *Quantum theory of atomic structure. 1 (1960)*, International series in pure and applied physics, McGraw-Hill Interamericana (1960), URL.

Slater, J. C. and Koster, G. F., Simplified LCAO Method for the Periodic Potential Problem, Phys. Rev. **94**, 1498 (1954), URL.

Sonier, J., Brewer, J., Kiefl, R., Miller, R., Morris, G., Stronach, C., Gardner, J., Dunsiger, S., Bonn, D., Hardy, W. et al., Anomalous weak magnetism in superconducting YBa2Cu3O6+ x, Science **292**, 1692 (2001), URL.

Sonier, J. E., Pacradouni, V., Sabok-Sayr, S. A., Hardy, W. N., Bonn, D. A., Liang, R. and Mook, H. A., Detection of the Unusual Magnetic Orders in the Pseudogap

Region of a High-Temperature Superconducting $YBa_2Cu_3\mathbf{O}_{6.6}$ Crystal by Muon-Spin Relaxation, Phys. Rev. Lett. **103**, 167002 (2009), URL.

Souza, I., Marzari, N. and Vanderbilt, D., Maximally localized Wannier functions for entangled energy bands, Phys. Rev. B **65**, 035109 (2001), URL.

Stoner, E. C., Collective electron ferromagnetism, Proceedings of the Royal Society of London. Series A, Mathematical and Physical Sciences **165**, 372 (1938), URL.

Ulmke, M., Ferromagnetism in the Hubbard model on fcc-type lattices, The European Physical Journal B-Condensed Matter and Complex Systems **1**, 301 (1998), URL.

Varma, C. M., Non-Fermi-liquid states and pairing instability of a general model of copper oxide metals, Phys. Rev. B **55**, 14554 (1997), URL.

Varma, C. M., Theory of the pseudogap state of the cuprates, Phys. Rev. B **73**, 155113 (2006), URL.

Vaugier, L., Jiang, H. and Biermann, S., Hubbard U and Hund exchange J in transition metal oxides: Screening versus localization trends from constrained random phase approximation, Phys. Rev. B **86**, 165105 (2012), URL.

Vollhardt, D., Blümer, N., Held, K. and Kollar, M., *Band-Ferromagnetism: Ground-State and Finite-Temperature Phenomena, Vol. 580 of Lecture Notes in Physics*, chap. Metallic Ferromagnetism An Electronic Correlation Phenomenon, p. 191, Springer, New York (2001), edited by K. Baberschke, M. Donath, and W. Nolting, arXiv:cond-mat/0012203.

Vollhardt, D., Blümer, N., Held, K., Kollar, M., Schlipf, J. and Ulmke, M., Non-perturbative approaches to magnetism in strongly correlated electron systems, Zeitschrift für Physik B Condensed Matter **103**, 283 (1997), URL.

Vollhardt, D., Blümer, N., Held, K., Kollar, M., Schlipf, J., Ulmke, M. and Wahle, J., Metallic ferromagnetism: Progress in our understanding of an old strong-coupling problem, in Advances in Solid State Physics 38, pp. 383–396, Springer (1999), URL.

Wahle, J., Blümer, N., Schlipf, J., Held, K. and Vollhardt, D., Microscopic conditions favoring itinerant ferromagnetism, Phys. Rev. B **58**, 12749 (1998), URL.

Wang, X., Gull, E., de' Medici, L., Capone, M. and Millis, A. J., Antiferromagnetism and the gap of a Mott insulator: Results from analytic continuation of the self-energy, Phys. Rev. B **80**, 045101 (2009), URL.

Wang, X., Han, M. J., de' Medici, L., Park, H., Marianetti, C. A. and Millis, A. J., Covalency, double-counting, and the metal-insulator phase diagram in transition metal oxides, Phys. Rev. B **86**, 195136 (2012), URL.

Werner, P., Comanac, A., de' Medici, L., Troyer, M. and Millis, A. J., Continuous-Time Solver for Quantum Impurity Models, Phys. Rev. Lett. **97**, 076405 (2006), URL.

Werner, P., Gull, E. and Millis, A. J., Metal-insulator phase diagram and orbital selectivity in three-orbital models with rotationally invariant Hund coupling, Phys. Rev. B **79**, 115119 (2009), URL.

Werner, P., Gull, E., Troyer, M. and Millis, A. J., Spin Freezing Transition and Non-Fermi-Liquid Self-Energy in a Three-Orbital Model, Phys. Rev. Lett. **101**, 166405 (2008), URL.

Werner, P. and Millis, A. J., Hybridization expansion impurity solver: General formulation and application to Kondo lattice and two-orbital models, Phys. Rev. B **74**, 155107 (2006), URL.

Wikipedia, Analytic continuation (2013), URL, [Online; accessed 03:08, 10 April 2013].

Wilson, K. G., The renormalization group: Critical phenomena and the Kondo problem, Rev. Mod. Phys. **47**, 773 (1975), URL.

Wolfram, T. and Ellialtioglu, S., *Electronic and Optical Properties of D-Band Perovskites*, Cambridge University Press (2006), URL.

Yoshimatsu, K., Horiba, K., Kumigashira, H., Yoshida, T., Fujimori, A. and Oshima, M., Metallic Quantum Well States in Artificial Structures of Strongly Correlated Oxide, Science **333**, 319 (2011), URL.

Yoshimatsu, K., Okabe, T., Kumigashira, H., Okamoto, S., Aizaki, S., Fujimori, A. and Oshima, M., Dimensional-Crossover-Driven Metal-Insulator Transition in $SrVO_3$ Ultrathin Films, Phys. Rev. Lett. **104**, 147601 (2010), URL.

Zaanen, J., Sawatzky, G. A. and Allen, J. W., Band gaps and electronic structure of transition-metal compounds, Phys. Rev. Lett. **55**, 418 (1985), URL.

Zgid, D., Gull, E. and Chan, G. K.-L., Truncated configuration interaction expansions as solvers for correlated quantum impurity models and dynamical mean-field theory, Phys. Rev. B **86**, 165128 (2012), URL.

Zhang, F. C. and Rice, T. M., Effective Hamiltonian for the superconducting Cu oxides, Phys. Rev. B **37**, 3759 (1988), URL.

Appendix A

Derivation of the onsite Coulomb interaction

In this appendix, we present in details the derivation of the onsite interaction H_{onsite} (2.21) by using Slater's integrals and the connection to the form with Kanamori's notations.

As in Section 2.2, the general Coulomb interaction in the second quantization representation is

$$\begin{aligned} H &= \frac{1}{2}\sum_{\sigma\sigma'}\int d^3r \int d^3r' \Psi^\dagger_\sigma(\mathbf{r})\Psi^\dagger_{\sigma'}(\mathbf{r}')V(\mathbf{r},\mathbf{r}')\Psi_{\sigma'}(\mathbf{r}')\Psi_\sigma(\mathbf{r}) \\ &= \frac{1}{2}\sum_{\alpha\beta,\gamma\delta} V_{\alpha\beta,\gamma\delta} c^\dagger_{\alpha\sigma} c^\dagger_{\beta\sigma'} c_{\gamma\sigma'} c_{\delta\sigma}, \end{aligned} \tag{A.1}$$

where the Coulomb matrix is

$$V_{\alpha\beta,\gamma\delta} = \int d^3r \int d^3r' \psi^\dagger_{\alpha\sigma}(\mathbf{r})\psi^\dagger_{\beta\sigma'}(\mathbf{r}')V(\mathbf{r},\mathbf{r}')\psi_{\gamma\sigma'}(\mathbf{r}')\Psi_{\delta\sigma}(\mathbf{r}). \tag{A.2}$$

The notation here is slightly different from Section 2.2 where $\alpha, \beta, \gamma, \delta$ are indices for both site and orbital to simplify the formulas. From Slater (1960), $V(\mathbf{r},\mathbf{r}')$ is assumed to be spherically symmetric, i.e. $V(\mathbf{r},\mathbf{r}') = V(|\mathbf{r}-\mathbf{r}'|)$, one can expand it in terms of spherical harmonics $Y_{lm}(\theta,\phi)$. For simplicity, assume that $V(\mathbf{r},\mathbf{r}')$ has the form in

free space $V(\mathbf{r},\mathbf{r}') = \dfrac{1}{|r-r'|}$

$$\frac{1}{|r-r'|} = \sum_{k=0}^{\infty}\sum_{m=-k}^{k}\frac{4\pi}{(2k+1)}\frac{r_<^k}{r_>^{k+1}}Y_{km}^*(\theta',\phi')Y_{km}(\theta,\phi). \tag{A.3}$$

where the notation $r_<$ ($r_>$) is the smaller (larger) of r and r'.

With $\alpha = (n,l,m)$, single-particle wavefunctions (without spin part) can be written as

$$\psi_\alpha(r) = R_{inl}(r)Y_{lm}(\theta,\phi). \tag{A.4}$$

here the index $\alpha = (i,n,l,m)$ contains the site index i and the three indices similar to the one used in eigenstates of electron in hydrogen atom.

Combined (A.3) and (A.4), the Coulomb matrix becomes

$$V_{\alpha\beta,\gamma\delta} = \sum_{k=0}^{\infty}\sum_{m=-k}^{k}R^{(k)}_{\alpha\beta,\gamma\delta}Y^{(k,m)}_{\alpha\beta,\gamma\delta}, \tag{A.5}$$

where $\hat{r} = (\theta,\phi)$

$$R^{(k)}_{\alpha\beta,\gamma\delta} = \int dr r^2 \int dr' r'^2 R^*_{i_\alpha n_\alpha l_\alpha}(r)R^*_{i_\beta n_\beta l_\beta}(r')R_{i_\gamma n_\gamma l_\gamma}(r')R_{i_\delta n_\delta l_\delta}(r)\frac{r_<^k}{r_>^{k+1}}, \tag{A.6}$$

and

$$\begin{aligned}
Y^{(k,m)}_{\alpha\beta,\gamma\delta} &= \frac{4\pi}{(2k+1)}\int d\hat{r}d\hat{r}' Y^*_{l_\alpha m_\alpha}(\hat{r})Y^*_{l_\beta m_\beta}(\hat{r}')Y^*_{km}(\hat{r}')Y_{km}(\hat{r})Y_{l_\gamma m_\gamma}(\hat{r}')Y_{l_\delta m_\delta}(\hat{r}) \\
&= \sqrt{\frac{4\pi}{(2k+1)}}\int d\hat{r}Y^*_{l_\alpha m_\alpha}(\hat{r})Y_{km}(\hat{r})Y_{l_\delta m_\delta}(\hat{r})\times \\
&\times\sqrt{\frac{4\pi}{(2k+1)}}\int d\hat{r}'Y^*_{l_\beta m_\beta}(\hat{r}')Y^*_{km}(\hat{r}')Y_{l_\gamma m_\gamma}(\hat{r}') \\
&= \delta_{m,m_\alpha-m_\delta}\delta_{m,m_\gamma-m_\beta}c^{(k)}_{l_\alpha m_\alpha,l_\delta m_\delta}c^{(k)*}_{l_\gamma m_\gamma,l_\beta m_\beta}.
\end{aligned} \tag{A.7}$$

The Kronecker δ occurs after integrating the azimuth angle ϕ. $c^{(k)}_{lm,l'm'}$ is the Gaunt's number, defined as

$$c^{(k)}_{lm,l'm'} = \sqrt{\frac{4\pi}{(2k+1)}} \int d\hat{r} Y^*_{lm}(\hat{r}) Y_{km}(\hat{r}) Y_{l'm'}(\hat{r}). \tag{A.8}$$

In solids, the Coulomb interaction is strongly screened by nearby electrons, the on-site interaction is the most important while off-site interaction is ignored, thus all site index can be neglected for simplicity. On the other hand, Coulomb interaction between orbitals with different shell n or angular momentum l is small, we focus on the interaction acting on orbitals of the same angular momentum, thus $l_\alpha = l$ and $n_\alpha = n$ and are neglected in the next formulas. Therefore, we rewrite (A.6) as

$$R^{(k)}_{\alpha\beta,\gamma\delta} = F_k. \tag{A.9}$$

F_k are Slater integrals, which are usually real numbers because the radial parts of the wavefunctions are real.

The expression for the Coulomb matrix elements for given l thus becomes $V_{\alpha\beta,\gamma\delta} \rightarrow V_{m_1 m_2; m_3 m_4}$

$$V_{m_1 m_2; m_3 m_4} = \sum_{k=0}^{\infty} \sum_{m=-k}^{k} \delta_{m,m_1-m_4} \delta_{m,m_3-m_2} F_k c^{(k)}_{lm_1,lm_4} c^{(k)*}_{lm_3,lm_2}. \tag{A.10}$$

$$H = \frac{1}{2} \sum V_{m_1 m_2; m_3 m_4} c^\dagger_{m_1\sigma} c^\dagger_{m_2\sigma'} c_{m_3\sigma'} c_{m_4\sigma}. \tag{A.11}$$

Eq. (A.10) is still complicated even though only one value of l is considered. To be more simplified, one can consider diagonal terms of the matrix (density-density interactions) and some important off-diagonal terms (exchange and pair-hopping terms),

other terms are neglected. The Hamiltonian thus becomes

$$\begin{aligned} H =& \frac{1}{2} \sum_{mm',\sigma\sigma'} V_{mm',m'm} c^{\dagger}_{m\sigma} c^{\dagger}_{m'\sigma'} c_{m'\sigma'} c_{m\sigma} \\ &+ \frac{1}{2} \sum_{m\neq m',\sigma\sigma'} V_{mm',mm'} c^{\dagger}_{m\sigma} c^{\dagger}_{m'\sigma'} c_{m\sigma'} c_{m'\sigma} \\ &+ \frac{1}{2} \sum_{m\neq m',\sigma\sigma'} V_{mm,m'm'} c^{\dagger}_{m\sigma} c^{\dagger}_{m\sigma'} c_{m'\sigma'} c_{m'\sigma}. \end{aligned} \tag{A.12}$$

The second and third terms of (A.12) have $m \neq m'$, if not then the terms $V_{mm,mm} c^{\dagger}_{m\sigma} c^{\dagger}_{m\sigma'} c_{m\sigma'} c_{m\sigma}$ would be counted three times.

Detailed calculations (using Mathematica program) give

$$U_{mm'} = V_{mm',m'm}$$

$$= \begin{pmatrix} & xy & yz & 3z^2-r^2 & xz & x^2-y^2 \\ xy & U & U-2J_1 & U-2J_2 & U-2J_1 & U-2J_3 \\ yz & U-2J_1 & U & U-2J_4 & U-2J_1 & U-2J_1 \\ 3z^2-r^2 & U-2J_2 & U-2J_4 & U & U-2J_4 & U-2J_2 \\ xz & U-2J_1 & U-2J_1 & U-2J_4 & U & U-2J_1 \\ x^2-y^2 & U-2J_3 & U-2J_1 & U-2J_2 & U-2J_1 & U \end{pmatrix}, \tag{A.13}$$

and

$$J_{mm'} = V_{mm',mm'} = V_{mm,m'm'}$$

$$= \begin{pmatrix} & xy & yz & 3z^2-r^2 & xz & x^2-y^2 \\ xy & U & J_1 & J_2 & J_1 & J_3 \\ yz & J_1 & U & J_4 & J_1 & J_1 \\ 3z^2-r^2 & J_2 & J_4 & U & J_4 & J_2 \\ xz & J_1 & J_1 & J_4 & U & J_1 \\ x^2-y^2 & J_3 & J_1 & J_2 & J_1 & U \end{pmatrix}, \tag{A.14}$$

where, using notations from Pavarini et al. (2012)

$$\begin{aligned} U &= U_{avg} + \frac{8}{7}J_{avg}, \\ J_1 &= \frac{3}{49}F_2 + \frac{20}{441}F_4, \quad J_2 = -\frac{10}{7}J_{avg} + 3J_1, \\ J_3 &= \frac{30}{7}J_{avg} - 5J_1, \quad\quad J_4 = \frac{20}{7}J_{avg} - 3J_1, \end{aligned} \tag{A.15}$$

and U_{avg} and J_{avg} are average values for the Hubbard coefficient and Hund's coupling

$$\begin{aligned} U_{avg} &= \frac{1}{(2l+1)^2}\sum_{m,m'} U_{mm'}, \\ U_{avg} - J_{avg} &= \frac{1}{2l(2l+1)}\sum_{m,m'}(U_{mm'} - J_{mm'}). \end{aligned} \tag{A.16}$$

Eq. (A.12) thus becomes

$$\begin{aligned} H = &\frac{1}{2}\sum_{mm',\sigma\sigma'} U_{mm'} c^\dagger_{m\sigma} c^\dagger_{m'\sigma'} c_{m'\sigma'} c_{m\sigma} \\ &+ \frac{1}{2}\sum_{m\neq m',\sigma\sigma'} J_{mm'} c^\dagger_{m\sigma} c^\dagger_{m'\sigma'} c_{m\sigma'} c_{m'\sigma} \\ &+ \frac{1}{2}\sum_{m\neq m',\sigma\sigma'} J_{mm'} c^\dagger_{m\sigma} c^\dagger_{m\sigma'} c_{m'\sigma'} c_{m'\sigma}. \end{aligned} \tag{A.17}$$

The final form of the onsite interaction is

$$\begin{aligned} H = &U\sum_m n_{m\uparrow} n_{m\downarrow} + \sum_{m\neq m'} U_{mm'} n_{m\uparrow} n_{m'\downarrow} + \\ &+ \sum_{m>m'\sigma} (U_{mm'} - J_{mm'}) n_{m\sigma} n_{m'\sigma} + \\ &+ \sum_{m\neq m'} J_{mm'} c^\dagger_{m\uparrow} c^\dagger_{m'\downarrow} c_{m\downarrow} c_{m'\uparrow} + \sum_{m\neq m'} J_{mm'} c^\dagger_{m\uparrow} c^\dagger_{m\downarrow} c_{m'\downarrow} c_{m'\uparrow}, \end{aligned} \tag{A.18}$$

where $U_{mm'}$ and $J_{mm'}$ matrices are in (A.13) and (A.14), $U = U_{avg} + \frac{8}{7}J_{avg}$ as shown

in (A.15).

In the case of d system, for the $J_{mm'}$ matrix, the off-diagonal elements J_1, J_2, J_3, J_4 are close to each other and $J_i \approx 0.7J_{avg}$. If, by approximation, setting $J_i = J \approx 0.7J_{avg}$, (A.18) becomes the familiar Kanamori interaction with exchange and pair hopping terms

$$\begin{aligned} H = & U \sum_{m} n_{m\uparrow} n_{m\downarrow} + (U - 2J) \sum_{m \neq m'} n_{m\uparrow} n_{m'\downarrow} + \\ & + (U - 3J) \sum_{m > m' \sigma} n_{m\sigma} n_{m'\sigma} + \\ & + J \sum_{m \neq m'} c^{\dagger}_{m\uparrow} c^{\dagger}_{m'\downarrow} c_{m\downarrow} c_{m'\uparrow} + J \sum_{m \neq m'} c^{\dagger}_{m\uparrow} c^{\dagger}_{m\downarrow} c_{m'\downarrow} c_{m'\uparrow}. \end{aligned} \tag{A.19}$$

Moreover, if downfolding into the model containing only two e_g bands (e_g systems) or three t_{2g} bands (t_{2g} systems), (A.18) becomes the Slater-Kanamori interaction (A.19) exactly.

Rotationally invariant property of the interacting Hamiltonian is important so that the form of the interaction is unchanged under arbitrary unitary transformation of the basis, there is no ambiguity of putting U and J into d orbitals. The approximated Kanamori Hamiltonian is not but nearly rotationally invariant. However, when going to 3 t_{2g} model or 2 e_g model, the rotational invariant retained [Georges et al. (2013)]. For example, for t_{2g} bands, one can transform the Hamiltonian into

$$H = -\frac{U - 8J}{2} \hat{N} + \frac{U - 3J}{2} \hat{N}^2 - \frac{J}{2} \hat{L}^2 - 2J\hat{S}^2. \tag{A.20}$$

where $\hat{N}$, $\hat{L}$ and $\hat{S}$ are total particle number, angular momentum and total spin operators, respectively. From (A.20), it is easy to see that t_{2g} Hamiltonian is rotationally invariant. When eliminating exchange and pair hopping terms, the Hamiltonian has the form of density-density interaction and is no longer rotationally invariant.

Appendix B

Analytic continuation with MaxEnt method

In mathematics, analytic continuation is "a technique to extend the domain of a given analytic function" [Wikipedia (2013)]. In physics, the term is also used for a technique to extend a function F from a discrete sequence into a domain U in which F is analytic. The typical example is the continuation of the imaginary time (or Matsubara frequency) Green's functions to obtain the retard one analytic in the upper-half plane

$$G_R(\omega) = G(i\omega_n \to \omega + i\delta). \tag{B.1}$$

The analytic continuation works based on a theorem in complex analysis: if two functions f and g are analytic in a domain U and there exists a sequence $\{z_n\}$ converging to $z_0 \in U$ such that $f(z_n) = g(z_n)$, then $f \equiv g$ [Abrikosov et al. (1975)]. Thus for the case of the Matsubara Green's function $G(i\omega_n)$, if one finds $F(z)$ analytic in the upper-half plane such that $F(i\omega_n) = G(i\omega_n)$ for $\forall\omega_n$ then $F(z)$ is the retarded Green's function $G_R(z)$.

In a simple explanation, as

$$G(i\omega_n) = \int \frac{A(\omega)d\omega}{i\omega_n - \omega} = \mathbf{K} \cdot \mathbf{A}, \tag{B.2}$$

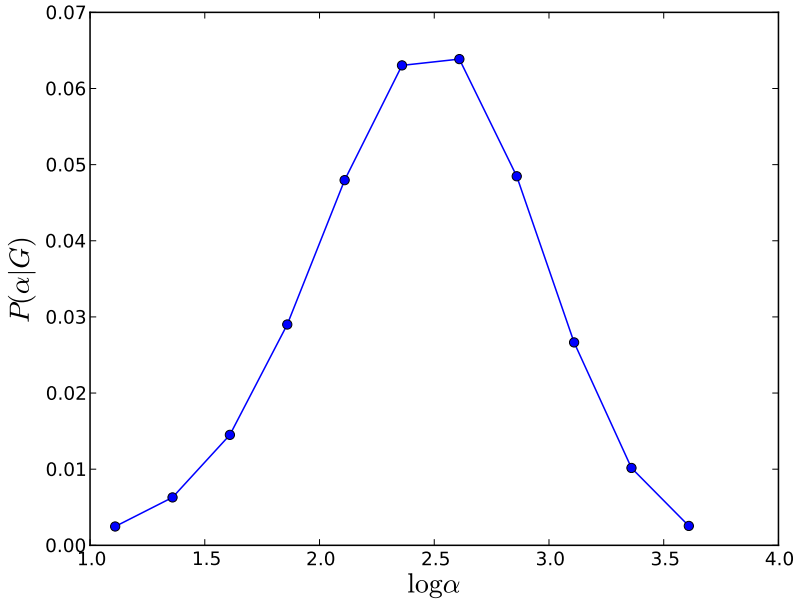

Figure B.1: An example of probability distribution $P(\alpha|G)$ of the scaling parameter α given $G(i\omega_n)$. The x axis is in $\log\alpha$.

where the spectral function $A(\omega) = -\frac{1}{\pi} ImG_R(\omega)$, if $A(\omega)$ is known, the retarded Green's function in the real axis $G_R(\omega)$ is easily obtained thanks to the Kramers-Kronig relation

$$ReG_R(\omega) = \frac{1}{\pi} \mathrm{P} \int \frac{ImG_R(x)}{x - \omega} dx. \tag{B.3}$$

Therefore, analytic continuation in this case is to solve the inverse problem (B.2) for $A(\omega)$.

However, this inverse problem is difficult to solve because the matrix $\mathbf{K}$ in (B.2) is very ill-conditioned. For example, singular value decomposition of $\mathbf{K}$ gives results from ~ 10 to 10^{-16} (the machine epsilon) after 20 singular values (consider $\beta = 10$, 50 Matsubara frequencies ω_n and 300 real frequencies ω). Brute-force inversion is thus very unstable. Maximum entropy (MaxEnt) is a popular method to obtain the spectral function $A(\omega)$. The idea of MaxEnt is to obtain $A(\omega)$ so that the probability $P(A|G)$ for $A(\omega)$ given $G(i\omega_n)$ is largest, which leads to the maximum of the probability entropy. The details of the method can be found in Jarrell and Gubernatis (1996);

Comanac (2007). In this appendix, we only present how to use MaxEnt efficiently to achieve the spectral function.

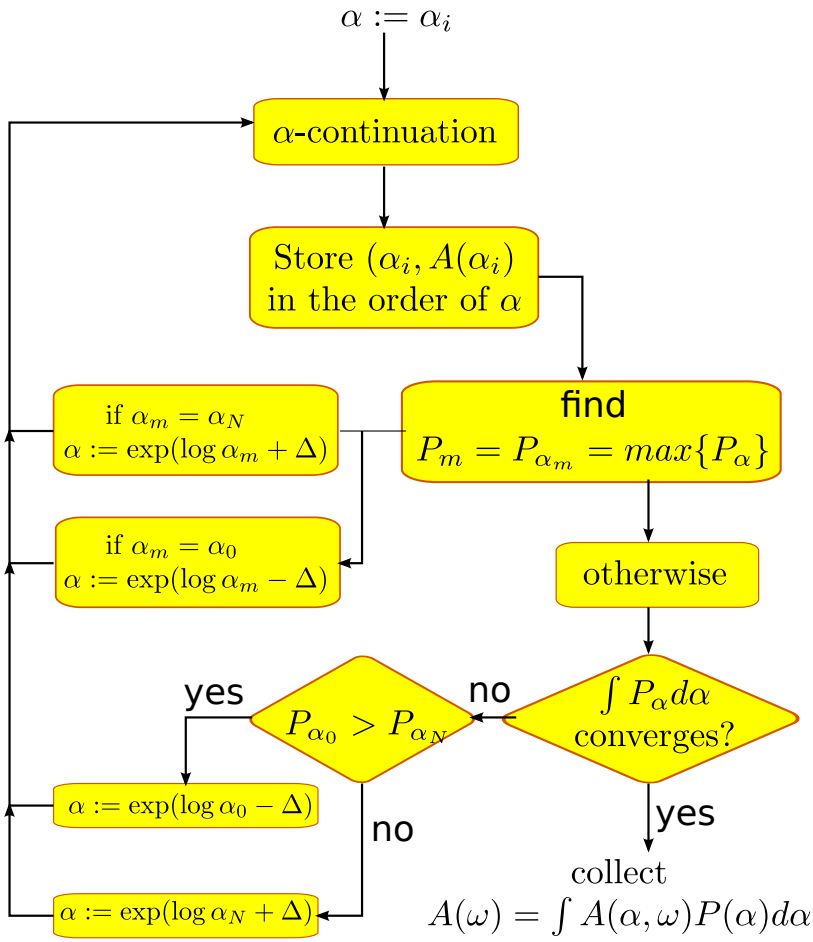

Figure B.2: Flow diagram for an efficient MaxEnt process to generate $A(\omega)$ from all $A(\alpha, \omega)$ with significant probability $P(\alpha) = P(\alpha|G)$. Notice that $(\alpha_i, A(\alpha_i)$ must be stored in an order set of α, i.e. $\alpha_i < \alpha_{i+1}$.

The probability $P(A|G)$ for $A(\omega)$ given $G(i\omega_n)$ is

$$P(A|G) = \frac{1}{Z_\alpha} \exp\left[\alpha S(A) - \frac{1}{2}\chi^2\right], \tag{B.4}$$

where $S(A)$ is the entropy and $\chi^2 = (\mathbf{K} \cdot \mathbf{A} - \mathbf{G})^T \cdot \hat{C}^{-1} \cdot (\mathbf{K} \cdot \mathbf{A} - \mathbf{G})$ with $\hat{C}$ the covariance matrix generated from the Monte Carlo sampling error of the simulation [Comanac (2007)].

For the covariance matrix $\hat{C}$, in the case where there is no Monte Carlo error stored after the simulation, the error can be estimated from the difference of the two Green's functions of two consecutive iteration $\delta G = |G_i - G_{i+1}|$. As the Green's function is nearly independent of time $\langle \delta G(\tau_i) \delta G(\tau_j) \rangle = g^2 \delta_{ij}$ [Wang et al. (2009)], it is easy to estimate the value of g. The constant g is then used in generating the covariance matrix for $G(i\omega_n)$ or $\Sigma(i\omega_n)$.

$A(\omega)$ is obtained by maximizing (B.4). The quality of $A(\omega)$ depends on the scaling parameter α. Usually $A(\omega)$ is obtained with the value of α chosen such that the probability $P(\alpha|G)$ is maximized. The proper spectral function should be

$$\bar{A}(\omega) = \int A(\alpha, \omega) P(\alpha) d\alpha \tag{B.5}$$

where $P(\alpha) = P(\alpha|G)$ has the distribution as in Fig. B.1.

Based on the robust shape of $P(\alpha|G)$ (Fig. B.1), we propose an approach to analytically continue $G(i\omega_n)$ or $\Sigma(i\omega_n)$ which is α worry-free while the result is stable because of using (B.5). Given α_0 as the initial value (α_0 can be of the order of 1), the flow diagram in Fig. B.2 describes our algorithm. The final $A(\omega)$ contains all important spectra $A(\alpha, \omega)$, the result is expected to be the most probable spectral function for the given Green's function $G(i\omega_n)$. Moreover, there is no need to search for an appropriate scaling parameter α as this algorithm will search and focus on the range of important α.

After the analytic continuation is set up, within DMFT framework (QMC solver), one can have two ways for continuation and obtaining $A(\omega)$

1. $A(\omega)$ is obtained directly from the Matsubara Green's function given by the impurity solver or when updating the lattice Green's function.

2. $A(\omega)$ is obtained indirectly by first continuing the self energy $\Sigma_R(\omega) = \Sigma(i\omega_n \to \omega + i\delta)$ and then use this $\Sigma(\omega)$ to construct the retarded Green's function [Wang

et al. (2009)].

Appendix C

Lattice distortion

In perovskite with $GdFeO_3$ distoriton, the concept of e_g and t_{2g} bands become ambiguous because of the octahedral rotation if using a global axis for all octahedra in the unit cell. Choosing an appropriate local basis can regain the well-defined t_{2g} and e_g bands. It also reduces the off-diagonal elements of the Green's function, which is the source of severe sign problem in the QMC impurity solver.

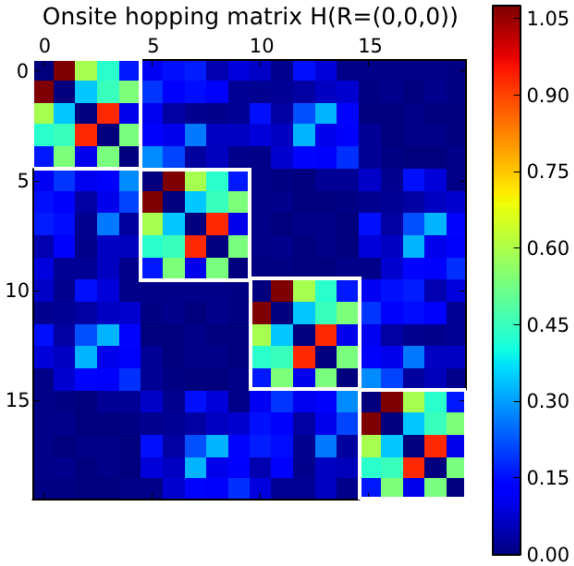

Figure C.1: The original hopping matrix $\hat{h}(\mathbf{R} = (0,0,0))$ for the case of $GdFeO_3$-distorted perovskite with the wavefunction projected onto the subspace of 5 d orbitals. The hopping matrix is 20×20 representing 4 octahedra, each of them has 5 d orbitals.

Finding a local basis means for each octahedron in the unit cell, one needs to find a local coordinates $x'y'z'$ so that the off-diagonal terms in that coordinates is minimized. It thus becomes an optimization problem, given three Euler angles θ, ϕ, γ, one has to find the optimized values of these angles to minimize the off-diagonal elements of the noninteracting density matrix elements or the Green's function.

However, there exists a simpler approximation for this procedure. Consider the tight binding matrix $\hat{h}_{band}(\mathbf{k})$ in (2.10), in real space it is $\hat{h}(\mathbf{R}) = \frac{1}{N}\sum_{\mathbf{k}} e^{i\mathbf{kR}}\hat{h}(\mathbf{k})$, the onsite hopping $\hat{h}(\mathbf{R} = (0,0,0))$ contributes the most to the off-diagonal terms (see Fig. C.1). Eliminating the off-diagonal elements of $\hat{h}(\mathbf{R} = (0,0,0))$ is already good enough to reduce significantly the off-diagonal elements of the Green's function. Therefore, we can simply rotate the basis such that each octahedral block of $\hat{h}(\mathbf{R} = (0,0,0))$ is diagonalized.

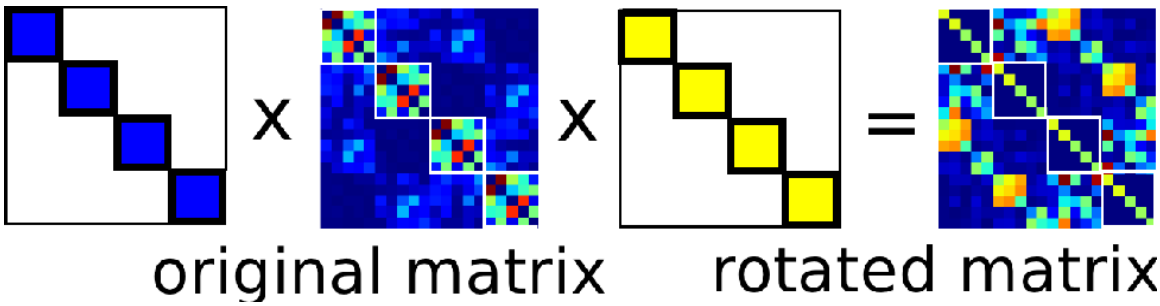

Figure C.2: Apply 4 different transformation matrices to diagonalize 4 diagonal blocks corresponding to 4 different octahedra in the unit cell. These tranformation matrices are rotation matrices needed to minimize the off-diagonal elements of the Green's function.

We demonstrate the procedure in Fig. C.2. Consider the tilted structure in the d-only model with 5 d bands, there are 4 5×5 blocks along the diagonal line which needs to be diagonalized, other blocks are left untouched. Finding transformation matrix to diagonalize a 5×5 matrix is trivial. We thus have 4 5×5 transformation matrices to diagonalize these blocks. These transformation matrices represents rotation matrices needed to rotate the basis and minimize the off-diagonal elements of the Green's function. With these transformation matrices, the DMFT procedure

becomes straightforward. Our procedure to treat the $GdFeO_3$ distortion for DMFT is similar to the approach in Pavarini et al. (2005).

In the case where the distortion is purely because of octahedral rotation, this procedure of minimizing the off-diagonal terms is equivalent to rotating the coordinates to the local coordinates where each axis is along each direction of the octahedron.

Appendix D

Full charge self consistency effect

Throughout the thesis, we run DMFT calculations directly with the fixed tight binding Hamiltonian obtained from the DFT+MLWF method ("one-shot" DMFT). The self consistency procedure [Kotliar et al. (2006); Aichhorn et al. (2009); Haule et al. (2010)], in which the density matrix from DMFT calculation is used as an input in another DFT calculation to adjust the tight binding Hamiltonian so that the charge self consistency is maintained, is neglected. The common belief is that the self consistency does not affect much the final result [Aichhorn et al. (2011); Wang et al. (2012)]. Fig. 4.4 also shares the same thought, in which the DFT+U results (with self consistency effect) are not much different from the Hartree approximation. However, it might be that the self consistency can affect the standard double counting corrections in a different way compared with the one-shot calculation [Aichhorn et al. (2011)]. In this appendix, we study rigorously one case $SrVO_3$ with fully-charged self consistent DMFT calculation to understand how it affects the result.

We use the Wien2K+TRIQS code [Aichhorn et al. (2011); Ferrero and Parcollet (2011)] for the calculation. In this code, the full-potential (linearized) augmented plane-wave (FLAPW) [Blaha et al. (2011)] is used for the DFT calculation, which allows to project the wavefunction into the subspace of localized d and oxygen p orbitals for the DMFT calculation. This projector method works with high reliability and is computationally inexpensive, thus enabling the full-charge self consistency to

U (eV)		full-charge FLL	one-shot FLL	one-shot fixed Δ
5	Δ	7.41	7.17	7.41
	N_d	2.55	2.48	2.52
9	Δ	15.37	14.24	15.37
	N_d	2.51	2.36	2.48
12	Δ	21.20	19.44	21.20
	N_d	2.50	2.30	2.45

Table D.1: Summary of d occupancy and Δ for $SrVO_3$ using FLL double counting corrections, considering the effect from full-charge self consistency (full-charge FLL) or neglecting it (one-shot FLL or one-shot fixed). These calculations use the Wien2k+TRIQS code with projector method for obtaining the localized orbitals, the noninteracting d occupancy obtained from this method is 2.60.

run automatically. To avoid the problem of comparison using different basis sets between MLWF (which is used in most of the calculations) and projector methods, in this appendix, we use only the basis set of p-d subspace is from projector method (provided by Wien2K+TRIQS) for both fully-charged self consistent and one-shot DMFT calculations for comparing the results consistently. The FLL double counting correction is used, as it has been shown to give results closer to experimental data (see Table 4.1 or Karolak et al. (2010)). The onsite interaction is in the form of Slater integrals F_0, F_2, F_4 [Czyżyk and Sawatzky (1994)] related to the Kanamori's notations by

$$U = \bar{U} + \frac{8}{7}\bar{J}, \tag{D.1}$$

$$J = \frac{5}{7}\bar{J}, \tag{D.2}$$

where $\bar{U} = F_0$ and $\bar{J} = \dfrac{F_2 + F_4}{14}$ are the average values of interaction strength.

Table D.1 summarizes the d occupancy and Δ from full charge and one-shot DMFT calculations. The effect of full charge self consistency is to maintain the d occupancy closer to the noninteracting DFT value $N_d = 2.60$, this is similar to

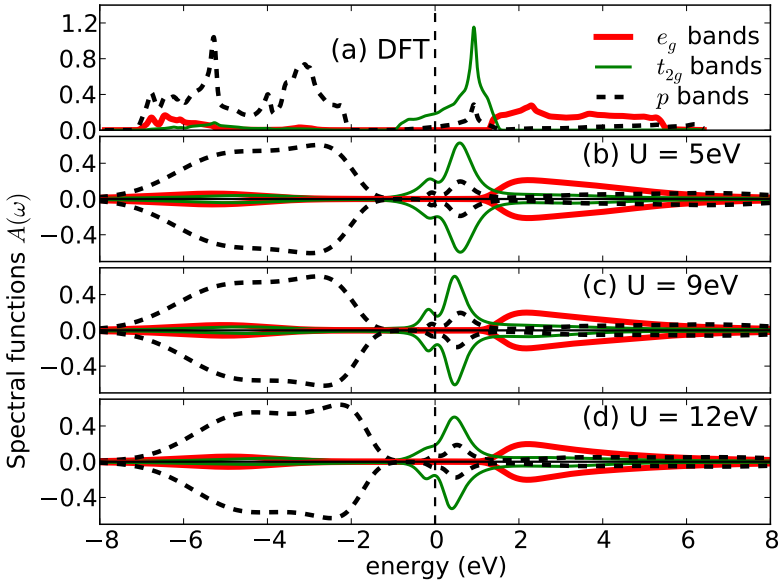

Figure D.1: (Color online) Spectral functions for the e_g, t_{2g} and oxygen p bands of $SrVO_3$ from band structure calculation (a) and full-charge self consistent (positive curves) and "one-shot" (negative curves) DMFT calculations for $U = 5, 9, 12eV$ and $J = 0.65eV$ (b,c,d). The double counting correction and the d occupancy values are shown in the first and the third columns of Table D.1 respectively.

the DFT+U calculation shown in Fig. 4.4, the d occupancy decreases slightly as U increases. If keeping Δ the same as the value in full charge calculation, the one-shot DMFT calculation gives the d occupancy about 0.3 to 0.5 different from the full-charge calculations. The decrease is larger if using the same FLL double counting correction for the one-shot calculation.

Figure D.1 shows the comparison at several U values between full-charge self consistent and one-shot DMFT calculations together with the DFT density of states for reference. There are some important results from this figure. First, full-charge self consistent calculation is almost the same as the one-shot DMFT as long as the d occupancies of the two calculations are adjusted to be the same. Second, for different U values within the standard DFT+DMFT, the d occupancy close to the DFT values, the covalency is so strong that metal-insulator transition cannot occur. Third,

oxygen p bands are slightly shifted closer to the Fermi level with respect to the DFT calculation but stay almost at the same position for different U values.

Therefore, it is reasonable that in our calculation, we neglect the full charge self consistency, which is more computationally expensive and do not allow to adjust the double counting correction arbitrarily. As the full charge self consistent calculation maintains the d occupancy and the oxygen p band position almost unchanged for different U values, these two values can be used as criteria to determine the double counting correction, i.e. to locate a material in the phase diagram.

Appendix E

Determine the metal-insulator transition

Specifying if a state is metal or insulator and studying the metal-insulator transition (MIT) is a fundamental question in strongly correlated systems. Chapter 4 is devoted for the MIT. In this appendix, we presents some methods to determine the state of a system and the critical value for the MIT. Metallic and insulating states are defined based on the spectral function (or density of states) at the Fermi level ν_F. If $\nu_F \neq 0$, it is a metal, otherwise there exists an energy gap at the Fermi level and the system is an insulator.

While this is not a problem in Hartree approximation as the spectra are obtained easily, it is different for DMFT calculation. As described in Section 2.3,the solution after solving the Hamiltonian is the Green's functions represented in imaginary time $G(\tau)$ or Matsubara frequency $G(i\omega_n)$ because of using CT-HYB impurity solver, which causes difficulties in determining metallic/insulating state of a system. Depending on specific situation, we can determine these states in two different ways.

In a direct approach, one checks directly the spectral function for the spectral weight at the Fermi level. It is however difficult because of the analytical continuation to obtain the spectra from $G(\tau)$ or $G(i\omega_n)$. However, as only the low energy range near the Fermi level is important, it is sufficient to analytically continue with low

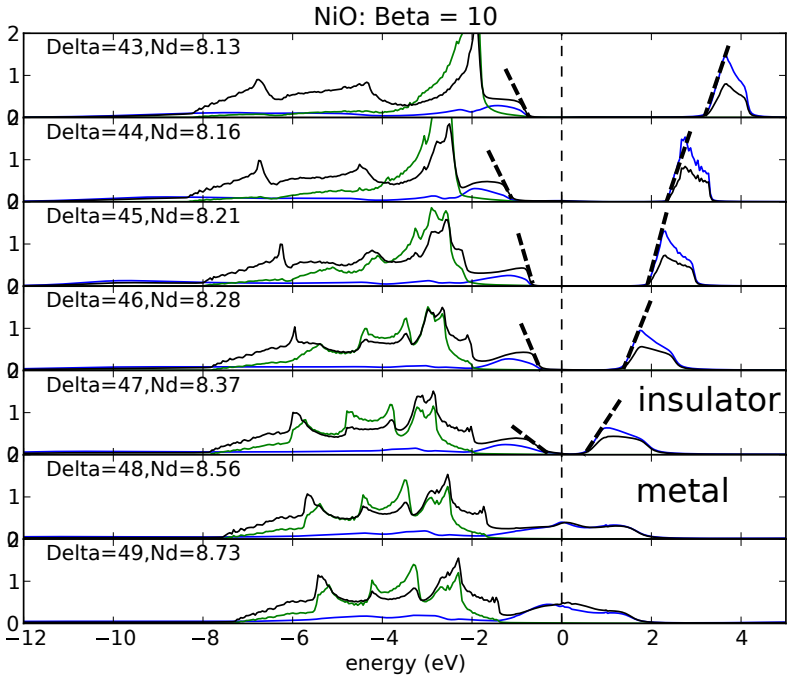

Figure E.1: A demonstration: the metal-insulator transition for NiO at $U = 8eV, J = 1eV$ and inverse temperature $\beta = 10eV^{-1}$. The bare energy d level is adjusted by the double counting correction Δ so that the MIT occurs. The vertical dashed line marks the Fermi level. The thick black dashed lines are fitting lines for determining the energy gap. The MIT occurs as $47eV < \Delta < 49eV$. It is insulating for $\Delta < 48eV$ and metallic for $\Delta = 48$ and $49eV$.

QMC statistics data. For an insulating state, the energy gap is interpolated from fitting the lower and upper band edge near the Fermi level and the MIT point can be extrapolated from a set of band gaps. Figure E.1 is an example for determining the MIT directly from the spectral function. In this figure, the MIT occurs when $47eV < \Delta < 48eV$. By extrapolating the gap (as a function of Δ) to zero, the critical value $\Delta = 47.4eV$ for the MIT.

While direct approach is more complicated because of the analytical continuation, indirect approaches based on results in Matsubara frequency or imaginary time are simpler. The first method is based on the self energy: $Im\Sigma_R(\omega \to 0) = 0$ and

$Re\Sigma_R(\omega \to 0) = Re\Sigma(i\omega_n \to 0)$. The spectral weight at the Fermi level ν_F is

$$\begin{aligned}\nu_F &= -\frac{1}{\pi} ImG_R(\omega \to 0) \\ &= \frac{1}{N}\sum_{\mathbf{k}} \delta\left(\omega + \mu - \epsilon_{\mathbf{k}} - Re\Sigma(\omega)\right)\big|_{\omega\to 0} \\ &= \frac{1}{N}\sum_{\mathbf{k}} \delta(\mu - \epsilon_{\mathbf{k}} - Re\Sigma(\omega \to 0)).\end{aligned} \tag{E.1}$$

The system is metallic or $\nu_F \neq 0$ if $\exists \mathbf{k} \in BZ1$ so that

$$\mu - \epsilon_{\mathbf{k}} - Re\Sigma(\omega \to 0) = 0. \tag{E.2}$$

Otherwise, it is an insulator. As $Re\Sigma_R(\omega \to 0) = Re\Sigma(i\omega_n \to 0) \approx Re\Sigma(i\omega_n = \frac{i\pi}{\beta})$, it is easy to check if $Re\Sigma(i\omega_n = \frac{i\pi}{\beta})$ belongs to the bands given by $\epsilon_{\mathbf{k}} - \mu$. This method however has certain limitations: $\hat{h}_{band}(\mathbf{k})$ should be diagonal which is not the case in general, and the approximation $Re\Sigma_R(\omega \to 0) \approx Re\Sigma(i\omega_n = \frac{i\pi}{\beta})$ may not work well at high temperature.

The second method is to determine $A(\omega = 0)$ from the directly measured imaginary time Green function $G(\tau)$ via

$$\frac{\beta}{\pi} G(\tau = \beta/2) = \frac{\beta}{\pi}\int d\omega \frac{A(\omega)}{2\cosh(\beta\omega/2)} \to A(\omega = 0) \text{ as } T \to 0 \tag{E.3}$$

We identify the material as insulating if $\beta G(\tau = \beta/2)$ decreases as T is decreased and as metallic if $\beta G(\tau = \beta/2)$ increases as T is decreased. The metal insulator transition point can be estimated from the crossing point in a plot of $\beta G(\tau = \beta/2)$ against a parameter such as J at several different temperatures as in Figure E.2.

The direct approach despite is useful as physical quantities such as the energy gap or the spectral function are obtained, however the analytical continuation requires time for running if large number of data points is considered. This approach is

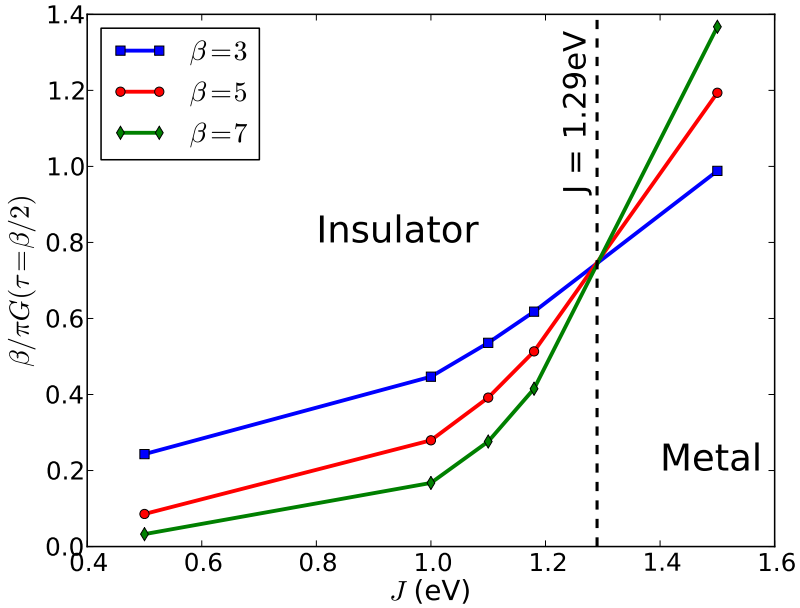

Figure E.2: (Color online) The plot J vs. $\beta G(\tau = \beta/2)$ at fixed $U = 6eV$ for $CaRuO_3$ with three different inverse temperature $\beta = 1/T = 3, 5, 7eV^{-1}$. The intersection of the three β-curves gives the critical $J = J_c \approx 1.29eV$ for the metal-insulator transition. The vertical dashed line marks the critical value $J = J_c = 1.29eV$, separating two regions, insulating and metallic states.

proved to be more powerful and is intensively used in Chapter 4.

For indirect approaches, while we do not use the $Re\Sigma(\omega \to 0)$ method because of difficulties for our study with tilted structure, $\beta G(\tau = \beta/2)$ can be used but may be unstable because of the temperature dependence. As in single-site dynamical mean field theory, the metal-insulator phase boundary has a complicated structure at low T, with a line of first order transitions emerging $T = 0$ second order transition at interaction values U_{c2}, J_{c2} and terminating at a critical endpoint U_{c1}, J_{c1}, T_{c1}, with U_{c1} typically $0.8 - 0.9U_{c2}$ and T_{c1} very low [Georges et al. (1996)]. With $\beta G(\tau = \beta/2)$ method at the temperatures we employ, the metal insulator transition point found is closer to U_{c1} than U_{c2}. The method also costs more computational time because it requires calculations for different temperature, it is applied in Chapter 3 because data for different temperature is already obtained.

Appendix F

CTQMC impurity solver

The continuous time Quantum Monte Carlo impurity solver (CTQMC) in the hybridization expansion version (CT-HYB) is the main solver that we use for every work in this thesis. The details of the solver can be found in Werner et al. (2006); Werner and Millis (2006); Haule (2007); Gull et al. (2011). In this appendix, we only present some technical notes to run the impurity solver efficiently and obtain reliable results.

Following Werner and Millis (2006), the impurity Hamiltonian (2.47) is rewritten as

$$H_{imp} = H_{loc} + H_{bath} + H_{hyb} + H_{hyb}^{\dagger}, \tag{F.1}$$

where the "local" Hamiltonian H_{loc} contains the interaction and the bare energy levels of the impurity

$$H_{loc} = \sum_{\alpha\beta} \bar{h}_{\alpha\beta} c_{\alpha}^{\dagger} c_{\beta} - \mu \sum_{\alpha} n_{\alpha} + \sum_{\alpha\beta\gamma\delta} I_{\alpha\beta\gamma\delta} c_{\alpha}^{\dagger} c_{\beta} c_{\gamma}^{\dagger} c_{\delta}, \tag{F.2}$$

$H_{bath} = \sum_{\mathbf{k}} \epsilon_{\mathbf{k}} a_{\mathbf{k}}^{\dagger} a_{\mathbf{k}}$ and $H_{hyb} = \sum_{\mathbf{k}\alpha} V_{\mathbf{k}}^{\alpha} a_{\mathbf{k}}^{\dagger} c_{\alpha}$; $\alpha, \beta, \gamma, \delta$ are indices of the impurity sites (see Section 2.3).

To formulate the formula for Monte Carlo method, one has to write the partition function $Z = \mathrm{Tr}[\exp(-\beta H_{imp}]$ as a sum of all possible configurations. In the hy-

bridization expansion approach, it can be done by expanding the term H_{hyb} [Werner and Millis (2006)]

$$\begin{aligned} Z &= \mathrm{Tr}[\exp(-\beta(H_{loc}+H_{bath}+H_{hyb})] \\ &= \sum_n \left(\frac{1}{n!}\right)^2 \int d\tau_1 \dots d\tau_n d\tau_1' \dots d\tau_n' \times \\ &\times \mathrm{Tr}\left[T_\tau e^{-\int (H_{loc}^{(\tau)}+H_{bath}^{(\tau)})d\tau} H_{hyb}^{(\tau_1)} \dots H_{hyb}^{(\tau_n)} H_{hyb}^{(\tau_1')\dagger} \dots H_{hyb}^{(\tau_n')\dagger}\right] \end{aligned} \tag{F.3}$$

$$\begin{aligned} Z \sim &\sum_n \int d\tau_1 \dots d\tau_{2n} \det \Delta \times \\ &\times \mathrm{Tr}\left[e^{-(\beta-\tau_{2n})H_{loc}} O_{2n} e^{-(\tau_{2n}-\tau_{2n-1})H_{loc}} \cdots e^{-(\tau_2-\tau_1)H_{loc}} O_1 e^{-\tau_1 H_{loc}}\right]. \end{aligned} \tag{F.4}$$

The bath fermions $a_{\mathbf{k}}^\dagger$ and $a_{\mathbf{k}}$ can be integrated out exactly as they are only in the quadratic form, resulting in the determinant of the hybridization function $\det\Delta$ in (F.4). The operators O_i are either $c^\dagger$ or c, impurity creation and annihilation operators. The trace of $\{O_i\}$ operators is the result of the expansion in H_{hyb}. The final form (F.4) is ready for Monte Carlo simulation.

From (F.4), the basic input for the CT-HYB solver contains the hybridization function $\Delta(\tau)$, the parameters to control the QMC simulation and the "local" Hamiltonian matrix H_{loc}.

The hybridization Δ (2.49) is directly obtained from the Weiss field G_0. As $\Delta(\tau)$ (in imaginary time) is required for the CT-HYB impurity solver while the Matsubara frequency form $\Delta(i\omega_n)$ is necessary for the DMFT self consistent loop. The inverse Fourier transformation $\Delta(i\omega_n) \to \Delta(\tau)$ needs to be conducted carefully by including the asymptotes of $\Delta(i\omega_n)$ up to $\dfrac{1}{\omega_n^2}$ in order to obtain a smooth $\Delta(\tau)$. The number of time slices τ_i should be large, e.g. our number of time slices is 10000, which allows the Fourier transformation of the output impurity Green's function $G(\tau)$, which also has the same number of time slices, to the Matsubara Green's function $G(i\omega_n)$ easily by using simple trapezoidal or Simpson's rule for integration.

There are several important parameters to control the QMC process. The first two parameters are the number of Monte Carlo (MC) measurements N and the number of MC updates between two consecutive measurements N_m. Because in the MC process, each random walk of the Markov chain in the configuration space should be independent to each other. In practice, that correlation exists which is represented by autocorrelation time measurement. N_m is introduced to reduce the correlation between two consecutive configurations. The total updates is $N_m \times N$. Depending on specific situation, N and N_m are adjusted correspondingly. At the beginning, $N_m = 100$ and $N = 50 \times 10^6$ may be chosen and will be adjusted after some test calculations for an optimized values.

Another QMC parameter is the number of MC measurement for thermalization N_T. QMC solver needs to "warm up" for N_T measurements, after that it can produce relatively independent random walk for the Markov chain independent of the initial conditions. For most of the cases (intermediate and high temperature calculations), this parameter is unimportant as the process is thermalized quickly. Only for very low temperature cases (such as in Figure F.1), the system becomes thermalized slower, N_T should be set more carefully. The inset of Figure F.1 shows the signal for simulation with not enough thermalization time, the imaginary part of the self energy for the first Matsubara point deviate away from the thermalized calculation. We think the value $N_T \sim 10^5$ can be a reasonable range of values as it is applicable for a wide range of temperature and also does not require much computational time.

Depending on the form of H_{loc} (especially $I_{\alpha\beta\gamma\delta} c^\dagger_\alpha c_\beta c^\dagger_\gamma c_\delta$), there are different ways to speed up the process, mostly based on the conserved quantity (or the operator $\hat{L}$ which commutes with H_{loc}). It is because in the simulation, the most time-consuming step is the calculation of the trace in (F.4). Knowing conserved quantities allows to block diagonalize $\hat{O}_n$, thus speed up the matrix multiplication and the trace calculation. In the interaction form that we use in the thesis (2.23) (see also Appendix A

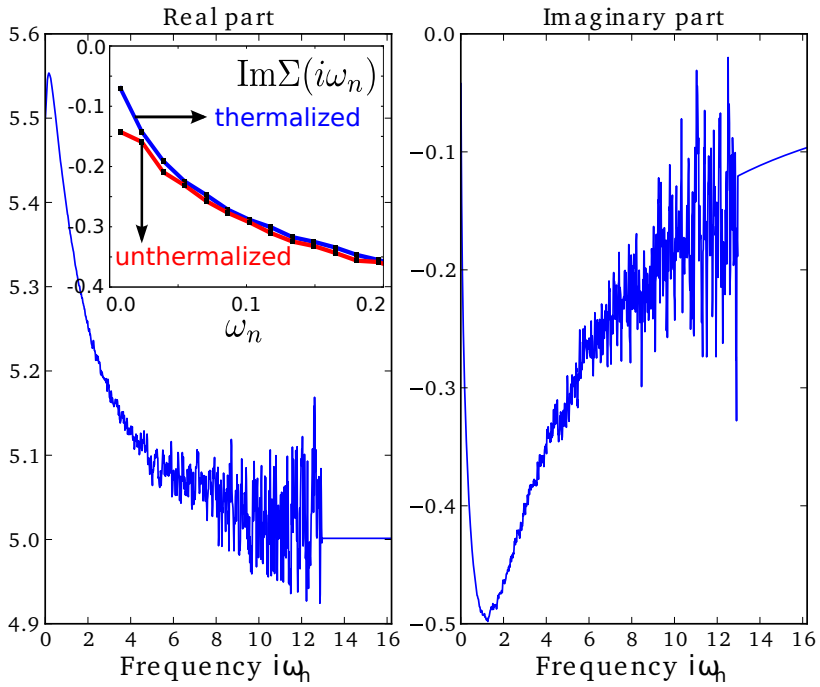

Figure F.1: An example of the self energy $\Sigma(i\omega_n)$ from a converged QMC simulation: a 3-orbital model calculation with rotationally invariant interaction at very low temperature $T = 0.0025eV$ for $U = 2.3eV, J = 0.4eV$ and bandwidth $W = 2.5eV$. QMC parameters are $N = 100 \times 10^6, N_m = 50$ and $N_T = 10^6$. The part with $\omega_n > 13$ is replaced by the asymptotic curve. Inset: thermalized calculation ($N_T = 10^6$) vs. unthermalized calculation ($N_T = 300$) for the same model and parameters.

for details), assume that $\bar{h}_{\alpha\beta}$ is diagonal, there are two cases

1. Rotationally invariant interaction (2.23): first, the total occupancies with spin up and down $\hat{N}_\uparrow$ and $\hat{N}_\downarrow$ are commonly used as conserved quantities. Recently, Parragh et al. (2012) found that $(\hat{n}_{\alpha\uparrow} - \hat{n}_{\alpha\downarrow})^2$ for all orbital α are also good conserved quantities, the use of these numbers can also speed up the calculation to 2-3 times more for the 3-orbital interaction.

2. Ising interaction (when there are no exchange and pair hopping terms in (2.23)), $[n_\alpha, H_{loc}] = 0$ for all α allows very effective block diagonalization. In this special case, "segment" algorithm [Werner et al. (2006)] is applied which can speed up

the simulation to more than 5 times (compared with the rotationally invariant interaction with N_σ conserved number). However, this form of interaction may give deep landscape in the QMC, especially at low temperature, that traps the Markov chain in one place in the configuration space, which may require certain global update to avoid that issue. In the physical sense, it is not rotationally invariant thus is an approximation to the interaction used in multiorbital systems.

It is not easy to find a criterion for the convergence of a QMC simulation. In principle one has to check the QMC error to see if it is smaller than some ϵ which is not known, it is also inconvenient as there are $10 \to 20$ QMC simulations running automatically for a DMFT calculation. In practice, one can check the output self energy which has increasingly large QMC error as the frequency increases. Figure F.1 is an example of a QMC simulation which is well-converged. Our rule of thumb is that the simulation converges when the output self energy for $\omega_n < \omega_c$ (we choose the cutoff $\omega_c = 6 \to 7U$) has the real part approaches a constant (the Hartree shift) as $\frac{1}{\omega_n^2}$ and the imaginary part tends to approach 0 as $\frac{1}{\omega_n}$. The number of QMC measurements N is adjusted until these behaviors are observed, it will then be used for the DMFT calculations.